



HAL
open science

Exploring interface mechanisms in metal-ion batteries via advanced EQCM

Pierre Lemaire

► **To cite this version:**

Pierre Lemaire. Exploring interface mechanisms in metal-ion batteries via advanced EQCM. Material chemistry. Sorbonne Université, 2020. English. NNT : 2020SORUS211 . tel-03347410

HAL Id: tel-03347410

<https://theses.hal.science/tel-03347410>

Submitted on 17 Sep 2021

HAL is a multi-disciplinary open access archive for the deposit and dissemination of scientific research documents, whether they are published or not. The documents may come from teaching and research institutions in France or abroad, or from public or private research centers.

L'archive ouverte pluridisciplinaire **HAL**, est destinée au dépôt et à la diffusion de documents scientifiques de niveau recherche, publiés ou non, émanant des établissements d'enseignement et de recherche français ou étrangers, des laboratoires publics ou privés.



Sorbonne Université

Ecole doctorale 397 – Physique et Chimie des Matériaux

Collège de France: Chaire de Chimie du Solide et Energie

Exploring interface mechanisms in metal-ion batteries *via* advanced EQCM

By Pierre Lemaire

Ph.D. thesis of Physics and Chemistry of Materials

Supervised by Jean-Marie Tarascon and Özlem Sel

Presented and defended publicly on December 16th, 2020

In front of the jury:

Dr. Véronique Balland	Associate Professor, LEM, Paris	Referee
Prof. Patrice Simon	Professor, CIRIMAT, Toulouse	Referee
Dr. Fannie Alloin	Research Director, LEPMI, Grenoble	Examiner
Dr. Erik Berg	Associate Professor, Uppsala University	Examiner
Prof. Mathieu Salanne	Professor, PHENIX, Paris	Examiner
Dr. Hubert Perrot	Research Director, LISE, Paris	Invited member
Dr. Özlem Sel	Research Scientist, LISE, Paris	Co-director
Prof. Jean-Marie Tarascon	Professor, CSE, Paris	Director



Except where otherwise noted, this work is licensed under
<http://creativecommons.org/licenses/by-nc-nd/3.0/>

Sorbonne Université

Ecole doctorale 397 – Physique et Chimie des Matériaux

Collège de France : Chaire de Chimie du Solide et Energie

Exploration des mécanismes interfaciaux présents dans les batteries métal-ion par EQCM avancée

Par Pierre Lemaire

Thèse de doctorat de Physique et Chimie des Matériaux

Dirigée par Jean-Marie Tarascon et Özlem Sel

Présentée et soutenue publiquement le 16 Décembre 2020

Devant un jury composé de :

Dr. Véronique Balland	Maître de Conférences, LEM, Paris	Rapporteuse
Prof. Patrice Simon	Professeur, CIRIMAT, Toulouse	Rapporteur
Dr. Fannie Alloin	Directrice de Recherche, LEPMI, Grenoble	Examinatrice
Dr. Erik Berg	Maître de Conférences, Uppsala University	Examineur
Prof. Mathieu Salanne	Professeur, PHENIX, Paris	Examineur
Dr. Hubert Perrot	Directeur de Recherche, LISE, Paris	Membre invité
Dr. Özlem Sel	Chargée de Recherche, LISE, Paris	Co-directrice
Prof. Jean-Marie Tarascon	Professeur, CSE, Paris	Directeur

Acknowledgments

These three years have been a long and challenging journey but they were worth it. I have been lucky to work in an extraordinary environment that is the Collège de France, and to meet amazing people always opened to share about science. For all these reasons, I would like to thank Jean-Marie Tarascon for giving me the opportunity to be a part of the CSE lab. His energy, his passion for science and his demanding nature have always been a motivation to push my limits and to give the best of myself to reach my targets. I am also thankful for his great availability helping me successfully complete this thesis.

I would like to acknowledge the great help of Daniel Alves Dalla Corte who helped me settle down during the initial months of my Ph.D. with my subject but more importantly in the lab. I sincerely thank Özlem Sel for her enthusiasm and optimism (in comparison with me), she has been a great mentor and of great help during these three years. I would like to extend my acknowledgments to Hubert Perrot with whom I had fruitful discussions about QCM.

Some of the work presented in this manuscript would not have been possible without the help and the collaboration of Antonella Iadecola (XAS), Alessandra Serva and Mathieu Salanne (MD), Paul Pearce and Thomas Marchandier (XRD, Rietveld refinement) that I sincerely acknowledge. This work could not have been carried out without the Collège de France and the funding from the European Research Council (ERC) (FP/2014)/ERC Grant-Project 670116-ARPEMA.

I am grateful to Véronique Balland and Patrice Simon for accepting the role of referee of this thesis and of course to Fannie Alloin, Erik Berg and Mathieu Salanne for agreeing to be part of the jury. I thank all of them for their time and I hope the manuscript made them think about something else during this difficult period.

Of course, I am extending my acknowledgments to all the lab members with whom I shared a part of these three years. I particularly thank Sathiya and Claudio for their daily kindness. I really enjoyed discussing with Ivette who “endured” to work with me for the beginning of her thesis. And last, but not least, I am immensely grateful to have met Fanny, Léa, Nicolas and Thomas who greatly contributed to my good mood in and out the lab.

Finally, I would like to thank my girlfriend's family and my family for their great support during this period and especially my family without whom, none of this would have been possible. And the best for last, my girlfriend Auriane, she has always been positive and cheerful for the last six years and I want to thank her warmly for her lovely encouragements and her patience during these past three years, I dedicate this thesis to her.

Table of Contents

Acknowledgments	5
Table of Contents	7
Broader context and thesis outline	11
○ From global warming to battery advent.....	11
○ Battery market and applications	13
○ Thesis outline	14
Chapter I – The battery technology: State of the art	17
I.1 – Today’s battery to post Li-ion technologies.....	17
I.1.a – Concept discoveries and fundamentals	17
I.1.b – From Li batteries to Li-ion batteries.....	18
I.1.c – Post Li-ion battery technologies and their promises.....	22
I.2 – In the quest of better batteries	28
I.2.a – Higher energy materials	28
I.2.b – Improve the lifetime, the reliability and the power density	31
I.3 – Chapter conclusions	38
Chapter II – An overview of the electrogravimetric, hydrodynamic and viscoelastic techniques	41
II.1 – Introduction	41
II.2 – Quartz Crystal Microbalance theory and associated techniques	41
II.2.a – Quartz Crystal Microbalance fundamentals.....	41
II.2.b – Gravimetric and viscoelastic read-out methods	47
II.2.c – Comparison of the different QCM-based read-out methods.....	53
II.3 – Electrogravimetric, hydrodynamic and viscoelastic inputs to the battery field so far	55
II.3.a – EQCM-based methods for the study of Solid Electrolyte Interphase	55
II.3.b – Mechanical properties of the electrodes during cycling.....	57
II.3.c – Characterization of the cation insertion in battery compounds	58
II.4 – EQCM-based strategies developed and employed in this Ph.D. thesis.....	59
II.4.a – Classical EQCM-R measurements adapted to battery electrode characterization	59
II.4.b – Determination of the film hydrodynamic and viscoelastic properties	61
II.4.c – Dynamic characterization of the electrode-electrolyte interface	65

II.5 – Chapter conclusions	72
----------------------------------	----

Chapter III – Making advanced electrogravimetry as an affordable analytical tool for the battery interface characterization75

III.1 – Introduction.....	75
III.2 – Optimization of the electrode preparation on EQCM resonators	76
III.2.a – Description of the preparation protocol.....	76
III.2.b – Evaluation of the suitable conditions for electrode preparation by EQCM-R.....	80
III.3 – Design and validation of airtight EQCM cell testing workbench.....	82
III.3.a – Cell presentation.....	82
III.3.b – Cell evaluation	84
III.3.c – Calibration factor estimation	87
III.4 – Verification of hydrodynamic and viscoelastic properties in electrolyte	89
III.4.a – Rigidity assessment.....	89
III.4.b – <i>In situ</i> hydrodynamic spectroscopy of the composite electrode	90
III.5 – Electrochemical-gravimetric measurements of an intercalation material	92
III.5.a – Viscoelastic properties upon cycling.....	92
III.5.b – Direct outputs of EQCM-R on an intercalation compounds.....	94
III.5.c – New insights on the insertion mechanism at electrode-electrolyte interface	96
III.6 – Simulation of the interface between the electrolyte and a model electrode	98
III.6.a – Interfacial density profiles of the different species involved	98
III.6.b – Energy landscape and solvation from the electrolyte bulk to the interface	100
III.7 – Chapter conclusions	102

Chapter IV – Probing the electrode-electrolyte interface of potassium-ion battery – Aqueous vs. Non-aqueous electrolytes 105

IV.1 – Introduction.....	105
IV.2 – Phase preparation and characterization.....	106
IV.2.a – Morphological and structural description.....	106
IV.2.b – Water incorporation in the structure lattice.....	109
IV.2.c – Thickness control of the prepared films	111
IV.3 – Electrochemical and electrogravimetric analyses.....	112
IV.3.a – Rate capability assessment.....	112
IV.3.b – Determination of the rate-limiting step.....	116
IV.3.c – First evidence of the potassium solvation shell at the interface.....	119

IV.4 – Final evidence of the involved species at the EEI and their associated interfacial kinetics	122
IV.4.a – Identification of the nature of species and their dynamics at EEI	122
IV.4.b – Study of the interfacial kinetics associated to the involved species.....	125
IV.5 – Chapter conclusions.....	128

Chapter V – Elucidating the origin of the electrochemical capacity in proton-based battery: a framework to assess the water contribution at the interface
..... **131**

V.1 – Introduction	131
V.2 – Phase characterization.....	132
V.2.a – Morphological and structural description.....	132
V.2.b – Stoichiometry determination.....	133
V.3 – Electrochemical analyses	134
V.3.a – Cycling behavior	134
V.3.b – Assessment of the pseudocapacitive mechanism	136
V.4 – Electrochemical-gravimetric investigation	137
V.4.a – Validation of the gravimetric regime	137
V.4.b – Kinetic comparison between the two regions	139
V.4.c – Evidences of the water participation in the insertion mechanism	141
V.5 – Species determination and associated kinetics at the EEI	143
V.5.a – Identification of the nature of species and their dynamics at EEI	143
V.5.b – Outcomes of the kinetic study	146
V.6 – Chapter conclusions.....	148

General conclusions **153**

Materials & Methods **157**

M.1 – Material preparation and characterization	157
M.1.a – Used and synthesized battery materials.....	157
M.1.b – Material characterization.....	158
M.2 – Classical electrochemical characterization.....	161
M.2.a – Electrode preparation	161
M.2.b – Classical electrochemical setup	161
M.2.c – Electrochemical cycling	162
M.2.d – Diffusion coefficient determination.....	163
M.3 – Electrochemical-gravimetric analysis	166

M.3.a – EQCM electrode preparation	166
M.3.b – Airtight EQCM cell testing workbench	167
M.3.c – Verification of hydrodynamic and viscoelastic properties in electrolyte	168
M.3.d – Electrochemical-gravimetric measurements	168
M.3.e – Ac-electrogravimetry.....	169
M.4 – Classical Molecular Dynamics simulations.....	172
Glossary	173
References	179
Résumé.....	197
Abstract	198

Broader context and thesis outline

o From global warming to battery advent

The Paris Agreement on climate change was adopted by consensus (195 states) on 12 December 2015. Its aim is to strengthen the global response to the threat of climate change by keeping a global temperature rise this century well below 2 degrees Celsius above pre-industrial (the mid-19th century) levels and to pursue efforts to limit the temperature increase even further to 1.5 degrees Celsius.¹ Climate change is caused by natural processes such as volcanic eruptions, variations in Earth's orbit or changes in the solar radiation. However, human activities also have an impact on the average Earth temperature. Measurements show that averaged over the globe, the surface has warmed by about 0.95 °C since 1850, making 2019 the second warmest year.^{2,3} If the world continues along its present path, without any additional changes in policy, energy demand will rise by 2.1% each year until 2040, particularly driven by the strong growth of developing economies.⁴ To respond to this rising demand, historical and current energy systems, which are dominated by fossil fuels combustion (coal, oil and gas), cannot be relied upon. These hydrocarbon deposits represent around 85 % of the energy consumed in the world and it is the fundamental driver of global climate change by producing carbon dioxide (CO₂) and other greenhouse gases.^{5,6} An energy sector transformation is required to curtail CO₂ emission and global warming. It depends upon fundamental changes in to the way energy is produced and consumed: transition towards renewables in the energy supply, reduce energy consumption and improve the efficiency of our energy systems, electrify the transportation sector, as well as innovate on carbon capture, utilization and storage (CCUS) technologies (Figure 1a).

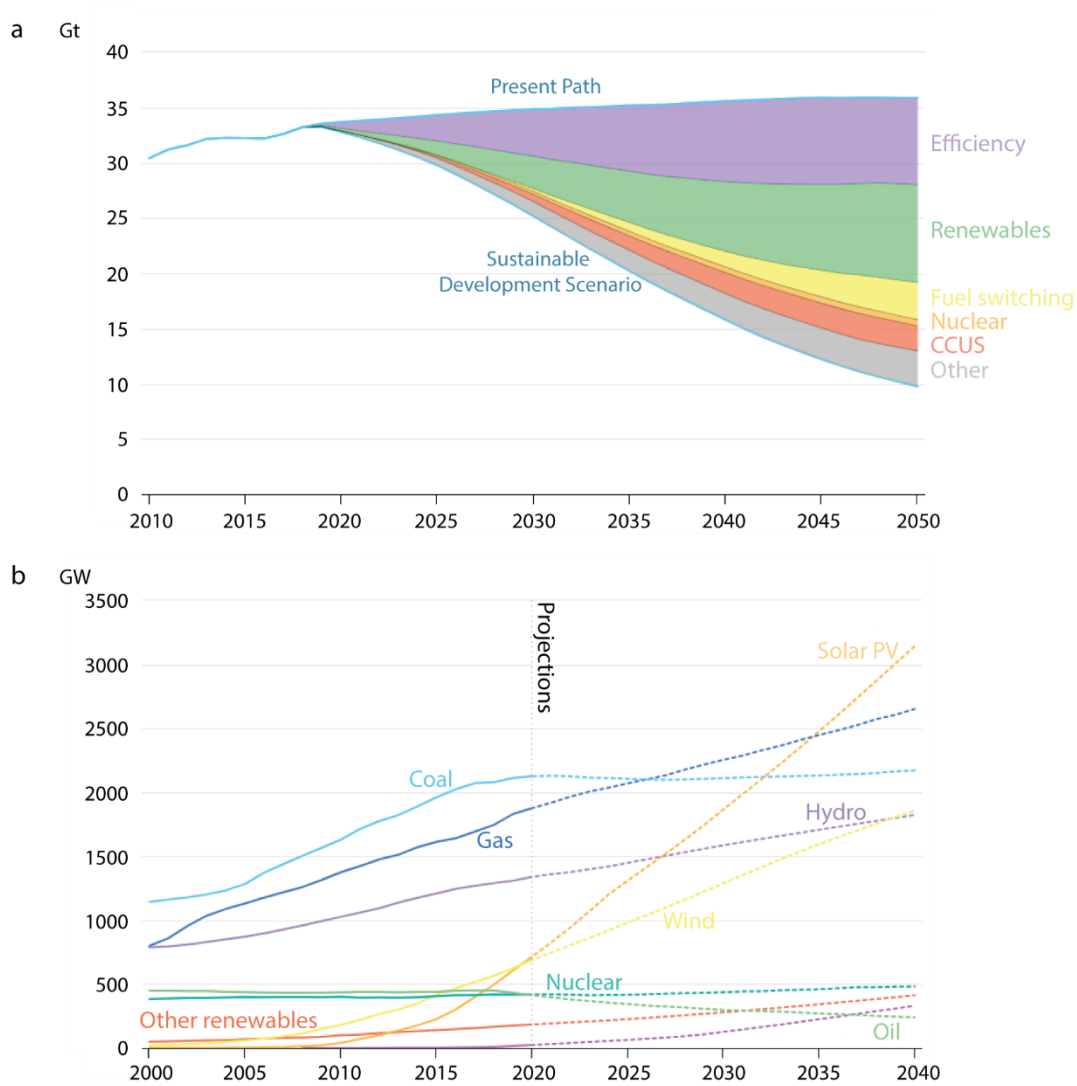


Figure 1: (a) CO₂ emissions reductions by measure in the Sustainable Development Scenario relative to the present path. (b) Current and future installed power generation capacity by source. Adapted from: *IEA World Energy Outlook 2019*.⁴

By 2040, low-carbon sources like wind and solar PV provide more than half of total electricity generation (Figure 1b). These sources are “unlimited” and available everywhere, but they suffer from intermittence. Their democratization nests in the development of energy storage technologies uncoupling the electricity production and its utilization, along with enabling flexibility to the electrical network. Energy storage technologies are many and varied and they can be divided into electrical, electrochemical, thermal and mechanical. Among these, electrochemical technologies, such as batteries, fuel cells and supercapacitors, have experienced major research and innovation in the recent years.

o Battery market and applications

In 2018, rechargeable batteries represent 81 billion U.S. \$ with a growth comprised between 7 and 9 % compared with the previous year and increasing since 1990.⁷ The Figure 2b shows that the Lead-acid technology is dominating the battery market, used as Start Light and Ignition batteries (SLI) in combustion engine vehicles, owing to its low cost and long cycle life. Nevertheless, the Lithium ion technology has gained more and more market shares since the last decade with the highest growth and the major part of the investments. This technology has the advantage of higher gravimetric and volumetric energy densities enabling the development of portable electronics and power tools (Figure 2b).

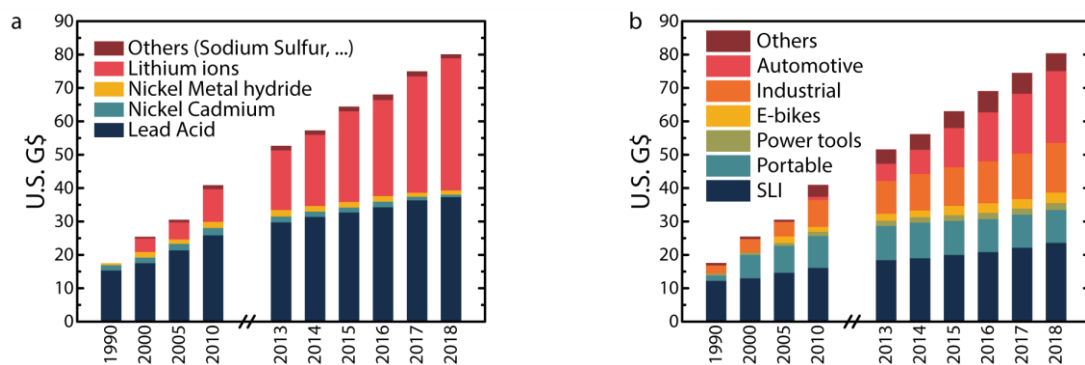


Figure 2: Market share of the worldwide rechargeable battery market from 1990 to 2018 in terms of (a) technologies and (b) applications. Adapted from: *Avicenne Energy 2019*.⁷

Within the last decade, batteries have become about four-times cheaper and can now store up to three-times more energy within the same volume.⁷ These progress have been enabled thanks to innovations in battery chemistry, cell engineering and optimization and growth of manufacturing volume (mass production). At this pace, battery prices are projected to drop below U.S. \$100 per kWh by 2025. This price target, which allows electric vehicles to achieve price parity with gasoline cars without any subsidies⁸ will be reached in 2020 by Tesla according to Elon Musk. The current strategy is to develop new electrode materials to improve the Li-ion battery performances such as the energy densities (*i.e.* higher range) and the rate capability (*i.e.* faster charge), in concert with cost reducing. However, such an approach only based on Li-ion technology improvements by material science is limited by the chemistry and the abundancy of the suitable elements. Another figure of merit is to explore the essential role played by the electrode-electrolyte interface (EEI) and its impact on the physicochemical properties of ion intercalation as the interface is known to control the battery lifetime and

reliability. Moreover, such a study can bring new insights to post Li-ion technologies. As the battery applications are not limited to mobility but also to stationary Energy Storage Systems, the emergence of new chemistries – safer, cheaper and more abundant – is predictable.

o Thesis outline

The aim of this thesis is to contribute to the better understanding of the role played by the electrode-electrolyte interface in the battery field and especially in the case of “beyond lithium-ion” chemistries. Advanced electrogravimetry techniques were specifically developed and employed for this purpose. Electrochemical characterization techniques and X-ray spectroscopies completed the panel of experimental tools.

It is structured into the following five chapters:

Chapter I begins with an introduction to the key steps, which led to the development of today’s Li-ion batteries before focusing to central topic of this Ph.D. manuscript: the mechanisms taking place at the electrode-electrolyte interface and especially the insertion mechanism.

Chapter II proposes an in-depth presentation of the QCM fundamentals and the available toolbox of QCM-based techniques. Moreover, a comprehensive analysis of the current literature gathering QCM-based techniques to the battery field is provided and the strategies developed during this Ph.D. thesis to characterize in the insertion/extraction mechanism are described.

Chapter III presents a package to prepare and to perform electrogravimetric studies on battery active materials in the suitable conditions to obtain reliable data. First results on the solvation shell of lithium ions at the electrode-electrolyte interface during insertion in LiFePO₄ phase are depicted.

Chapter IV further investigates the role of the desolvation step on the rate capability discrepancy between aqueous and non-aqueous electrolytes by moving to the study of the potassium ion insertion in Prussian Blue phase. A rationalization in terms of number molecules

pertaining to the solvation shell at the EEI in both electrolytes is proposed to explain the rate capability discrepancy.

Chapter V is dedicated to determine the water molecules role in the interfacial transfer process and their influence on the overall kinetics of a proton-based battery. Moreover, the potential-dependent mechanism involving different reacting species in the proton insertion is demonstrated.

Altogether, we hope this work will help in a wider acceptance of EQCM techniques by the battery community to study a wide panel of active electrode materials but also a broad variety of electrode-electrolyte interface phenomena such as ion solvation and transport for instance.

Chapter I – The battery technology: State of the art

I.1 – Today's battery to post Li-ion technologies

I.1.a – Concept discoveries and fundamentals

The first electrochemical storage device was Volta's cell (1800) that is built of alternating discs of zinc and copper separated by cardboard and using a brine solution as the electrolyte.⁹ This is the same cell that we build with young scientists during science fairs using a lemon as the electrolyte. The Volta cell evolved first into the Daniell cell (1836) constituted of two electrolytes, and then into the Leclanché cell (1866) that used a zinc anode and a manganese dioxide cathode.¹⁰ Today's small dry cell using an alkaline electrolyte, a zinc anode, and a manganese oxide cathode was not invented until 1949 by Union Carbide. These are all primary cells, and not usually rechargeable. Rechargeable, also known as secondary, batteries have evolved over the years from lead acid (Gaston Planté in 1859) through nickel–cadmium (1899) and nickel–metal hydride, NiMH, (mid-1980s) to Li-ion (1977).¹¹ To compare them, some metrics need to be introduced: the amount of electrical energy that a battery is able to deliver in total. It is expressed either per unit of weight (Wh.kg^{-1}) or per unit of volume (Wh.L^{-1}) or in terms of power density (W.kg^{-1} or W.L^{-1}). The energy density is a function of the cell potential (V) and capacity (Ah.kg^{-1}), both of which are linked directly to the chemistry of the system. The Figure I-1 compares these different chemistries of battery as a function of the previously defined measures. Last criterion of importance is to compare these technologies on the same level, along the battery value chain.¹² Here, they are calculated at cell-level, which permits an intrinsic comparison of the different chemistries before their integration in a pack for practical application.

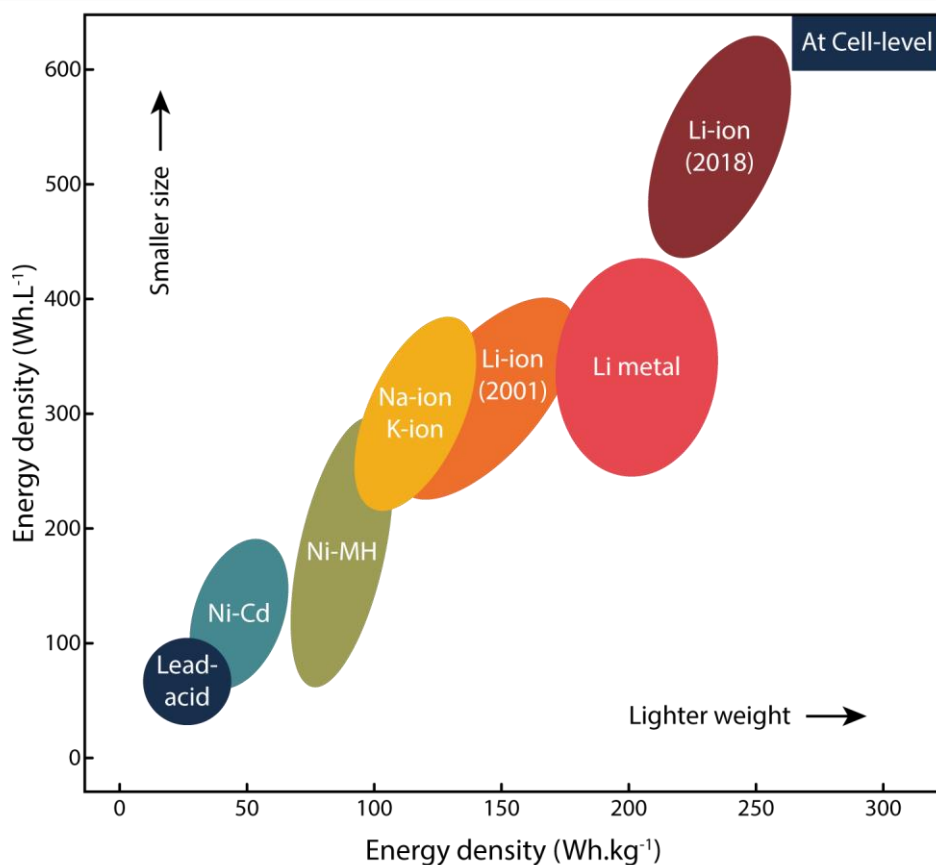


Figure I-1: Today's battery technologies compared in terms of volumetric and gravimetric energy density. Originally reported in 2001 by *Tarascon and Armand*¹³ and completed with more recent references.^{14,15}

Na and K-ion batteries, contrary to the Li-ion technology, are nowadays under development and are not yet commercialized; their concepts will be described in more details later in this chapter. Lastly, with the exception of Ni-Cd batteries that are banned by the European Union, all the others technologies listed in the Figure I-1 are still currently produced and employed in different applications depending on their intrinsic performances and cost. However, as shown in the Figure I-1, the lithium technology offers attractive performances in terms of volumetric and gravimetric energy density that explain its supremacy on the market sales.

I.1.b – From Li batteries to Li-ion batteries

The high energy density of a battery technology based on Li metal as anode relied initially on the fact that lithium is the lightest metal ($M = 6.94 \text{ g.mol}^{-1}$) and it has a low redox

potential (-3.04 V vs. SHE) as well as a high theoretical capacity (3862 mAh.g⁻¹), thus facilitating the design of storage systems with high energy density. In the 1970s, the discovery of the reversible reaction of chalcogenides^{16,17} (TiS₂, MoS₂, ...) with alkali metals, called the concept of intercalation, led to the development of the first Li metal secondary batteries. TiS₂ with its favorable layered-type structure was selected in 1972 by Exxon and M. Stanley Whittingham^{18,19} as the positive electrode for the first Li metal system. Then, in 1986, the company Moli Energy commercialized the first lithium battery using MoS₂ and Li metal as positive (cathode) and negative (anode) electrodes, respectively. Regardless of the positive electrode material, the Li metal battery follows these redox reactions:



with M = transition metal and A = O or S

As depicted in the Figure I-2a, the positive (cathode) and negative (anode) electrodes are separated by a thin electron-insulating layer, the separator, soaked with the electrolyte composed of a lithium salt and an organic solvent. During discharge, the reactions given by Equation I-1 and Equation I-2 take place and the lithium ions move from the negative to the positive electrode creating a flux of electrons in external circuit, the source of electrical energy.

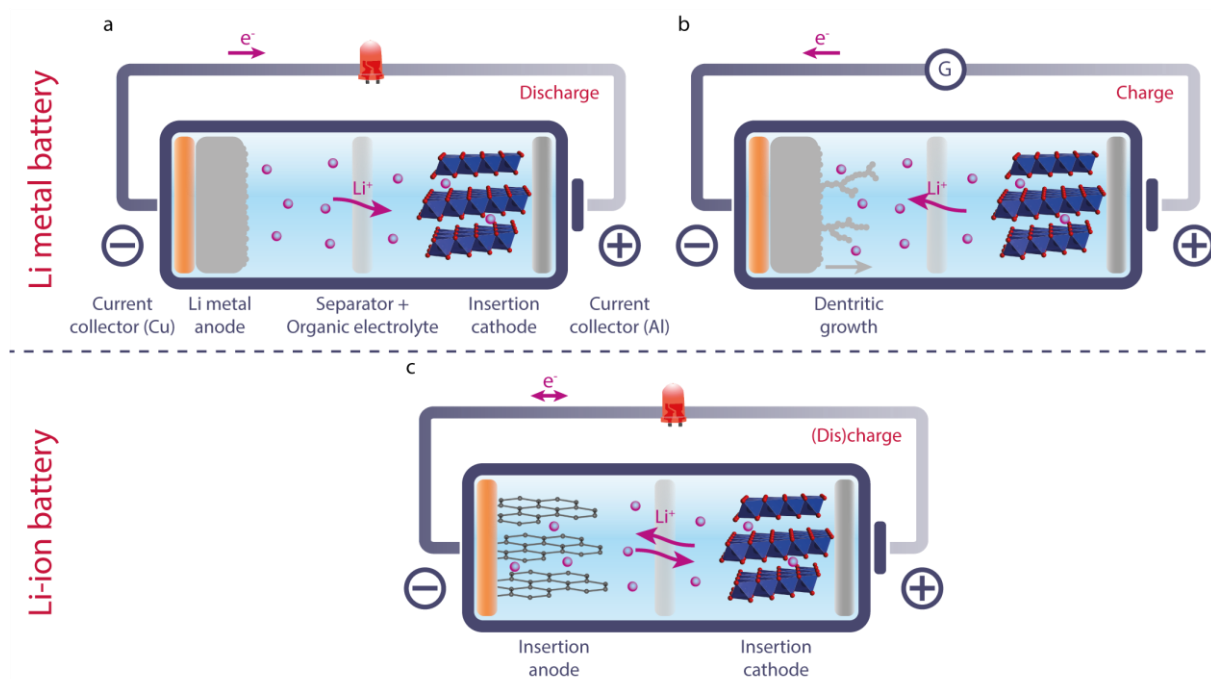


Figure I-2: Schematic representation of Li batteries. The ionic and electronic flows are symbolized for the Li metal battery (a), which can lead to the dendritic growth (b), and the Li-ion battery (c).

However, some unresolved safety issues remained in Li metal battery technology, among others, the reactivity of the flammable organic electrolyte with metallic Li and the dendritic growth of Li (Figure I-2b) on the anode upon successive plating/stripping are underlined. These filaments can eventually lead to short circuits and a possible inflammation of the cell²⁰ and are therefore detrimental to the commercial development. To circumvent these issues, the organic electrolyte has been replaced by a solid polymer electrolyte, which can prevent the formation of dendrites. Until August 2018, this technology could have been found in Parisian electric car sharing service called “Autolib”, which were developed by the company Bolloré under the name Bluecar. To improve the Li^+ diffusion within the polymer membrane and to prevent the dendritic growth, the cells needed to be continuously heated at around 60 °C.

The second idea forged ahead was the use of two intercalation materials of different potentials as the two electrodes, which is often called a rocking chair battery because of the flow of lithium ions back and forward between the two electrodes (Figure I-2c).²¹ However, the first attempts have given rise to cells with low potential range and capacity due to the high molecular weights of the electrode materials employed (*i.e.* Sulfur-based positive electrodes). This issue was overcome by John B. Goodenough in 1980 by orienting the choice of positive

electrode from Li_xTiS_2 to $\text{Li}_{1-x}\text{CoO}_2$, which demonstrated that the oxide electrodes offered an increase of positive electrode potential due to higher electronegativity of oxygen than sulfur.²² When it comes to the negative electrode, finding a material with a Li insertion potential low enough to achieve decent cell voltages was somewhat more complicated. The lithium intercalation into graphite electrodes was demonstrated in the work of Yazami from University of Grenoble²³ and in the patent of Bell Laboratories.²⁴ Nevertheless, these former studies did not take into account the co-intercalation of solvent molecules causing the disruption of the carbon structure, rendering infeasible for practical batteries. Akira Yoshino from Asahi Kasei corporation, in a seminal patent, described the benefits of lower temperature carbons such as petroleum coke in terms of resistance to solvent co-intercalation and reduction.²⁵ In 1983, Yoshino assembled a viable full rechargeable battery combining the petroleum coke anode with Goodenough's LiCoO_2 cathode, which was later commercialized by Sony in 1991 (80 Wh.kg^{-1} , 200 Wh.L^{-1}).²⁶ The finding of Sanyo's researchers²⁷ and the Jeff Dahn's laboratory²⁸ with Ethylene Carbonate (EC) as co-solvent, instead of Propylene Carbonate (PC), paved the way for the development of Li-ion batteries with a graphite anode without solvent co-intercalation. Graphite still remains to be the most widely used anode material owing to its theoretical specific capacity (372 mAh.g^{-1} , LiC_6), its high Coulombic efficiency and its better cycle performance.¹³ In 1993, Dominique Guyomard and Jean-Marie Tarascon reported a new electrolyte formulation, LiPF_6 in EC/DMC, for its improved oxidation stability, which remains one of the popular electrolytes until today.²⁹ All these improvements led to LiCoO_2 -based Li-ion batteries with three times higher energy densities (250 Wh.kg^{-1} , 600 Wh.L^{-1}) than that of the first generation devices by Sony.^{30,31}

Li-ion batteries have revolutionized our lives since they first entered the market in 1991. They have laid the foundation of a mobile, fossil fuel-free society, and are of the greatest benefit to humankind. Therefore, the works of Whittingham, Goodenough and Yoshino, which resulted in a lightweight and reliable cell, giving birth to the current Li-ion battery, have been rewarded the Nobel Prize in Chemistry in 2019.³²

I.1.c – Post Li-ion battery technologies and their promises

o Alkali metal-ion batteries

As depicted in the Figure I-1, the Li-ion technology presents the highest performances in terms of energy density. Therefore, the worldwide demand for Li-ion batteries has been growing, engendering an increase in the price of lithium resources.³³ Even if lithium is widely distributed in the Earth's crust and sea, its abundance is less than 20 ppm in the Earth's crust as shown in the Figure I-3.³⁴ Thus, the current production sites of lithium are restricted in South America, Australia, China and United States.^{15,35} In comparison, sodium and potassium are evenly distributed worldwide and are the most abundant elements on the Earth. Since no alloy is electrochemically formed between aluminum and potassium or sodium; aluminum foil can be used as a bipolar current collector for both negative and positive electrodes, which is not possible for Li-ion batteries. Na-ion and K-ion technologies are expected to be more sustainable^{36,37} and cost-effective, as they are free of rare and expensive 3d-metal elements, such as Co or Cu.

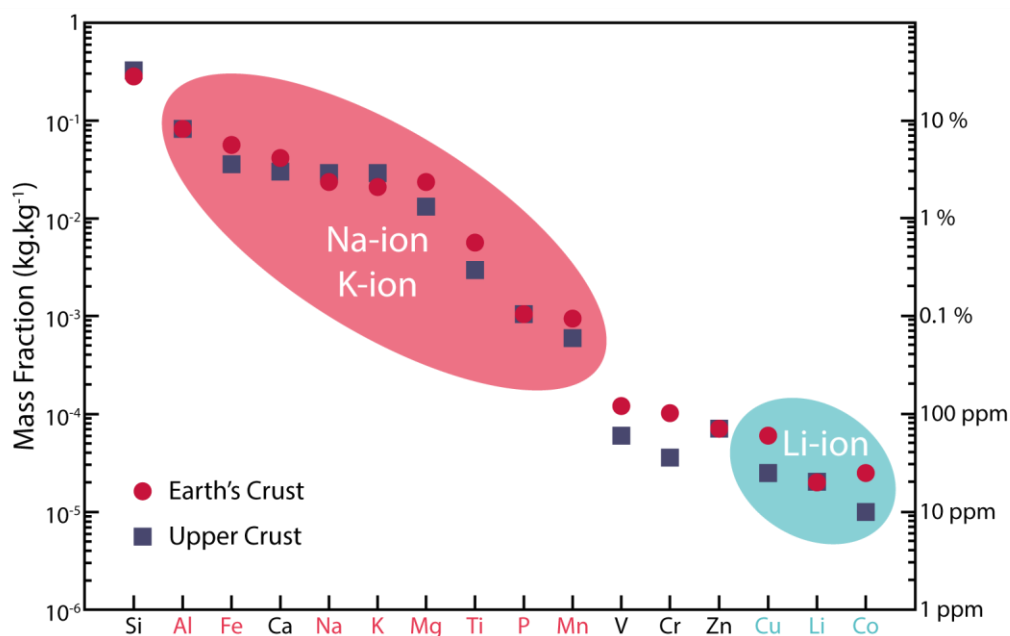


Figure I-3: Elemental abundance in the Earth's Crust. Adapted from references.^{15,34,38}

Sodium based systems have followed a parallel path to the Li-ion batteries, the study of insertion compounds has been evolved from sulfides to oxides compounds like NaCoO₂.³⁹

Conversely, the studies on potassium-based systems are relatively more recent and dated from 2004.⁴⁰

To be able to assess the potential of Na and K-ion batteries over Li-ion technology, physical properties and economic indicators for lithium, sodium and potassium as charge carriers are gathered in Table I-1. Sodium and potassium present a heavier atomic mass and a larger ionic radius compared with lithium ion explaining their lower attractiveness. Moreover, lithium has the lowest standard potential of the alkali metals that leads to high voltage batteries. Additionally, sodium and potassium exhibit higher reactivity to ambient moisture. Despite these drawbacks, geopolitical and environmental concerns as well as the niche markets make Na and K-ion batteries worth considering technologies, and stimulated the research on new host materials and their insertion mechanisms.

Table I-1: Comparison of physical properties and economic indicators for lithium, sodium and potassium as charge carriers for rechargeable batteries.^{15,41}

	Li ⁺	Na ⁺	K ⁺
Relative atomic mass (g.mol ⁻¹)	6.94	22.99	39.10
Standard potential (V vs. SHE)	-3.04	-2.71	-2.93
Melting point (°C)	180.5	97.7	63.4
Cost of carbonate (U.S. \$.ton ⁻¹)	6 500	200	1 000
Cost of industrial grade metals (U.S. \$.ton ⁻¹)	100 000	3 000	13 000
Theoretical capacity of metal electrode (mAh.g ⁻¹)	3861	1166	685
Theoretical capacity of ACoO ₂ (mAh.g ⁻¹)	274	235	206
Coordination preference	Octahedral and tetrahedral	Octahedral and prismatic	Prismatic

As a brief comparison to Li-ion cell, electrochemical insertion of Na⁺ into graphite is negligible, whereas K⁺ is electrochemically and reversibly inserted into graphite.⁴²⁻⁴⁴ The reversible capacity of 244 mAh.g⁻¹ is obtained for K-ion cell, which corresponds to 87.5 % of the theoretical capacity of 279 mAh.g⁻¹ by assuming reversible KC₈ formation.⁴³ In contrast to Li⁺ and K⁺, Na⁺ can solely be electrochemically inserted into non-graphitizable carbons,⁴⁵⁻⁴⁷

with a reversible capacity of sodium insertion reaching 300 mAh.g^{-1} . This latter value is higher than those of lithium and potassium cells and approaching that of graphite in Li-ion batteries. Two types of positive materials either layered oxide, Na_xMO_2 , or polyanion compound, $\text{Na}_3\text{V}_2(\text{PO}_4)_2\text{F}_3$ (NVPF), have emerged and are presently being pursued for Na-ion battery commercialization.^{48,49} Layered oxides and polyanion compounds are also under consideration for K-ion batteries, in addition to Prussian Blue Analogs which permit to reach higher working potential.^{41,50} However, K-ion battery research is still at its early stage, compared with other alkali metal-ion batteries.

Na and K-ion chemistries will be soon on the verge to be complementary solutions to the Li-ion cells that are over dominating the battery market for the last twenty years.⁵¹ Yet, key parameters for their optimization still need to be addressed, especially the physicochemical properties of cations governing the intercalation at the interface (Refer to last section of I.2.b.).

○ *Pseudocapacitors*

Unlike batteries that confer a high energy, supercapacitors exhibit high power delivery capability, long cycle lifespan and rapid charge/discharge kinetics.⁵² Both of these energy storage systems rely on electrochemical processes. Nonetheless, the cation insertion in batteries that enables redox reactions in bulk electrode materials is diffusion-controlled. On the other hand, supercapacitors store charge by electroadsorption of electrolyte ions onto the surface of the electrode, in the double-layer region, no redox reactions are required. Therefore, this difference in terms of electrochemical processes give rise to their different charge storage properties.

Midway between these two technologies, pseudocapacitive electrode materials store charge *via* Faradaic processes, like batteries, that involve fast, reversible redox reactions. In addition, they present electrochemical signatures similar to capacitive processes like supercapacitors.⁵³ This similarity is explained by the community to be due to a series of faradaic redox couples with a distribution of potentials; however, this was recently contested and explained with concentration-dependent activity coefficients resulting from interactions

between reactants.^{54,55} Nonetheless, with these features, pseudocapacitors aim to bridge the gap between the batteries and supercapacitors, gathering their respective benefits: battery-level energy density combined with the cycle life and power density of supercapacitors, as depicted in the Figure I-4a. The term pseudocapacitance was firstly introduced by David C. Grahame in 1941⁵⁶ and then used in the studies of Conway and Gileadi in the 1960s to describe electrochemical charge transfer reactions associated with surface adsorption.^{57,58} Trasatti and coworkers were the first to report pseudocapacitive behavior in transition metal oxides on ruthenium oxide thin film in sulfuric acid, RuO_2 .⁵⁹ Since then, other materials were introduced to exhibit pseudocapacitance, such as hydrated RuO_2 ⁶⁰ ($\text{RuO}_2 \cdot 0.5\text{H}_2\text{O}$), amorphous hydrated $\text{MnO}_2 \cdot x\text{H}_2\text{O}$ ⁶¹, conducting polymers⁶² (polyaniline (PANI), polypyrrole (PPY) or derivatives of polythiophenes (like PEDOT)), Li^+ intercalation in T-Nb₂O₅⁶³ or two-dimensional transition metal carbides, nitrides and carbonitrides (MXenes).⁶⁴

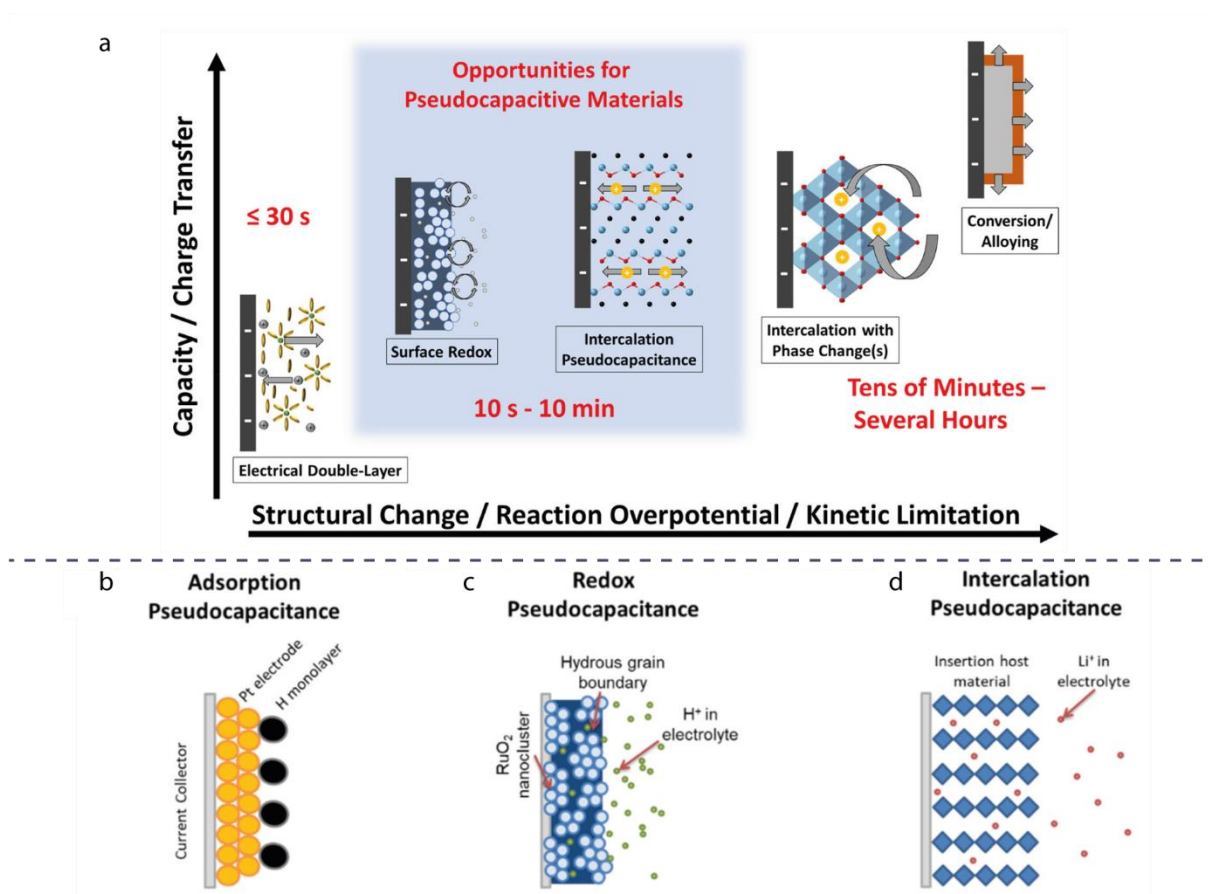


Figure I-4: (a) Comparison of electrochemical energy storage mechanisms in terms of their characteristic capacity and the associated degree of structural changes of the electrodes, reaction overpotential and kinetic limitations. The panels (b), (c) and (d) present different types of reversible redox mechanisms that give rise to pseudocapacitance. Adapted from references.^{65,66}

Even though these materials present pseudocapacitive behavior, they feature different Faradaic mechanisms, which can further be generalized into three distinct electrochemical processes. Underpotential deposition (Figure I-4b) occurs when ions are deposited on a 2D metal-electrolyte interface at potentials more positive than their reversible redox potentials (*e.g.* H^+ on Pt or Pd^{2+} on Au). The Figure I-4c displays redox pseudocapacitance where a redox species is electrochemically adsorbed onto the surface or near surface of the material in a Faradaic redox system (*e.g.* RuO_2 or MnO_2). Lastly, intercalation pseudocapacitance (Figure I-4d) occurs when ions are inserted into a redox-active material with no crystallographic phase change and in a short time scale (*e.g.* Nb_2O_5). To identify the origin of ion intercalation pseudocapacitance, two cases need to be distinguished: “intrinsic” and “extrinsic” pseudocapacitive materials.^{53,66} For intrinsic ones, charge-storage properties are not related to their crystalline grain sizes or morphologies. Whereas, some battery materials (such as $LiCoO_2$ ⁶⁷ or V_2O_5), that only show diffusion-controlled capacity in the bulk state, can demonstrate a pseudocapacitive behavior upon decreasing the particle dimensions to nanosize or to thin films, *i.e.* the so-called extrinsic pseudocapacitance.

Intercalation pseudocapacitive materials has the potential to bridge the two worlds of power and energy electrochemical storage *i.e.* supercapacitors and batteries. As these materials do not suffer from drastic structural changes during ion intercalation, the electrode-electrolyte interface kinetically governs the electrochemical process. Therefore, this family of materials is a perfect playground for interface studies, with the aim of improving their performances and battery's ones.

○ *Battery chemistries on an upward trend*

Secondary Zn- O_2 batteries were first demonstrated in the 1970s.^{68,69} Then, twenty years later, Li- O_2 batteries were developed by Abraham and coworkers.⁷⁰ This cell chemistry utilizes O_2 molecules from the air as an indefinite active material, instead of solid materials, therefore drastically increasing the energy density. However, metal-oxygen cells suffer from poor reversibility and limited cycling due to the irreversible discharge products, electrolyte evaporation, as well as from the attack of water and oxygen at the metal surface. Despite the hype around this high energy density chemistry, owing to unsolved issues both at the material

and cell levels, metal-oxygen batteries are unlikely to have a significant commercial impact in the near future.⁷¹

The popular Zn-MnO₂ system has enjoyed a revival for the last five years moving from primary to rechargeable battery. This transition was made possible thanks to advances in electrolyte formulations. The classical alkaline electrolyte generates side-products like Zn(OH)₂ or ZnO, which prevents the reversibility of the system.^{72,73} The utilization of a mild acidic electrolyte composed of zinc and manganese sulfate salts permits to obtain long cyclability at high C-rate. However, no performances are reported as a function of either high temperatures or low C-rate where side reactions are intensified. Moreover, the reactional mechanism is far from being fully resolved and remains highly controversial. The earliest reports described a mechanism based on reversible Zn²⁺ insertion/extraction into/from the tunnels of α -MnO₂.^{74,75} Then, a mechanism based on conversion between α -MnO₂ and H⁺ without zinc intercalation was proposed.⁷⁶ The simultaneity of both processes was also proposed with the successive H⁺ and Zn²⁺ insertion/extraction in the MnO₂ cathode.⁷⁷ More recently, dissolution/deposition mechanism of MnO₂ was also proposed with different scenarios: without any insertion of H⁺ or Zn²⁺ ⁷⁸, with their insertion⁷⁹ or with a conversion reaction between MnO₂ and MnOOH.⁸⁰ As depicted here, the proposed mechanisms do not seem to intersect. Nevertheless, studies are converging on one point: the formation of a zinc hydroxy-sulfate phase Zn₄(SO₄)(OH)₆ on the cathode electrode due to pH change.^{81,82}

Solid electrolytes (SE) are envisaged to replace liquid electrolytes, to circumvent the security related drawbacks such as flammability. If only a SE replaces the liquid electrolyte, the volumetric energy density remains unchanged, however, the gravimetric energy density decreases. SEs may counterbalance this disadvantage, by enabling the utilization of high-voltage cathodes, from 4.2 to 5 V vs. Li⁺/Li, permitting an increase of 20 % in energy density.⁸³ As their polymer counterparts, SEs may enable high capacity lithium-metal anodes, as their mechanical strength may prevent dendrite growth. The successful integration of SEs would offer an increase of up to 70 % in energy density. All-solid-state batteries have experienced fast growing interest. Nevertheless, they currently suffer from engineering issues: poor interfacial kinetics between SE and active materials, lack of mechanical integrity and Li dendrite growth.^{84–86} At the moment, these challenges render this technology immature for an eventual commercialization, despite the claims of several EV manufacturers.

I.2 – In the quest of better batteries

I.2.a – Higher energy materials

o Transition metal substitution and commercial cathode materials

According to various surveys⁷, one third of the commercial batteries sold in the world in 2014 used LiCoO_2 (LCO) as cathode materials, owing to its reversible capacity of 140 mAh.g^{-1} . The difficulty to remove more than 0.5 Li^+ without damaging the LCO crystalline structure makes the theoretical capacity of 275 mAh.g^{-1} unachievable. To circumvent its capacity limitation along with the high cost and ethical issues associated with the use of cobalt, it was substituted for low-cost and more abundant transition metals, such as nickel and manganese by ion exchange from $\alpha\text{-NaMnO}_2$. However, pure LiNiO_2 cathodes are not favorable because the Ni^{2+} ions have a tendency to substitute Li^+ sites during synthesis and delithiation, blocking the Li diffusion pathways.⁸⁷ The cycling performance of LiMnO_2 is not satisfactory either, due to the several issues including the tendency of the layered structure to change into spinel during Li ion extraction⁸⁸, as well as leaching out Mn during cycling.⁸⁹

Mixed partial substitution of Ni with Co was demonstrated to stabilize the layered structure by reducing the cationic disorder.⁹⁰ Therefore, the $\text{LiNi}_{0.8}\text{Co}_{0.15}\text{Al}_{0.05}\text{O}_2$ (NCA, $\approx 200 \text{ mAh.g}^{-1}$) cathode with a small addition of Al, which improves both thermal stability and electrochemical performance⁹¹, has experienced a widespread commercialization thanks to Panasonic for Tesla EVs. During the course of uninterrupted research to reduce Co content and so the cost, $\text{Li}(\text{Ni}_{0.5}\text{Mn}_{0.5})\text{O}_2$ (NMO) was proposed for its similar energy density to LCO. However, cation mixing can cause low Li diffusivity and may result in unappealing rate capability.⁹² Against the economical flow, adding Co into NMO was found to be an effective way to enhance the structure stability further.⁹³ $\text{LiNi}_x\text{Co}_y\text{Mn}_z\text{O}_2$ (NMC) has comparable or higher specific capacity than LCO and similar operating voltage while having lower cost since the Co content is reduced. $\text{LiNi}_{0.33}\text{Co}_{0.33}\text{Mn}_{0.33}\text{O}_2$, also called NMC 111 or NMC 333, was the most common form of NMC; however, the actual trend is to increase the Ni content (Ni-rich layered oxide) for higher energy/power density and lower Co content, like NMC 622 or NMC 811.

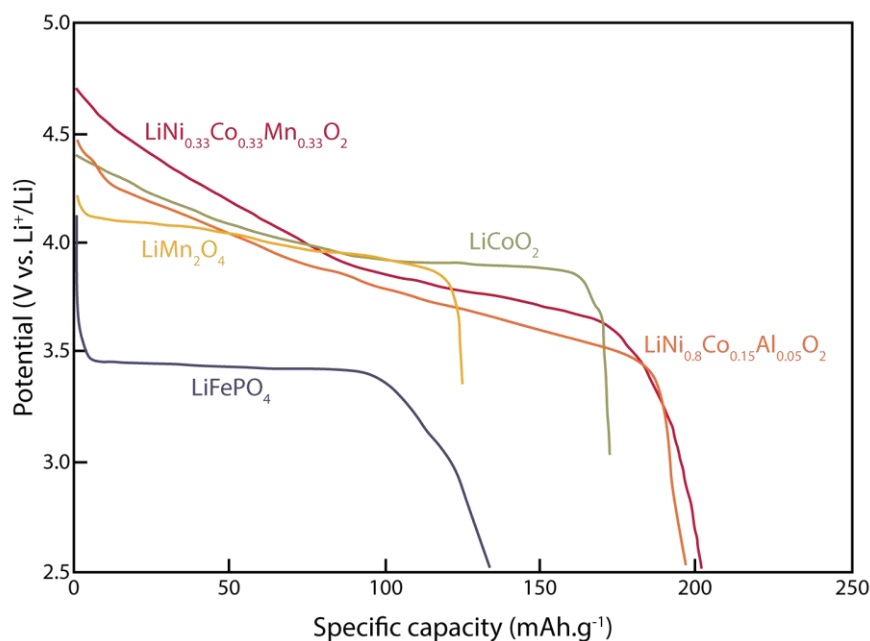


Figure I-5: Typical discharge profiles of commercial intercalation cathodes. Adapted from: *Nitta et al.*⁹⁴

Together with transition metal oxides, other families of cathode compounds were explored. Polyanion compounds are composed of large $(XO_4)^{3-}$ ($X = S, P, Si, As, Mo, W$), which increase cathode redox potential against pure oxide (*e.g.* inductive effect) while also stabilizing its structure.⁹⁵ The most representative material is the olivine structure is $LiFePO_4$ (LFP), known for its thermal stability and high power capability. The major weaknesses of the LFP cathode are its relatively low average potential and low electrical and ionic conductivity. Reduction in particle size in combination with carbon coating⁹⁶ permits to increase its rate performance. For sake of comparison, the discharge profiles of the different cathode compounds mentioned previously are reported in the Figure I-5. Interestingly, while LCO was the most popular until 2014, it now accounts for solely one tenth of the sale market; while NMC and LFP constitutes two fifths and one third, respectively, due to the higher performance for the former and the low cost for the latter.⁷

o *Li substitution and anionic redox*

To push further the energy density limit of the previously presented cathodes, layered oxides with a larger content of Li compared to the $LiMO_2$ family were investigated.^{97,98} Li_2MO_3 type materials present a similar structure; however, some transition metals from the metallic

layer are substituted by Li. They can be described by the following formula $\text{Li}(\text{Li}_{1/3}\text{M}_{2/3})\text{O}_2$ and are called Li-rich materials. These compounds have the ability to remove more than one lithium from their structure, leading to an increase of their specific capacity.

Kalyani *et al.* were the first to explore the electrochemical properties of Li-rich materials with 3d transition metals. Li was removed from Li_2MnO_3 when charged above 4.5 V, that they attributed to the $\text{Mn}^{5+}/\text{Mn}^{4+}$ redox couple.⁹⁹ Nevertheless, such electrochemical activity is abnormal, as the octahedral Mn^{4+} cannot be further oxidized to release Li^+ during charge. Dahn and coworkers provided more insights on charge compensation process by studying the Li-rich system: $\text{Li}(\text{Li}_{1/3-2x/3}\text{Ni}_x\text{Mn}_{2/3-x/3})\text{O}_2$ with x between 1/6 and 1/2. The materials can reversibly cycle over 225 $\text{mAh}\cdot\text{g}^{-1}$ with an oxygen loss upon Li removal between 4.5 and 4.7 V vs. Li^+/Li .¹⁰⁰ Eventually, specific capacity of the NMC family was improved by this strategy giving rise to the promising Li-rich NMC for the Li-ion market¹⁰¹ and to an abundant literature.

These high energy density cathode materials have several drawbacks, the reason behind their non-commercialization. They need to be charged to high potential on the first cycle before demonstrating a reversible cycling behavior on the next cycles. The charge compensation process can be partially attributed to the redox of metal cations; therefore, the release of oxygen from the material was proposed¹⁰² and proved by measuring O_2 gas release using differential electrochemical mass spectroscopy (DEMS).¹⁰³ Besides, CO_2 gas is produced due to high reactivity of this type of materials, especially in the case of Ni-rich counterparts, with carbonate-based electrolytes at high potentials.¹⁰⁴ In addition, they suffer from voltage decay and hysteresis upon cycling which complicate their integration in industrial applications.¹⁰⁵

The previous section focused on the strategies to obtain cathode materials with higher energy densities as they are still the capacity-limiting electrode in a full cell. However, the negative side is not disregarded. If their large volume expansion and irreversible capacity at the first cycle are controlled, Li-alloy based anode materials (Silicon, Tin, ...) has the potential to be a worthy option to replace the widely used graphite anode, because of their relatively large specific capacity and abundancy.^{106,107} Nonetheless, energy density is not the only key parameter to take into account. Reliability and power density play a major part in the development of better battery cells.

I.2.b – Improve the lifetime, the reliability and the power density

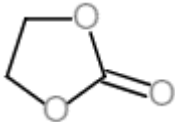
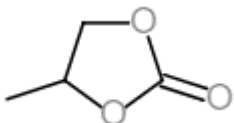
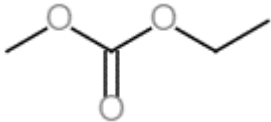
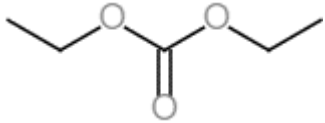
o *Electrolytes and Solid Electrolyte Interphase*

Sandwiched between the positive and negative electrodes, the electrolyte permits the Li^+ diffusion and migration in Li-ion batteries. Typical liquid electrolyte is composed of a lithium salt dissolved in an organic aprotic solvent. The ideal electrolyte should fulfill the following requirements:¹⁰⁸ i. Dissolution of lithium salt to a sufficient concentration, *i.e.* a high dielectric constant (ϵ_R). ii. Fluid enough to permit a facile ion transport, *i.e.* a low viscosity (η). iii. Liquid in a wide temperature range, *i.e.* a low melting point (T_m) and a high boiling point (T_b). iv. Wide electrochemical stability window. v. Safe, economical and environmentally benign.

The Table I-2 summarizes the physicochemical properties of the typical electrolyte solvents for Li-ion batteries. Among these solvents, cyclic carbonate esters attracted the research attention earned by their high dielectric constant and, hence, their ability to dissolve a wide variety of lithium salts. PC was initially used for its wide liquid range and because lithium can be electrodeposited from a solution of LiClO_4 in PC.¹⁰⁹ However, when PC is utilized as the main solvent with a graphite anode, only poor cycling performance is attained. Dahn and coworkers established the reason behind this drastic loss of capacity, which originated from co-intercalation of PC in graphite anode, causing its exfoliation.²⁸ In comparison, EC does not exhibit this unpleasant feature. EC has comparable viscosity and slightly higher dielectric constant than PC. Besides, its dielectric constant is even higher than the most common solvent: water ($\epsilon_R = 79$). However, EC presents a high melting point (36 °C), unfavorable feature for an ambient temperature electrolyte. When mixed with other co-solvents (*e.g.* those proposed in the Table I-2), its melting point can be sufficiently decreased and the liquid range can be extended.¹¹⁰ Since the work of Tarascon and Guyomard²⁹ in 1993, EC has become the core component of modern Li-ion battery electrolytes when mixed with linear carbonates like DMC, EMC or DEC (Table I-2). These co-solvents permit to reduce the viscosity and promote ion transport. A synergetic effect is achieved when cyclic and linear carbonates are mixed, benefiting from the high solvation power of lithium salts by cyclic carbonates and low viscosity of linear carbonates.¹⁰⁸ Moreover, these mixed electrolytes remain electrochemically stable on a wide potential range.

Concerning the lithium salts, few are chemically stable under such conditions. The majority of commercial cells uses lithium hexafluorophosphate (LiPF_6) salt due to its overall well-balanced properties. However, LiPF_6 suffers from chemical and thermal instability; especially in the presence of traces of water, HF is formed. Other lithium salts are available mainly for research purposes (due to their intrinsic drawbacks) such as lithium perchlorate LiClO_4 (safety hazard), lithium bis(trifluoromethanesulfonyl)imide LiTFSI (instable above 4 V vs. Li^+/Li) or lithium bis(oxalate)borate LiBOB (poor performance below 0 °C).

Table I-2: Physicochemical properties of typical organic solvent for Li-ion batteries.¹⁰⁸

Solvent	Molar mass (g.mol ⁻¹)	ρ_l (g.cm ⁻³)	T_m/T_b (°C)	ϵ_R	η_l (mPa.s)
Ethylene carbonate (EC) 	88	1.321	36.4/248	89.78	
Propylene carbonate (PC) 	102	1.200	-48.8/242	64.92	2.53
Dimethyl carbonate (DMC) 	90	1.063	4.6/91	3.107	0.59
Ethyl methyl carbonate (EMC) 	104	1.006	-53/110	2.958	0.65
Diethyl carbonate (DEC) 	118	0.969	-74.3/126	2.805	0.75

Although the carbonate-based electrolytes have been selected partly due to their wide electrochemical window, some high voltage cathode materials like Ni-rich compounds and especially graphite anode operate outside their thermodynamic stability window. In the latter case, the electrolyte molecules are reduced at the surface of the negative electrode forming a new phase composed of solvent and salt by-products at the interface between the electrode and the electrolyte. This new phase called Solid Electrolyte Interphase (SEI), without which Li-ion batteries could not function, was first introduced by Peled^{111,112} for the alkali metals, and

later on extended to carbon materials by Dahn *et al.*²⁸ This electrolyte reduction due to thermodynamic instability versus the anode potential should normally be detrimental to the proper battery operation. However, the formed phase acts as a barrier preventing the electrolyte from further degradation, which enables the utilization of low potential negative electrodes, leading to higher energy density batteries. A similar passivation film on the cathode surface or Cathode Electrolyte Interface (CEI) was also evidenced.^{113–115}

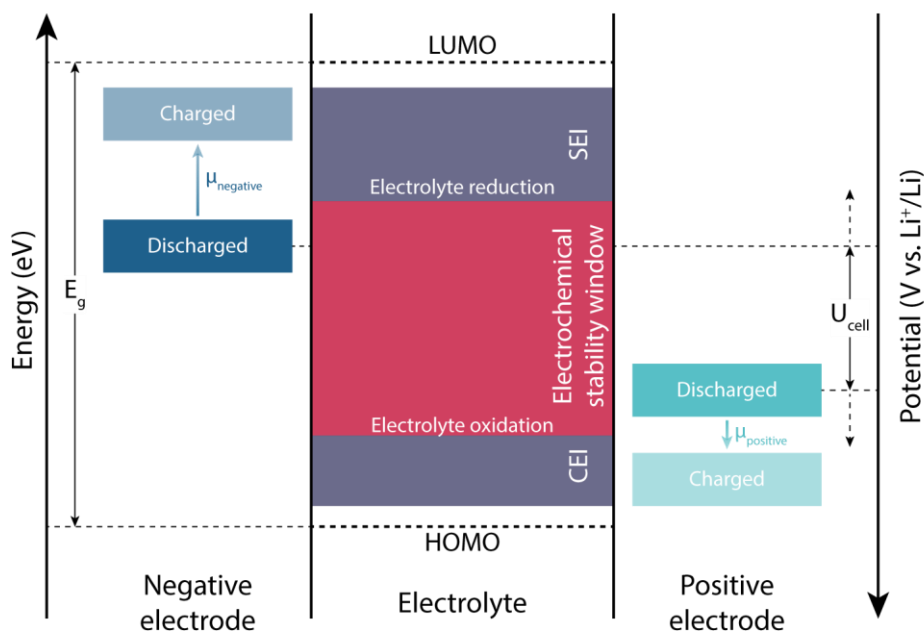


Figure I-6: Energy diagram of the SEI and CEI formation at the surface of negative and positive electrodes during the battery charge. Adapted from references.^{116,117}

The Figure I-6 depicts the energetic levels of the electrodes (*e.g.* Fermi level) with respect to the highest occupied molecular orbital (HOMO) and lowest unoccupied molecular orbital (LUMO) of the solvent to explain the formation of both SEI and CEI at the negative and positive electrodes of a Li-ion battery, respectively. The energy levels of HOMO and LUMO of the solvent to signify the redox potentials where the electrolyte oxidation/reduction take place were consciously not employed here to explain the SEI/CEI formation.¹¹⁷ HOMO and LUMO are calculated on isolated molecules, which are not participating in redox reactions. While redox potentials are directly related to the Gibbs free energy difference of the reactants and products. In the case of water, it has a band gap of 8.9 eV¹¹⁸ while its thermodynamic potential window is only 1.23 V.¹¹⁹ Moreover, presence of salts and other molecules significantly affect the redox potentials. Therefore, potential of electrolyte reduction at

negative potentials and potential of electrolyte oxidation at positive potentials are more accurate.

A suitable SEI should act as an electronic insulator to avoid further electrolyte oxidation/reduction but enable a fast transfer of lithium ions.¹¹⁶ The formation kinetics pertaining to the SEI formation should be fast and rapidly self-limiting to reduce the irreversible losses. Besides, it should display a uniform morphology and composition. Finally, it should be flexible and elastic to accommodate the volume changes of the active material upon repeated charge/discharge cycles. Two models were proposed in the 1990s to describe the morphology of the SEI. The mosaic model, in which different interphase components are deposited in a three dimensional heterogeneous SEI, was introduced by Peled *et al.*^{111,112} Aurbach and coworkers proposed a bilayer morphology for the SEI where inorganic compound is found at the surface of the active particles while polymeric species form a porous shell around them.¹²⁰

The initial formation of the SEI for commercial cells is performed at the end of the cell assembly under carefully controlled conditions as the main part of the SEI establishment occurs during the first cycles.¹²¹ These steps are vital to ensure long cycle life, good rate capability and improved safety of the Li-ion batteries. However, the SEI stability is still not fully controlled at long-term, its thickening contributes to the overall aging of today's Li-ion batteries.¹²²

o Influence of the solvation shell on the electrolyte physicochemical properties and cation intercalation

It is widely admitted by the battery community that rate capability of alkali metal-ion batteries are influenced by the transport properties of these alkali metal ions in the bulk of the electrolyte, *e.g.* ionic conductivity and transference number.¹²³ K⁺ ions are weaker acids than Na⁺, which are even weaker than Li⁺, this difference of Lewis acidity results in smaller Stokes' radii in various solvents. The Figure I-7a depicts their Shannon's ionic¹²⁴ radii and Stokes' radii in propylene carbonate. According to Matsuda *et al.*, their Stokes' radii in PC increase in the opposite direction of their Shannon's ionic radii.¹²⁵ Lithium ion charge is more

localized leading to a stronger interaction with solvent molecules and therefore a bigger solvation sheath. Then, the conventional vehicle-type mechanism in dilute electrolytes explains the better ion transport properties of Na^+ and K^+ compared to Li^+ .

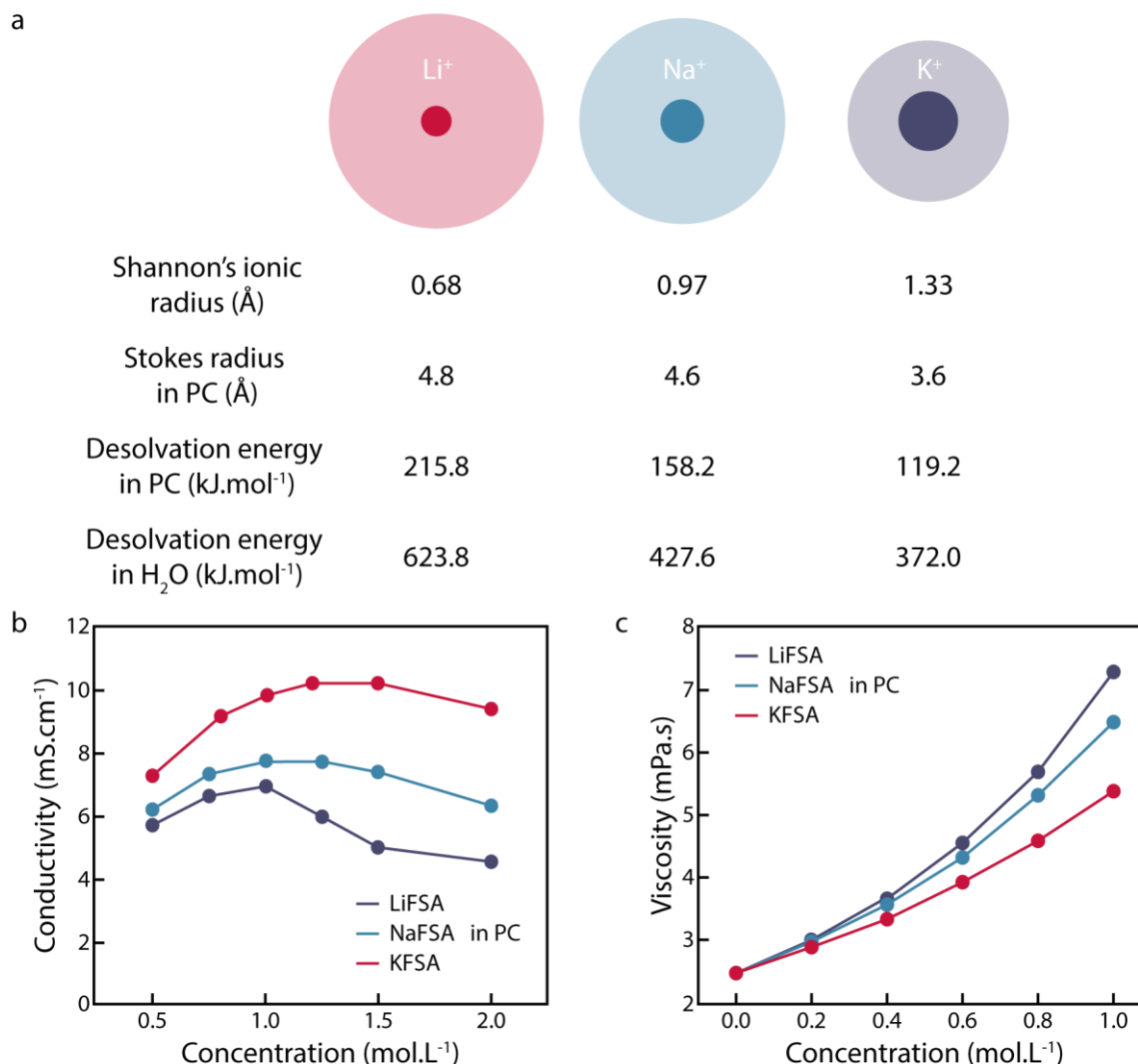


Figure I-7: Physicochemical properties of alkali metal ions in the bulk of the electrolyte. (a) Comparison of their Shannon's ionic radius and Stokes radius in propylene carbonate. Concentration dependence of (b) the ionic conductivities and (c) the viscosity of alkali metal ions salts in PC at room temperature. Adapted from: *Kubota et al.*^{15,126}

The better ionic transport properties are shown for a specific example in the Figure I-7b and c. *Kubota et al.* compared the ionic conductivity and viscosity values for a concentration range of bis(fluorosulfonyl)amide salts for the three different alkali metal ions in PC.¹⁵ Ionic conductivity values present the following order of $\text{LiFSA} < \text{NaFSA} < \text{KFSA}$ in PC. Moreover, KFSA then NFSA exhibit lower viscosity than LiFSA. However, potassium salts usually have poorer solubility than Na and Li salts due to their lower charge density, which narrows the spectrum of the solvent candidates.

As stated earlier, the battery community have been using the electrolyte transport properties as the indicator parameter to explain the rate capability differences occurring in Na and K-ion batteries. However, limiting the cation intercalation mechanism solely to the process of the cation diffusion in the bulk of the electrolyte may not be sufficient. As depicted in the Figure I-8, the mentioned mechanism can be broken down into the following steps: i. The transport of the cation escorted by its solvation shell from the bulk of the electrolyte to the electrode interface. ii. The desolvation of the cation at the SEI-electrolyte interface or electrode-electrolyte interface. iii. The cation transport through the possibly existing SEI/CEI. iv. The intercalation of the bare cation in the host material, accepting an electron from the external circuit. v. The diffusion of the cation in the bulk of the material.

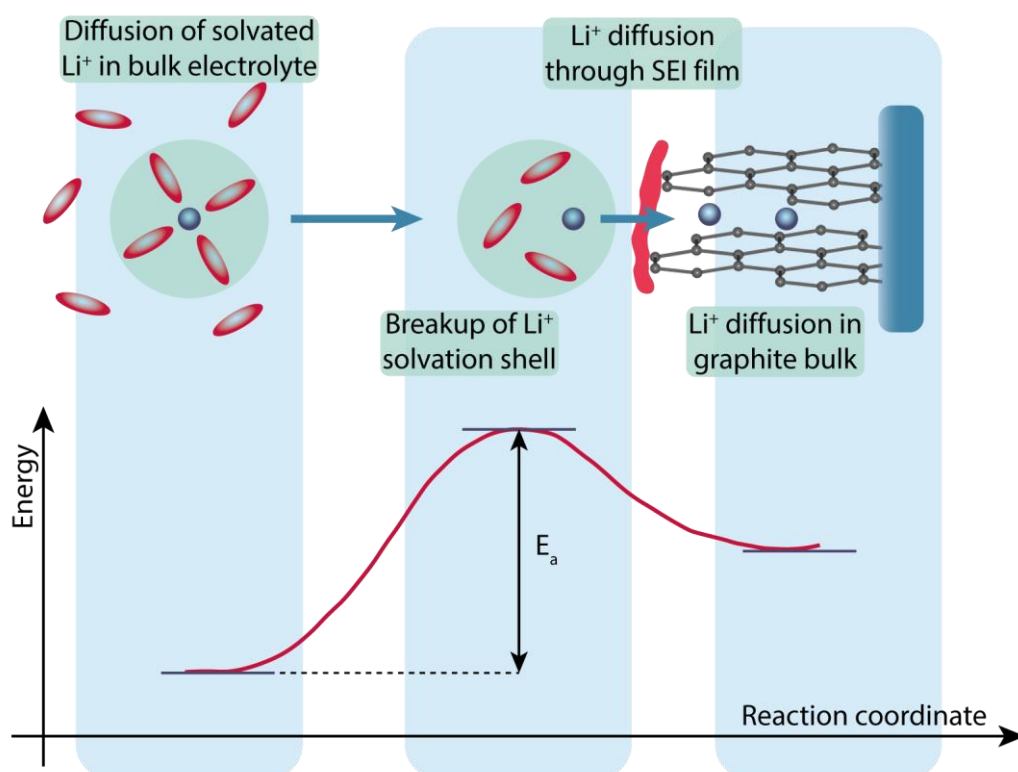


Figure I-8: The journey of a solvated Li^+ from the bulk of the electrolyte to the graphite negative electrode and its related energy diagram. Adapted from: Xu and Cresce.¹²⁷

The charge-transfer stage is a critical step, as the cation needs to lose its solvation shell to transfer from a liquid phase into a solid phase and at the same time an electron is transferred into the solid phase.^{128,129} From a theory point of view, an intermediate exists between the solvated stage and the intercalated stage, forming a transient step. The difference of energy between these two stages is the activation energy for charge transfer during intercalation (E_a), as shown in the Figure I-8. It can be related to the charge transfer

resistance (R_{CT}), obtained by temperature-dependent Electrochemical Impedance Spectroscopy (EIS), thanks to the Arrhenius equation.

Xu *et al.* studied thoroughly the intercalation mechanism of lithium ion in graphite using Nuclear Magnetic Resonance spectroscopy (NMR), ElectroSpray Ionization Mass Spectroscopy (ESI-MS) and EIS.^{127,130,131} The authors proposed that the solvation sheath structure of Li^+ plays a directing role in the interfacial chemistry; the molecules in the primary shell serve as the primary precursors for the SEI formation. Therefore, the preferential solvation of Li^+ by certain solvent molecules, as described in the previous subsection, can drive the composition and the quality of the formed SEI. Another significant consequence of Li^+ preferential solvation is that it governs the rate of lithiation process, how fast a Li^+ can be transported at the electrode-electrolyte interface. The stripping of the solvation shell – desolvation – is an energy-consuming step; therefore, it will affect the energy barrier of intercalation. EIS studies^{130,132} have demonstrated the significant participation of the desolvation process and the electrolyte composition dependence in the charge transfer component, the main impedance of a Li-ion cell. Complementary studies of the insertion mechanisms in cathode materials proposed a two-step process for the charge transfer, the so-called “adatom model”.^{133–136} Solvated ions are partially desolvated at the vicinity of the electrode resulting in the formation of an atom adsorbed on the electrode surface and the electron transfer from the electrode. Then, this adatom diffuses on the surface to an insertion site. Meanwhile, the adatom loses the remaining solvent molecules to be inserted into the electrode material. This model adds a new possible rate-limiting step: the surface conduction of adatoms and an electrode surface dependence in terms of active sites. The solvation was confirmed to be of primary importance to describe the rate capability of Li-ion battery; however, very few studies are brought to a conclusion concerning the interplay between the solvation shell (desolvation energy) and alkali metal-ion battery performance.

I.3 – Chapter conclusions

This first chapter intended to provide the key steps leading to the development of today’s Li-ion batteries. The concept discovery is not recent; however, the Li-ion chemistry, which permits to obtain the best performance in terms of gravimetric and volumetric capacity

so far, has known a fast takeoff over the last decades to now lead the battery market. Promising chemistries, such as alkali metal-ion or all-solid-state batteries, are on the verge to be complementary solutions to Li-ion batteries.

To meet the continuous demand from the growing markets, the batteries can be improved at least along the two axes: the energy density on one side and the reliability/lifetime on the other side. Thanks to cationic substitution strategies, the energy density was increased improving today's batteries and extensive research is still ongoing in this direction. The dynamic nature of the passivation layer (SEI) which is formed mainly at the negative electrode-electrolyte interface during cycling was demonstrated to be the main cause of the performance drop or failure of current batteries. In addition, the solvation shell of alkali metal ions at the interface seems to play a major role in the SEI formation and the rate capability. Therefore, understanding the mechanisms taking place at the electrode-electrolyte interface (EEI) and overall interactions of ions with electrode is a prerequisite to achieve any sort of optimization but requires appropriate tools. The term "electrode" is used in the rest of this manuscript instead of "active material" by abuse of language and therefore it is not referring to the composition electrode.

Therefore, the aim of this thesis is to explore the essential role played by the electrode-electrolyte interface (EEI) and its impact on the physicochemical properties of ion intercalation, which are of paramount importance to enhance battery lifetime and reliability. As the aforementioned mechanisms are mainly correlated to a mass change, *operando* methods pairing electrochemistry with simultaneous mass variation are expected to provide new insights. Therefore, during this Ph.D. thesis, the electrogravimetric-based techniques derived from electrochemical quartz crystal microbalance (EQCM) have been developed and adapted to accompany EEI characterization in battery research. Then, the technical developments and experimental strategies have been applied to model materials like LiFePO_4 , Prussian Blue analogs and as well as new protonic iridate phase H_xIrO_4 to study the EEI behavior and insertion mechanisms of lithium and potassium ions, as well as protons, depending on their solvation shell – in organic and aqueous electrolytes. The next chapter will be focused on the introduction of the EQCM derived electrogravimetric and electromechanical methods, from theoretical background to the literature already gathering

Chapter I

them with the field of battery, as well as the technical developments and experimental strategies that are developed during this PhD thesis.

Chapter II – An overview of the electrogravimetric, hydrodynamic and viscoelastic techniques

II.1 – Introduction

As presented in the previous chapter, the electrode-electrolyte interface is of main importance on the electrochemical performance of the battery, regardless of the considered metal-ion chemistry. However, appropriate tools giving fruitful insights on the processes occurring at this interface are scarce. To this end, the Electrochemical Quartz Crystal Microbalance (EQCM) based methods could meet the high standards to study this critical interface, especially when necessary developments are realized to make it compatible with today's battery tooling.

Therefore, this chapter will provide a detailed presentation of the theoretical background and techniques based on Quartz Crystal Microbalance and its coupling with electrochemical methods. Then, we propose a comprehensive analysis of the literature gathering battery studies employing QCM as gravimetric, hydrodynamic and viscoelastic indicators. This chapter ends by the strategies developed and employed throughout this Ph.D. thesis to make the QCM based techniques compatible for the battery electrode-electrolyte interface characterization.

II.2 – Quartz Crystal Microbalance theory and associated techniques

II.2.a – Quartz Crystal Microbalance fundamentals

o Piezoelectricity

The core principle behind Quartz Crystal Microbalance (QCM) is nested in the piezoelectricity effect. Its discovery dates back to the research of René Just Haüy; however, its study and interpretation are ascribed to the work of Pierre and Jacques Curie brothers (1880) on tourmaline, quartz and Rochelle salt.¹³⁷ They demonstrated the appearance of an electrical

field, which is proportional to the applied mechanical stress on these crystalline materials with no inversion symmetry. The converse effect was mathematically deduced by Gabriel Lippmann in 1881¹³⁸ and the Curie brothers confirmed its existence.¹³⁹ The practical applications of this phenomenon are several, starting by the development of sonar (sound navigation ranging) by Paul Langevin during the World War I (1917) to detect submarines to nowadays utilization in horology.

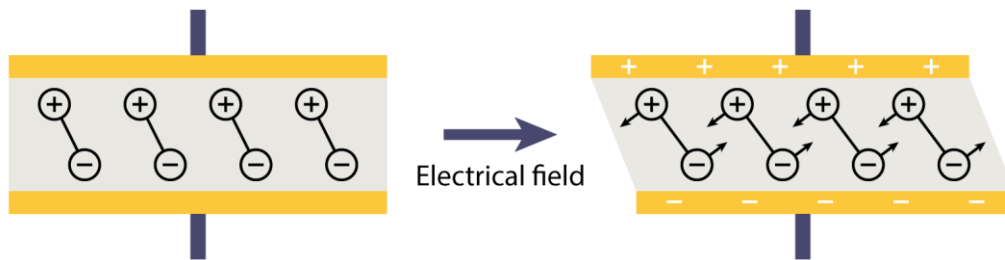


Figure II-1: Schematic representation of the piezoelectric effect on an AT-cut quartz crystal when an electric field is applied. Adapted from: *Buttry and Ward*.¹⁴⁰

Quartz (SiO_2) crystals were selected among the piezoelectric materials for its following benefits. It offers a low resistance to the propagation of acoustic waves and a high shear modulus. The conditions of synthesis are well controlled to obtain quartz with high purity and crystallinity. Moreover, it presents a high chemical stability especially in contact with the solutions.¹⁴¹ The vibration mode is dependent on the cut plane of the crystal. The AT-cut ($+35^\circ 15'$ compared to the (ZOX) plane) of the α -quartz single crystal is the most common due to its weak temperature dependence close to room temperature. This quartz slice is covered on both sides by a conducting layer, commonly gold. These parallel electrodes permit to apply an alternative potential difference, which keeps the quartz in its thickness shear vibration mode (in the case of AT-cut quartz), a transverse acoustic wave propagates across the thickness of the quartz crystal, as represented in the Figure II-1.

o Resonance frequency and Sauerbrey relationship

Thus, the assembled resonator vibrates at the characteristic frequency of the transverse acoustic wave. On resonance, the deformation pattern is a standing wave with antinodes at the surface, as depicted in the Figure II-2a. For the fundamental wave, the

wavelength of sound in the quartz (λ_0) is twice the thickness of the resonator. Therefore, the resonant frequency of the fundamental, f_0 , can be deduced thanks to the following equation:

$$f_0 = \frac{c_q}{\lambda_0} = \frac{c_q}{2t_q} = \frac{\sqrt{\frac{\mu_q}{\rho_q}}}{2t_q} \quad \text{Equation II-1}$$

where c_q is the transverse velocity in AT-cut quartz ($3.34 \cdot 10^5 \text{ cm}\cdot\text{s}^{-1}$), t_q is the thickness, ρ_q is the density of quartz ($2.648 \text{ g}\cdot\text{cm}^{-3}$) and μ_q is the shear modulus of the quartz crystal ($2.947 \cdot 10^{11} \text{ g}\cdot\text{cm}^{-1}\cdot\text{s}^{-2}$). This relation demonstrates that the quartz crystal resonant frequency only depends on its thickness. The thickness engineering of these AT-cut quartz permits to obtain a wide range of fundamental frequencies from 0.5 to 100 MHz depending on the application requirements.

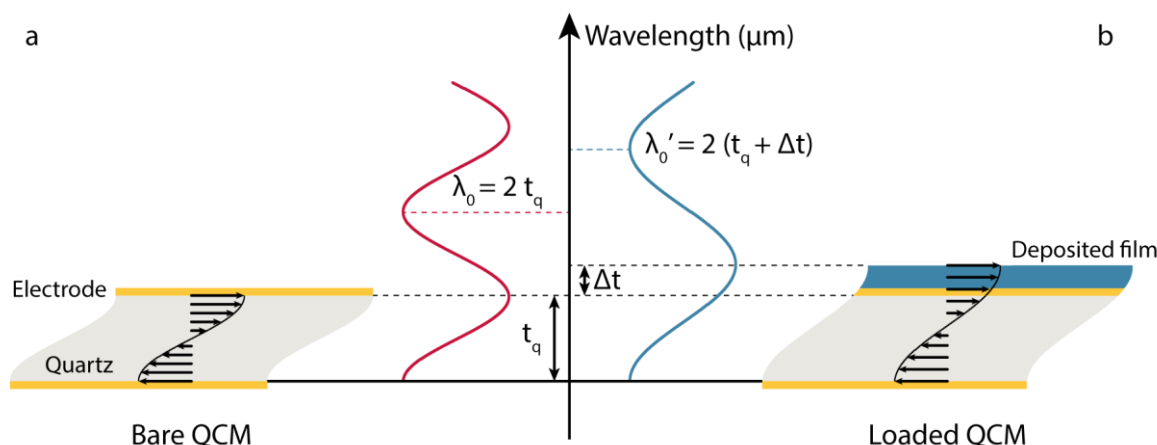


Figure II-2: Schematic representation of the standing wave establishment in (a) bare and (b) loaded QCMs. The resonance wavelength increases, so resonance frequency decreases with film deposition on the resonator surface.

When a uniform layer of a foreign material is added on one side of the quartz crystal, the layer then moves synchronously with the electrode. The acoustic wave can cross the crystal/foreign material interface and propagate through the foreign layer, as depicted in the Figure II-2b. The thickness change causes the modification of the standing wave parameters and therefore a frequency change. The following equation links the thickness change (Δt) to the frequency change (Δf) as an extension of the Equation II-1.

$$\frac{\Delta f}{f_0} = \frac{-\Delta t}{t_q} = \frac{-2f_0\Delta t}{\sqrt{\frac{\mu_q}{\rho_q}}} \quad \text{Equation II-2}$$

If the foreign layer is assumed to have the same physical properties as the quartz resonator, then the thickness change can be substituted into the previous equation leading to the Sauerbrey relationship (1959).¹⁴²

$$\Delta m = -\frac{A\sqrt{\rho_q\mu_q}}{2f_0^2}\Delta f = -C_f\Delta f \quad \text{Equation II-3}$$

where Δm is the mass change (ng), A is the piezoelectrically active area (cm²) and C_f is the sensitivity factor or calibration factor (ng/Hz). The Sauerbrey relationship is the key equation to convert the frequency change to mass change and explains the utilized terms to define these resonators: Quartz Crystal Microbalance (QCM). However, the Sauerbrey relationship is solely valid under certain conditions concerning the deposited layer. It has to be an ideal rigid film attached to the quartz crystal where the mass of the film should not exceed the 2 % of that of the crystal. In addition, the film is expected to be evenly distributed over the active area of the crystal. The Equation II-3 demonstrates the relationship between the resonant frequency change and the mass change of a quartz resonator, where an increase in mass induces a decrease in the resonant frequency, as depicted in the Figure II-2. The relationship between the wavelength of sound in the quartz and its resonant frequency was already given in Equation II-1.

The QCMs and the Sauerbrey relationship were firstly exploited to measure the thickness of films deposited under vacuum or gaseous environments. Since Nomura and Okuhara showed that a crystal completely immersed in a liquid could also be excited to stable oscillation, the QCM has become an analytical tool in electrochemistry.¹⁴³ This principle was exported to electrochemical applications, as the metallic substrates can be used as electrodes, giving rise to Electrochemical Quartz Crystal Microbalance (EQCM). The *in situ* studies following the copper and silver electrodeposition are pertinent examples, which are then also used for the calibration of the QCM devices (see III.3.c).

○ *Frequency response in a liquid medium – Kanazawa and Gordon equation*

The emergence of QCM measurements in the liquid media has stimulated the studies investigating the influence of liquid on the resonant frequency of a resonator, which, later on, have also found implications in QCMs coupled to electrochemical methods.

When the quartz surface is immersed in a liquid, the shear wave propagates from the quartz into the liquid volume in its vicinity. However, the wave is dampened and its amplitude decays moving away from the quartz. Importantly, the presence of the liquid introduces a new “layer” to the system resulting in a shift in resonant frequency, leading to a new baseline, by an amount corresponding to the mass of viscously coupled fluid layer.^{144,145} The effect of immersing the QCM in liquid results in a decrease in frequency, which can be estimated thanks to the Kanazawa and Gordon equation (1985):¹⁴⁶

$$\Delta f = -f_0^{\frac{3}{2}} \sqrt{\frac{\rho_l \eta_l}{\pi \rho_q \mu_q}} \quad \text{Equation II-4}$$

where ρ_l and η_l are the density (g.cm^{-3}) and viscosity of the liquid (Pa.s), respectively.

○ *Overtones and penetration depth*

Contrary to the descriptions given in the previous sections, here the quartz resonance is not restricted to the fundamental vibration mode; but overtones (harmonics) are also reachable. The antinodes at the surface condition for the establishment of a deformation imposes only odd overtones to be excited (Figure II-3a). The previous equations remain valid, so that the Sauerbrey relationship can be generalized to different overtones ($1 \leq n \leq 13$):

$$\Delta m = -\frac{A \sqrt{\rho_q \mu_q}}{2 f_0^2} \frac{\Delta f}{n} = -C_f \frac{\Delta f}{n} \quad \text{Equation II-5}$$

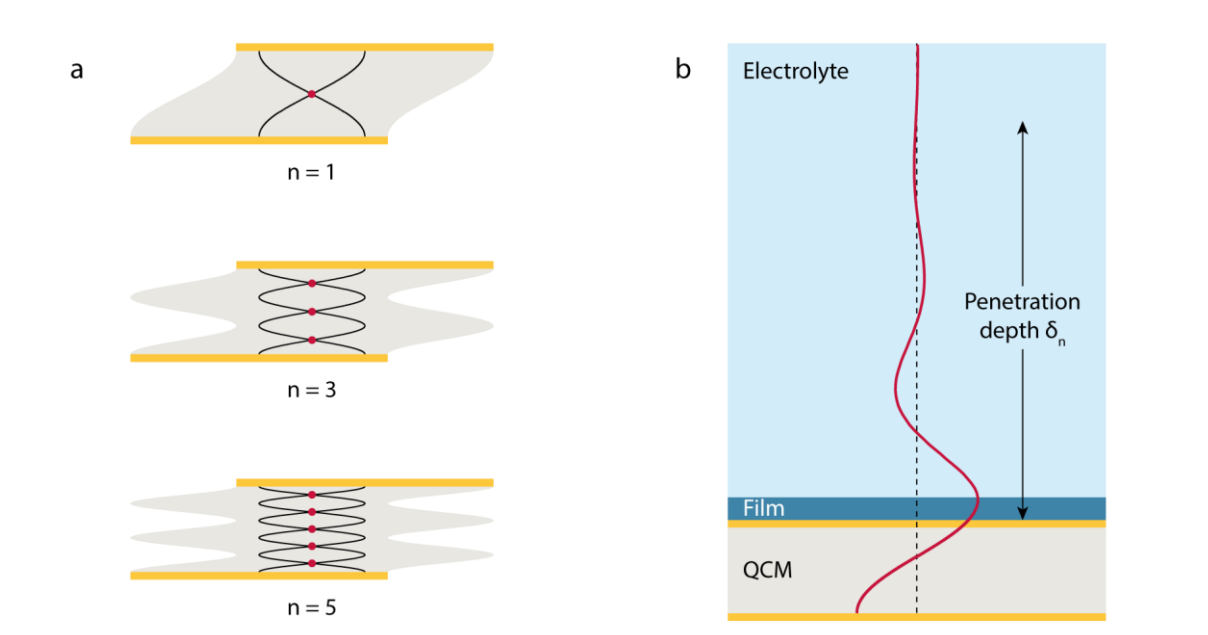


Figure II-3: (a) Schematic representation of the standing wave establishment for different overtones. (b) Acoustic wave propagation of a QCM sensor in contact with a stiff non-porous coating and an electrolyte.

In contrast to the situation in air, the transverse acoustic wave propagates for a short distance from the crystal surface to the liquid layer (Figure II-3b). This distance of the propagation is of the order of the penetration depth δ_n (decay length). It depends on the viscosity and density of the liquid, the fundamental resonance frequency, of course, but also on the overtone, as shown by:

$$\delta_n = \sqrt{\frac{\eta_l}{\pi n f_0 \rho_l}} \quad \text{Equation II-6}$$

For aqueous electrolytes with a 9 MHz resonator, the range of δ_n is approximately between 189 ($n = 1$) and 52 nm ($n = 13$). At a fixed viscosity/density ratio (same electrolyte), the penetration depth can be used as an *in situ* hydrodynamic probe using multiple overtone orders to characterize the morphology of the deposited film on the QCM sensor. This particular point is more precisely described later in this chapter (see II.4.b).

○ Species determination during electrochemical processes

As pointed out earlier, one metallic side of the quartz resonator can be used as a working electrode to perform electrochemical experiment, giving rise to Electrochemical Quartz Crystal Microbalance (EQCM). The coupling of electrochemistry to the mass change permits to attain mechanistic information on electrochemical processes with solid reaction products by calculating the following value:

$$\frac{M}{z} = F \frac{\Delta m}{\Delta Q} = -F C_f \frac{\Delta f}{\Delta Q} \quad \text{Equation II-7}$$

where M is the molar mass of the involved species ($\text{g}\cdot\text{mol}^{-1}$) and z is the number of electrons of the supposed electrochemical reaction. F is the Faraday constant ($96485 \text{ C}\cdot\text{mol}^{-1}$) and ΔQ is the charge change (C) measured during the electrochemical process. This value is the combination of the Sauerbrey relationship and the Faraday law and permits the determination of the involved species.

The studies using QCMs have a common element: the resonator. The fundamental frequency, the surface area or the electrode metal can differ from one study to another but the resonance principle is always the same. However, different equipment and operation methods exist with their very own capabilities; they are introduced and described in the following section.

II.2.b – Gravimetric and viscoelastic read-out methods

○ Oscillator circuit and QCM with motional resistance monitoring

An electrical equivalent circuit composed of equivalent circuit elements that represent its physical parameters under oscillation can model the quartz resonance. The so-called Butterworth-Van Dyke (BVD) equivalent circuit is used to describe an unperturbed (without additional film or electrolyte) quartz resonator, as represented in the Figure II-4a. In the series branch, the inductor, L_1 represents the inertial component related to the mass displaced during oscillation, the capacitor, C_1 represents the energy stored during oscillation and the

resistance, R_1 represents the energy dissipated during oscillation, which is also called the motional resistance. This series branch is referred as the motional branch as it defines the electromechanical characteristics of the quartz resonator. The parallel branch, referred as electrical branch, is composed of a capacitor, C_0 , which arises from the electrical capacitance of the dielectric medium, *i.e.* the quartz, sandwiched between the two electrodes on both side of the quartz.

QCM experiments, however, involve quartz crystal surface that are either immersed in liquid media, coated with films, or both, giving rise to a more complex electrical equivalent circuit (Figure II-4b). First, the liquid film has an influence on the resonant frequency as noted by the Kanazawa and Gordon equation (Equation II-4), which depends on its density, ρ_l and viscosity, η_l . It can be described as the addition of a mass loading density component, L_L and a resistive viscosity component, R_L of the liquid. Concerning the coatings that are deposited on the conducting electrode of the resonators, two cases can be distinguished. If the coating is “acoustically thin” and rigid, then it will vibrate in phase with the oscillator following the Sauerbrey equation and causing the addition of a mass loading, L_F and a dissipation of energy, R_F . Apart from this ideal case, the coating can be viscoelastic, defined with its own physical properties: viscosity (loss modulus), density and elasticity (storage modulus). This will result in the addition of an extra mass loading, L_V , a dissipation of energy, R_V and a stored energy arising from the elasticity, C_V to the circuit. Nonetheless, the electrical equivalent circuit of the practical assembly can be generalized to a classical BVD circuit (Figure II-4c).

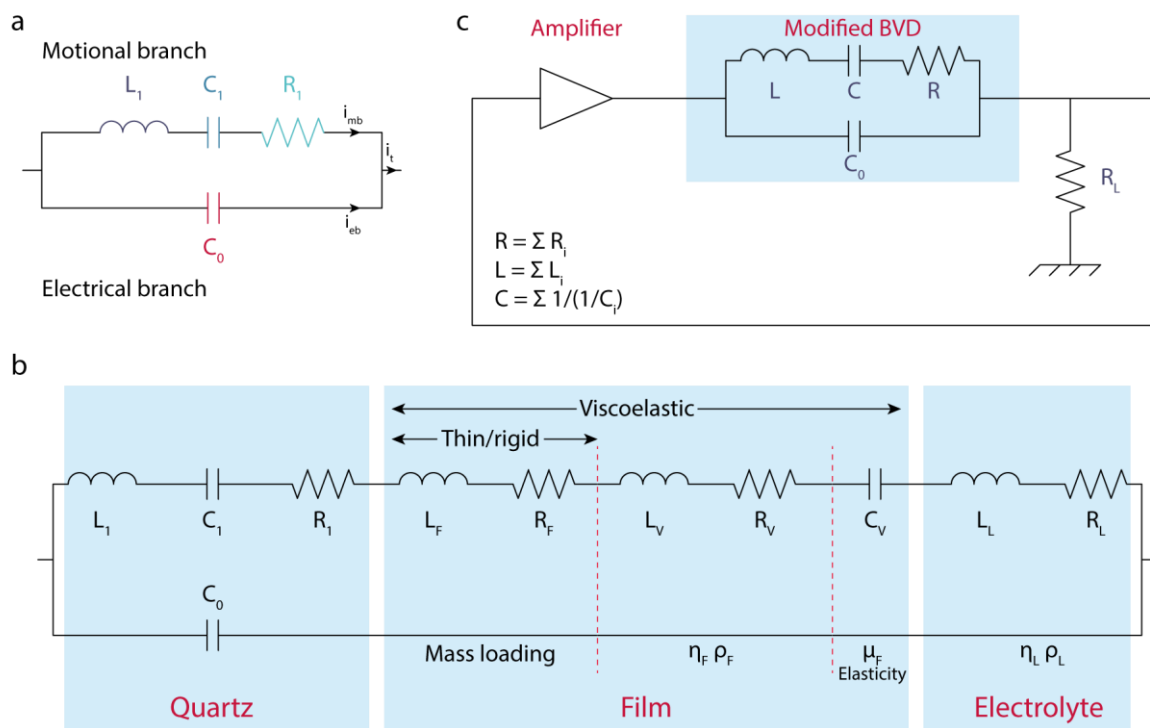


Figure II-4: (a) Butterworth-Van Dyke (BVD) equivalent circuit for an unperturbed QCM. (b) Modified BVD equivalent circuit for a QCM in contact with a viscoelastic film and an electrolyte. (c) Simplified electrical circuit of the QCM with motional resistance monitoring. Adapted from references.^{140,147,148}

When energy in a system is exchanged periodically between two forms, then resonance occurs at a characteristic resonant frequency. An electrical circuit with a capacitor and an inductor is the perfect example of the resonance phenomenon between electrical and magnetic energies. The fact that this phenomenon is also found between the energy stored in the quartz and the inertia of the displaced mass at the surface during oscillation explains the analogy between mechanical and electrical systems with the electrical equivalent circuit.¹⁴⁷ A common and mature method to obtain resonance of the system is based on an oscillator circuit, which consists of an amplifier and a quartz crystal resonator with a feedback loop, as depicted in the Figure II-4c. If the Barkhausen condition is fulfilled (the product of impedances of the amplifier and the resonator is equal to unity), a self-sustained oscillation occurs. The gain of the amplifier must compensate the losses in the feedback loop especially the energy dissipated during oscillation (motional resistance). The oscillator circuit is associated to a frequency counter, which directly measures the frequency in MHz. Alternatively, the output of the circuit can be mixed with a reference oscillator to count more precisely the frequency difference in kHz or less. In addition to resonant frequency, the motional resistance can also

be measured (QCM-R) by introducing an additional resistance R_L into the oscillator circuit and measuring the ohmic drop through this latter. However, to this purpose, the parasitic capacitance C_0 has to be canceled ($i_{eb} = 0$, see Figure II-4a) to obtain a measured current proportional to motional resistance ($i_t = i_{mb}$).

The motional resistance carries information about acoustic energy dissipation in the coating and the surrounding medium. This information is different from the frequency shift, which is related to acoustic energy storage. The motional resistance measurement in gaseous environment is optional but it is of prior importance for QCM applications dealing with liquid environment or a foreign film. In such cases, monitoring both frequency and motional resistance, QCM-R, allows for a much more assured data interpretation.¹⁴⁷

o Impedance analysis – Network analyzer

Contrary to QCM-R, impedance analysis (QCM-I) passively interrogates the resonator by a frequency-sweeping signal around its resonance frequency to analyze its electrical impedance/admittance behavior. Electrical admittance (inverse of impedance) can be expressed as a complex number $Y = G + iB$, with the real part, the conductance G and the imaginary part, the susceptance B . The Figure II-5a represents classical conductance and susceptance of a bare AT-cut quartz resonator in air. If the fixed dielectric capacitance of the resonator is compensated, the admittance of a generalized Butterworth-Van Dyke can be expressed as follows:

$$Y(f) = \frac{1}{R + i\left(2\pi fL - \frac{1}{2\pi fC}\right)} \quad \text{Equation II-8}$$

and its modulus by

$$|Y(f)| = \frac{1}{\left(R^2 + \left(2\pi fL - \frac{1}{2\pi fC}\right)^2\right)^{\frac{1}{2}}} \quad \text{Equation II-9}$$

The modulus presents a maximum at the resonant frequency, f_r , where:

$$f_r = \frac{1}{2\pi\sqrt{LC}} \quad \text{Equation II-10}$$

and

$$Y(f_r) = \frac{1}{R} \quad \text{Equation II-11}$$

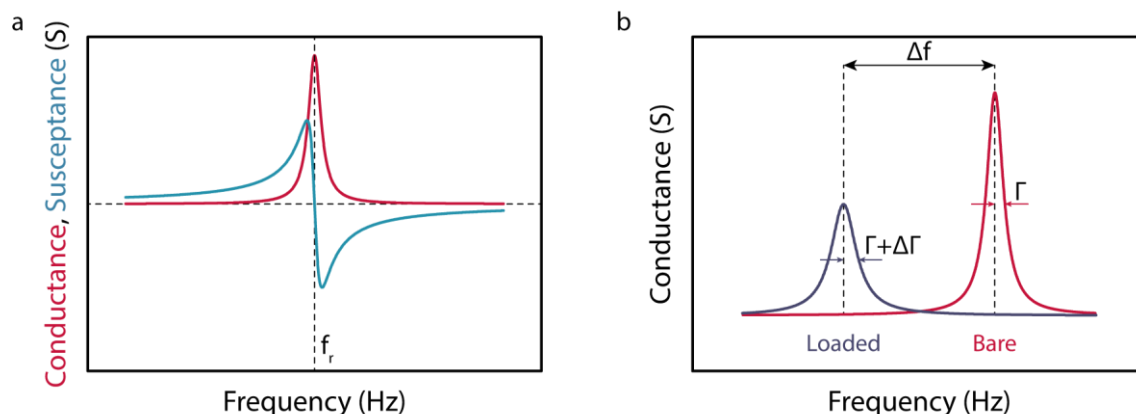


Figure II-5: Admittance analysis of QCM sensor by a network analyzer. (a) Classical conductance and susceptance for a QCM-sensor. (b) Frequency and half-bandwidth shifts displayed by conductance measurement on loaded and bare quartz resonators. Adapted from: *Arnau*.¹⁴⁷

At the resonant frequency, the admittance is only real component, so the susceptance admits a zero-crossing point. From the conductance representation, several key parameters can be extracted: the resonant frequency, f_r , the electrical components involved in the BVD circuit and the half-bandwidth Γ (half of the bandwidth at half maximum of the resonance peak) (Figure II-5b). The impedance of the quartz crystal sensor can be measured using a network analyzer to accurately determine the changes in frequency and half-bandwidth. The Figure II-5b shows these changes when passing from a bare quartz to a quartz loaded with a film and/or a liquid. The added layer causes a negative shift of the resonant frequency and a damping, *i.e.* increase of the half-bandwidth, due to energy dissipation.

In addition, the changes in frequency and half-bandwidth (bandwidth is $W = 2\Gamma$) can be correlated to the dissipation factor D of the deposited film or to the quality factor Q , thanks to the following relationship:

$$Q_n = \frac{f_n}{2\Gamma_n} = \frac{f_n}{W_n} = \frac{1}{D_n} \quad \text{Equation II-12}$$

These factors quantify the resonator damping and can be related to the sample's viscoelastic properties coated on the resonator. These measurements can be conducted at fundamental mode and on harmonics, providing possibilities to explore viscoelastic properties of the materials.

o *QCM with dissipation monitoring at different overtones*

In addition to previous read-out systems, a relatively recent method to access the key parameters of the resonance is to excite the resonator with a narrow radio frequency pulse having a frequency matching the expected resonance frequency (Figure II-6a). The excitation is intermittently turned off and resonance decays freely, also called the ring-down method or “pinging”. The Figure II-6b demonstrates that the resonance frequency and the dissipation factor (half-bandwidth) can be obtained from the fitting of the current-versus-time trace with a decaying cosine. It can be noted that the obtained signal is linked to the Figure II-5a presented in the previous subsection by a Fourier transform, passing from the time to the frequency domain. This approach was developed by Rodahl et al.^{149,150} This measurement methodology is the basis of the QCM-D where D is for “Dissipation monitoring” and the term QCM-D is a trademark owned by Q-Sense (Biolin Scientific). In addition, the different overtones can be excited successively.

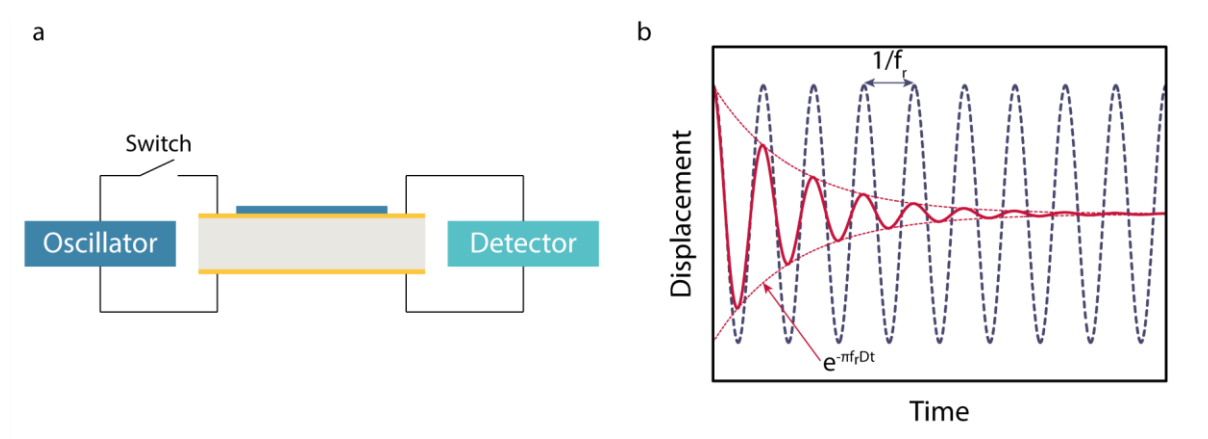


Figure II-6: (a) Schematic representation of the ring-down method. (b) Measurement of the damped oscillation allowing the determination of the resonant frequency and the dissipation factor. Adapted from: Rodahl et al.¹⁴⁹

The ring-down process is faster than impedance analysis, the excitation of the quartz crystal, recording and fitting of the decay curve occurs on the millisecond timescale (Γ^{-1} for

the order of magnitude). Thus, the QCM-D approach has the capability to provide real-time data acquisition. This can be used to decouple rigid from soft materials that show differences in terms of decay time constant when adsorbed on the crystal surface. Rigid materials, such as metal films for example, couple well with the oscillating quartz, and, when the driving voltage is turned off in a QCM-D experiment, the oscillation takes longer to decay. On the other hand, if the deposited mass is soft and viscoelastic, the coupling with the oscillating quartz is poor. The flexible viscoelastic mass dampens the crystal oscillation causing it to decay faster.

II.2.c – Comparison of the different QCM-based read-out methods

The three methods presented in II.2.b are well developed and offer unique information on gravimetric, hydrodynamic or viscoelastic changes (or their combination). However, besides their common feature of the resonant frequency change measurement, these methods differ on other criteria causing a trade-off between associated benefits and drawbacks (Table II-1).

Table II-1: Fair comparison of the QCM-based read-out methods

	Advantages	Disadvantages
QCM with motional resistance monitoring (QCM-R)	<ul style="list-style-type: none"> ◦ Affordable ◦ More stable frequency measurement¹⁵¹ ◦ Real-time data acquisition ◦ Easily extendable to electrochemical measurement 	<ul style="list-style-type: none"> ◦ Optimized for one particular overtone ◦ Motional resistance not directly related to half-bandwidth
Impedance analysis – Network analyzer (QCM-I)	<ul style="list-style-type: none"> ◦ Graphical representation ◦ Controlled data acquisition ◦ Multiple overtones ◦ Resonant frequency, half-bandwidth and electrical equivalent circuit components acquisition 	<ul style="list-style-type: none"> ◦ One overtone at once ◦ No real-time data acquisition ◦ Time consuming
Multiharmonic QCM with dissipation monitoring (QCM-D)	<ul style="list-style-type: none"> ◦ Multiple overtones ◦ Real-time data acquisition ◦ Resonant frequency change and dissipation factor acquisition ◦ Integrated software for viscoelastic data analysis 	<ul style="list-style-type: none"> ◦ Expensive ◦ Extendable to battery material analysis with difficulty ◦ “Black box” effect

Impedance analysis, QCM-I and QCM-D have the benefit over QCM-R to point out the viscoelastic properties of the deposited film on the QCM sensor, for instance, when immersed in an electrolyte and during electrochemical cycling. Nevertheless, in certain well-defined conditions, QCM-R is the method of choice to obtain reliable data with a higher stability and precision. This is what motivate our strategy to acquire new insights on the battery electrode-electrolyte interface by QCM with motional resistance coupled with electrochemical methods, *e.g.* cyclic voltammetry (CV) and galvanostatic charge/discharge (GCD), as it will be developed later in this chapter (see II.4.a). Beforehand, a comprehensive analysis of the literature using QCM-based techniques to study battery related phenomena is proposed in the next section.

II.3 – Electrogravimetric, hydrodynamic and viscoelastic inputs to the battery field so far

II.3.a – EQCM-based methods for the study of Solid Electrolyte Interphase

The use of EQCM-based methods for the characterization of batteries is mainly rooted in the better understanding of the Solid Electrolyte Interphase (SEI). As previously introduced (see I.2.b), the SEI is a new phase mainly formed at the surface of the negative electrode due to electrochemical instability of the electrolyte at such negative potentials. The understanding of the physical properties of this newly formed phase and its evolution are of prior importance for the good performance and enhanced safety of the battery.

Aurbach *et al.* were the first researchers to use the real-time assessment of mass variation provided by EQCM and the Sauerbrey equation (Equation II-3) in 1995, to study the surface film formation over a bare gold electrode in LiPF_6 and LiAsF_6 in propylene carbonate (PC).¹⁵² The M/z value (Equation II-7) was calculated during a negative sweep of potentials in PC-based electrolytes containing different salts and contaminants as water or carbon dioxide. Thanks to this procedure, they could demonstrate the potential-dependent formation mechanism of the SEI, with the solvent reduction at low potentials and the LiF film formation at higher potentials creating an inner inorganic layer covered by a polymeric layer. Then, SEI studies have moved to systems that are more realistic, starting by PVD-prepared carbon. Unlike previously employed model electrodes, the mass change appearing during the potential sweep turned out to be also dependent on the lithium ion insertion/extraction, which needs to be untangled from the mass change caused by solely SEI formation. In this context, Kwon and Evans managed to determine the SEI average density proving its mixed organic and inorganic composition with the initial formation of Li_2O in fluorine-free electrolytes.^{153,154} Such a methodology has been expanded to other active materials as electrodeposited Sn film¹⁵⁵ and recently drop-cast graphite¹⁵⁶ on the surface of EQCM resonators, leading to similar results but dependent on the electrolyte composition: salt and solvent. In the framework of this Ph.D. thesis, a similar strategy has been applied to prove the formation of a passivating layer composed of fluorinated products induced by the water

reduction in the trendy “Water-in-Salt” electrolyte¹⁵⁷ system but this study will not be described in this manuscript.

Although limited number of studies exist so far, the development of EQCM with dissipation monitoring has contributed to assessing viscoelastic properties of the SEI and changes in electrolyte viscosity, which were unreachable (or entangled) with classical EQCM measurements. Yang *et al.*^{158,159} attested the beneficial addition of fluoroethylene carbonate to the ethylene carbonate/ethyl methyl carbonate-based electrolyte for the cycling of tin anode. It gave rise to a stiffer and more homogeneous SEI, corroborating the observed better capacity retention. This type of methodology has been applied by the group of Levi and Aurbach to prove the better quality of SEI in LiTFSI than that formed using LiPF₆ + vinylene carbonate on high potential Li₄Ti₅O₁₂ (LTO) anodes.¹⁶⁰ Going further in this process, this study opened up the possibility of using EQCM-D to screen different electrolyte compositions leading to a more efficient SEI, and to access to the predictive information for the practical applications in a short time. Kitz and co-workers adopted an analogous strategy, to model bare electrodes, except that, Electrochemical Impedance Spectroscopy (EIS) and Online Electrochemical Mass Spectrometry (OEMS) were added to the tool panel in order to reveal the SEI formation mechanism. In agreement with the literature, the formation of a rigid LiF-rich interphase was shown to occur prior the emergence of a less rigid film of reduced solvent products during a negative sweep of potentials, demonstrating the highly dynamic nature of this interphase, in terms of both mechanical and electrochemical properties.¹⁶¹ The same experiments in presence of water demonstrated that the SEI becomes thicker and more rigid and this was explained by the formation of Li₂CO₃-rich early interphase preventing the formation of a soft reduced solvent-based film.¹⁶² The contribution of VC and FEC additives on SEI were also investigated. Both additives change the SEI composition causing an increase of the SEI shear modulus. However, the Li-ion conductivity in the SEI is increased in the case of VC and hindered for FEC.¹⁶³ Searching for complementary compositional information, EQCM-D coupled with surface-enhanced Raman spectroscopy evidenced the charging of an electric double layer composed mainly of accumulated Li⁺ solvated by EC molecules before the SEI formation explaining the SEI mainly composed of products coming from the EC reduction.¹⁶⁴

II.3.b – Mechanical properties of the electrodes during cycling

Mechanical and viscoelastic studies are not restricted to the evaluation of the SEI formation. It has also been extended to study the behavior of composite electrodes under battery operation conditions. EQCM-D has the benefit of simultaneous monitoring of dissipation at multiharmonics, over the manual operation of network analyzers at different overtones. Performing experiments of dissipation monitoring by EQCM-D or NAs proved its utility in distinguishing the gravimetric cases (where Sauerbrey equation applies) from those deviate from the “dense and rigid thin layer assumption”. The group of Levi and Aurbach developed the experimental and theoretical background permitting the extraction of the desired features; however, the literature is scarce and almost monopolized. Classical composite electrodes for battery application are multicomponent: the active material, a conductive agent *e.g.* carbon black and a binder to mechanically hold the different particles. Therefore, deviations from the idyllic “dense and rigid thin layer” condition may occur for the electrodes with different porous geometry and binders, contributing to the Δf of the resonators in contact with electrolyte by hydrodynamic and viscoelastic effects, respectively. Consequently, in addition to the gravimetric EQCM, two non-gravimetric cases, which involve the hydrodynamic effects (the behavior of porous and rough surface electrode in the electrolyte) and the viscoelastic effects (softening/stiffening of the electrode in the electrolyte) during charge/discharge, enabled the use of EQCM-D as a structural/morphological and mechanical/viscoelastic probe, respectively.

The examined aspect granted by EQCM-D is the particle-binder interaction. Shpigel *et al.* in 2015, firstly investigated the influence of the polymeric binder nature and electrolyte solvent on the elastic properties of the composite electrodes. The authors compared the Na Carboxymethyl cellulose (NaCMC) and PVDF binders in aqueous and organic electrolytes and demonstrated that NaCMC acted as a soft binder in aqueous but rigid in organic electrolyte, which was the opposite for the PVDF mainly due to solvent-dependent swelling behavior.¹⁶⁵ Later, they confirmed the mentioned arguments using fluid mechanic and viscoelastic modeling to untangle solid-liquid hydrodynamic interactions from the film viscoelastic properties.^{166,167} On the basis of this methodology, binders can be screened to find the “stellar” one having the optimized properties, *i.e.* moderately high elastic modulus to allow

reversible intercalation-induced volume changes of the composite electrode but not too soft to prevent the deterioration of the electronic conductivity. In recent studies, the strain accommodation enabled by the binder in a composite electrode was pushed to their limit under harsher conditions. The particle-binder interactions were also evaluated during the insertion of bigger cations like sodium ion in FePO_4 ¹⁶⁸ or during the fast charging of a model material like LiFePO_4 ¹⁶⁹, further demonstrating the importance of the binder properties on the battery cycling performance. These findings show the richness of information that EQCM-D can provide to the battery field and a more exhaustive list can be found in references.^{170–172}

II.3.c – Characterization of the cation insertion in battery compounds

In addition to the previous capabilities, EQCM has the ability to measure *in operando* the cation insertion/extraction into the battery material structure. This technique has been implemented for the study of several active Li-host electrode materials. Firstly, in 1997, Yang *et al.* demonstrated a two-step process for the Li^+ insertion in LiMn_2O_4 .¹⁷³ This was found to contrast with V_2O_5 which shows a scan rate dependent mechanism, in which lithium intercalates without and with solvent molecules (acetonitrile) at low and high rates, respectively.¹⁷⁴ Solvent molecules, especially water have also been evidenced to participate in the lithium ion insertion by co-intercalating in WO_3 ^{175,176}, Nb_2O_5 ¹⁷⁷ and MnO_2 ¹⁷⁸. In certain cases, the solvent co-intercalation was corroborated by the abnormal increase in the interlayer distance measured by XRD.¹⁷⁴ The benefit of the gravimetric methods in those cases was to verify the reversibility of the mass changes in electrochemical processes and the possible co-intercalation of solvent molecules. Such analyses have contributed to the understanding of the ion (de)-intercalation mechanisms, and have stimulated new studies using other charge carriers. The feasible magnesium ions intercalation in MnO_2 thanks to the shielding of magnesium charge by water molecules in organic electrolyte has been demonstrated by an EQCM study.¹⁷⁹ A similar behavior was found in the case of dual-ions batteries where EMC solvent molecules act as a lubricant for the fluent transport of anion inside the graphite electrode.¹⁸⁰ These gravimetric measurements are the direct fingerprint of the interactions between the solvent molecules and the cations while being inserted at the

electrode-electrolyte interface, dictating the battery performances as described in the previous chapter (see I.2.b).

Such benefits go well beyond the battery field since both EQCM and EQCM-D have provided highly relevant results on the interfacial properties of supercapacitor electrodes, evidencing for instance the permselectivity behavior and the electroadsorption of partially solvated cations, depending on the pore size of the carbon electrode.^{181,182}

II.4 – EQCM-based strategies developed and employed in this Ph.D. thesis

II.4.a – Classical EQCM-R measurements adapted to battery electrode characterization

The current literature described in the previous sections demonstrates that EQCM with dissipation monitoring is the technique of choice for battery electrode characterization, as it can be extended beyond the solely gravimetric measurement for characterizing the hydrodynamic and viscoelastic changes of the composite electrodes. Unfortunately, this technique suffers from certain inconveniences, especially in the data analysis/comprehension due to heavy set of equations. Moreover, this tool and the data analysis/modelling is expensive in time and budget to make it practical and compatible with the particular setup in the battery field. Therefore, this Ph.D. thesis aims at the development and adaptation of the classical EQCM-R technique to the battery electrode characterization. EQCM-R permits the resonance frequency change and the motional resistance (R) to be simultaneously monitored. As discussed and compared earlier, EQCM-D and EQCM-R both have their advantageous and disadvantageous and are not free from improvements. Here, EQCM-R will be privileged and exploited for its capacity in providing cheaper and more stable measurements compared to EQCM-D (see Table II-1 for the comparison).

In this work, AT-cut 9 MHz quartz resonators (Figure II-7a) patterned with gold electrodes on both sides were used as EQCM electrodes ($8.95 \text{ MHz} \pm 50 \text{ kHz}$, QA-A9M-AU(M)). The electroactive geometric surface area was equal to 0.196 cm^2 . The quartz resonator was

mounted between two perfluoro-elastomer O-rings known for their non-swelling behavior in organic electrolyte. Then, it was inserted in a labmade cell, designed specifically for EQCM measurements with its unique role of being used either with aqueous or organic electrolyte. This cell was developed conjointly by CSE lab and Sphere ENERGY, during this Ph.D. thesis. The characteristics of the cell and its design are precisely described in the Chapter III. The cell was kept at 25 °C during the experiment thanks to a temperature-controlled oven. A commercial SEIKO QCM922A microbalance (Figure II-7b) was connected to the cell through a BNC cable to monitor the resonance frequency change (Δf) along with the motional resistance (R) during the electrochemical processes. The microbalance was coupled with a SP-200 potentiostat (BioLogic) in the “WE to ground” configuration, which permitted the simultaneous recording of microbalance outputs and the realization of simultaneous electrochemical measurements, as depicted in the Figure II-7c. Finally, a computer centralized the control over the electrochemical and gravimetric measurements.

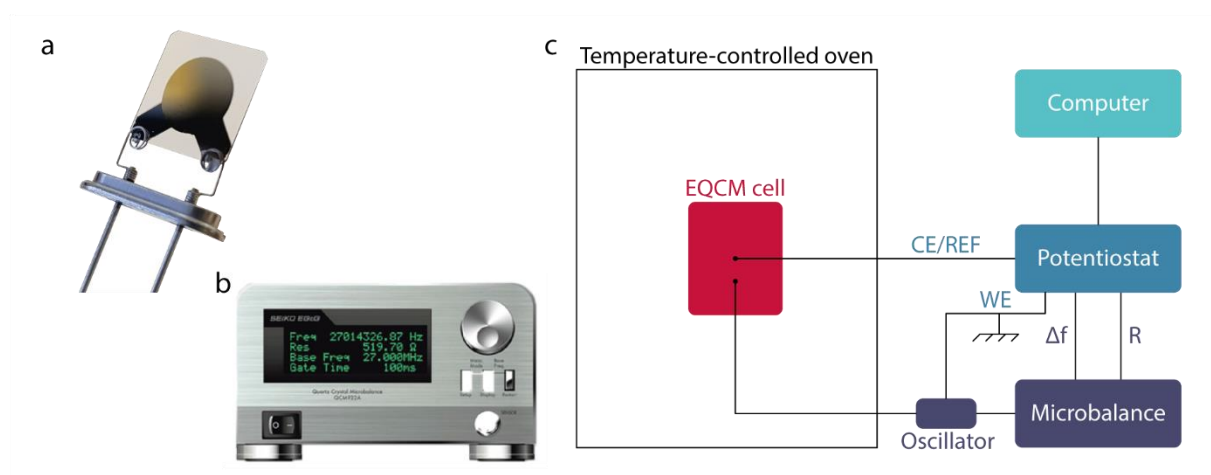


Figure II-7: (a) EQCM electrode and (b) SEIKO QCM922A microbalance used during this Ph.D. thesis, (c) schematic representation of the electrical circuit for frequency and electrochemical monitoring.

Since the principle goal of this Ph.D. thesis is to study phenomena taking place at the electrode-electrolyte interface of battery materials, a critical steps consists in the deposit of active particles on the gold electrode surface of the quartz resonators. The process to prepare composite electrode coatings on the QCM resonators are critical for performing EQCM-based measurements and will be described in the next chapter (see III.2). Meanwhile, in the next sub-section, the developed methodology to evaluate the characteristics of the resulting coatings (surface roughness, rigidity and porosity (revealing indications about the

hydrodynamic solid/electrolyte interactions and viscoelastic properties)) are depicted and the conditions where Sauerbrey equation can be conveniently used for frequency change analysis are detailed.

II.4.b – Determination of the film hydrodynamic and viscoelastic properties

Two criteria are of main importance to fulfill the gravimetric case and the Sauerbrey relationship (Equation II-5):

- i. the electrode coating needs to be stiff and rigidly attached to the quartz resonator both in air and in the electrolyte under Open-Circuit Potential and polarization.
- ii. the hydrodynamic solid-liquid interactions should not cause any dissipation in contact with the electrolyte, which is fulfilled in the case of a film with a moderate vertical and lateral non-homogeneity.^{171,172}

The steadiness of the resonant frequency and the dissipation factor over time when immersed in an electrolyte can prove that the condition i. is successfully fulfilled. Concerning the hydrodynamic solid-liquid interactions ii., the characteristic lateral geometric parameter of the porous electrode coating (d_{pore}) should be compared to the penetration length of the acoustic wave presented earlier (Equation II-6). As represented in the Figure II-8, if the average lateral size of the pores between the particles is lower than the penetration depth, δ_n , then the electrolyte inside the pores is trapped *i.e.* the liquid moves synchronously with the film hence with the quartz resonator. Such a behavior does not show any change in the dissipation factor. In other words, the composite film behaves as an extension of a flat uncoated crystal and in that case, the Kanazawa and Gordon equation (Equation II-4) defines the hydrodynamic solid-liquid interactions. Using QCM-D, the film is probed with smaller penetration depths as the overtone increases defining the *in situ* hydrodynamic spectroscopy of the coating on a QCM resonator.^{171,172}

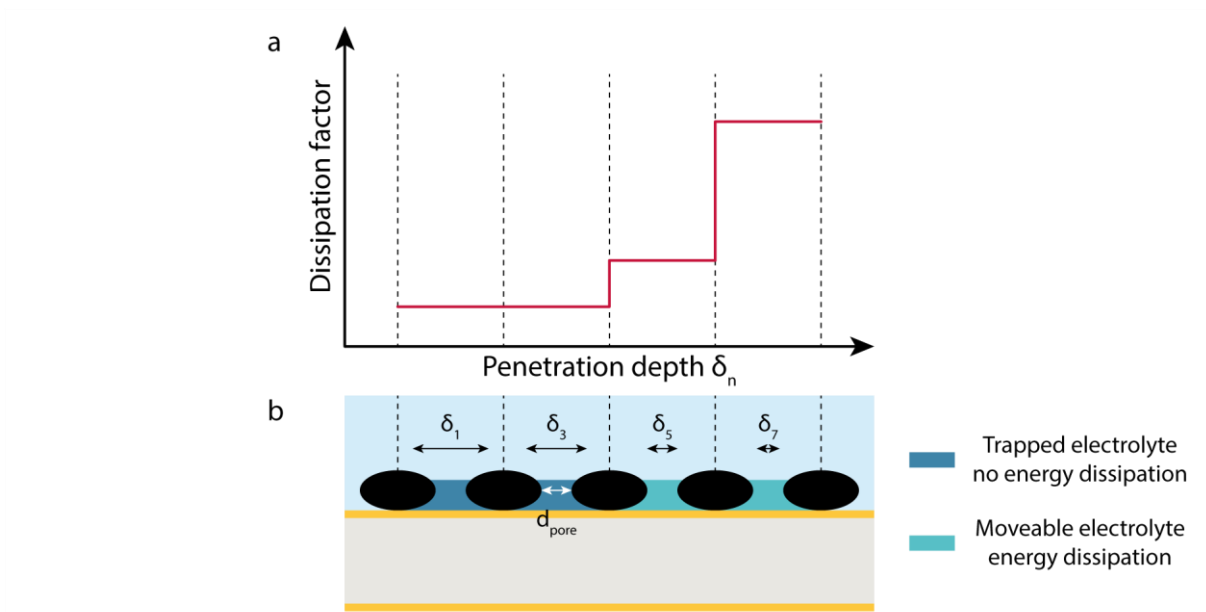


Figure II-8: *In situ* hydrodynamic spectroscopy of a quartz crystal resonator coated with an ideal film of particles. (a) Evolution of the dissipation factor as a function of the penetration depth, (b) Comparison between δ_n and the average lateral size of the pores (“trapped electrolyte” at lower overtone numbers become “moveable electrolyte” at the higher overtone numbers).

Practically, the resonant frequency, f , and the absolute dissipation factor, D , of the bare and loaded resonator in air were recorded at the different overtones with an Agilent 4294A impedance analyzer. The resonant frequency was obtained from the maximum of the electroacoustic admittance and the typical Butterworth-Van Dyke (BVD) equivalent circuit was used to fit this admittance to extract the values of the different component, defined in the Figure II-4a and Equation II-8. Then, the absolute dissipation factor was estimated thanks to the following equation:

$$D = \frac{R}{2\pi fL} \quad \text{Equation II-13}$$

The absolute dissipation factor has been replaced by the resonant width thanks to the Equation II-12. Then the resonant frequency and the resonant width of the loaded resonator in electrolyte was recorded at the different overtones with an AWS A20 Platform (Advanced Wave Sensors S.L., Spain) to be compared with their analogous values of the loaded resonator in air.

We can then define a shift of the complex resonance frequency \tilde{f}^{148} as:

$$\Delta\tilde{f} = \Delta f + i\Delta\Gamma = \Delta f + i\frac{\Delta W}{2} \quad \text{Equation II-14}$$

This equation can be generalized in the case of a multi-harmonic measurement where different overtones (n) of the resonant frequency are used:

$$\frac{\Delta\tilde{f}}{n} = \frac{\Delta f}{n} + i\frac{\Delta W}{2n} \quad \text{Equation II-15}$$

Kanazawa and Gordon equation (Equation II-4), introduced in the subsection II.2.a, describes the hydrodynamic interaction between a rigid and flat surface with an electrolyte and proves the validity of the Sauerbrey equation for EQCM measurement in electrolyte and but also for different overtone orders, also known as the Gordon-Kanazawa-Mason equation:¹⁴⁸

$$\frac{\Delta\tilde{f}}{n} = -(1-i)\frac{f_0^{\frac{3}{2}}}{n^{\frac{1}{2}}}\left(\frac{\eta_l\rho_l}{\pi\mu_q\rho_q}\right)^{\frac{1}{2}} \quad \text{Equation II-16}$$

Through normalization of this equation by $\rho_l f_0^2$, it can be demonstrated that $\frac{\Delta\tilde{f}}{n}$ depends solely on the quartz properties and the penetration depth (Equation II-6). The Kanazawa and Gordon equation can therefore be simplified by the following equation:^{148,172,183}

$$\frac{\Delta\tilde{f}}{n\rho_l f_0^2} = -(1-i)\delta\frac{1}{\sqrt{\mu_q\rho_q}} = \frac{\Delta f}{n\rho_l f_0^2} + i\frac{\Delta W}{2n\rho_l f_0^2} \quad \text{Equation II-17}$$

with:

$$\frac{\Delta f}{n\rho_l f_0^2} = -\delta\frac{1}{\sqrt{\mu_q\rho_q}} \quad \text{Equation II-18}$$

And

$$\frac{\Delta W}{2n\rho_l f_0^2} = \delta\frac{1}{\sqrt{\mu_q\rho_q}} \quad \text{Equation II-19}$$

This simplification demonstrates the linear relationship of the normalized resonant frequency and the normalized frequency width with the penetration depth. This linear relationship proves the flat behavior of the deposited film on the resonator when immersed

in an electrolyte under Open-Circuit Potential. Shift of frequency in the Kanazawa and Gordon equation is expressed between the bare resonator in air and immersed in a liquid. To be accurate, as the aim is to evidence the rigidity and the flatness of the film, shifts of frequency and resonance widths are calculated against that of the coating in air rather than to the bare quartz crystal.

This methodology based on *in situ* hydrodynamic spectroscopy has been used to demonstrate the appropriate properties of the composite electrodes made of the different active materials and binder studied during this Ph.D. thesis. However, these spectroscopic studies were performed without any polarization; this was counterbalanced by the measurement of the motional resistance by EQCM-R during cycling of the active material. Small variation of the motional resistance indicates the retention of the film rigid properties upon cycling. To go further in the analyses, the motional resistance can be converted to resonance width, W , thanks to the following equation:¹⁴⁸

$$W = \frac{32Ae_{26}^2 \rho_q^2 f_0^3}{\pi \sqrt{\mu_q \rho_q}^3} R \quad \text{Equation II-20}$$

where e_{26} is the piezoelectric stress coefficient ($9.65 \cdot 10^{-2}$ A.s.m⁻² for AT-cut quartz). In comparison to R , W has the unit of frequency (Hz) so it can be related to the resonance frequency change. This constant value was calculated in our case to be equal to 13.6 Hz/ Ω . The condition of the gravimetric sensing is defined as: $|\Delta W| \ll |\Delta f/n|$, with n the overtone equals to 1 in the present case.

Once all of these conditions are satisfied, the gravimetric regime applies and the measured resonant frequency can be directly translated into mass change occurring at the electrode-electrolyte interface. Gravimetric measurements can in that case give rise to in-depth studies on the species involved in the charge compensation process and/or any irreversible mass accumulation on electrodes. Nonetheless, EQCM measurements coupled to cyclic voltammetry (CV) or galvanostatic charge/discharge (GCD) cannot discriminate in a straightforward way, between different species pertaining to the same potential region. To overcome this drawback, a complementary method, QCM coupled with EIS (the so-called *ac*-electrogravimetry) has also been employed to battery electrodes characterization. This method, highly promising to distinguish among the involved species according to their

respective kinetics of interfacial transfer (insertion, intercalation, electroadsorption, etc.) is detailed in the next sub-section.

II.4.c – Dynamic characterization of the electrode-electrolyte interface

Ac-electrogravimetry (electrogravimetric impedance) is the coupling between the QCM and electrochemical impedance spectroscopy (EIS) which has been invented and further developed at the *Laboratoire Interfaces et Systèmes Electrochimiques* (LISE-UMR 8235, Sorbonne University, CNRS).¹⁸⁴ This technique is a pertinent method to study the interfacial transfer mechanisms of different species (anions, cations or solvent molecules) directly or indirectly involved in the charge compensation process associated to an electrochemical process. With a basic description, species transferred at the interfaces with different kinetics can be separated (thanks to EIS coupling) and can be identified by their atomic weight (by virtue of QCM coupling), as well as their concentration variation in the electrode can be estimated.

Ac-electrogravimetry measurements were carried out by using a four-channel frequency response analyzer (Solartron 1254 FRA) and a lab-made potentiostat and QCM. The QCM was used under dynamic regime, working electrode (gold patterned quartz resonator) was polarized at a selected potential, and a small-amplitude potential perturbation (40 mV rms) was superimposed. The frequency range was between 63 kHz and 10 mHz. The microbalance frequency change, Δf_m , corresponding to the mass response, Δm , of the working electrode was measured simultaneously with the AC response, ΔI , of the electrochemical system. The resulting signals were sent to the four-channel Frequency Response Analyzer (FRA), which allowed the electrogravimetric transfer function $(\Delta m / \Delta E)(\omega)$ and the classical electrochemical impedance $(\Delta E / \Delta I)(\omega)$ to be obtained simultaneously at a given potential. Then the experimental $(\Delta q / \Delta E)(\omega)$ was calculated from electrochemical impedance thanks to the Equation II-33 and Equation II-34.

A model that involves the transfer of one cation, one anion and one free solvent at the electrode-electrolyte interface has been selected to explain the theory behind this non-classical EQCM methodology. This model is the basis for the fitting of the experimental data

of this Ph.D. thesis. A schematic of a deposited film on a gold electrode of a QCM resonator in contact with an electrolyte is represented in the Figure II-9. Ionic transfer occurs at the interface between the active material and the electrolyte. The flux of species i (c: cation, a: anion, s: solvent), J_i , is considered positive if the species is expelled from the active material:

$$J_i > 0 \text{ for } x > 0$$

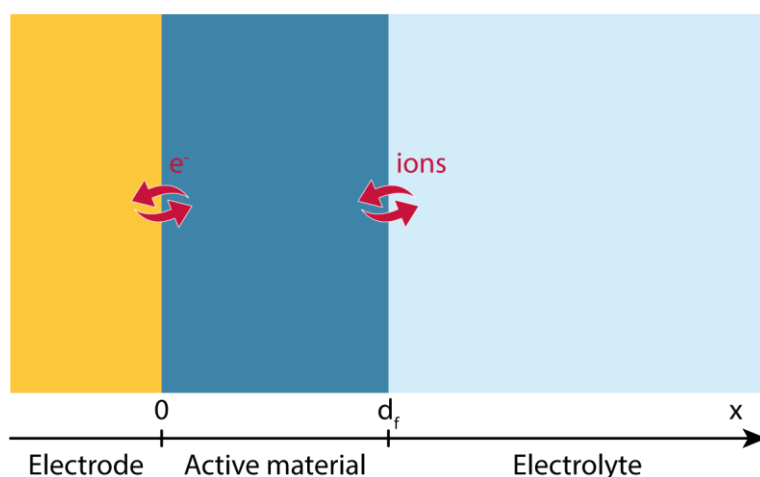


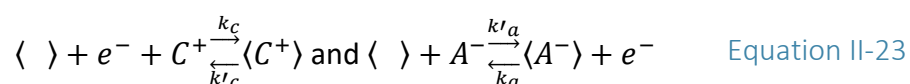
Figure II-9: Schematic of the EQCM electrode / Active material / Electrolyte stacking, defining electrode modified with the active material/electrolyte interface.

If both cations (c), anions (a) and solvent (s) are involved in the charge compensation process directly or indirectly, the associated mass variation per surface unit, Δm , and the charge variation per surface unit, Δq , which flows through the interface between the gold electrode and the active material, are equal to:

$$\Delta m = M_c \Delta \xi_c + M_a \Delta \xi_a + M_s \Delta \xi_s \quad \text{Equation II-21}$$

$$\Delta q = -F(\Delta \xi_c - \Delta \xi_a) \quad \text{Equation II-22}$$

where M_i and ξ_i are the molar mass and the number of moles of species i exchanged per surface unit, respectively. Concerning the particular case of solvents molecules, they can participate in the charge compensation process and therefore contribute in the mass change; however as they are not charged, they do not participate in the charge variation. The generalized mechanism for insertion or electroadsorption by a cation or an anion in a free site $\langle \rangle$ can be described by the following reactions:



Consequently, the molar flux of species (c, a or s) is $J_i = \frac{d\xi}{dt}$ and the concentration of species, i, in the active material film of thickness, d_f can be written in the form:

$$C_i = \frac{\xi_i}{d_f} \quad \text{Equation II-24}$$

The species transfer at the electrode-electrolyte interface are only taken into account as rate-limiting steps, since the species transports inside the active material and in the solution are supposed to be fast enough. This assumption needs to be verified by diffusion coefficient determination in the liquid phase and especially in the solid phase. By using the laws of heterogeneous kinetics and reaction formulae, the flux of cations and anions are:

$$J_a(d_f) = -d_f \frac{dC_a}{dt} = k_a(C_a - C_{a,min}) - k'_a(C_{a,max} - C_a)C_{a,sol} \quad \text{Equation II-25}$$

$$J_c(d_f) = -d_f \frac{dC_c}{dt} = k'_c(C_c - C_{c,min}) - k_c(C_{c,max} - C_c)C_{c,sol} \quad \text{Equation II-26}$$

By using the Hillman solvation model¹⁸⁵, the same relationship can be used for the solvent flux:

$$J_s(d_f) = -d_f \frac{dC_s}{dt} = k'_s(C_s - C_{s,min}) - k_s(C_{s,max} - C_s) \quad \text{Equation II-27}$$

where:

C_i is the concentration of species i in the film, $C_{i,sol}$ is the concentration of species i in the solution by assuming that the diffusion of the ions in solution does not limit the global kinetics.

$(C_{i,max} - C_i)$ is the concentration in free sites for species i at time t, with $C_{i,max}$ is the maximum concentration of the free sites in the film for species i.

$(C_i - C_{i,min})$ is the concentration of species i in the film, where $C_{i,min}$ is the minimum concentration of species i in the film.

The two kinetic constants can be defined as:

$$k_i = k_{i_0} e^{[b_i(E-E^\circ_i)]} \text{ and } k'_i = k'_{i_0} e^{[b'_i(E-E^\circ_i)]} \quad \text{Equation II-28}$$

Where E is the potential, E°_i is the apparent normal potential, $(E - E^\circ_i)$ is the overvoltage, k_{i_0} , k'_{i_0} , b_i and b'_i are constants.

Under the effect of a sinusoidal potential perturbation with low amplitude, ΔE , imposed to the gold surface/film/electrolyte system, sinusoidal fluctuations of concentration, ΔC_i , and flux, ΔJ_i , are observed such as:

$$\Delta J_i = -d_f \frac{dC_i}{dt} = -j\omega d_f \Delta C_i \quad \text{Equation II-29}$$

The expression of the global insertion/expulsion flux, ΔJ_i , which depends on the concentration and potential perturbations, at the film/electrolyte interface is:

$$\Delta J_i = \left. \frac{\partial J_i}{\partial C_i} \right|_E \Delta C_i + \left. \frac{\partial J_i}{\partial E} \right|_{C_i} \Delta E = K_i \Delta C_i (d_f) + G_i \Delta E \quad \text{Equation II-30}$$

where ω is the angular frequency equal to $2\pi f$, f is the perturbation frequency and K_i and G_i are the partial derivatives of the flux, J_i , with respect to the concentration and the potential, $K_i = \left(\frac{\partial J_i}{\partial C_i} \right)_E$ and $G_i = \left(\frac{\partial J_i}{\partial E} \right)_{C_i}$. K_i is the kinetic rate of transfer and G_i is the inverse of the transfer resistance, Rt_i , of the species at the film/electrolyte interface: $Rt_i = \frac{1}{FG_i}$. For each transferred species, the ionic transfer resistance is a good estimation of the ease of the transfer.

Then, the change of the concentration, ΔC_i , of each species with potential ΔE can be calculated using Equation II-29 and Equation II-30, leading to the concentration/potential TF:

$$\frac{\Delta C_i}{\Delta E}(\omega) = \frac{-G_i}{j\omega d_f + K_i} \quad \text{Equation II-31}$$

Using the concentration/potential TF, the charge/potential transfer function can be calculated:

$$\begin{aligned} \frac{\Delta q}{\Delta E}(\omega) &= -F d_f \left(\frac{\Delta C_c}{\Delta E}(\omega) - \frac{\Delta C_a}{\Delta E}(\omega) \right) \\ &= -F d_f \left(\frac{-G_c}{j\omega d_f + K_c} + \frac{G_a}{j\omega d_f + K_a} \right) \end{aligned} \quad \text{Equation II-32}$$

The Faradaic impedance relative to the global ionic transfer of charged species involved in the charge compensation is:

$$Z_F(\omega) = \frac{\Delta E}{\Delta I_F}(\omega) = \frac{1}{j\omega \frac{\Delta q}{\Delta E}(\omega)}$$

$$= \frac{1}{j\omega F d_f \left(\frac{G_c}{j\omega d_f + K_c} - \frac{G_a}{j\omega d_f + K_a} \right)}$$

Equation II-33

Finally, the classical electrochemical impedance can be estimated incorporating the electrolyte resistance R_{el} and the interfacial capacitance C_{dl} :

$$\frac{\Delta E}{\Delta I}(\omega) = R_{el} + \frac{1}{j\omega C_{dl} + \frac{1}{Z_F(\omega)}}$$

$$= R_{el} + \frac{1}{j\omega C_{dl} + j\omega F d_f \left(\frac{G_c}{j\omega d_f + K_c} - \frac{G_a}{j\omega d_f + K_a} \right)}$$

Equation II-34

The second main transfer function can be calculated theoretically taking also into account the charged and uncharged species:

$$\frac{\Delta m}{\Delta E}(\omega) = d_f \left(M_c \frac{\Delta C_c}{\Delta E}(\omega) + M_a \frac{\Delta C_a}{\Delta E}(\omega) + M_s \frac{\Delta C_s}{\Delta E}(\omega) \right)$$

$$= -d_f \left(M_c \frac{G_c}{j\omega d_f + K_c} + M_a \frac{G_a}{j\omega d_f + K_a} + M_s \frac{G_s}{j\omega d_f + K_s} \right)$$

Equation II-35

To illustrate what the experimental *ac*-electrogravimetry data may look like, the $\Delta q/\Delta E(\omega)$ and $\Delta m/\Delta E(\omega)$ transfer functions are shown schematically in Figure II-10.

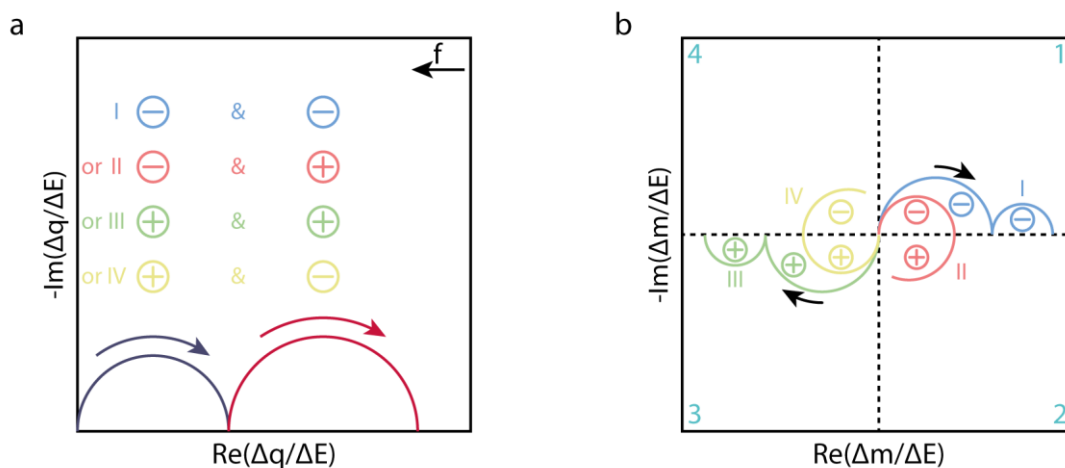


Figure II-10: Representation of the possible experimental transfer functions for (a) $\Delta q/\Delta E(\omega)$ and (b) $\Delta m/\Delta E(\omega)$ in the case of two charged species.

For a single ion transfer at the electrode-electrolyte interface, a typical cation and anion contribution appear characteristically on the 3rd and 1st quadrant (Cartesian system) of the mass/potential TF, respectively. It is important to note that the mass/potential TF is the only TF that can discriminate between the cations or anions and identify them by their molar mass (M_i in Equation II-35). In a more complex electrochemical process, where a multi-ion transfer occurs, the above mentioned TFs may look like as shown in Figure II-10. The contribution of two charged species may translate into two loops in $\Delta q/\Delta E(\omega)$ (Figure II-10a), if the respective time constants of the participating ions are different enough. However, the four different configuration given in the Figure II-10a result in the same response in terms of $\Delta q/\Delta E(\omega)$ TF. The strength of the mass/potential TF is more evident in the Figure II-10b, where four possibilities of ionic transfers (two anions, an anion/cation, two cations and a cation/anion) can be distinguished, with further kinetic resolution depending on the dynamics of interfacial transfer. For sake of clarity, the solvent contribution was not taken into account, which can participate in charge compensation: i. in the free form with the same direction of a cation flux *i.e.* an additional negative loop, or an anion flux *i.e.* an additional positive loop in the $\Delta m/\Delta E(\omega)$ TF, ii. in the solvation shell of a cation or an anion. It should be stressed that the solvent molecules do not contribute to the $\Delta q/\Delta E(\omega)$ TF (uncharged species), explaining the advantage of *ac*-electrogravimetry over classical EIS where only the $\Delta q/\Delta E(\omega)$ can be measured for the latter and solvent molecules role cannot be investigated.

Partial mass/potential TF can be also estimated by removing the cation contribution, calculating $\Delta m/\Delta E^{a,s}(\omega)$.

$$\frac{\Delta m^{a,s}}{\Delta E}(\omega) = \frac{\Delta m}{\Delta E}(\omega) + \frac{M_c}{F} \frac{\Delta q}{\Delta E}(\omega) \quad \text{Equation II-36}$$

$$\frac{\Delta m^{a,s}}{\Delta E}(\omega) = d_f \left((M_a + M_c) \frac{\Delta C_a}{\Delta E}(\omega) + M_s \frac{\Delta C_s}{\Delta E}(\omega) \right) \quad \text{Equation II-37}$$

This TF acts as a cross-check procedure to discriminate between two possible cations or to amplify the anion contribution as its apparent molar mass is $M_a + M_c$. A partial mass/potential TF can be also estimated for an anion $\Delta m/\Delta E^{c,s}(\omega)$ but not in the case of a solvent molecule.

The derivative of the concentration for each species with respect to the potential can be calculated by considering the low frequency limit of $\Delta C_i/\Delta E(\omega)$.

$$\frac{\Delta C_i}{\Delta E}(\omega) = \frac{-G_i}{j\omega d_f + K_i} \xrightarrow{\omega \rightarrow 0} -\frac{G_i}{K_i} \quad \text{Equation II-38}$$

Then ΔC_i is obtained by integrating $-\frac{G_i}{K_i}$ with respect to the potential. To finish, Δm_i is acquired by multiplying ΔC_i by the volume of active material. The global mass variation at each potential can therefore be calculated with the sum of each Δm_i in order to be compared with the classical EQCM measurement, as a cross-check calculation to verify the fitting procedure and the adequacy of the selected model.

Overall, the strong asset of *ac*-electrogravimetry compared to conventional EQCM-based methods is nested in its capability to assess the dynamic aspect of the mass/charge transfer and the exact identification of the different species contributing to the (electro)chemical processes. This coupled methodology stands far from the limitations of EQCM by allowing the precise deconvolution of the global mass variation (under gravimetric regime) during faradaic and/or capacitive processes to give access to unique information such as: i. the kinetics of the species transferred to the electrode-electrolyte interfaces, ii. identification of species by their molecular weight with a clear distinction between ions, anions/cations, solvated ions (number of solvates) and solvent contributions and iii. the relative changes in concentration of these species within the electrode. Until now, *ac*-electrogravimetry has been employed to study the influence of the solvation shell on the

lithium insertion into model materials by the LISE, but it was mostly applied to pseudo-capacitive process analyses.^{176,178} Within this Ph.D. thesis, it has been extended to battery-like systems, with various materials and electrolyte compositions, especially in organic-based electrolytes.

II.5 – Chapter conclusions

This chapter proposed an in-depth presentation of the QCM basics and of the associated theoretical foundation, together with various QCM-based techniques currently available and their coupling to electrochemical methods. Although using the same piezoelectric quartz crystal resonators, these techniques differ by their measurement principle and read-out methods. The oscillator circuit is the basics of the resonant frequency measurement. The (un)loaded quartz oscillation can be modelled by the BVD equivalent circuit in which the electronic components represent its physical parameters permitting the resonant frequency and the motional resistance to be determined (QCM-R). The latter is related to the energy dissipated during oscillations. Network analyzers (impedance analysis) propose a more accurate and complete measurement of these physical parameters and can be easily extended to the study at different overtones (QCM-I). Contrary to impedance analysis, QCM with dissipation monitoring (QCM-D) permits the simultaneous recording of both resonant frequency and dissipation factor. These techniques have their own advantages and disadvantages; and one should carefully choose one/or a combination of these methods and get the maximum of their benefits, depending on the targeted study.

Then, a comprehensive analysis of the current literature gathering QCM-based techniques applicable to the battery field has been given. Historically, QCM coupled to electrochemistry (EQCM) was firstly used to study the SEI formation on a model electrode (Au). Recently, microbalance studies of SEI have enjoyed a revival thanks to the development of EQCM with dissipation monitoring in the battery domain, which permits the characterization of viscoelastic layer at the surface of the resonator. This new inclination of the EQCM has been extended towards a better understanding of the composite electrode behavior under cycling. In addition, gravimetric measurements have also been performed to

assess the reversibility of particle lithiation and the contribution of solvent molecules in the insertion process.

With this perspective, the scope of this Ph.D. was to gather the advantages of QCM-based techniques for a practical use in the battery domain to give better insights on the insertion/extraction mechanism of alkali metal ions in electrode materials, associated to ions desolvation/solvation processes. The study was also extended to proton insertion and the importance of water in assisting the charge carrier in such systems. However, obtaining reliable and artifact-free information from QCM-based techniques is not an easy task. To this end, appropriate strategies are developed to get the best of the each methodology. EQCM with motional resistance monitoring (EQCM-R) over EQCM-D has been selected for its ease of application to battery material study. Nevertheless, the deposited film of active material needs to follow certain rules to fulfill the gravimetric regime, which is of paramount importance for further analyses. A methodology based on *in situ* hydrodynamic spectroscopy was therefore employed to prove its stiffness and its rigid bond with the quartz, as well as its homogeneity. Another novelty of our approach is to use *ac*-electrogravimetry to characterize the cation and its solvation shell at the interface before its insertion and its associated kinetics. As a conclusion of the literature analysis, the first milestone, which need to be mastered, is the deposition of the composite electrode without lateral or vertical inhomogeneity permitting to validate the gravimetric conditions. Moreover, a suitable EQCM-cell development was missing in the field, one of the bottleneck for the EQCM studies in the battery domain.

Chapter III – Making advanced electrogravimetry as an affordable analytical tool for the battery interface characterization

III.1 – Introduction

As introduced in the previous chapter, EQCM with motional resistance monitoring was privileged as an *operando* analytical method because it is more comprehensible, more user-friendly and more compatible with today's battery tooling. Rather than quantitatively measuring the viscoelastic properties of the deposited composite electrode upon cycling, EQCM-R assesses the motional resistance as a viscoelastic indicator. However, it is also suggested that a proper analytical approach (classical EQCM, multiharmonic EQCM-D or proposed EQCM-R) has to be defined or be used complementarily, suitable to the field of study (*i.e.* here for batteries). A fair comparison, pros and cons of different types of EQCM based methods are provided in the Chapter II.

To widen the spectrum of EQCM measurements applicable to battery materials characterization, we propose herein a strategy that combines thin film preparation on QCM specific substrates, design of EQCM cells, and suitable measurements protocols. This includes an optimized spray coating technique to elaborate routinely and reliably composite electrode deposits at the surface of EQCM resonators, with the technique being tunable according to the physicochemical properties of the components (active material, binder, etc.). A major development is on the design of hermetically sealed and versatile EQCM cell to mimic battery conditions that can be used either with aqueous or non-aqueous electrolytes. Moreover, our designed EQCM cell can be coupled to lab-made and commercial microbalances to assess the nature of the electrode material (stiff, soft) and its interaction with the electrolyte. For proof of concept, we demonstrated the reliability and reproducibility of our electrochemical and gravimetric measurements made by EQCM-R on a model battery material, LiFePO_4 .

To convey such a new tooling and a comprehensive strategy, this chapter will be structured as follows. The importance of mastering the thin film deposition on the QCM substrate is first described prior to addressing the design of new EQCM cells for operating in

both aqueous and organic media. Secondly, we present how to ensure conformity of the hydrodynamic and viscoelastic properties of the coating with gravimetric regime requirements prior to showing the implementation into the EQCM-R in studying model LiFePO_4 electrodes. Lastly, the outcome of both the proposed methodology and new tooling are used to propose new insights on insertion mechanism in aqueous and organic electrolyte Li-ion battery, with respect to the state of the art of the field.

III.2 – Optimization of the electrode preparation on EQCM resonators

III.2.a – Description of the preparation protocol

Previous EQCM-D studies clearly indicate that when the electrode surface is rough or the electrode itself is porous, additional contribution to frequency changes may occur depending on the pore width, *i.e.* the hydrodynamic effect of the trapped or mobile liquid in the pores (see II.4.b).^{170,172} Therefore, the deposition of the composite layer without lateral or vertical inhomogeneity should be one of the primary concern in the good practice of the EQCM analyses. Guided by this idea, a considerable amount of effort has been devoted in this thesis towards the development of the most suitable protocol leading to a homogeneous film rigidly attached on the surface of the QCM resonator. To this end, a deposition process based on spray coating was elaborated. Other techniques, enlisting physical vapor deposition^{153,154}, electrodeposition^{176,179,186} and sol-gel processes^{173–175,177} offer the benefit of fabricating thin, rigid, dense and fairly smooth surface layer on the QCM resonator. However, they are limited to a few battery materials due to the limited temperature range of metal coated-quartz resonator stability (< 300 °C). Therefore, an important asset of the spray-coating based deposition process is its feasible implementation to various active materials that can be synthesized beforehand and deposited under “soft conditions” without any perturbation to the resonator properties. If necessary, there are options for working at higher electrode preparation temperatures by using GaPO_4 as resonator material with the possibility of reaching up to 600°C.¹⁸⁷ We should recall that spray coating was firstly introduced by Levi *et al.*¹⁸⁸ in 2009 to characterize the ionic fluxes in microporous carbons as supercapacitor electrodes. However, the procedure was succinctly described, and in certain cases leads to

non-continuous coatings, depending on the active materials particle size and the nature of the binder.¹⁷² Therefore, revisiting the essential steps of EQCM electrode preparation was crucial to get full benefit from EQCM-based methods in the battery field.

To mimic the electrode used in practical batteries, composite electrodes made of an active material, a conductive agent and a binder were targeted. For this specific study, commercial LiFePO_4 (LFP) having sub-micrometer particles (≈ 200 nm) were employed as active material to obtain a thin, compact and multi-layered coating. Polyvinylidene fluoride (PVDF) has been chosen as a binder because of its high chemical inertness, its good mechanical properties and its less hydrophobic nature compared to Polytetrafluoroethylene (PTFE) for aqueous cycling. To facilitate the composite film preparation under softer conditions, the copolymer Poly(vinylidene fluoride)-co-hexafluoropropylene (PVDF-HFP) was selected due to its lower melting temperature compared to that of classical PVDF. The outlines of the protocol are depicted in the Figure III-1.

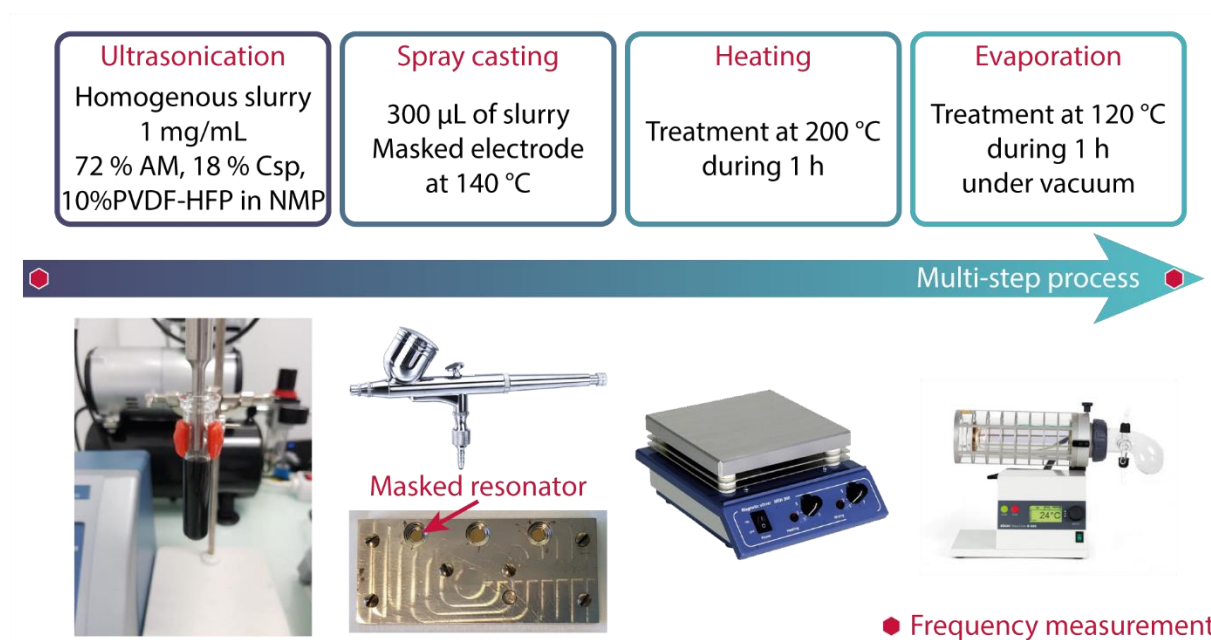


Figure III-1: Outlines of the different steps permitting a composite electrode on the surface of a QCM resonator to be obtained. First, the selected materials – active material (AM), conductive agent (Csp) and binder (PVDF-HFP) – are mixed and solubilized in the case of the binder in 1-Methyl-2-pyrrolidinone (NMP) by using an ultrasonication horn. NMP is not prone to evaporation which is a good point considering the elevation of temperature during the ultrasonication step. The vial can also be cooled down with an ice bath. The 9 MHz Au-coated quartz resonator is mounted into a designed mask leaving uncovered only the desired electrode heated at a temperature of 140 °C. A small volume (300 μ L) of the homogeneous slurry is sprayed on the surface of the electrode. The film is exposed to a heating treatment at 200 °C to permit the spreading of the PVDF-HFP binder from the agglomerates. To conclude the multi-step process, the film is kept at 120 °C under vacuum to displace the evaporation equilibrium of the non-volatile solvent. Further details are given in the Materials & Methods.

However, the fine-tuning of the process is rooted in mastering a few details through the various steps. The ultrasonication step for instance permits to obtain a homogeneous slurry with different PVDF-HFP/LFP weight concentrations. The combination of the proper heating temperature and the small droplets created by the spray enables the fast evaporation of the solvent. Here, air has been used as the spray gas vector but it can be replaced by argon or nitrogen depending upon the nature of the active material. At this stage, for the sake of comparison, exactly the same protocol was applied by replacing the spray coating by the classical drop casting.

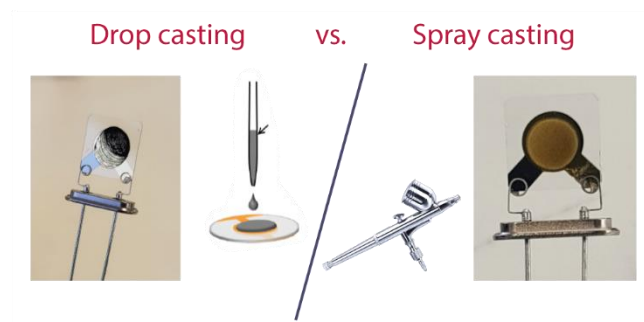


Figure III-2: Macroscopic results and visual inspection of the QCM resonators coated with the composite electrode – comparison between the drop casting and spray coating techniques.

The Figure III-2 shows the morphology differences between the coatings obtained by those two deposition techniques that is in favor of spray coating. The drop casting demonstrates the coffee-ring effect¹⁸⁹ compared to the macroscopic homogeneous layer obtained by the spray coating method. However, at the microscopic scale, agglomerates of materials can be found at the surface of the electrode, even for the spray-coated electrode (Figure III-3a).

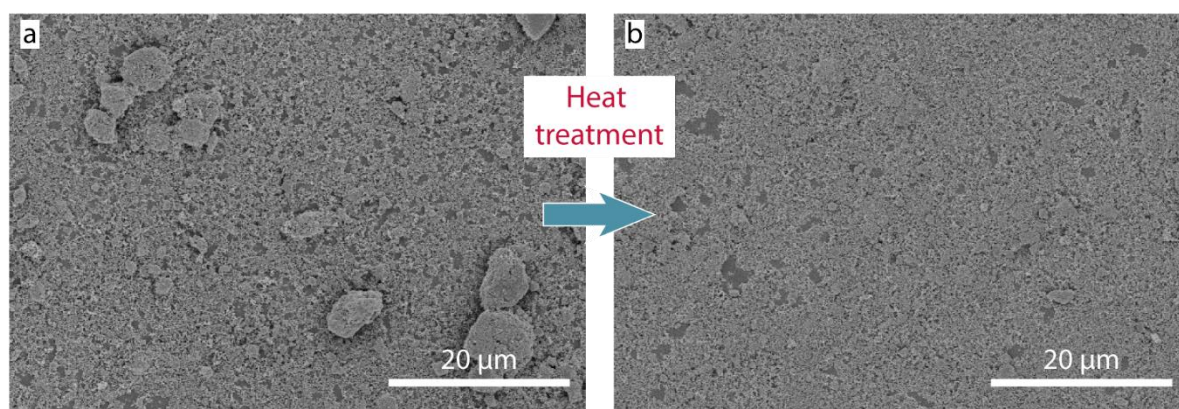


Figure III-3: SEM images of the composite LFP electrode just after the spray coating step (a) and after the heating treatment (b).

To circumvent this issue, the film is exposed to a heating treatment at 200 °C to enable the spreading of the PVDF-HFP thermoplastic binder ($T_{\text{melting}} = 150 \text{ °C}^{190}$) and minimizing its coating roughness so that a laterally homogeneous and flat film as revealed by SEM images (Figure III-3b) is observed. Such a heating treatment should not affect the resonator properties, which are reported to be maintained until 573 °C at which the α - β phase transition in quartz occurs.¹⁹¹ The resonant frequency of a bare quartz, like the motional resistance, remains constant before and after the heating treatment, confirming the absence of an effect on piezoelectric properties.

Recently, a vacuum filtration-and-transfer (VFT) technique was described for the same purpose,¹⁹² with in this case the active material been filtered through a cellulose membrane then transferred to surface of the resonator by dissolving the cellulose with acetone. The authors claimed that this method overqualified spray drying for obtaining homogeneous coatings with relative ease and reproducibility. However, this protocol does not permit the use of common binders of the battery field and especially PVDF, which are soluble in polar solvent as is the case for cellulose, in the preparation process. The presence of a suitable binder is an important factor to obtain rigidly attached films at the surface of the QCM resonator,¹⁶⁷ therefore, being applicable to only certain binders is a drawback of the VFT method. To counteract this absence, a film of PVDF can be deposited on the top of the prepared electrode; however, it is at the expense of the composite electrode permeability and hydrodynamic.

III.2.b – Evaluation of the suitable conditions for electrode preparation by EQCM-R

The resonant frequencies of the bare and loaded resonator (by drop casting or spray coating) were measured in air at room temperature to obtain the frequency change and the expected mass of the composite electrode thanks to the Sauerbrey equation (Equation II-5), and therefore the loading. The same measurements were done to get the motional resistance (R) change of the resonator after the coating. Putting aside the macroscopic aspect of the composite electrode, its frequency change and motional resistance (R) obtained by spray coating and drop casting have been compared as a function of slurry concentration in material as depicted in Figure III-4. It is noted that the resonators have been prepared using rigorously the same conditions, *i.e.* especially the cast and sprayed volume of 300 μL . The Figure III-4a shows the as expected quasi-linear behavior between the frequency change and the slurry concentration for the spray coating method. As for the drop casting, it demonstrates a linear behavior for concentration below 1 mg/mL then the frequency change seems to stagnate. In the linear region, for the same concentration, the frequency changes obtained by spray coating are lower than by drop casting. Consequently, based on the LiFePO_4 sample specimen used, the spray coating is a more suitable option to obtain a wide range of predictable

frequency change, therefore loading and the presented figure can be used as a calibration curve (Figure III-4a).

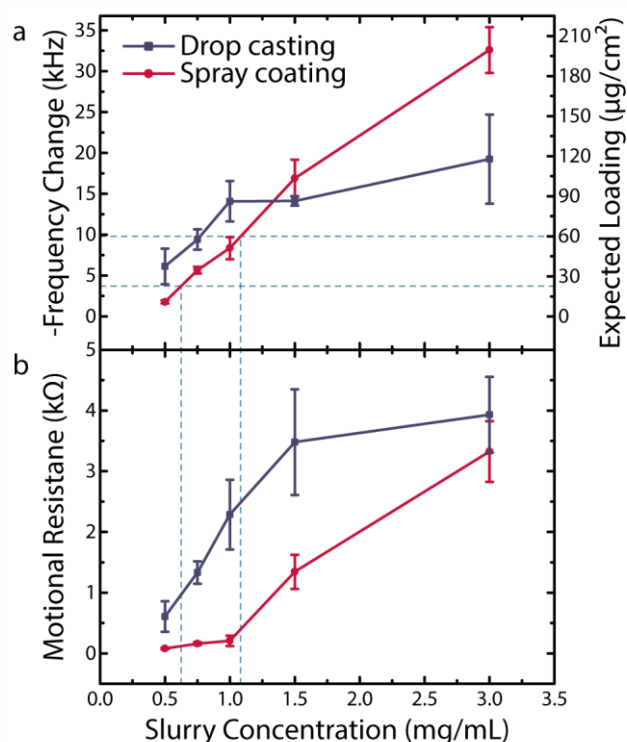


Figure III-4: (a) Frequency changes, expected loadings and (b) motional resistances of composite films measured in air prepared by drop casting or spray coating techniques as a function of the slurry concentration (the cast and sprayed volume are kept at a constant value of 300 μL). To obtain the error bars, the experiments have been replicated three times.

The motional resistance (R) values are used to evaluate the coating quality obtained by the two methods. The R values for the drop cast coatings (Figure III-4b) show a linear behavior as the slurry concentration increases and a plateau at values exceeding 1.5 $\text{mg}\cdot\text{mL}^{-1}$. This saturation coincides roughly with frequency change saturation observed in Figure III-4a. Significantly lower R values were observed for the spray coated resonators, however they also exhibit a threshold and substantially increase for concentration values higher than 1 $\text{mg}\cdot\text{mL}^{-1}$. Considering the high R values for high slurry concentrations, we can assert the deviation from the gravimetric conditions, especially significant for drop-cast coatings. Therefore, the respective loadings given at the high end of the Figure III-4a are only estimated and may deviate from the genuine values, due to the energy dissipation. However, even when the loading is higher, the spray coating results in relatively lower motional resistance. Before the threshold, the R values are low ($< 150 \Omega$) compared to that of the bare electrode (10Ω).

Smaller error bars in the case of spray coating are also noted. The full resonance width change (ΔW) was also calculated thanks to a procedure described in the Chapter II (Equation II-20). The condition of the gravimetric sensing, *i.e.* $|\Delta W| \ll |\Delta f|$ was found only in the case of spray coating for slurry concentration strictly below 1.5 mg/mL (Figure III-5), for the electrode composition of this study.

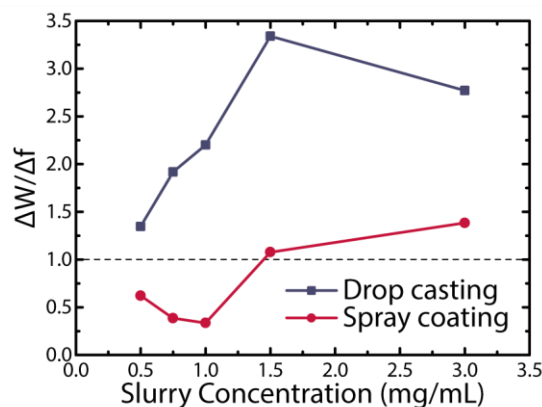


Figure III-5: $\Delta W/\Delta f$ ratio of composite LFP films measured in air prepared by drop casting or spray coating techniques as a function of the slurry concentration.

Therefore, the spray coating has been selected to obtain composite LFP films with higher reproducibility and lower motional resistance. A slurry concentration of 1 mg/mL has been chosen as uppermost point to obtain loadings in a range between 20 and 60 $\mu\text{g}\cdot\text{cm}^{-2}$ and employed in the electrogravimetric investigations, thereafter. It is noted that these conditions are specific to LFP nanoparticles and the PVDF-HFP binder employed here and should be redefined using the methodology described above depending on the active material and/or binder.

III.3 – Design and validation of airtight EQCM cell testing workbench

III.3.a – Cell presentation

Past and present cells to perform EQCM measurements suffer, among others, from lack of airtightness, incompatibility with battery-like architecture (small volume of electrolyte, electrode geometry and positioning) and/or a cumbersome assembly. These drawbacks can hinder the wider exploitation of EQCM in the battery field. Therefore, we designed and built

a dedicated tooling with required cell characteristics. Specific cell designs are represented in the Figure III-6.

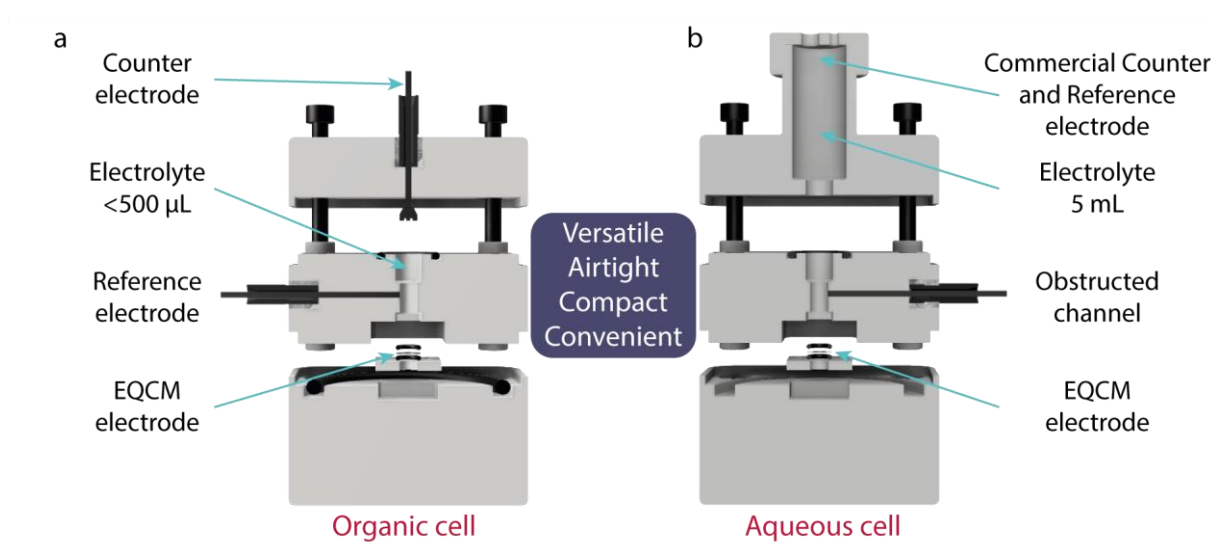


Figure III-6: Graphical representation of the EQCM cell designed for battery electrode testing in (a) organic and (b) aqueous electrolytes.

The assembly is convenient to be manipulated in a glovebox, during the loading of air sensitive components into the cell (*e.g.* metallic Li electrodes, electrolytes, etc.), but it is designed to be used for performing electrochemical tests outside the glovebox thanks to its hermetic closing mechanism. Polypropylene (PP) has been selected as the core cell material because of its numerous advantages: good resistance to fatigue, chemical resistance to almost all organic solvents, low density and hydrophobic property, which makes it easier to dry when switching from aqueous to organic electrolytes. Within this new design, the oscillator is connected to the cell thanks to a BNC connector as represented in the Figure III-7 and to the potentiostat *via* 2 mm banana plugs to obtain reliable connections.

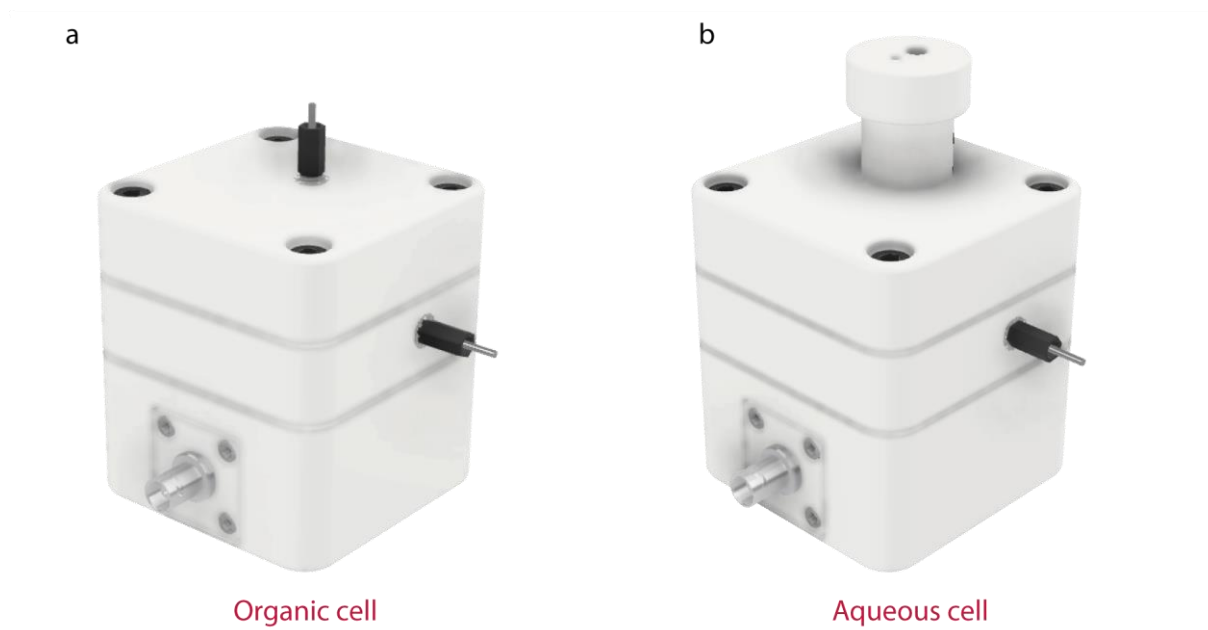


Figure III-7: 3D rendering of the versatile EQCM cell developed for battery electrode testing in (a) organic and (b) aqueous electrolytes.

Using such standard connections, this cell can be easily interrogated by different lab-made or commercial methods of read-out: EQCM, EQCM-R or Network analyzer and it can be made compatible with available EQCM-D apparatus. We have a pending patent entitled: “Test cell for the EQCM characterization of electrochemical systems” to protect our designs.

III.3.b – Cell evaluation

The designed cell has undergone a battery of tests to confirm the desired features: impedance, battery-like configuration and airtightness as well as the temperature influence on the resonant frequency. The cell impedance, as deduced by impedance spectroscopy (Figure III-8), presents a negative straight-line characteristic of an inductance in series with a resistance which values were calculated as 308 nH and 35.6 m Ω , respectively. The smallness of these values demonstrates only minor influence of the cell impedance to the electrochemical impedance spectroscopy (EIS) measurements, which expands the versatility of EQCM cell to other coupled methods, *e.g.* QCM coupled to EIS, the already presented *ac*-electrogravimetry (see II.4.c).

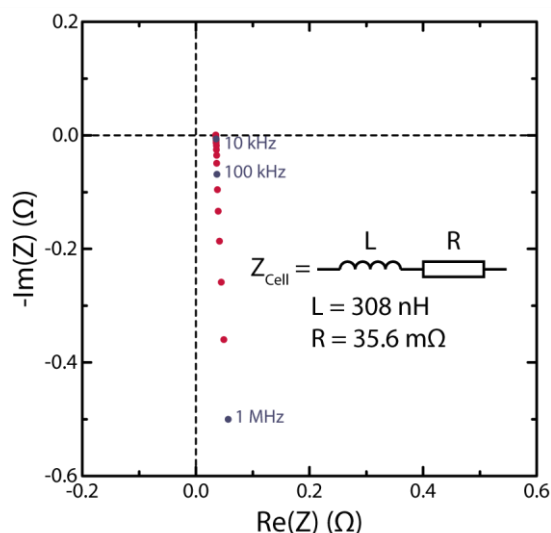


Figure III-8: Impedance response of the developed EQCM cell fitted with an L-R equivalent circuit.

The required specifications for development of an EQCM cell hosting an organic electrolyte were to mimic the configuration used in a practical Li-based battery. Therefore, the counter electrode faces the resonator with the same surface. The distance between them has been minimized to obtain a volume of electrolyte comprised between 300 and 500 μL . Additionally, the cell can host a reference electrode through a lateral opening. In this chapter, we used a piece of lithium metal placed at the tip of a stainless steel rod as reference electrode to obtain a more realistic measurement of the different potentials, working and counter electrodes. To avoid leakage of the electrolyte, perfluoroelastomer O-rings known for their non-swelling behavior in organic electrolyte were used in conjunction with four screws to impose pressure and provide the complete airtightness to the cell. The efficacy of the cell against water uptake upon time has been monitored by Karl Fischer titration (Figure III-9) and after two weeks, a water contamination by less than 60 ppm was measured. Therefore, the electrochemical measurements in organic electrolyte can be performed in a non-inert atmosphere without the risk of water or oxygen contamination. Moreover, this EQCM cell has a compact geometry that facilitates the transfer in and out of the glovebox through a small antechamber. Last and worth mentioning is the versatility of our cell setup that enables to perform battery testing in aqueous electrolyte by replacing the top part of the cell (Figure III-6b and Figure III-7b) to increase the electrolyte volume for enabling the use of commercial counter and reference electrodes (aqueous-based).

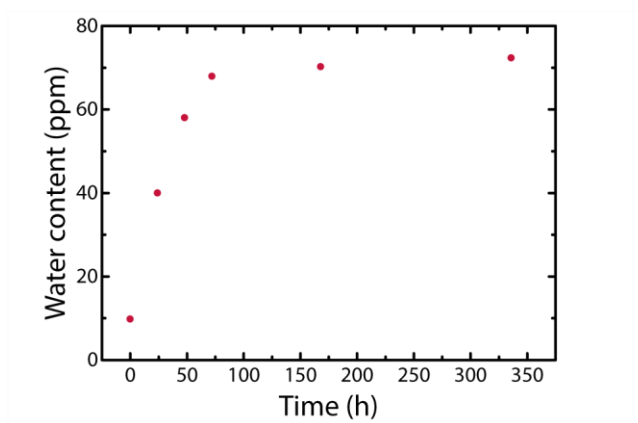


Figure III-9: Water content in the EQCM cell filled with an organic electrolyte, monitored by Karl Fischer titration after different time of exposure to the atmosphere.

At this stage, it was mandatory to check any eventual perturbation of the quartz resonant frequency by our new cell confinement. Bearing in mind that AT-cut quartz crystals are typically used due to their low sensitivity to temperature¹⁹³, we have inspected the temperature dependence of the resonant frequency, f , in this specific cell design. Intervals of different temperature has been applied to the EQCM cell equipped with a bare resonator and its Δf value has been monitored over time, represented in the Figure III-10.

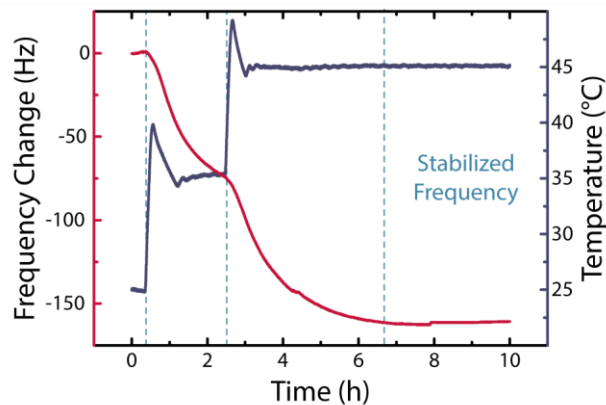


Figure III-10: Resonant frequency response of the resonator to temperature stimuli.

A drastic decrease of the f values appears synchronously with the temperature rise. However, the f stabilization is much slower than that of temperature. Thus, the temperature is an important factor to take into account during long cycling and makes f measurement practically incompatible with glovebox conditions. Therefore, it is recommend to launch experiments after sitting the EQCM cell at Open-Circuit Potential (OCP) for 4 h to obtain the frequency stability before performing battery cycling tests at 25 °C. Pleasantly, it can be noted that the frequency change is totally reversible with the temperature.

III.3.c – Calibration factor estimation

The calibration or sensitivity factor C_f from the Sauerbrey equation (Equation II-5) that is also an essential input parameter, has been estimated experimentally thanks to the classical Cu electrodeposition on the gold electrode of the quartz resonators. For the sake of comparison, both galvanostatic electrogeneration and cyclic voltammetry were employed and the results are presented in the Figure III-11.

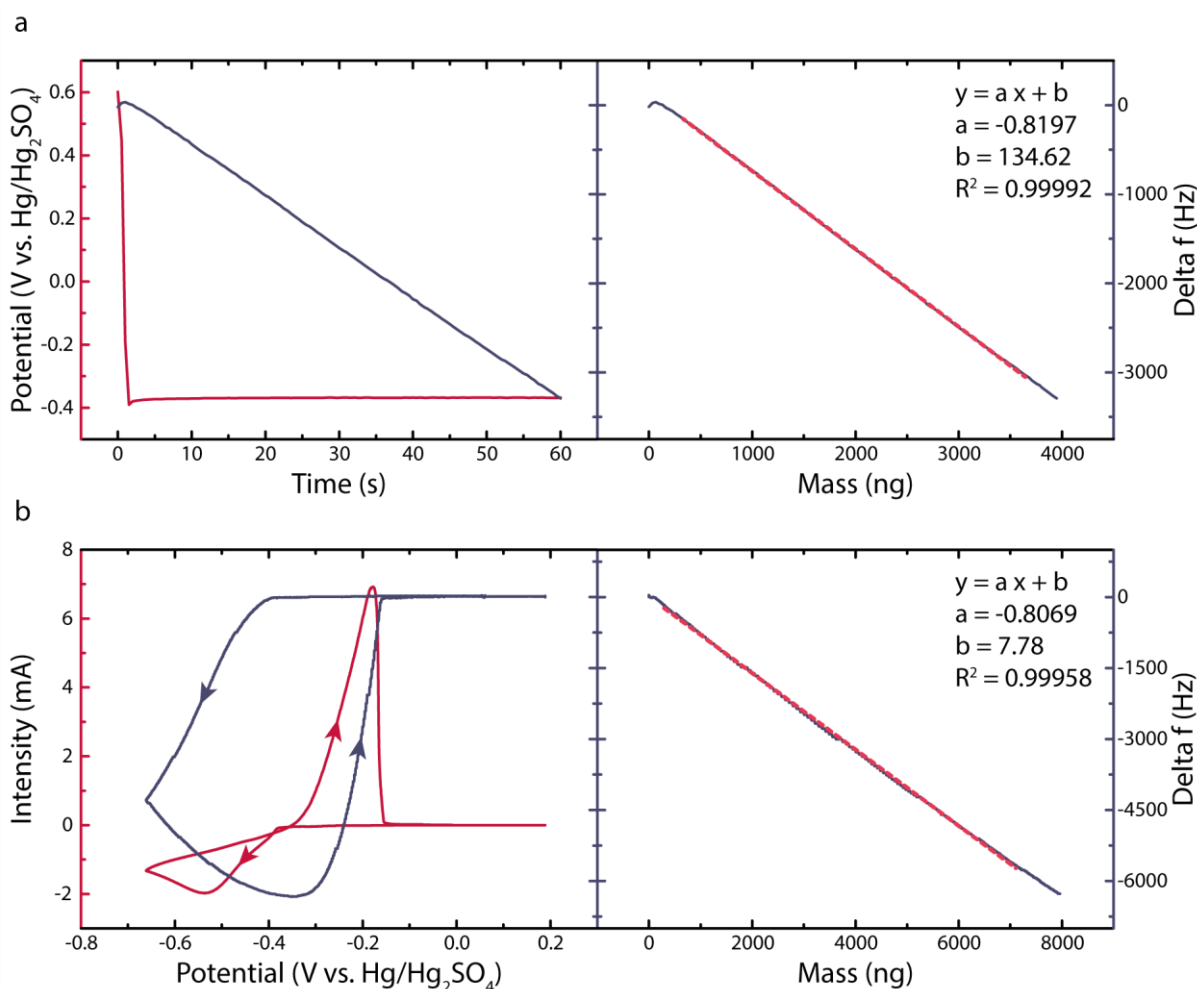


Figure III-11: Electrodeposition of copper in CuSO_4 0.05 mol.L^{-1} and H_2SO_4 0.5 mol.L^{-1} by (a left) galvanostatic method at -1 mA.cm^{-2} (b left) cyclic voltammetry at 25 mV.s^{-1} (a b right) Frequency change as a function of the estimated mass.

The slope between the Δf and the Δm (estimated by the Faraday's law) provides the experimental C_f value. To obtain good statistics, the experiments were performed several times with different applied current densities and scan rates represented in the Table III-1.

Table III-1: Sensitivity factors obtained during copper electrodeposition by galvanostatic (left) and cyclic voltammetry (right) techniques

j (mA.cm ⁻²)	C_f (ng.Hz ⁻¹)	v_b (mV.s ⁻¹)	C_f (ng.Hz ⁻¹)
-1	1.26	5	1.18
	1.14		1.19
	1.16	10	1.19
	1.22		1.20
	1.22	25	1.24
1.21	1.23		
$-2.5 \cdot 10^{-3}$	1.20	50	1.24
	1.24		1.25
	1.18		
	1.25		

It leads to the experimental C_f value of 1.21 ± 0.03 ng.Hz⁻¹ that is used for the electrogravimetric studies, thereafter, instead of the theoretical value of 1.08 ng.Hz⁻¹. This difference has no explanation and can be found in the literature. Lastly, the motional resistance (R) during the electrodeposition/stripping of copper was also recorded and it is plotted in the Figure III-12.

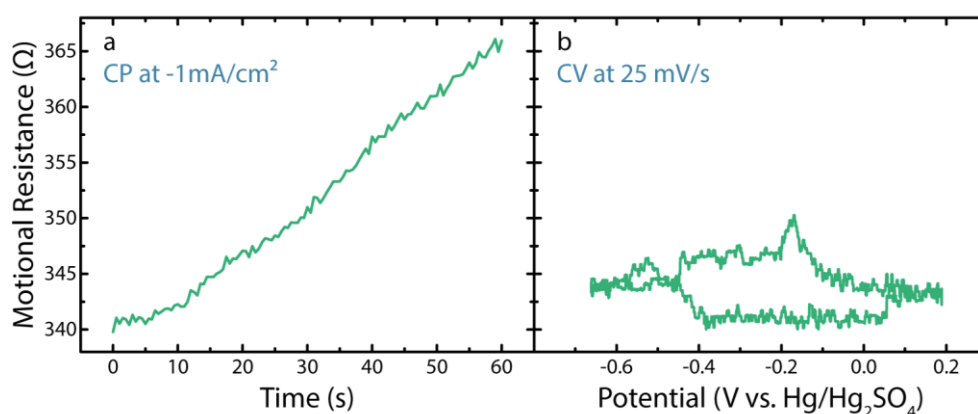


Figure III-12: Motional resistance measurement during electrodeposition in CuSO_4 0.05 mol.L⁻¹ and H_2SO_4 0.5 mol.L⁻¹ (a) galvanostatic at -1 mA.cm⁻² and in (b) cyclic voltammetry at 25 mV.s⁻¹.

A ΔR value of 25 Ω was measured for the electrodeposition by galvanostatic method, while the cyclic voltammetry demonstrates a transient variation of solely 10 Ω . Both processes

(Figure III-11 and Figure III-12) lead to the high $\Delta f/\Delta R$ ratios (or $|\Delta W| \ll |\Delta f|$), indicator for the rigidity of the metallic layer.¹⁹⁴ A slightly higher $\Delta f/\Delta R$ ratio is noticed for the film obtained by CV, which can be explained by an electrodeposition method-dependent morphology leading to slight difference in hydrodynamic properties.

III.4 – Verification of hydrodynamic and viscoelastic properties in electrolyte

III.4.a – Rigidity assessment

At this stage, by combining optimized coating process and the new cell design developed during this Ph.D. thesis, we have made part of the requirements towards the development of an EQCM based research tool compatible with battery testing. However, to conveniently interpret the EQCM results into exploitable mass change, another important aspect has to be checked. When the coating is transferred to electrolyte, its hydrodynamic and viscoelastic properties need to remain negligible, so that they do not intervene to the microbalance functioning as explained in the previous chapter. The optimized coating procedure of our work is expected to minimize the vertical and lateral inhomogeneity of the LFP composite film and thus, minimize the oscillation energy dissipation originated from the rough surface/electrolyte interactions. However, for a definite validation, QCM with dissipation monitoring was performed following the protocol described in the previous chapter (see II.4.b).

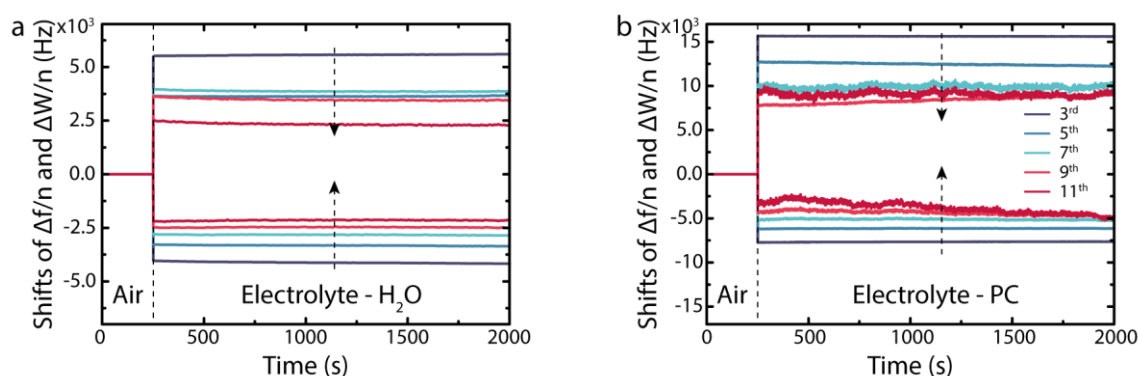


Figure III-13: Shifts of frequency $\Delta f/n$ (negative) and resonance width $\Delta W/n$ (positive) at different overtones ($n = 3$ to $n = 11$) as a function of time, when the composite film is transferred from air to electrolyte. (a) in water and (b) in propylene carbonate.

The resonant frequency, f , and the absolute dissipation factor, D , was recorded at the different overtone orders, n , during the passage from air to the electrolyte solution (1 mol.L⁻¹ LiClO₄ in water or propylene carbonate) under Open-Circuit Potential (OCP). The absolute dissipation factor has been replaced by the resonant width thanks to the relation: $W = f \times D$ (Equation II-12). Such measurements are depicted in the Figure III-13. Independently of the solvent, $\Delta f/n$ and $\Delta W/n$ demonstrated a non-time-dependent behavior and an algebraically decrease with the overtone order. The steadiness of the signals at each overtones manifests the rigidity of the film and the rigid bonding between the coating and the quartz, in agreement with the previous studies.^{166,167,172}

III.4.b – *In situ* hydrodynamic spectroscopy of the composite electrode

To obtain further insights on the solid-liquid interaction (the hydrodynamic properties), $\Delta f/n$ and $\Delta W/2n$ normalized by $\rho_l f_0^2$ (where ρ_l is the density of the studied liquid) are plotted as a function of the penetration depth of the shear wave (Equation II-6), δ , across the boundary layer between the resonator and the electrolyte in the Figure III-14.

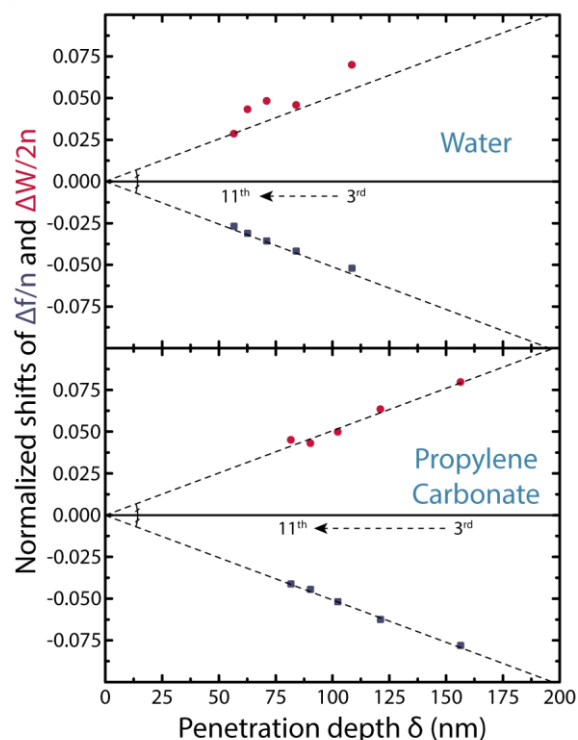


Figure III-14: Normalized (by overtone order as well as by $\rho_l f_0^2$) shifts of frequency $\Delta f/n$ (blue) and resonance width $\Delta W/2n$ (red) as a function of the penetration depth. Shifts are referenced to that of the film in air rather than to the bare crystal. The top (bottom) panel represents the measurement performed in water (propylene carbonate).

This figure shows that the penetration depth values are smaller in the case of aqueous electrolyte due to the lower density and viscosity of water. QCM-D is therefore more sensitive in aqueous than in organic electrolyte, which may explain the slightly more scattered $\Delta W/2n$ data, for the former. In both solvents, $\Delta f/n$ and $\Delta W/2n$ versus δ data present straight lines with a quite similar slope (in absolute value). The modified Kanazawa and Gordon equation,¹⁴⁶ which describes the hydrodynamic interaction between a film with a flat surface and a Newtonian liquid leads the normalized frequency and resonance width shifts to solely depend on the penetration depth, δ , according to the Equation II-18 and Equation II-19.

These two values leads to a straight line as a function of the penetration depth of which slope only depends on the intrinsic properties of the quartz, its density ρ_q and shear modulus μ_q . Here, the straight lines with similar slopes depicted in the Figure III-14 are QCM-D signature of the hydrodynamic interaction between liquid and stiff solid film with plane surface. In conclusion, our coating process of the composite LFP film is optimized and fulfills the gravimetric conditions under OCP and therefore, the Sauerbrey relationship can be employed to treat microbalance data.

III.5 – Electrochemical-gravimetric measurements of an intercalation material

III.5.a – Viscoelastic properties upon cycling

After validation of the metrics regarding the EQCM cell design and mastering the coating attributes, the analytical approach has been implemented to battery testing. For proof of concept, LiFePO_4 is particularly suitable as an active material due to its versatile cyclability both in organic and aqueous electrolytes. As the redox potential nicely falls into the thermodynamic stability of the electrolyte, it eliminates the risks of parasitic reactions¹⁹⁵ (transition metal dissolution and growth of a Cathode-Electrolyte Interface). Frequency change and absolute motional resistance were simultaneously measured on LFP-based deposits during cyclic voltammetry at various scan rates in water or in propylene carbonate based electrolyte in 1 mol.L^{-1} of LiClO_4 . The results for each electrolyte and each scan rate are gathered in the Figure III-15.

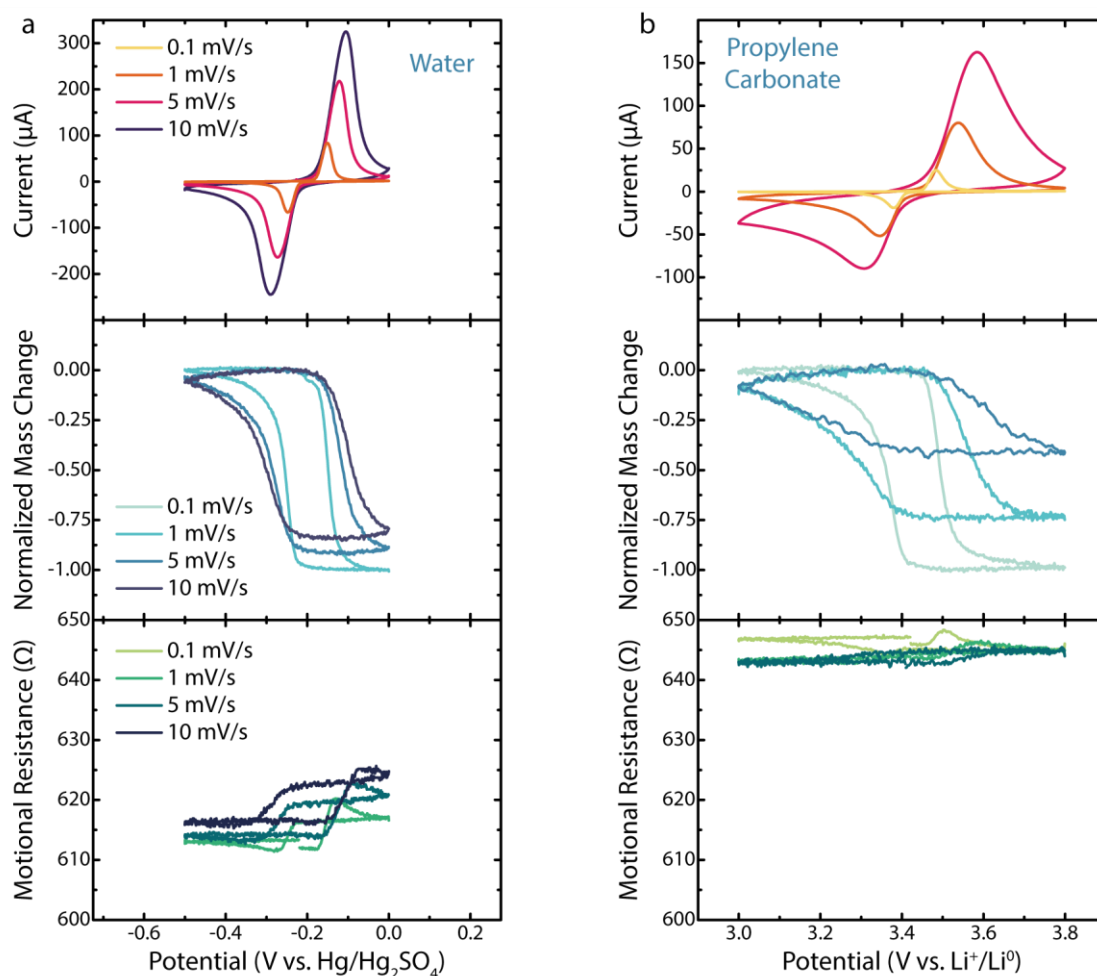


Figure III-15: Cyclic voltammetry of LFP composite electrodes at different scan rates, in 1 mol.L⁻¹ LiClO₄ (a) in water and (b) in propylene carbonate. Current, frequency change and absolute motional resistance were simultaneously measured. The frequency change was converted into mass change and normalized by the active material loading. The fifth cycle is here represented for each scan rate.

The small variation (less than 2 %) of the motional resistance in both electrolytes during CV (Figure III-15, third row) reveals the rigidity retention¹⁸⁸ during the lithium insertion/extraction. Such an EQCM-R testing protocol ensures that the Sauerbrey equation applies for extracting the Δm from the measured Δf values, using Equation II-5 and the experimental C_f value determined previously in the subsection III.3.c In addition, it is reinforced by the small full resonance width changes compared to the frequency changes ($|\Delta W| \ll |\Delta f|$) during cycling in both electrolytes (Figure III-16). As the measurements were not performed on the same electrode with identical loading, the Δm has been normalized to be able to compare the electrogravimetric behavior in two different electrolytes (Figure III-15, middle panel).

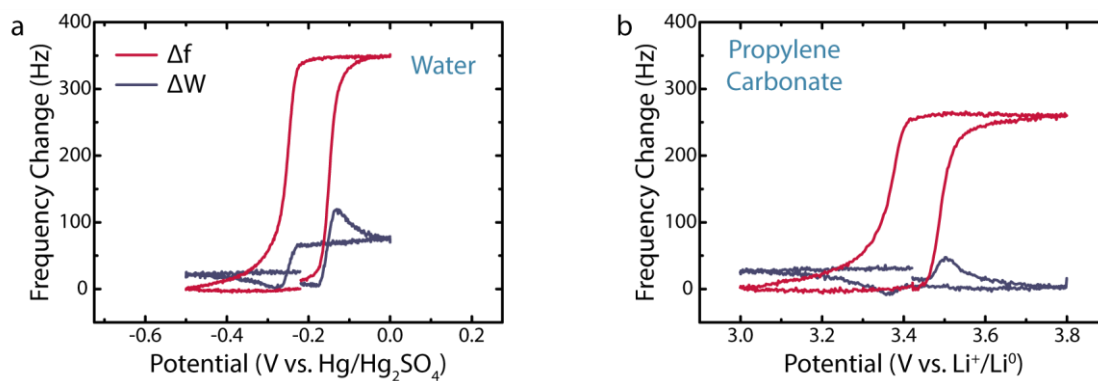


Figure III-16: Comparison of frequency and full resonance width changes during cyclic voltammetry of LFP composite electrodes, in 1 mol.L⁻¹ LiClO₄ (a) in water at a scan rate of 1 mV.s⁻¹ and (b) in propylene carbonate at 0.1 mV.s⁻¹. The fifth cycle is here represented.

III.5.b – Direct outputs of EQCM-R on an intercalation compounds

Classical electrochemical response of LFP was observed in both organic and aqueous electrolytes with redox peaks centered around 3.44 V vs. Li⁺/Li⁰. Aqueous electrolyte presents sharper peaks than organic electrolyte even if it has been performed at faster scan rates. The potential difference of the redox peaks is also smaller in aqueous electrolyte as well as the hysteresis in normalized Δm responses. Since this hysteresis is more pronounced in organic electrolyte, the mass variation spreads on a larger potential window. The difference between the maximum and the minimum mass directly reflects the (de)lithiation stoichiometry in Li_xFePO₄. Its dependence on the scan rate can be correlated with the dynamic of lithium ions insertion/extraction into the electrode material. In comparison to thick composite electrode used in practical application, it must be stressed that coatings of limited masses provide a facile accessibility of the electrolyte to the intercalation particles. This enables the full lithiation/delithiation occurring in a shorter period of time.

Exploring further the differences between aqueous and non-aqueous electrolytes, we note for the former an increase in the scan rate results in a slight decrease of the normalized Δm (Figure III-15a, middle panel). This contrasts with the organic electrolyte, which shows a substantially smaller normalized Δm with increasing scan rate, in an extent that solely half of the particles is delithiated at a 5 mV.s⁻¹ scan rate (Figure III-15b, middle panel). Therefore, electrogravimetric measurements clearly prove a better rate capability of LFP in aqueous rather than in organic electrolyte. Additionally, by performing electrogravimetric analyses on

both aqueous and non-aqueous electrolytes over long cycling (more than 50 cycles) we note a sustained synchronization between the redox peaks and the mass variation upon cycling (Figure III-17), indicative of the robustness of our measurements.

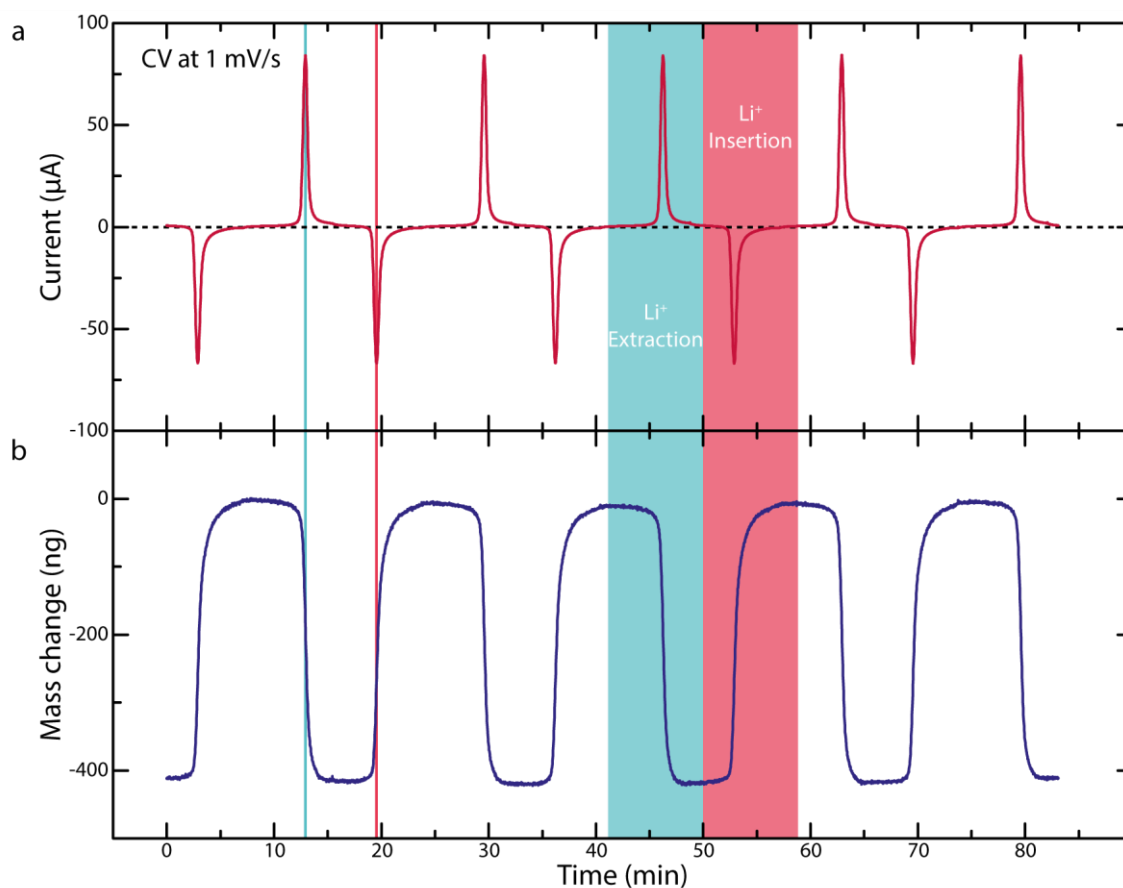


Figure III-17: Electrochemical-gravimetric measurement of composite LFP electrode in cyclic voltammetry at $1 \text{ mV}\cdot\text{s}^{-1}$ in $1 \text{ mol}\cdot\text{L}^{-1}$ LiClO_4 in water. (a) Current and (b) mass response, simultaneously measured by EQCM.

Moreover, we intriguingly observed in both water and organic electrolytes a linear drift of the Q versus time, which cannot be explained by a SEI formation especially in water (Figure III-18a). This drift was identified as intrinsic to our potentiostat and to all brands, with presence of a brand-dependent slope (Figure III-18b). Having identified this problem, the Q curve has been corrected by this slope coefficient, as represented in the Figure III-18a, before being translated into theoretical $\Delta m_{\text{Faraday}}$.

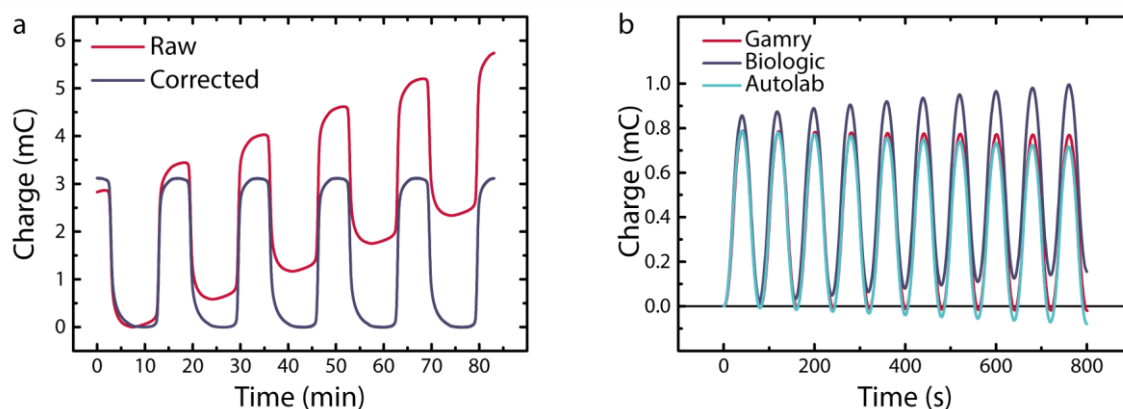


Figure III-18: (a) Raw and corrected charge measurement during the CV of LFP electrode at 1 mV/s in 1 mol/L LiClO₄ in water. (b) Charge visualization of CVs performed on a dummy cell at 10 mV/s on 3 different commercial potentiostats.

III.5.c – New insights on the insertion mechanism at electrode-electrolyte interface

Next, we compared (Figure III-19a) the electrochemical mass variation, $\Delta m_{Faraday}$, associated to the lithium ion insertion/extraction processed from the charge (Q) passing through the system (thanks to the Faraday's law) against the mass variation Δm_{EQCM} estimated by the Sauerbrey equation. A striking result is the large difference between the $\Delta m_{Faraday}$ and the Δm_{EQCM} that can be observed in aqueous electrolyte, but in propylene-based electrolyte as well (Figure III-19b) and of greater amplitude. In both cases Δm_{EQCM} is substantially higher than $\Delta m_{Faraday}$ and this cannot be ascribed to the evolution upon cycling of the hydrodynamic or viscoelastic property of the film as every parameters have previously been verified.

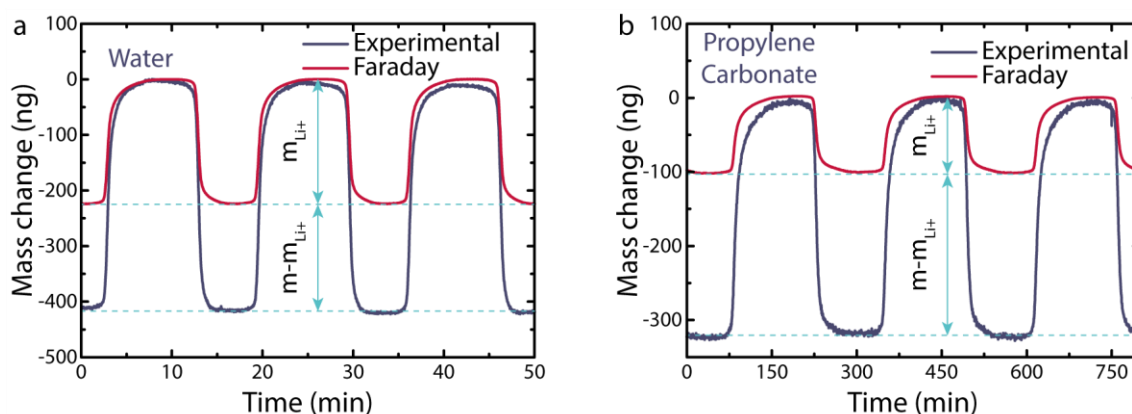


Figure III-19: Experimental (Δm_{EQCM}) and electrochemical mass comparison ($\Delta m_{Faraday}$), (a) CV at $1 \text{ mV}\cdot\text{s}^{-1}$ in water and (b) CV at $0.1 \text{ mV}\cdot\text{s}^{-1}$ in propylene carbonate.

Tsionsky and co-workers proposed the formation of a “viscous layer” at the flat electrode/electrolyte interface.¹⁹⁶ This increase of the local viscosity compared to the bulk of the electrolyte is due to the accumulation of cations in the double layer region when the electrode is negatively polarized and may contribute to frequency measurements. However, this contribution can partly explain the phenomenon and is negligible in comparison with this recorded mass difference. Since the incorporation of solvent molecules into LiFePO_4 is impossible from structural point of view, we hypothesize that the solvent molecules could play a key role at the LFP-electrolyte interface. To elucidate the contribution of the solvent, the data was processed for scan rates for which the full delithiation is possible in both electrolytes (*i.e.* for aqueous $1 \text{ mV}\cdot\text{s}^{-1}$ and organic $0.1 \text{ mV}\cdot\text{s}^{-1}$). Supposing the involved complex $[\text{Li}, z \text{ Solvent}]^+$, the number of solvent molecules associated to the Li^+ at the EEI can be determined thanks to the following equation:

$$z = \frac{n_{\text{Solvent}}}{n_{\text{Li}^+}} = \frac{M_{\text{Li}^+}}{M_{\text{Solvent}}} \times \frac{m - m_{\text{Li}^+}}{m_{\text{Li}^+}} \quad \text{Equation III-1}$$

where n_i and M_i are the number of moles and the molar mass, respectively, of the lithium or the solvent molecules (water or propylene carbonate). The entities, m and m_{Li^+} are the experimental mass and the electrochemical mass (calculated from the Faraday’s law), respectively.

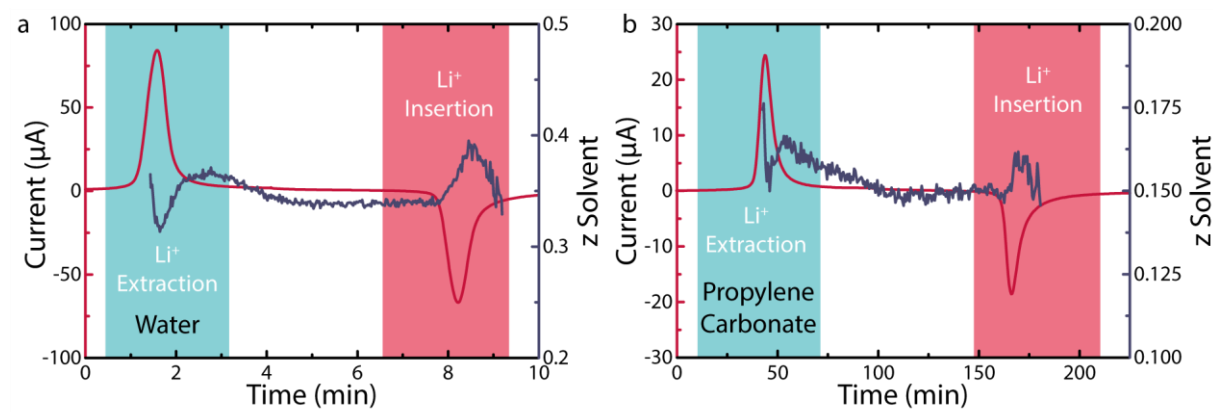


Figure III-20: Determination of the number of solvents involved in the lithium insertion/extraction process (a) in CV at 1 mV.s⁻¹ in water and (b) in CV at 0.1 mV.s⁻¹ in propylene carbonate.

The results of these calculations are plotted in Figure III-20a and Figure III-20b for H₂O-based and PC-based electrolytes, respectively. The number of solvent molecules involved in the lithium insertion/extraction process of LiFePO₄ in water media (Figure III-20a) averages at 0.35 with a decrease during the extraction and an increase during insertion. This value is lower and equal to 0.15 in propylene carbonate-based electrolyte (Figure III-20b) with however the same “up and down” feature during lithium insertion and extraction. These results were found in a reproducible way in at least three experiments. Altogether, these results provide experimental evidence for the logical depletion and accumulation of solvent molecules at the EEI when lithium ions are extracted and inserted, respectively, with the amplitude of this feature been solvent dependent and the most pronounced in aqueous media.

III.6 – Simulation of the interface between the electrolyte and a model electrode

III.6.a – Interfacial density profiles of the different species involved

To obtain fruitful information on the interaction between Li cations and solvent molecules at the interface, a model gold electrode in contact with our electrolytes was simulated by classical Molecular Dynamics (MD). The computational details are given in the Materials and Methods. The Figure III-21 shows the density profiles in the direction normal to the Au (100) surface (z) for both 1 mol.L⁻¹ LiClO₄ (a,c) in H₂O and (b,d) in PC. By looking at the

magnified zoom of the region close to the Au surface (Figure III-21c and d), one can immediately appreciate the remarkable difference in the density profile of Li^+ ions (green) in the aqueous and non-aqueous solvent. In water, a very intense and sharp peak is found at about $z = 2.5 \text{ \AA}$, followed by a less intense peak, while this is not the case in PC, where the second peak has a higher intensity than the first one.

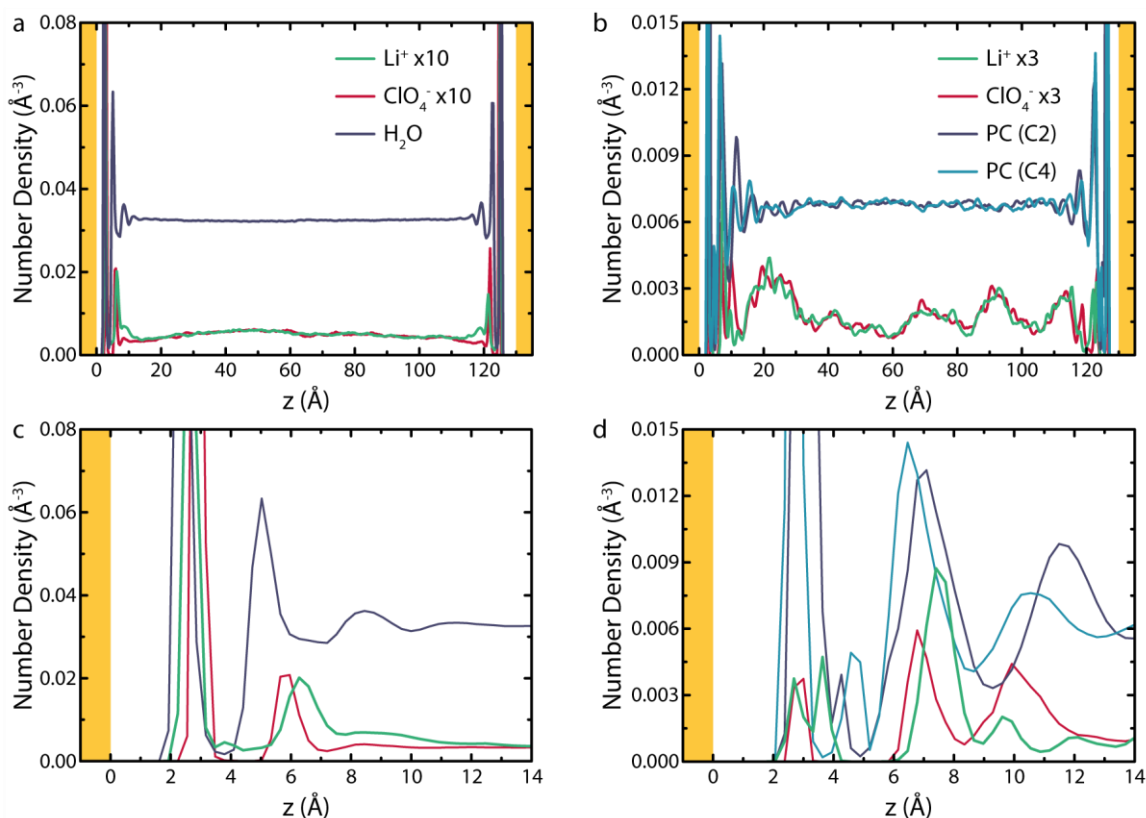


Figure III-21: Density profiles in the direction normal to the Au (100) surface (z) for 1 mol.L^{-1} LiClO_4 (a) in H_2O and (b) in PC. In the case of PC, C2 refers to the carbon atom of the ring linked to the methyl group, while C4 is the carbon atom of the carbonyl group. Magnified views of the region close to the electrode surface are provided in panels (c) and (d).

In both solvents, the first peak corresponds to inner-sphere adsorption, where Li^+ cations are solvated within the topmost solvent layer in contact with the metal surface. By contrast, the second peak corresponds to outer-sphere adsorption, where Li^+ cations are separated from the metal by one solvent layer. Therefore, we can conclude that inner-sphere adsorption is preferred for Li^+ in water, while outer-sphere adsorption is more probable in propylene carbonate.

III.6.b – Energy landscape and solvation from the electrolyte bulk to the interface

From the Li^+ density profile, it is now possible to compute the potential of mean force (PMF , free energy) through the following expression:

$$PMF = -k_B T \ln(P(z)) \quad \text{Equation III-2}$$

where $P(z)$ is the probability to find the ion at a certain distance from the electrode (obtained from the density profile of Figure III-21), k_B the Boltzmann's constant ($1.38 \cdot 10^{-23} \text{ J.K}^{-1}$) and T the temperature (K).

Note that a maximum in the density profile corresponds to a minimum in the PMF and *vice-versa*. From right to left, the PMF provides an estimate of the energy required to bring the ion from the bulk to a distance z from the interface. The results are shown in Figure III-22a and Figure III-22b for Li^+ in H_2O and Li^+ in PC, respectively. As already noted for the density profiles, the Li^+ PMF in the aqueous and organic solvent are remarkably different. In both cases, the most important feature is the highest free energy barrier, observed at z around 7 Å. This is the barrier that Li^+ cations have to overcome to pass from outer- to inner-sphere adsorption and thus arrive in direct contact with the surface. As it can be seen in the Figure III-22a and Figure III-22b, a much higher barrier of about 185 meV is observed in PC versus only 47 meV in water. Moreover, in case of PC, a second barrier (~41 meV) is present at $z = 10\text{-}12$ Å, suggesting that an energetic penalty also exists for Li^+ to access the interfacial region.

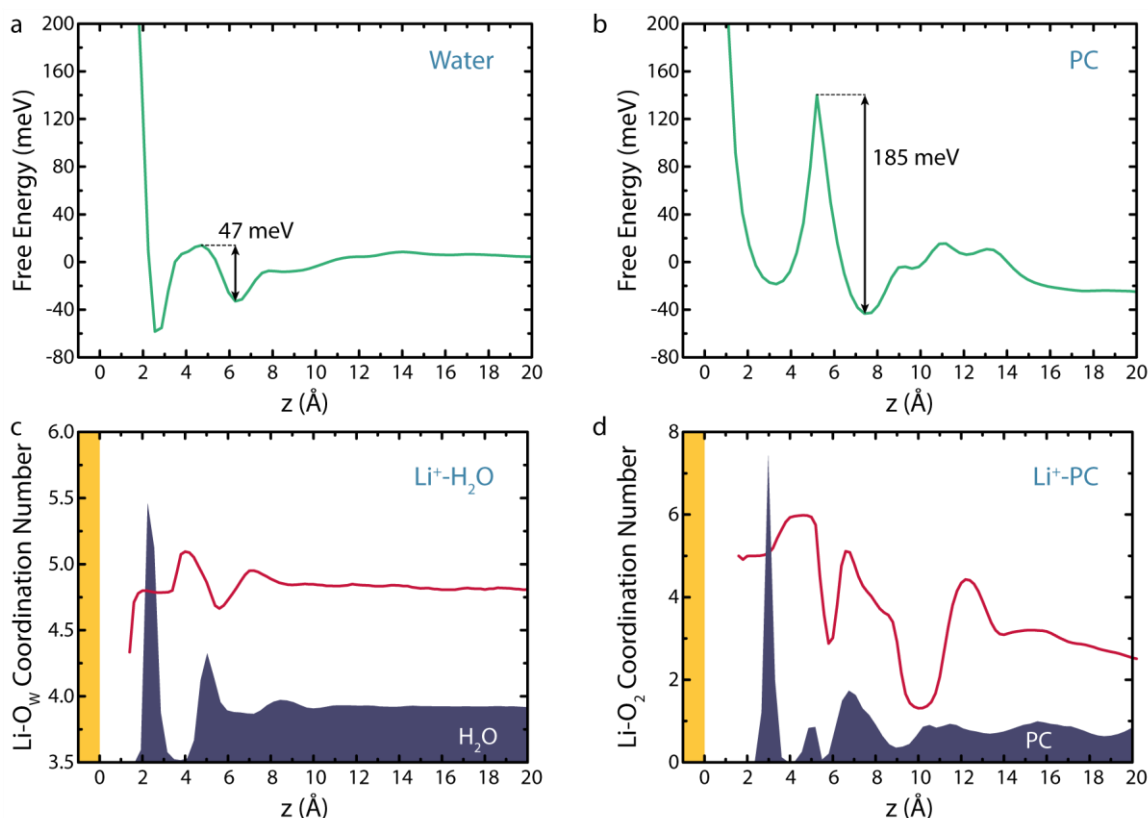


Figure III-22: Li^+ potential of mean force (PMF, free energy in meV) in the direction normal to the Au (100) surface (z) for 1 mol.L^{-1} LiClO_4 (a) in H_2O and (b) in PC. Evolution of the Li-solvent coordination number as a function of the distance z from the electrode surface (red line) (c) in water and (d) in PC. A cut-off distance of 3 \AA (*i.e.* first minimum of the Li-O, with O the oxygen atom of H_2O or the carbonyl group oxygen atom of PC) radial distribution function has been used. The density profiles of water and PC (blue), and Au (orange) are also plotted.

In order to complement the picture, we have then analyzed the evolution of the Li-solvent coordination number as a function of the distance z from the electrode in the two systems. A cut-off distance of 3 \AA , that corresponds to the first minimum of the Li-O (where O is the oxygen atom of H_2O or the carbonyl group oxygen atom of PC) radial distribution function, has been chosen. In water (Figure III-22c), the Li- H_2O coordination number shows only small variations as a function of z (from 4.5 to 5), with an average coordination number in the bulk region of 4.8. This number is in very good agreement with an experimental neutron scattering study of 1 mol.L^{-1} LiCl in water, reporting that Li^+ is coordinated by 4-5 H_2O molecules with an average occupancy of 4.85.¹⁹⁷ In particular, the coordination number in the first water layer in contact with the Au surface ($z = 2\text{-}3 \text{ \AA}$) is almost identical to the one in the bulk, and the Li^+ hydration shell is stripped off only once the ion leaves this water layer and reaches the metal surface ($z < 2 \text{ \AA}$). Very different is the evolution of the Li-solvent coordination number in propylene carbonate (Figure III-22d), which shows much larger

fluctuations as a function of z , with numbers in between 1 and 6. This result indicates that the Li-PC solvation shell is not very stable and it can be stripped off also far from the surface, at variance with water. Inspection of snapshots extracted from the MD simulation (a representative one is provided in the Figure III-23), reveals that these fluctuations are connected to strong $\text{Li}^+\text{-ClO}_4^-$ ion pairing, with the formation of clusters of ion pairs. However, when approaching a distance z from the surface of less than $\approx 10 \text{ \AA}$, the size of the clusters is reduced and some Li^+ are not involved in ion-pairs. The energy barrier in the PMF at $z \approx 10 \text{ \AA}$ to access the interfacial region, which exists only for Li^+ in PC, can be explained by a change in the Li^+ coordination.

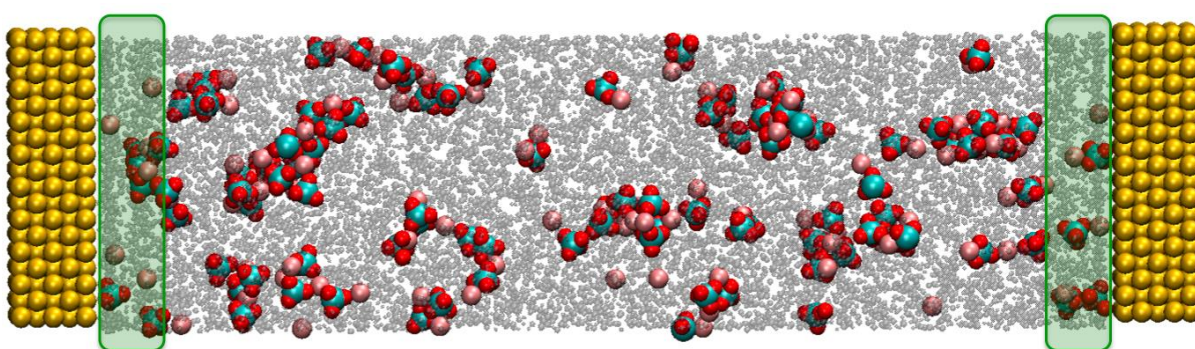


Figure III-23: Representative snapshot extracted from the MD simulation of $1 \text{ mol.L}^{-1} \text{ LiClO}_4$ in PC between two planar Au (100) electrodes at a fixed difference potential of 0 V. Li^+ cations are represented in pink, ClO_4^- anions in cyan/red and PC solvent with grey points. The green rectangles highlight the interfacial region up to a distance of 10 \AA from the Au surface.

III.7 – Chapter conclusions

We have reported a comprehensive new protocol that combines a multi-step coating process, the design of a new hardware and verification steps to securely interpret the EQCM results into exploitable mass changes, hence facilitating the ingress of this user-friendly characterization tool in battery research. Regarding our coating process, it includes multi-steps offering reproducible film deposits with a lateral and vertical homogeneity that can be tuned depending on the characteristics of the active material and/or binder. For proof of concept, we have used the well-known LiFePO_4 phase as a model material and the quality of the films obtained for gravimetric measurements was secured *via* QCM-D measurements at multiharmonic that successfully revealed the hydrodynamic behavior of a flat surface film, rigidly attached to the resonator in both aqueous and non-aqueous electrolytes.

Most of the publications employing EQCM in organic media, describe measurements performed in a glovebox or restricted to one brand of frequency read-out. To alleviate these burdens we have developed a new cell dedicated to EQCM measurement for battery, and also supercapacitor testing. It offers several advantages: mimic the battery configuration, ensure airtightness (no exposure to any contaminant) while having low impedance and being reproducible. Moreover, besides its versatility of hosting either aqueous or non-aqueous electrolyte, it is compatible with the complementary techniques comprised in the QCM toolbox: EQCM, EQCM-R, network analyzer and EQCM-D.

Additionally, the practicality of our approach, mainly for analyzing active materials that can suffer from the larger constraints during cycling is rooted in the dual monitoring of motional resistance and frequency. Hence, our suggestion is of using EQCM-R as a convenient qualitative viscoelastic indicator, which can be completed by EQCM-D if viscoelasticity is predominant. Let us reiterate that a small variation of the motional resistance during cycling attests that the rigidity of the composite LFP films is preserved during (de)insertion of Li^+ . Checking these properties is essential to avoid a large dissipation of energy when modified QCM resonators are immersed in an electrolyte, which may result in an over/under estimation of the real mass change.

New trends in the battery field, such as the use of aqueous electrolytes as alternatives to organic counterparts, brings the necessity to revisit even the model materials behavior, under the new operation conditions, hence the ever-increasing interest for the EQCM technique. For example, the higher rate capability of LFP particles in aqueous electrolytes compared with organic counterparts, even in practical batteries¹⁹⁸, has been demonstrated but underlying reasons are poorly understood. Addressing this question by our EQCM-R based strategy led us to directly assess the partial or total LFP delithiation conditions, depending on the potential scan rate, in two different media. We unambiguously proved that the Li^+ insertion/extraction mechanism in LiFePO_4 is solvent-dependent. Moreover, by comparing the experimental Δm_{EQCM} and theoretical $\Delta m_{Faraday}$ mass changes accompanying the insertion and extraction of Li^+ ions in both electrolytes, we provide evidence for a solvent-assisted insertion process with the number of solvent molecules pertaining to the solvation shell being markedly greater for water than for propylene carbonate-based electrolytes. This higher concentration variation of water molecules at the EEI of composite LFP electrode

enables a faster insertion/extraction at the vicinity of the active material particle. Song *et al.*¹⁹⁹ reported similar conclusions based on EQCM studies performed with binder-free coatings. However, they solely obtained an approximate estimation of the number of solvent molecules involved the interfacial mechanism, because of gravimetric curves presenting unexpected profiles. We believe that the reason is rooted in the absence of binder in their coatings, hence re-insisting that binders are essential to accommodate the strain caused by the Li⁺ insertion in LFP, avoiding its viscoelastic evolution.^{168,169}

Such findings are independently supported by our Molecular Dynamics and *ab initio* calculations²⁰⁰ that show the formation of a chemisorbed H₂O molecules at the interface with LiFePO₄ which facilitates the lithium desolvation process near the surface and therefore accelerates the Li-ion transport across the EEI. This scenario do not occur in presence of big organic molecules alike propylene carbonate owing to steric hindrance and the higher free energy cost to bring the Li⁺ close to the electrode. These calculations, combined with our experimental findings regarding the depletion/increase of the solvent concentration during the lithium insertion/extraction demonstrate the lithium desolvation from its water shell near the active material surface while in organic media the removal of the organic solvation shell happens further apart from the interface. This implies a higher energy of desolvation in non-aqueous rather than in aqueous electrolyte, hence accounting for the solvent-dependent rate capability trends observed with LFP. The strong interaction between Li⁺ and ClO₄⁻ (ion pairing) especially in organic electrolyte can also be an explanation.

This chapter was limited to LiFePO₄; however, our developments of the EQCM tooling for battery research together with means of getting insights on the behavior of solvated Li⁺ ions at EEI can be extended to other charge carriers (Na⁺, K⁺, ...) and electrode materials, in view of screening/predicting in which electrolyte composition, optimum performance can be reached. To this end, we aimed to rationalize the peculiar solvent-dependent EEI behavior of lithium insertion by the particular case of the K-ion chemistry in the next chapter. In addition to the EQCM based methods employed here for EEI study, we proposed a better quantification of interfacial insertion kinetics of intervening species (*i.e.* K⁺ and solvent molecules) by performing EQCM and EIS coupling, *ac*-electrogravimetry.

Chapter IV – Probing the electrode-electrolyte interface of potassium-ion battery – Aqueous vs. Non-aqueous electrolytes

IV.1 – Introduction

The previous chapter evidenced that the insertion process in Li-ion host material (shown for LFP) is assisted by solvent molecules at the electrode-electrolyte interface (EEI). In addition, this solvent-assisted mechanism seems to govern the rate capability difference found between the organic and aqueous electrolytes, attributed to a higher desolvation energy of Li ions at the organic electrolyte interface than that occurs in aqueous analogue. In conformity with this result, a part of the literature (see I.2.b) expressed the importance of the solvation shell on the alkali metal cation intercalation in the host material. However, it is still widely admitted by the battery community that rate capability of alkali metal-ion batteries are only influenced by the ions' transport properties in the bulk of the electrolyte. The better ionic transport properties when moving from lithium to potassium ions is rationalized by the weaker Lewis acidity of the latter.¹⁵ This results in a smaller Stokes radius, *i.e.* cation and its solvation shell, and therefore an easier vehicle-type displacement in the bulk of the electrolyte when a concentration gradient is imposed (Figure I-7). Another parameter, not to be disregarded, is the desolvation energy of the cation in the bulk of the electrolyte, which is modified in moving from Li⁺ to Cs⁺ within the alkali metal column. Regardless of the nature of the electrolyte (non-aqueous or aqueous), the desolvation energy decreases when moving from lithium to potassium ion. It can be noted that the dehydration energy is yet always higher than desolvation energy in an organic electrolyte.^{15,126}

To strengthen the results obtained with the Li-ion host in the previous chapter concerning the solvent-assisted insertion mechanism and the prominence of the solvation shell on the rate capability, other alkali metal-ion batteries should be investigated. With potassium ions, featuring a smaller and weaker solvation shell in the bulk of the electrolyte, the K-ion chemistry should be the ideal candidate to untangle the different steps taking place during the cation insertion and to confirm the significance of the desolvation stage. In this regard, a K-ion host, Prussian Blue (PB) has been selected as a model compound, fulfilling the

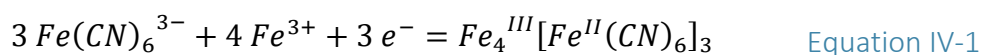
same criteria as LFP in the previous chapter. Potassium ions can be inserted in the PB phase either in aqueous and non-aqueous electrolytes. Another benefit is that this phase can be electrodeposited, enabling an easy thickness and morphology control, thanks to electrochemistry. It can be noted that FePO_4 is also known as K-ion host; however, K^+ can only be inserted in the amorphous and porous phase, which is incompatible with purely gravimetric measurement.²⁰¹

To conduct such EEI study, this chapter will be structured as follows. After the electrodeposition of the Prussian Blue phase, the structure and morphology of the resulting films are characterized to evidence their “unambiguous controlled deposition” and conformity for an *operando* EQCM study. Then, electrochemical and electrochemical-gravimetric analyses are performed to demonstrate the prominence of the ions’ desolvation step on the battery kinetics. To clearly identify the species involved in the interfacial processes and to estimate their respective insertion kinetics, EIS and EQCM coupling, *ac*-electrogravimetry is employed. The electrochemical-gravimetric analyses results are integrated to propose a clear grasp of the dynamic electrode-electrolyte interface during the insertion process.

IV.2 – Phase preparation and characterization

IV.2.a – Morphological and structural description

The Prussian Blue phase was prepared by electrodeposition at the surface of gold patterned quartz resonators in an acidic solution containing ferric and ferricyanide ions. Experimental details of the electrodeposition protocol are provided in the Materials & Methods section. A constant $-40 \mu\text{A}\cdot\text{cm}^{-2}$ cathodic current was applied during different period of time (t_{ED}): 150, 300, 450 and 600 s, to obtain theoretical thicknesses of 100, 200, 300 and 400 nm, respectively. The electrochemical curves for electrodeposition procedure are plotted in the Figure IV-1a. It shows a plateau of potential, which is independent of the deposition time, characteristic of the $\text{Fe}_4^{\text{III}}[\text{Fe}^{\text{II}}(\text{CN})_6]_3$ electrodeposition (Prussian Blue) following this equation:



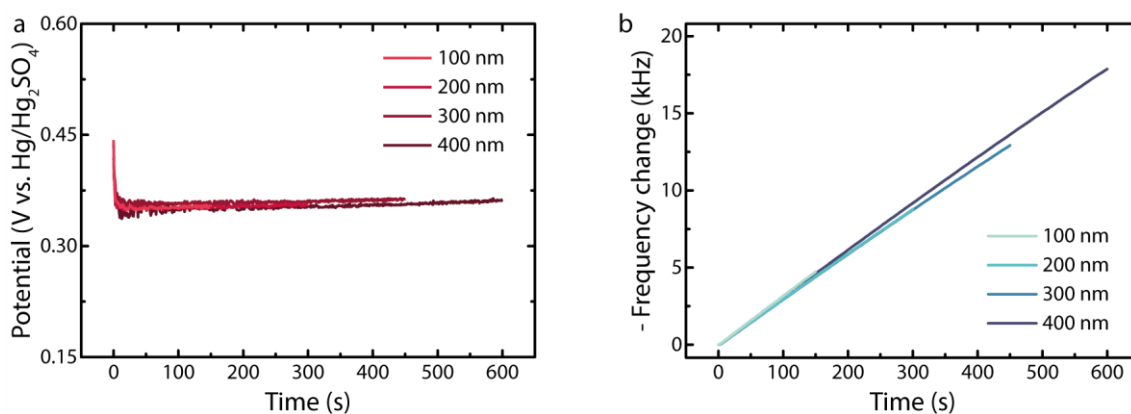


Figure IV-1: Electrodeposition of Prussian Blue films. (a) Chronopotentiometry at $-40 \mu\text{A}\cdot\text{cm}^{-2}$ in $\text{HCl } 0.01 \text{ mol}\cdot\text{L}^{-1}$, $\text{K}_3[\text{Fe}(\text{CN})_6] 0.02 \text{ mol}\cdot\text{L}^{-1}$ and $\text{FeCl}_3 0.02 \text{ mol}\cdot\text{L}^{-1}$ and (b) *operando* frequency change measurement by EQCM during different periods of time.

The resonant frequency of the quartz resonator was monitored during the electrodeposition process and the opposite of the frequency change (directly proportional to the mass change) is represented in the Figure IV-1b. The mass linearly increases and its slope is practically independent of the electrodeposition time, indicating the formation of films with different thickness but similar molar mass. In addition to the resonators used as substrates for EQCM studies, a relatively thick film ($1 \mu\text{m}$, t_{ED} of 1500 s) of PB was also prepared on a gold disk electrode. X-ray diffraction was used to characterize the electrodeposited phase, the XRD pattern is presented in the Figure IV-2a. It shows both intense peaks characteristic of the gold substrate and relatively less intense peaks, which can be indexed in a cubic $Fm\bar{3}m$ unit cell. Despite the broadness of the peaks demonstrating the low crystallinity of the produced phase, they correspond to the reported $\text{Fe}_4^{\text{III}}[\text{Fe}^{\text{II}}(\text{CN})_6]_3$ Prussian Blue phase. The Figure IV-2b depicts the structural model deduced from the Rietveld refinement, which shows a cubic structure with a characteristic distance of 10.1 \AA .

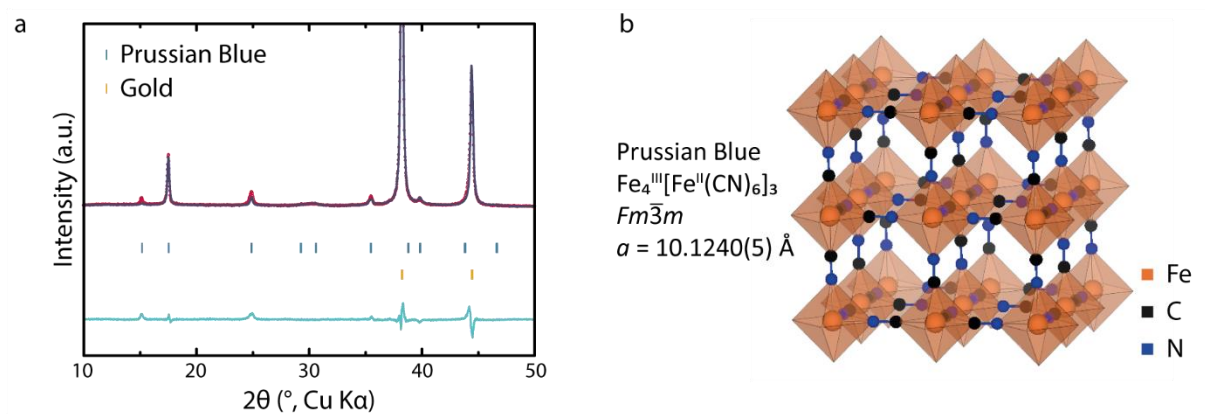


Figure IV-2: (a) Rietveld refinement of XRD patterns of a 1 μm thick Prussian Blue film on a gold substrate. The red circles, dark blue continuous line and bottom blue line represent the observed, calculated and difference patterns, respectively. Prussian Blue phase and gold are indexed by blue and orange bars, respectively. (b) The corresponding structural model.

The FEG-SEM images, shown in the Figure IV-3a-d, indicate that the electrodeposited films are conformal and flat at the surface of the quartz resonator, independently of the film thickness. However, the vacuum conditions of the SEM chamber dry out the films leading to the cracks formation. The role of water in the PB structure will be discussed later. Nonetheless, EDX mapping analysis was performed, displaying the presence of iron-rich domains on the gold electrode surface (Figure IV-3e,f). EDX coupled with FEG-SEM and supported by the XRD analyses indicate that the Prussian Blue (PB) phase is successfully synthesized.

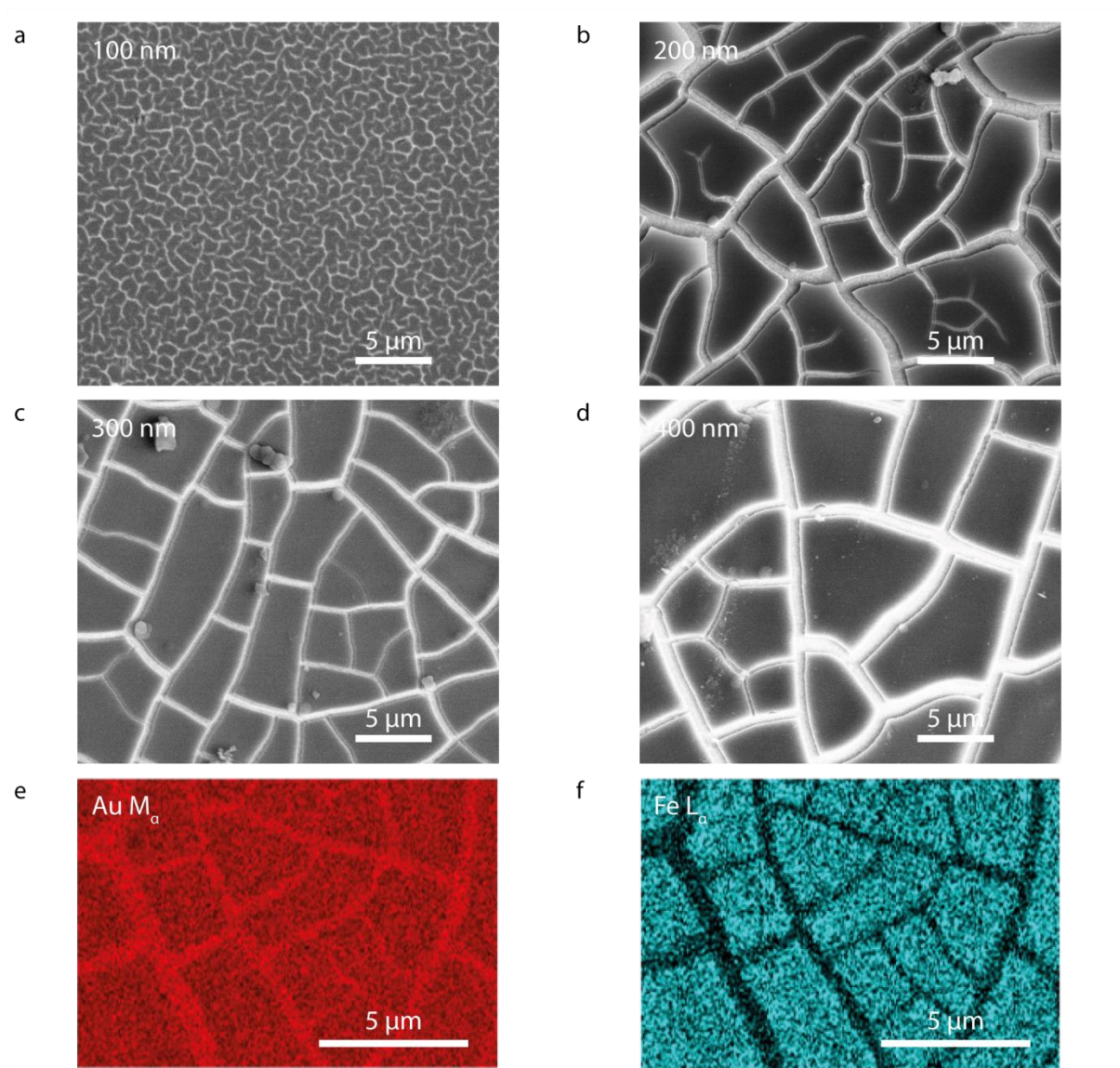


Figure IV-3: (a-d) FEG-SEM images of Prussian Blue films electrodeposited at the surface of a gold electrode of a quartz resonator. EDX mapping analysis the 200 nm thick PB film for (e) iron and (f) gold.

IV.2.b – Water incorporation in the structure lattice

QCM with motional resistance monitoring enabled the estimation of the incorporated water in the structure lattice. To do so, the frequency and the motional resistance of the resonators, before and after PB electrodeposition, were measured in air. The frequency changes were converted to the mass changes using Sauerbrey equation and allowed the experimental value of the electrodeposited PB mass to be estimated. The Figure IV-4a shows that the experimental mass is linear with the electrodeposition time. The electrodeposited

films, at least in the t_{ED} range of $150 \leq t_{ED} \leq 600$ s, do not show any indication of electronic conductivity loss, supported by the absence of a plateau in the experimental mass vs. t_{ED} plot in Figure IV-4a. On the other hand, the motional resistance seems to exhibit a threshold for the films generated with a t_{ED} of more than 450 s, and a R value that increases drastically at t_{ED} of 600 s. It is noted that before this threshold value, the motional resistance is very low ($< 30 \Omega$, for $t_{ED} \leq 450$ s) and falls within the suitable range for conducting electrochemical-gravimetric measurements. Even though the film obtained at $t_{ED} = 600$ s demonstrates a significant increase in the motional resistance, the $|\Delta W| \ll |\Delta f|$ condition for meaningful gravimetric sensing (Equation II-20) is still fulfilled. *In situ* hydrodynamic spectroscopy was not performed for these coatings, considering the significantly low motional resistance values for $t_{ED} \leq 450$ s and the morphological features of the coatings (flat surface, low roughness).

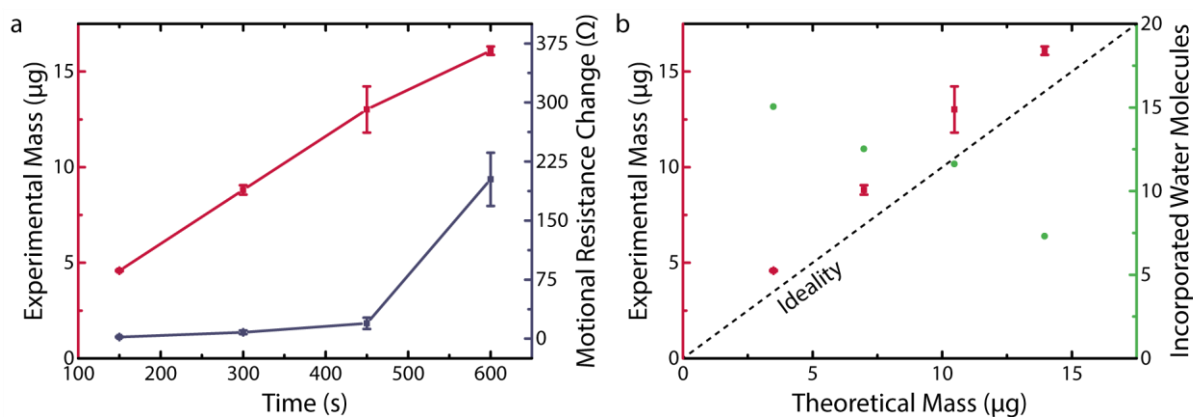


Figure IV-4: (a) Experimental mass and motional resistance for PB films, measured in air. (b) Comparison of the experimental and the theoretical mass of the PB films and the respective number of associated incorporated water molecules. PB films with four different thicknesses, obtained at $t_{ED} = 150, 300, 150$ and 600 s, are presented.

The experimental mass of the electrodeposited PB films obtained from QCM measurements were compared to their theoretical counterparts (estimated by the Faraday's law). The Figure IV-4b reveals a clear difference between these two set of values. For each film thicknesses, the experimental mass is slightly higher than the theoretical value. This phenomenon was already encountered by Buser *et al.* who provided evidence for the incorporation of between 14 and 16 water molecules into the unit cell.²⁰² For the films obtained at $t_{ED} \leq 450$ s, our results corroborated these values. Powder neutron diffraction demonstrated that 6 water molecules are coordinated to Fe^{III} at empty nitrogen sites and the remaining are present either as isolated molecules at the center of the unit cell or as water molecules hydrogen bonded to the coordinated ones.²⁰³

IV.2.c – Thickness control of the prepared films

The thickness of the electrodeposited films was estimated by two techniques. To begin with, cross section FEG-SEM images of the coatings were examined to measure its thickness at different spots of the sample, as represented in the Figure IV-5.

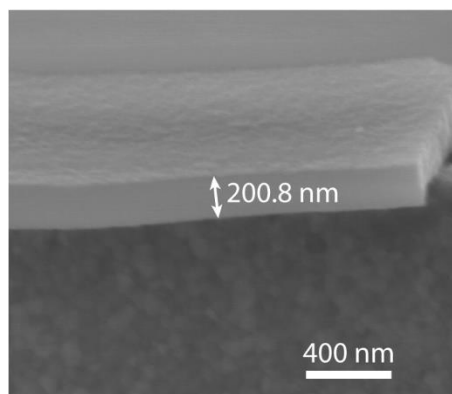
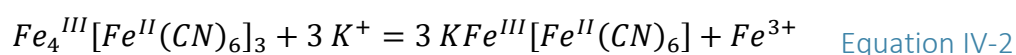
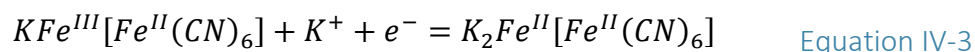


Figure IV-5: Thickness estimation of the electrodeposited film by FEG-SEM through a cross section sample.

For the sake of comparison, the film thickness was also estimated *via* electrochemistry. The films obtained with 4 different t_{ED} were cycled 15 times in aqueous medium containing $0.25 \text{ mol.L}^{-1} \text{ K}_2\text{SO}_4$ at pH 3.5 to insert potassium ions in the structure, by leaching one iron during the first cycles, as described in the following equation:



In the following cycles, the potassium ions are reversibly inserted and extracted from the structure, as depicted in the Equation IV-3.



The quantity of potassium ions stored into the structure was assessed thanks to the charge passing through the system upon oxidation. Then, using the following equation, the thicknesses of four different films can be estimated:

$$t_{film} = \frac{Q_{ox} N_A d^3}{4FS} \quad \text{Equation IV-4}$$

where Q_{ox} is the measured charge in oxidation (C), N_A is the Avogadro constant ($6.02 \cdot 10^{23} \text{ mol}^{-1}$), d is the characteristic distance of the corresponding PB unit cell, estimated earlier by

Rietveld refinement (1.01 nm), 4 is the effective iron atoms in each unit cell, F is the Faraday's constant (96485 C.mol⁻¹) and S is the specific surface area, assimilated to the geometric surface thanks to the film flatness (0.196 cm²).

The Figure IV-6 gathers the thicknesses estimated by these two techniques and compares them with the theoretical ones.

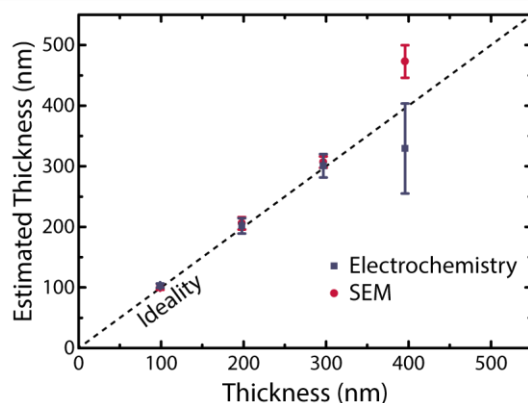


Figure IV-6: Comparison of the estimated and theoretical thicknesses of PB films by FEG-SEM and electrochemistry.

The Figure IV-6 suggests a good agreement between the measured thicknesses and the theoretical ones for $t_{film} \leq 300$ nm. For the film of theoretically 400 nm, SEM cross section demonstrates that the film is thicker. However, the electrochemistry displays a lower value of the thickness, which means that part of this film is electrochemically inactive.

These characterizations, besides confirming a true Prussian Blue phase formation at the surface of the gold patterned quartz resonator, also permitted the optimization of the PB thin films for the EEI study by electrochemical and electrogravimetric analyses. The films with nominal thicknesses ≤ 300 nm are suitable, evidenced by their low motional resistance change with respect to their loadings and the morphological features (*i.e.* flat surface).

IV.3 – Electrochemical and electrogravimetric analyses

IV.3.a – Rate capability assessment

After the 15 cycles of pre-treatment, the potassium ions are inserted in the PB structure, as shown in Equation IV-5. The rate capability assessment is performed on PB films

of different thickness, which were cycled in an aqueous electrolyte composed of K_2SO_4 0.25 mol.L^{-1} (pH 3.5) and in non-aqueous electrolyte composed of KPF_6 0.5 mol.L^{-1} in EC:DEC 1:1. The potassium ions concentration was kept constant at 0.5 mol.L^{-1} between the two media, for the sake of comparison. Here K_2SO_4 salt was preferred over KCl to avoid the Cl^- insertion into the PB structure^{204,205} and the organic electrolyte is the most frequently used by the battery community according to Hwang *et al.*⁴¹ The film was solely reversibly cycled between Prussian Blue ($KFe^{III}[Fe^{II}(CN)_6]$) and Prussian White ($K_2Fe^{II}[Fe^{II}(CN)_6]$) (Equation IV-4), without reaching the Prussian Green phase ($Fe^{III}[Fe^{III}(CN)_6]$). Frequency change (translated into mass change) and absolute motional resistance were simultaneously monitored during cyclic voltammetry at various scan rates. The results obtained for each electrolyte and at each scan rate are gathered in the Figure IV-7. Although all films have been cycled, results are solely reported for the 100 nm thick film as no difference was detected.

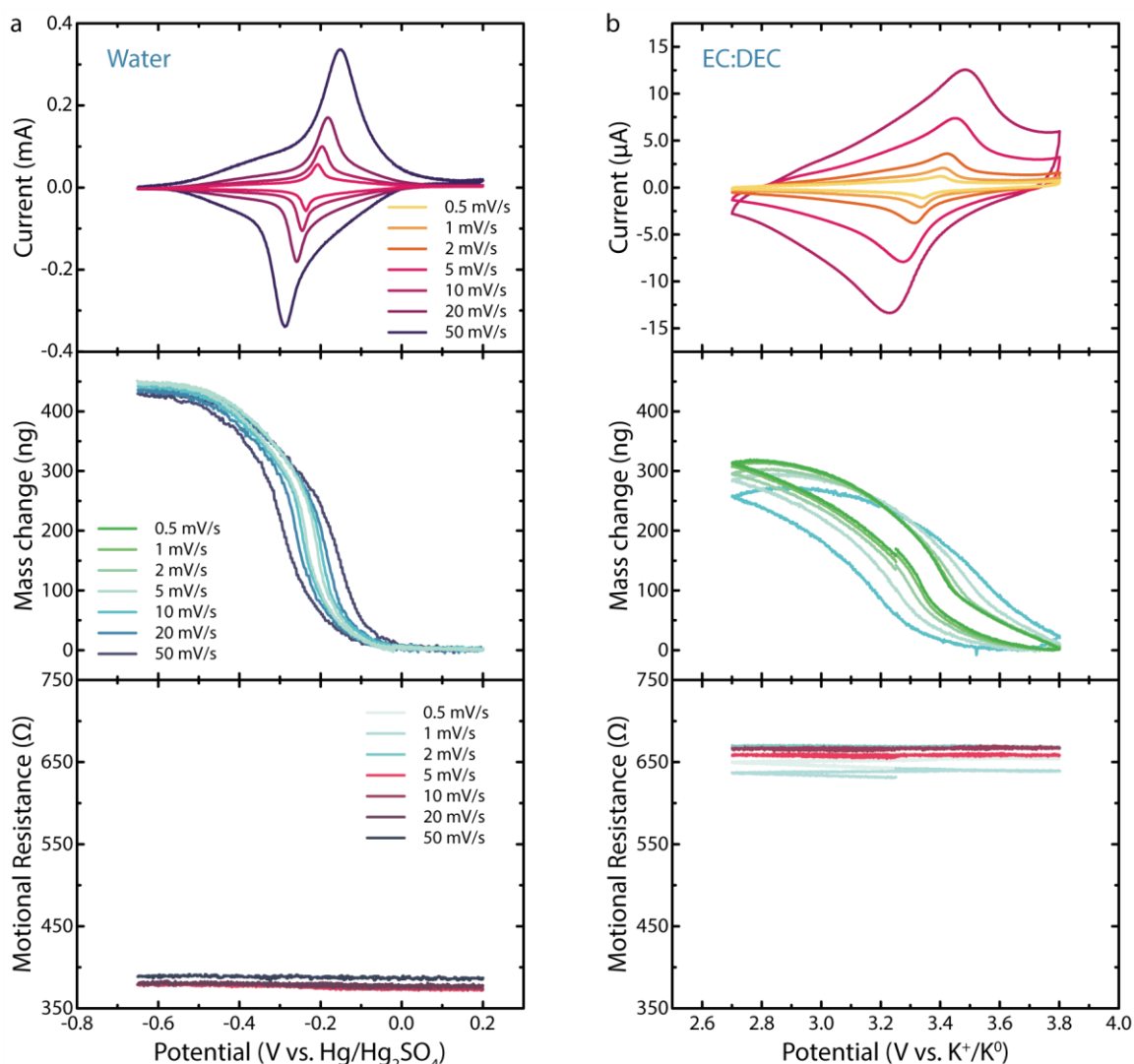


Figure IV-7: Cyclic voltammetry of a 100 nm thick PB film at different scan rates, in (a) 0.25 mol.L⁻¹ K₂SO₄ in H₂O (pH 3.5) and (b) 0.5 mol.L⁻¹ KPF₆ in EC:DEC. Current, frequency change and absolute motional resistance were simultaneously measured. The frequency change was converted into mass change, using Sauerbrey equation. The fifth cycle is here represented for each scan rate.

The motional resistance (Figure IV-7, third row) increases from aqueous to non-aqueous electrolyte, which is easily explainable by the Kanazawa and Gordon equation (Equation II-4) and the increase of liquid viscosity and density (Table I-2). In addition, R shows no variation in both electrolytes during CV regardless of the scan rates. The steadiness of the motional resistance monitoring proves the rigidity retention¹⁸⁸ during the potassium insertion/extraction and therefore the purely gravimetric regime ($|\Delta W| \ll |\Delta f|$). It is noted that for the present binder-free inorganic coatings, EQCM-R is perfectly suitable to evaluate the gravimetric regime.

Classical electrochemical response (Figure IV-7, first row) of PB was observed in both organic and aqueous electrolytes with redox peaks centered on 3.4 V vs. K^+/K^0 . Aqueous electrolyte presents sharper peaks than organic electrolyte even if it has been performed at faster scan rates. Moreover, non-aqueous electrolyte shows a larger hysteresis between oxidation and reduction peaks. Altogether, these features evidence the lower rate capability of the PB phase in non-aqueous electrolyte. To quantify the difference in the rate capability, the charge passing through the system during reduction was measured for the various scan rate in both electrolytes (Figure IV-8). A great difference in discharge capacity is observed between the two electrolytes even if the scan rate range is one lower of magnitude lower for the non-aqueous electrolyte.

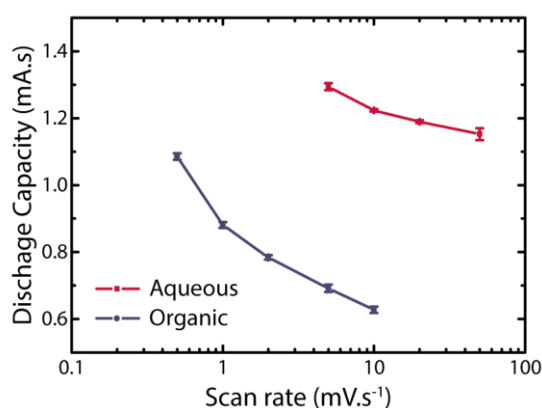


Figure IV-8: Rate capability assessment of the 100 nm thick PB film in aqueous ($0.25 \text{ mol.L}^{-1} \text{ K}_2\text{SO}_4$ in H_2O (pH 3.5)) and non-aqueous electrolyte ($0.5 \text{ mol.L}^{-1} \text{ KPF}_6$ in EC:DEC) by mean of the discharge capacity.

The similarity of the results with the LFP phase proves that changing the alkali metal ion does not affect the rate capability trend found between aqueous and non-aqueous electrolytes. The mass response of the electrodes (middle panels in the Figure IV-7) is also a mean to reveal the difference of rate capability. A more pronounced hysteresis is observed in organic electrolyte and it is confirmed further in the spreading of the mass change over a larger potential window. Lastly, the scan rate is increasing, almost no difference is visible in the total mass variation in water-based electrolyte at the opposite of the organic counterpart, further stressing the rate capability difference between both electrolytes.

IV.3.b –Determination of the rate-limiting step

The EQCM analyses in the previous section clearly demonstrated a difference in rate capability due to a change in the electrolyte solvent (H₂O to EC:DEC), but a remaining question regards the origin of such a difference. As mentioned in the Chapter I (see I.2.b), the insertion mechanism can be broken down into various steps: i. diffusion of the solvated cation from the bulk of the electrolyte to the electrode interface, ii. the desolvation of the cation, iii. the insertion of the bare cation in the host material related to the charge transfer and iv. the diffusion of the cation in the bulk of the material.¹²⁷ These different steps are sketched in the Figure IV-9. To explain the difference of kinetics, the rate-limiting step needs to be identified.

Naively, this difference of behavior is explained in the literature by the dissimilarity in liquid ionic conductivity of the two types of electrolytes. These two ionic conductivities were experimentally measured for both aqueous and non-aqueous electrolytes and are equal to 42.8 mS.cm⁻¹ and 6.39 mS.cm⁻¹, respectively. A significant dissimilarity is found; however, using the Nernst-Einstein equation, the liquid ionic diffusion coefficient of potassium ion is in the same order of magnitude of 10⁻⁵ cm².s⁻¹ for both electrolytes. This diffusion coefficient is high compared to that in the bulk of the material, making the liquid diffusion unlikely to be the rate-limiting step.

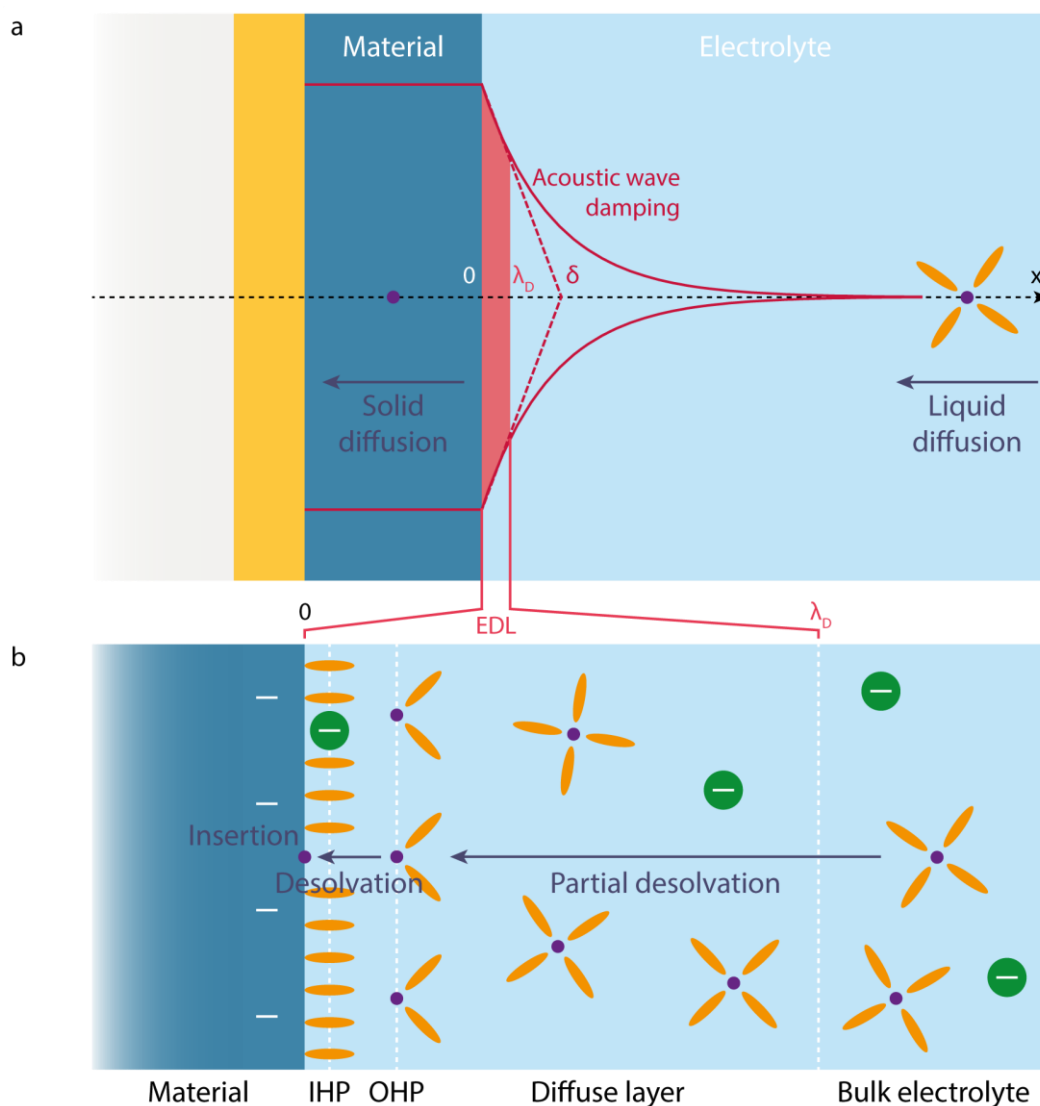


Figure IV-9: Schematic representation of the insertion of an alkali metal cation in a host material. (a) Comparison between the penetration depth of acoustic wave from the QCM to the solution (δ) and the electrochemical double layer characteristic length (λ_D). (b) Close-up snapshot of the electrochemical double layer during cation insertion.

As a next step, the K^+ diffusion coefficient in PB was scrutinized by two different electrochemical techniques. Firstly, PITT was used at different potentials during potassium insertion and extraction in both electrolytes, according to the protocol developed in Materials & Methods section. PITT analyses was applied to the PB films with different thicknesses; the results are gathered in the Figure IV-10. The first prominent result is the good agreement between the diffusion coefficient estimated during ion insertion and extraction, regardless of the film thickness and the electrolyte. Moreover, the solid diffusion coefficient is logically independent of the film thickness. Finally, the absolute value of the diffusion coefficient is also equivalent ($\approx 10^{-12} \text{ cm}^2 \cdot \text{s}^{-1}$) in water-based and EC:DEC-based electrolytes. As expected, the

solid diffusion coefficient of potassium ion is several orders of magnitude smaller than the liquid ionic diffusion coefficient.

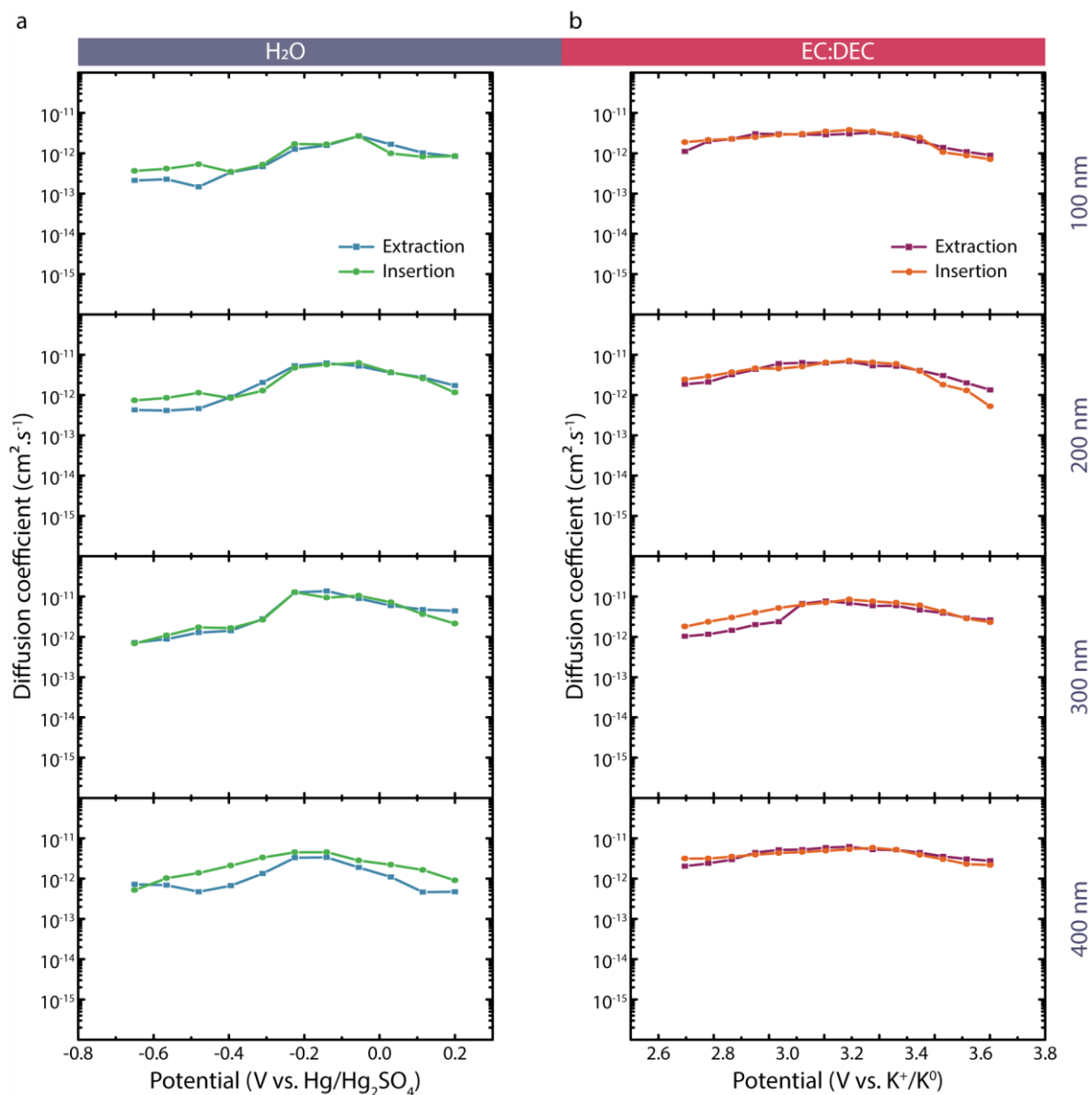


Figure IV-10: Solid diffusion coefficient determination of potassium ion in the bulk of the PB phase for different thicknesses in (a) water-based and (b) EC:DEC-based electrolytes.

For the sake of comparison, the solid diffusion coefficient of potassium ion was also estimated by using the Randles-Sevcik equation and the CV responses, performed earlier for rate capability assessment (Figure IV-7, upper panels). The Figure IV-11c gathers the results obtained for insertion and extraction peaks, for the different film thicknesses in the two electrolytes.

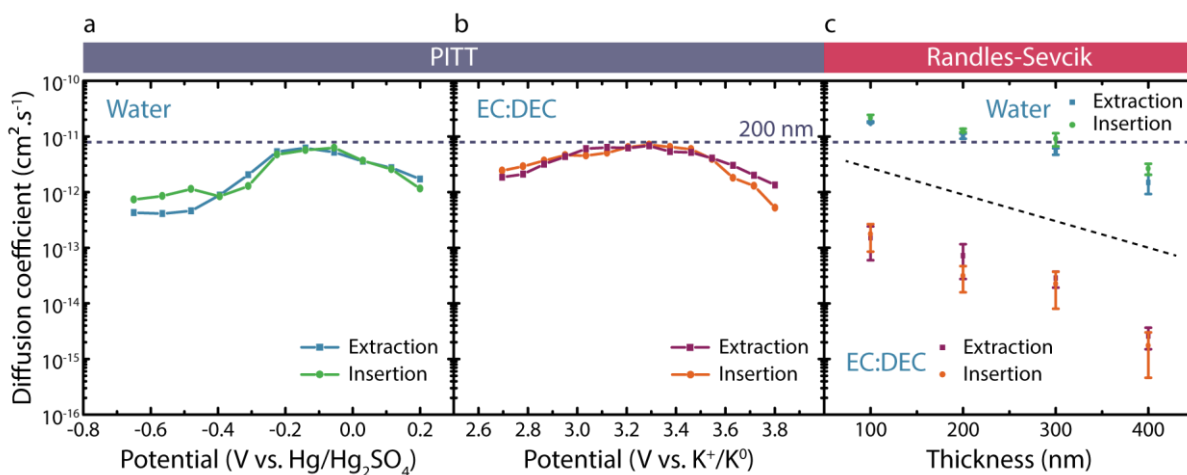


Figure IV-11: Comparison of the solid diffusion coefficient of potassium ion in PB films, obtained (a,b) by PITT and (c) by the Randles-Sevcik equation. For the PITT results obtained at different film thicknesses refer to Figure IV-10.

As for PITT results, no difference is detected between insertion and extraction process and the absolute values of diffusion coefficient are very close from one thickness to another. However, a massive dissimilarity is present between aqueous and non-aqueous electrolytes, when the solid diffusion coefficient is estimated by the Randles-Sevcik equation (Figure IV-11c). Two orders of magnitude separates the two electrolytes. The results obtained by the Randles-Sevcik equation were compared with the previous PITT results for the 200 nm thick film in the Figure IV-11. A good agreement exists between the results in water-based electrolyte by the Randles-Sevcik equation and the PITT measurements in both electrolytes. This equality demonstrates that the solid diffusion is not the rate-limiting step. As the Randles-Sevcik is a dynamic technique by nature, compare to PITT, which is performed at equilibrium. Therefore, another phenomenon needs to be considered to account for the measured disparity. Regarding the two remaining steps, *i.e.* desolvation and charge transfer, it can be supposed that the charge transfer only depends on the material, which has been kept constant during this study. Then, the desolvation taking place at the particular EEI can be hypothesized as the prominent step, affecting the battery performance by impeding the insertion kinetics.

IV.3.c – First evidence of the potassium solvation shell at the interface

The desolvation process taking place at the interface can be probed by *operando* EQCM analyses, therefore the mass per electron, $F\Delta m/\Delta Q$ value (Equation II-7), was calculated for

both electrolytes. The results are plotted in the Figure IV-12. The experimental value are compared with the molar mass of a bare potassium ions, to some extent, in the same manner as it was performed in the Figure III-19, where the experimental mass change was compared to the theoretical one due to the sole lithium ions insertion. Similar results between insertion and extraction are found in both electrolytes. However, the trends are totally different when electrolytes are compared. In aqueous electrolyte, the $F\Delta m/\Delta Q$ peaks around the insertion/extraction redox potential of potassium insertion into the Prussian Blue phase. Whereas, in the organic counterpart, this value remains steady on a larger potential window, with an absolute value very close to the bare K^+ . On the other hand, a more complex response is observed for the aqueous case, exhibiting a molar mass higher than K^+ , which is a first hint towards the participation of water molecules into the insertion mechanism. Such a mass difference corresponds to a nearly 90 Hz difference between theoretical and experimental frequency changes. It can be noted that the lower values on the extremities of the potential window may indicate the presence of H_3O^+ or H^+ into the charge compensation process, as already reported.^{184,186}

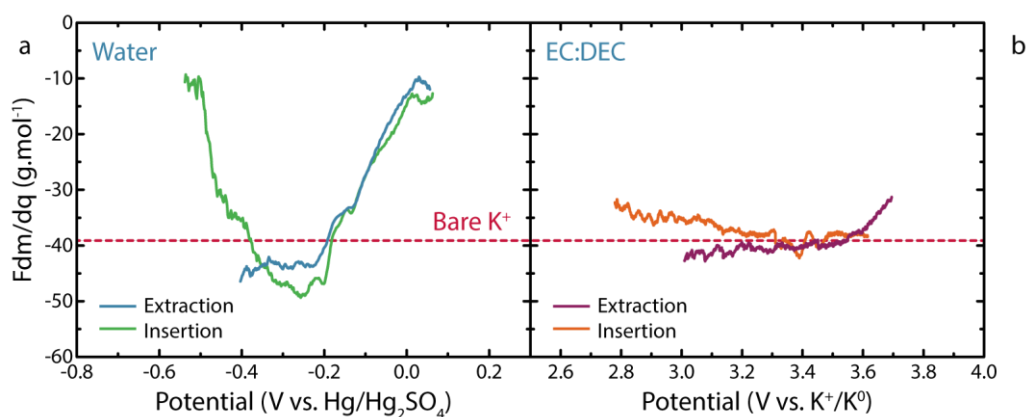


Figure IV-12: $F\Delta m/\Delta Q$ value calculated for a 100 nm thick film (a) in 0.25 mol.L⁻¹ K₂SO₄ (pH 3.5) water-based electrolyte during a CV at 10 mV.s⁻¹ and (b) in 0.5 mol.L⁻¹ KPF₆ EC:DEC-based electrolyte during a CV at 0.5 mV.s⁻¹. The corresponding EQCM data are presented in Figure IV-7.

As schematically pictured in the Figure IV-9a, the desolvation process occurs in the particular electrochemical double layer (EDL) region, which is at the close vicinity of the polarized material. To demonstrate the participation of this process in the QCM measurements, the hydrodynamic layer formed at the surface of the vibrating resonator needs to be compared with the charged interface. The Chapter II introduced the penetration depth, δ , as the characteristic dimension of the moving liquid layer, as represented in the

Figure IV-9a. The δ values are here equal to 189 and 225 nm in water and EC:DEC, respectively (with $\rho_l = 1145 \text{ kg.m}^{-3}$ and $\eta_l = 1.64 \cdot 10^{-3} \text{ Pa.s}$ for the EC:DEC mixture, according to Wang *et al.*²⁰⁶) (for 9 MHz resonators used in this study). The characteristic dimension of the EDL is the Debye length, λ_D , can be obtained thanks to the following equation:

$$\lambda_D = \sqrt{\frac{\varepsilon_0 \varepsilon_R k_B T}{2 \cdot 10^3 N_A e^2 I}} \quad \text{Equation IV-6}$$

where ε_0 is the vacuum permittivity ($8.84 \cdot 10^{-12} \text{ F.m}^{-1}$), ε_R is the relative permittivity (80.1 for water and 40.6 for the EC:DEC mixture²⁰⁷), k_B is the Boltzmann constant ($1.38 \cdot 10^{-23} \text{ J.K}^{-1}$), T is the temperature (K), N_A is the Avogadro constant ($6.02 \cdot 10^{23} \text{ mol}^{-1}$), e is the elementary charge ($1.60 \cdot 10^{-19} \text{ C}$) and I is the electrolyte ionic strength defined as:

$$I = \frac{1}{2} \sum_i z_i^2 C_i \quad \text{Equation IV-7}$$

where z_i is the charge number of ion and C_i is its molar concentration.

A value of 0.355 nm was calculated for the K_2SO_4 0.25 mol.L⁻¹ aqueous electrolyte while 0.309 nm was found for KPF_6 0.5 mol.L⁻¹ EC:DEC-based electrolyte. These values are significantly smaller than the respective penetration depths (189 and 225 nm). To fully relate these two variables, the velocity of the moving layer needs to be assessed at the extremity of the EDL. As depicted in the Figure IV-9a, the velocity of the damped acoustic wave follows an exponential decay parallel to the surface normal, as:

$$v(x) = v_0 \exp(-x/\delta) \quad \text{Equation IV-8}$$

For both electrolytes, the $v(\lambda_D)/v_0$ ratio gives rise to the value of 0.998, meaning that any ions present in the EDL region are moving in phase with the solid surface, even though they are not rigidly attached to it.¹⁹⁶ Therefore, according to the aforementioned analytical treatment, the ions fluxes and especially the desolvation process occurring in the close vicinity of the EDL contribute to the frequency change, are detected and quantifiable. As mentioned in the previous chapter, Tsionsky and co-workers proposed the formation of a “viscous layer” in the EDL region on a flat surface.^{196,208} The accumulation of cations in this region due to the negative polarization causes an increase in the local viscosity, which can contribute to the

frequency change. Their interpretation originates from the observation of a frequency shift of -5 Hz with a 6 MHz quartz resonator, corresponding to -11.3 Hz with the 9 MHz quartz resonators used in this study. Therefore, this contribution is negligible in the case of PB film with a relatively flat surface, especially when the difference between the experimental and theoretical frequency changes are around 90 Hz for the aqueous electrolyte and matching for non-aqueous ones. Moreover, no energy, *i.e.* no motional resistance change, is dissipated due to viscoelastic changes during the potassium insertion/extraction in our PB electrode (Figure IV-7, lower panels). These results combined, demonstrate that the desolvation process taking place at the interface is at the origin of the difference between theoretical and experimental frequency shifts.

Shortly, the analyses of the operando electrogravimetry results have indicated the absence of organic solvent molecules in the environment the potassium ions, whereas they are still partially hydrated (0.66 water molecules per K^+ obtained from the Figure IV-12a) at the electrode-electrolyte interface and particularly in the EDL region. Note that water co-insertion was discarded in our explanatory, since there is no difference detected in potassium ions' solid diffusion coefficient between aqueous and non-aqueous electrolytes.

IV.4 – Final evidence of the involved species at the EEI and their associated interfacial kinetics

IV.4.a – Identification of the nature of species and their dynamics at EEI

At this stage, pairing EQCM with EIS measurement (the so-called *ac*-electrogravimetry) was used to deconvolute the complex insertion processes at the EEI by identifying the species by their molar mass, together with the respective kinetics of interfacial transfer. Alike typical EIS measurements, a suitable model for each system needs to be developed to extract parameters related to the interfacial transfer and the desolvation process. The fitting methodology of the *ac*-electrogravimetry measurements has been previously described in the Chapter II (see II.4.c).

Ac-electrogravimetry was employed for the electrode-electrolyte interface analysis of PB film as shown schematically in the Figure II-9. The measurements were carried out at

various stationary potentials in the same potential range used for the EQCM measurements (Figure IV-7), both in aqueous and non-aqueous electrolytes. The *ac*-electrogravimetry results obtained at -0.25 V vs. Hg/Hg₂SO₄ and 3.2 V vs. K⁺/K⁰ are shown in the Figure IV-13a,c and b,d, respectively.

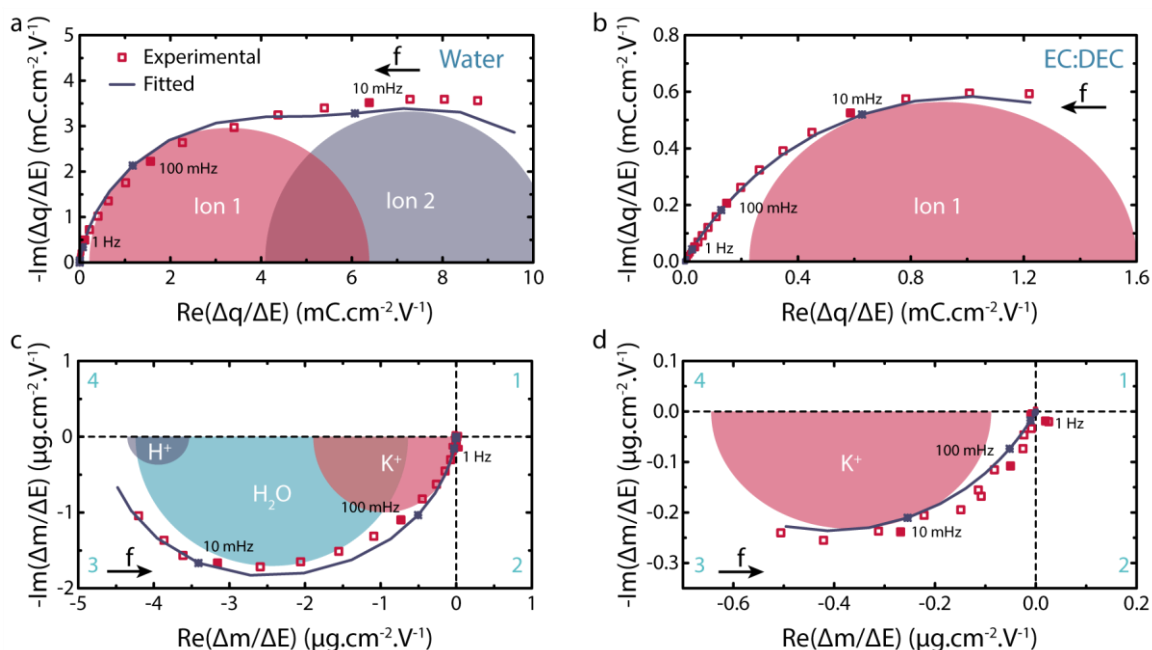


Figure IV-13: *Ac*-electrogravimetry analyses of 100 nm thick Prussian Blue films in (a,c) water and (b,d) ED:DEC-based electrolytes. (a,b) Charge/potential $\Delta q/\Delta E(\omega)$ and (b,d) mass/potential $\Delta m/\Delta E(\omega)$ transfer functions at -0.25 V vs. Hg/Hg₂SO₄ for aqueous electrolyte and at 3.2 V vs. K⁺/K⁰ for non-aqueous electrolyte, both experimental and theoretical curves are given. The different loops, which are drawn to guide the eye based on the fitting parameters, are labelled with the involved species. The fitting parameters are gathered in Figure IV-14a,b.

The charge/potential transfer function (TF), $\Delta q/\Delta E(\omega)$, has been presented instead of classical impedance representation (*i.e.* potential/intensity, $\Delta E/\Delta I(\omega)$) where the following relation exists between the two: $\frac{\Delta E}{\Delta I}(\omega) = R_{el} + \frac{1}{j\omega(C_{dl} + \frac{\Delta q}{\Delta E}(\omega))}$ (with R_{el} : the electrolyte resistance and C_{dl} : the double layer capacitance). This representation is more convenient to decouple the contribution of charged species, as one loop corresponds to one charged species. For aqueous electrolyte, the collected spectrum of $\Delta q/\Delta E(\omega)$ at -0.25 V vs. Hg/Hg₂SO₄ shows two loops implying that two charged species (ion 1 and ion 2) are involved in the charge compensation process (Figure IV-13a). Then, to identify and clarify the contribution of the charged and also uncharged species (free electrolyte molecules), the experimental mass/potential transfer function $m/\Delta E(\omega)$, the second main TF of the

measurement is analyzed (Figure IV-13c). One big loop appears in the 3rd quadrant. As mentioned in the Chapter II, the loops in the 3rd quadrant are characteristic for cation contribution or free solvent molecules, transferred in the same flux direction as cations. The correlation of these two TFs indicates the contribution of, at least two distinct cations and possibly one solvent molecule in the same flux direction. Then, the experimental TFs were fitted with a model described in the Chapter II. Concerning experimental $\Delta q/\Delta E(\omega)$ TF, it was fitted with the theoretical equation given in Equation II-32, involving two cationic species. A good agreement is found between the experimental and theoretical curve in the Figure IV-13a, both in terms of shape and frequency distribution. The fitting parameters, K_i (kinetics of transfer) and G_i (related to interfacial transfer resistance) are obtained for the two cations. At this stage, it is not possible to identify these ionic contributions. To do so, the mass/potential transfer function $\Delta m/\Delta E(\omega)$ is fitted using theoretical equation given in Equation II-35. The K_i and G_i parameters previously estimated in the fitting of the $\Delta q/\Delta E(\omega)$ TF are used. Three cationic species were considered to fit the mass/potential TF: K^+ , H^+ and H_3O^+ . Two possible couples were investigated, keeping in common K^+ : K^+/H^+ and K^+/H_3O^+ . Both have been tested to fit the mass/potential TF but neither of them were satisfactory due to the impossibility to fit the massive negative loop with the combination between their molar mass and their estimated fitting parameters K_i and G_i . Water molecules were injected into the model permitting a better agreement between the fitting and the experimental mass/potential TF. The different permutations of the listed species were considered and the various partial mass/potential TFs (Equation II-37, a cross-check procedure of the fitting) were tested. In the end, only the model enlisting K^+ , H_2O and H^+ at high, medium and low frequency, respectively, resulted in a satisfactory fitting, in terms of shape and frequencies.

Concerning the *ac*-electrogravimetry in the non-aqueous medium, the same fitting protocol was performed. The collected spectrum of $\Delta q/\Delta E(\omega)$ at 3.2 V vs. K^+/K^0 , represented in the Figure IV-13b, shows only loop implying that only one ion (ion 1) is involved in the interfacial process. One loop is also present in the 3rd quadrant of the mass/potential TF, demonstrating the participation of one cation or free solvent molecules in the same flux direction as the cation. Despite the measurement down to the LF range of about 1 mHz, the loops are not closed and do not form a complete semi-circle due to the instrumental and time limitations (2-3 h for each potential), demonstrating the slow kinetics of the interfacial ionic

transfer. A model using one cation was employed to fit the experimental spectrum of charge/potential TF and obtain the kinetic parameters, K_i and G_i . A good agreement was obtained between the experimental and fitted curves in the Figure IV-13b. These parameters were kept constant and potassium ions were assumed to be the sole involved species. In these terms, the experimental and theoretical mass/potential TFs match well without the addition of an additional contribution of an uncharged species (Figure IV-13d).

Thus, *ac*-electrogravimetry has demonstrated the contribution of the sole contribution of potassium ions in the non-aqueous electrolyte. As for the aqueous electrolyte, the water molecules and as well as protons are involved in the insertion mechanism of the potassium ions, at the EEI of the Prussian Blue phase. These results are in a good agreement with classical EQCM measurements (Figure IV-7 and Figure IV-12).

IV.4.b – Study of the interfacial kinetics associated to the involved species

A similar fitting procedure described for the -0.25 V vs. Hg/Hg₂SO₄ and 3.2 V vs. K⁺/K⁰ was carried out for all the other measurements performed in the potential range of both electrolytes. The results of the fitting procedure provided the K_i (kinetics of transfer), G_i (related to interfacial transfer resistance by $Rt_i = \frac{1}{FG_i}$) and M_i parameter (molar mass, thus identification of the species). Although in different quantity and kinetics of transfer, the contribution of the different involved species determined in the previous section (K⁺, H⁺ and H₂O) is found to be persistent at all the potentials studied. The obtained values are shown in the Figure IV-14a,b.

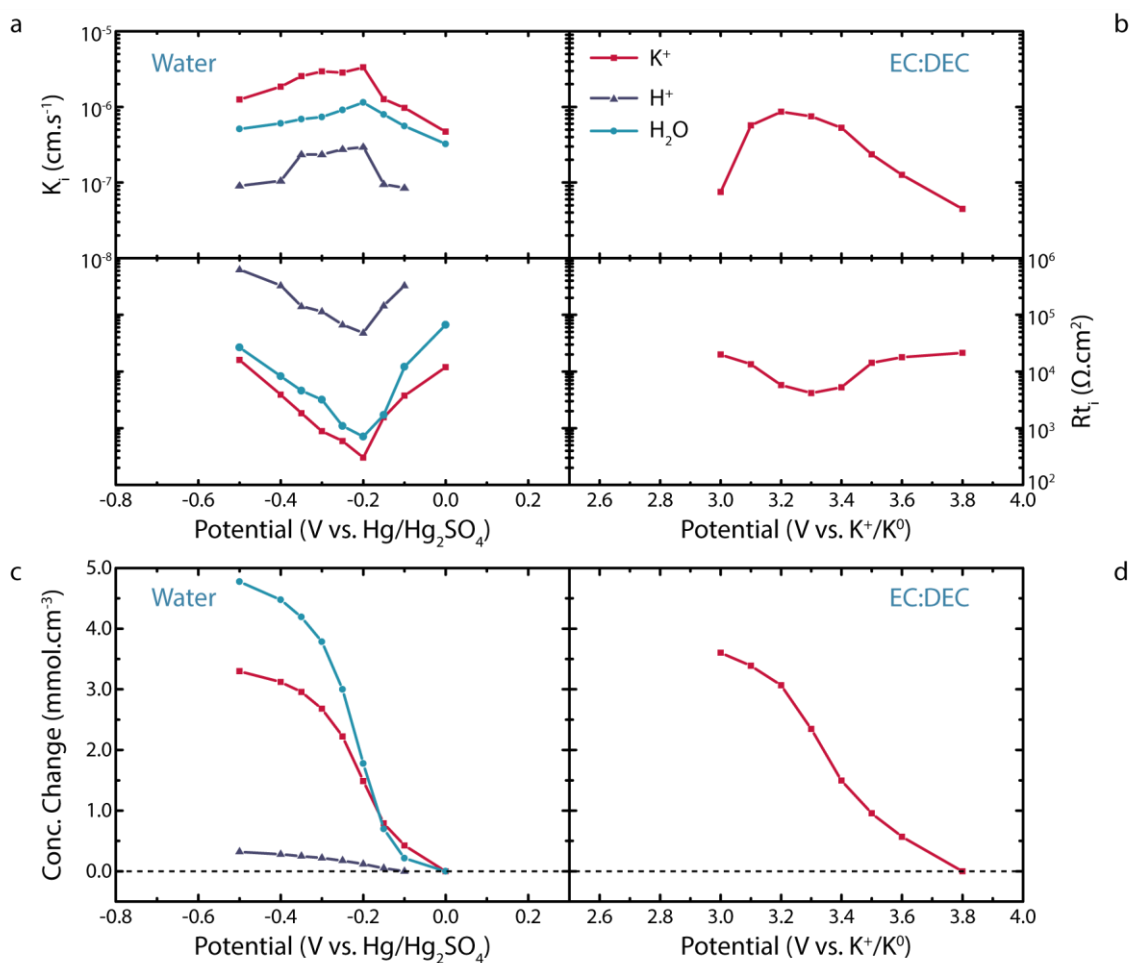


Figure IV-14: Outcomes of *ac*-electrogravimetry analyses of 100 nm thick Prussian Blue films in (a,c) water and (b,d) ED:DEC-based electrolytes. (a,b) Evolution of kinetic parameters, K_i , and interfacial transfer resistances, Rt_i , and (c,d) relative concentration variation of each species, represented as a function of the potential. As water molecules are not incorporated into the material, the water concentration is only estimated and has no physical meaning.

The *ac*-electrogravimetry analysis performed in water-based electrolyte shows that the interfacial kinetic of transfer, K_i , of the involved species is ranked as follows: $K^+ > H_2O > H^+$, independently of the potential. Their kinetics of transfer are quite steady over the potential window with a peak centered around the insertion/extraction redox potential and the water kinetics seem to follow potassium ions in terms of shape and values. Regarding the interfacial transfer resistance, Rt_i , a V-shaped response is found for each species. The minimum value of their resistance is yet again centered on the redox potential, in perfect agreement with the sharp and well-defined mass change response observed by EQCM in the Figure IV-7a middle panel. It can also be noted that the Rt_i values are 2-3 orders of magnitude higher in the case of H⁺ compared to the two other species, demonstrating the difficulty of protons to be inserted into the PB structure. Concerning the non-aqueous electrolyte and the

kinetic of potassium ions (Figure IV-14b), the peak shape is more pronounced and still centered on the redox potential. The lower K^+ kinetic of transfer values in non-aqueous electrolyte compared to aqueous counterpart explains the difference in rate capability. Moreover, the Rt_i as a function of potential shows a V-shape, but significantly broader in comparison to that obtained in aqueous electrolyte. This observation also explains the reason behind the more spread-out mass change over a larger potential window in the EQCM analyses (Figure IV-7b, middle panel).

The relative concentration variation of the three different species has been calculated from the *ac*-electrogravimetry analyses (Equation II-38) and are represented in the Figure IV-14a,b. Firstly, in aqueous electrolyte, the concentration of H^+ intervening in the insertion mechanism is highly negligible in comparison with K^+ or H_2O contribution. The K^+ concentration variation is similar in both media with a sharper variation in aqueous electrolyte. The shape of the water contribution is following that of potassium ions with a higher concentration variation. The concentration ratio between water and potassium ions is equal to 1.4, which is higher than 0.6 water molecule per potassium ions evidenced in with $F\Delta m/\Delta Q$ measurement from CV at $10\text{ mV}\cdot\text{s}^{-1}$ (Figure IV-12a). This discrepancy is most likely due to the way of measurement; *ac*-electrogravimetry provides a snapshot of the interface at quasi-equilibrium at the opposite of the CV (depending on the studied scan rate).

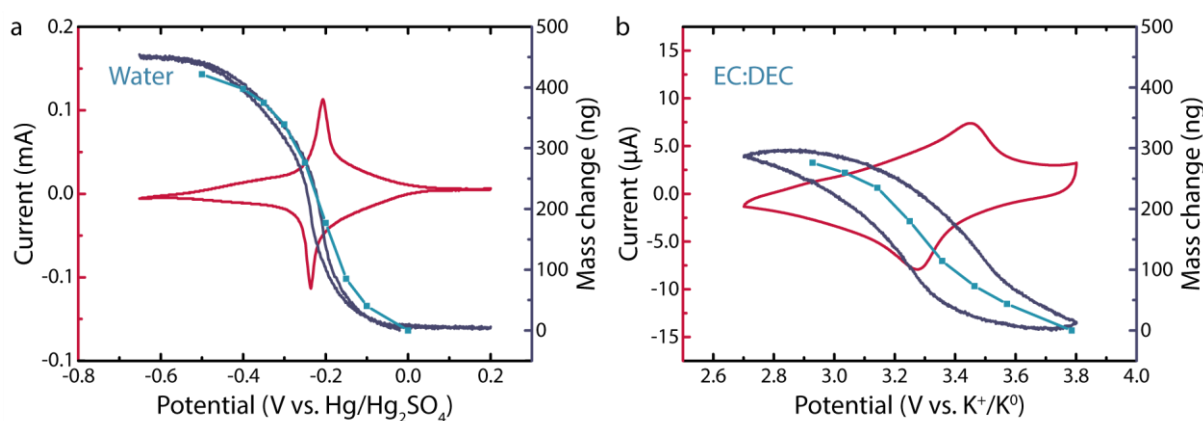


Figure IV-15: Comparison of the mass variation by classical EQCM measurement at $5\text{ mV}\cdot\text{s}^{-1}$ with recalculated mass variation by *ac*-electrogravimetry in (a) water and (b) ED:DEC-based electrolytes.

Finally, in order to confirm the good exploitation of the *ac*-electrogravimetry fitting procedure, the global mass variation was recalculated from the concentration change of the different species involved and compared with the results obtained by EQCM in the Figure IV-7,

middle panel. Such comparisons are plotted in the Figure IV-15. These results nicely compare, hence validating the employed models and the described *ac*-electrogravimetry analyses.

IV.5 – Chapter conclusions

Throughout the Chapter III, the metal-ion insertion mechanism at the EEI of a Li-ion host was intensively investigated, leading to significant contributions towards understanding the solvent-assisted insertion mechanism and the prominence of the solvation shell on the rate capability. To strengthen these findings and explore their applicability to other metal-ions, here K-ion chemistry is scrutinized which also simplified the system (compared to Li-ion chemistry), since it features a smaller and weaker solvation shell. The EEI mechanism was characterized *via* advanced electrochemical and electrogravimetric techniques, including *ac*-electrogravimetry, extending the capacity of the EQCM analyses to study interfacial dynamics. Firstly, the electrodeposited model material – Prussian Blue – was characterized from a morphological and structural point of view to verify the formation of the desired K-ion host. PB films with a thickness between 100 and 300 nm were confirmed to be ideal in terms of surface properties (flatness, free of major surface roughness) and the motional resistance was verified prior conducting electrogravimetric analyses. This step is strongly recommended and crucial for the correct interpretation of the microbalance responses.

K⁺ insertion in Prussian Blue phase was demonstrated to follow the same rate capability discrepancy between aqueous and non-aqueous electrolytes, as is the case for Li-ion chemistry shown for LFP. This difference is unambiguously confirmed thanks to the direct visualization of the potassium insertion by *operando* EQCM and the decrease of the total mass uptake with increasing scan rate for the organic electrolyte. To identify the origin of this discrepancy, in-depth electrochemical analyses were performed to highlight the rate-limiting step in the insertion mechanism. PITT and Randles-Sevcik type analysis of CV responses were both employed to study the solid diffusion coefficient of potassium ion in the PB phase. They have shown that the potassium solid diffusion cannot be the limiting step either, and reveal a fast and unaltered charge transfer that do not affect the overall kinetics, hence calling for another explanation. Therefore, the desolvation process occurring in the electrode-electrolyte

interface and especially in the electrochemical double layer region was hypothesized to be the reason behind the kinetic discrepancy between aqueous and non-aqueous electrolyte.

Electrogravimetric measurements demonstrated the presence of an additional frequency change compared to the theoretical mass uptake due to the sole potassium insertion ($F\Delta m/\Delta Q > M_{K^+}$). Among the possibilities to account for such an observation are the contribution of a “viscous layer”, the viscoelastic change of the PB film upon cycling and the water co-insertion. According to the literature, the contribution of the former is negligible (about 10 Hz, less than the additional frequency observed in our experiments). The motional resistance monitoring upon cycling by EQCM-R confirmed the absence of any viscoelastic change during K^+ insertion in PB thin films. For the latter, regarding of water co-insertion, it was equally discarded since the solid diffusion coefficient was not affected when switching from organic to aqueous electrolyte. Simple calculations proved the possible assessment of the ionic flux happening in the double layer region by EQCM measurements. Thus, the extra mass uptake demonstrated the participation of the solvent molecules during the cation insertion at the electrode-electrolyte interface. As a complementary method, *ac*-electrogravimetry analyses strengthened these result by confirming the presence of water molecules with close kinetics to the inserting potassium cation, most likely in the electrochemical double layer region. The passing through a transition step, between solvated cation in the bulk and a bare cation in the material, where the cation is partially solvated at the interface was firstly introduced by Bruce and Saidi¹³³ and paved the way to new modelling of the interface.^{209,210} However, in contrast to Li-ion chemistry, no organic molecules were found in the close proximity of the potassium ion before its insertion. In addition, the difference in rate capability was confirmed by the *ac*-electrogravimetry kinetic study.

Finally, studies on Li-ion (LFP) and K-ion (PB) chemistries demonstrated that in non-aqueous electrolytes, when using heavier alkali metals, the number of solvent molecules participating in the partial solvation shell at the interface decreases. However, the desolvation energy in the bulk of the electrolyte decreases when moving from lithium to potassium ions, explaining the better rate capability. In contrast, the water-based electrolytes do not follow this trend, since the desolvation energy is always higher in aqueous electrolyte and yet exhibit better power performance. A partially hydrated cation (close transfer kinetics between the cation and solvent molecules) is always found in the electrochemical double layer region.

These results are defying common belief and need to be corroborated by Molecular Dynamics calculations to fully support our proposed insertion mechanism happening at the electrode-electrolyte interface, simulations are underway. Recently, Li *et al.* proposed a possible explanation with the formation of a layer of water molecules in the inner Helmholtz plane (IHP) enhancing the surface diffusion of the cation to an insertion site.²¹¹ This phenomenon was demonstrated in non-aqueous electrolyte where water was used as an additive for Mg²⁺ insertion in WO₃.²¹² Another parameter, which can have its importance on the insertion process, is the anion nature and its concentration, as they are specifically adsorbed in the IHP (Figure IV-9b).²¹³

Through investigation of two distinct alkali metal-ion chemistries (Li-ion and K-ion), the desolvation process occurring at the EEI is found to be the origin of the rate capability difference in aqueous and non-aqueous electrolytes. In continuity with the EEI analyses, the next chapter will be dedicated to the water molecules role in the interfacial transfer process and their influence on the overall kinetics, this time in a proton-based battery (pseudo-alkali metal).

Chapter V – Elucidating the origin of the electrochemical capacity in proton-based battery: a framework to assess the water contribution at the interface

V.1 – Introduction

Aside from energy density, sustainability is another overriding figure of merit driving the development of new battery technologies. In this regard, the need for greener batteries has become a pressing concern and boosted the research for new chemistries such as the emerging K-ion technology, presented earlier, which stand as an environment-friendly alternative to Li for the grid. Within this context, considerable attention is currently given to aqueous systems which offer advantages compared to nonaqueous counterparts, in terms of: safety, cost, ionic conductivity or processibility.²¹⁴ Recently, a tremendous attention has been given to promising aqueous Zn-based battery systems (*i.e.* Zn-air, Zn-Ni and Zn-MnO₂) as well those employing TiO₂ as electrode materials. For the latter, some studies have demonstrated the intercalation of aluminum²¹⁵ or lithium²¹⁶ cations. However, more interesting and counterintuitive results have been found and proven the preferential intercalation of protons even in mild acidic conditions.²¹⁷ Kim *et al.* managed to quantitatively deconvolute the contributions of the electrical double-layer capacitive charge storage and the reversible faradaic reactions which provided a confirmation of the faster proton intercalation compared to that of lithium. The proton insertion has also been mentioned for the Zn/MnO₂ system, described in the Chapter I.⁷⁷ Despite the widespread fresh literature on the subject, the mechanism taking place at the electrode-electrolyte interface (EEI) and particularly the water participation, is still not elucidated.

In order to better understand the science behind the EEI of proton-based batteries, the new protonic phase H_xIrO₄ discovered by our group²¹⁸ has been selected as a model compound. The reasons for this choice are twofold. Firstly, it presents less complex redox chemistry because of a sole redox center, which is Ir. Secondly, it offers a reasonable capacity of 175 mA.h.g⁻¹ *via* a reversible two-step redox process in concentrated acidic electrolyte. However, its total reactivity mechanism based on pseudocapacitance has not yet been fully unrevealed, partially due to the lack of suitable analytical tools. Moreover, pseudocapacitive

materials are the perfect playground to study the phenomena taking place at the interface as they are kinetically governing the electrochemical process.

To convey such study, this chapter will be structured as follows. After the characterization of the pristine H_xIrO_4 phase, in-depth electrochemical and XAS investigation was performed to determine the faradaic mechanism taking place into this pseudocapacitive materials, mechanisms are described earlier (see I.1.c). Then, classical EQCM coupled with XRD and TGA was employed to prove a potential-dependent two-step process where water molecules are involved in addition to protons. Lastly, *ac*-electrogravimetry, which is complementary to classical EQCM, was employed here to provide insights into the underlying science governing the EEI of this proton-based battery permitting the deconvolution of the contribution of each species (charged or uncharged) involved (in)directly in the charge storage mechanism.

V.2 – Phase characterization

V.2.a – Morphological and structural description

X-ray diffraction was first used to characterize the pristine material, namely H_xIrO_4 , obtained by acid leaching of the Li_3IrO_4 phase. The synthesis is precisely described in the Materials & Methods. Figure V-1a shows sharp Bragg peaks characteristic of a well-crystallized compound that we have indexed in a hexagonal $R\bar{3}m$ unit cell as the parent phase. The Figure V-1b depicts the structural model deduced from the refinement. Nevertheless, due to the small scattering factor of protons for X-rays, their structural positions within the structure have not been determined but solely speculated. The structural model shows a layered structure with an interlayer distance of 4.7 Å and having the hydroxyl group (see below) pointing towards the van der Waals layer as reported earlier.²¹⁸ The SEM image indicates well-defined particles with a particle size distribution in the range of 2 to 4 μm with a small specific surface area of 2.23 m².g⁻¹.

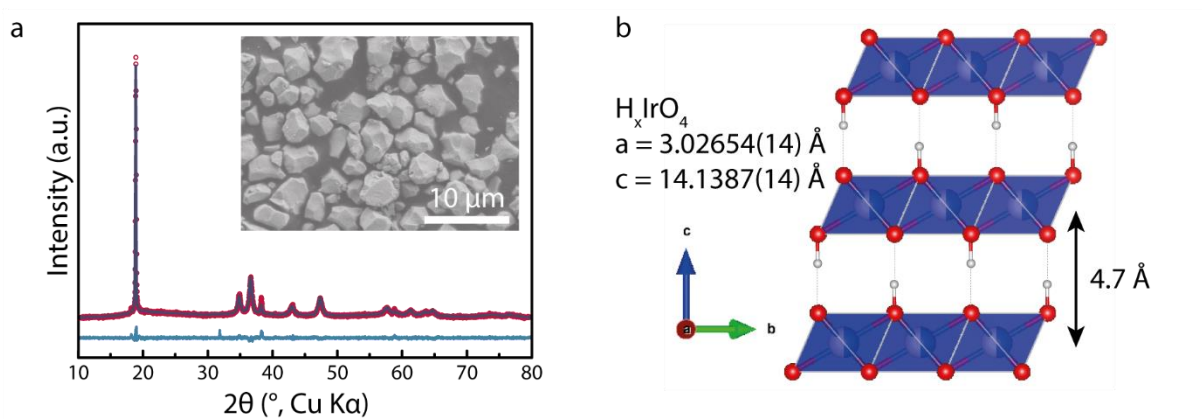
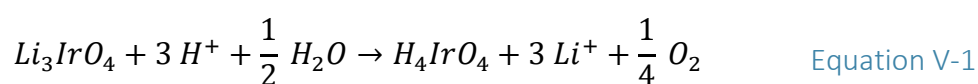


Figure V-1: (a) Rietveld refinement of XRD patterns of H_xIrO_4 . The red circles, dark blue continuous line, and bottom blue line represent the observed, calculated, and difference patterns, respectively. Inset: FEG-SEM image. (b) The corresponding structural model where the proton positions have been supposed.

V.2.b – Stoichiometry determination

X-ray absorption spectroscopy has been used to determine the Iridium oxidation state of the pristine phase. From the comparison of the WL energy with some selected references, we can conclude that the Ir oxidation state is +IV in the pristine material (Figure V-2a); therefore we propose the formula of H_4IrO_4 for the leached material supposing the absence of residual Li in the material. Consequently, the leaching process enlists both an ion exchange and a reduction process according to the reaction listed below.



The appearance of gas bubbles (O_2) released from the particles during the acid leaching is consistent with the chemical reaction. It is worth mentioning that this proton stoichiometry deviates from the original value found in our previous study²¹⁸ (3.4 hydrogen atoms). This is simply due to a modification of the acid leaching protocol moving from a concentration of 0.1 mol.L⁻¹ H_2SO_4 to 1 mol.L⁻¹, hence favoring H^+ uptake.

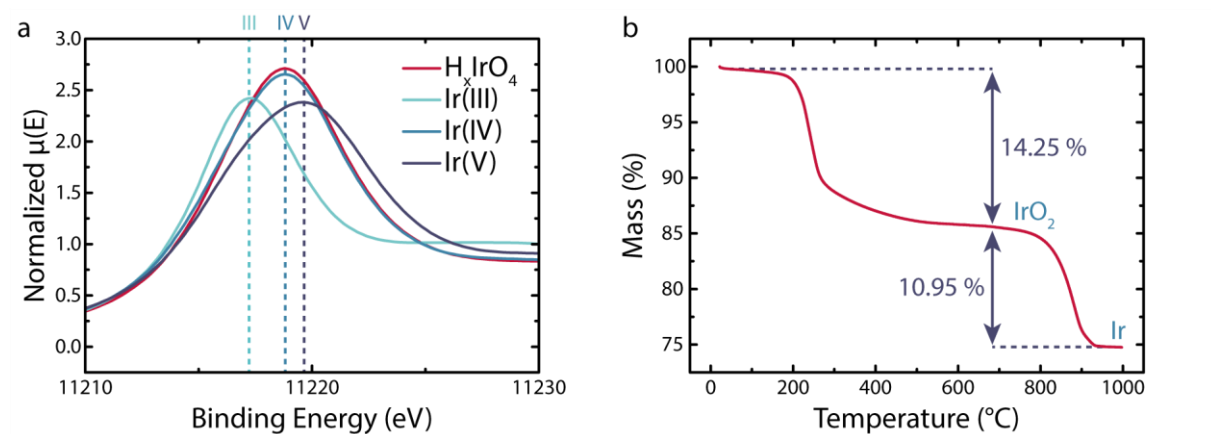
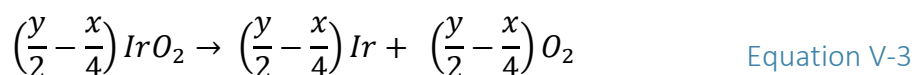
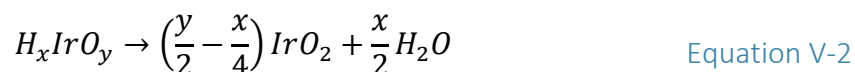


Figure V-2: (a) White Line energy position at the Ir L₃-edge of the pristine material and three reference samples. (b) TGA curve with the mass losses associated to each process.

Concerning the phase thermal stability, thermogravimetric analysis was performed and the profile of the collected TGA curve (Figure V-2b) displays two steps mass losses with onset temperature of 220 and 900 °C. The first one is ascribed to structural and not physisorbed water molecules, owing to its elevated removal temperature (220 °C). The second mass loss (≈ 900 °C) is in contrast attributed to the departure of O₂. XRD measurements (not shown) indicate the presence of IrO₂ and Ir on the samples retrieved from the TGA experiments stopped at 700 and 1000 °C, respectively. These results lead to propose the following decomposition pathway:



Altogether, from the quantification of the two mass losses and assuming formula of the pristine material to be H_xIrO_y, we obtained values of x = 4.0 and y = 3.9, leading to the stoichiometry of H_{4.0}IrO_{3.9}, in agreement with the formula deduced by XAS.

V.3 – Electrochemical analyses

V.3.a – Cycling behavior

This new layered protonic phase was further tested for its electrochemical performance in an acidic aqueous electrolyte (HClO₄ 0.5 mol.L⁻¹) using a three-electrode PFA

Swagelok cell. The self-standing electrodes of active material were tested either by cyclic voltammetry or in galvanostatic mode (galvanostatic cycling with potential limitation, GCPL). The Figure V-3a shows the variation of the potential as a function of x , the quantity of protons. Upon oxidation (charge) from the open circuit voltage (OCV) ($x = 4$), the material releases 1 H^+ (H_3IrO_4), while on the subsequent reduction (discharge) 1.75 H^+ are inserted ($\text{H}_{4.75}\text{IrO}_4$), which are totally reversibly deinserted during the following oxidation (H_3IrO_4). From simple charge counting this implies that the material evolves back and forth from $\text{H}_3\text{Ir}^{5+}\text{O}_4$ (charged) to $\text{H}_{4.75}\text{Ir}_{0.25}^{4+}\text{Ir}_{0.75}^{3+}\text{O}_4$ (discharged) leading to a reversible capacity of 175 mA.h.g^{-1} . Moreover, this electrode shows a high-energy efficiency (98.3 %) as indicated by the small polarization between charge and discharge (25 mV at 1C).

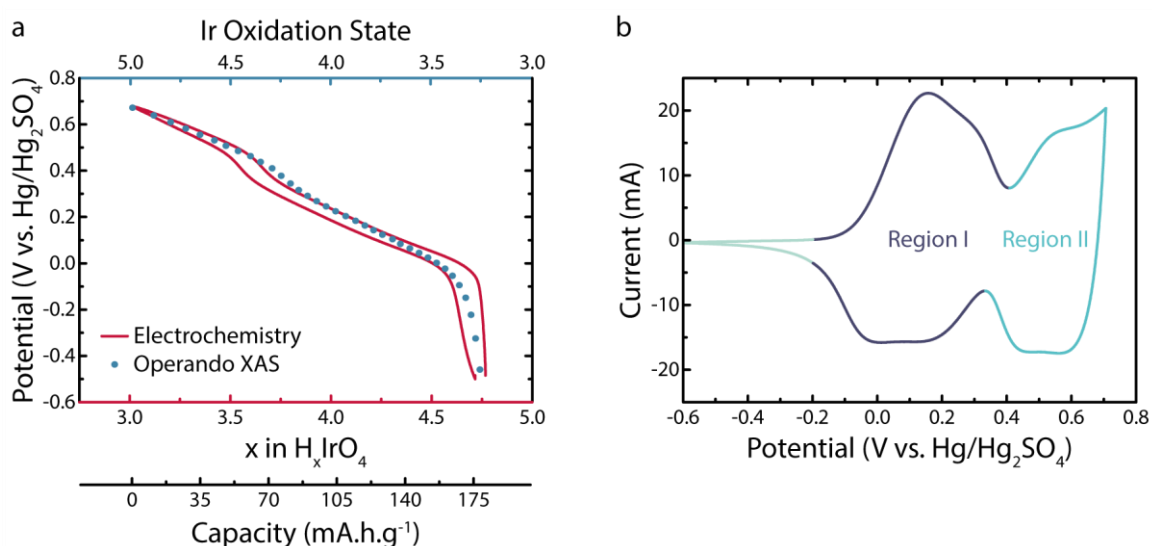


Figure V-3: Electrochemical properties of H_xIrO_4 in HClO_4 0.5 mol.L^{-1} . (a) Galvanostatic cycling at 1C as a function of the proton stoichiometry and the Iridium oxidation state (obtained during the discharge). (b) Cyclic voltammetry at a scan rate of 5 mV.s^{-1} .

Cyclic voltammetry experiments were also collected to characterize the protonic phase and two regions can be differentiated (Figure V-3b). The first one at low potentials (going from -0.2 to $0.39 \text{ V vs. Hg/Hg}_2\text{SO}_4$) and the second one at high potentials (0.39 to $0.7 \text{ V vs. Hg/Hg}_2\text{SO}_4$) will be referred hereafter as Region I and Region II, respectively. It is worth mentioning that pushing further the oxidation of the material is not limited by the proton deinsertion but rather restricted by the water splitting at $0.75 \text{ V vs. Hg/Hg}_2\text{SO}_4$.

V.3.b – Assessment of the pseudocapacitive mechanism

To get insights in the redox processes pertaining to the different regions and how they affect the iridium oxidation state, *operando* XAS measurements were carried out during the battery cycling at various stages of discharge and charge that is for different H^+ content. The first derivative of the XAS data along with the electrochemical curve is reported in the Figure V-4.

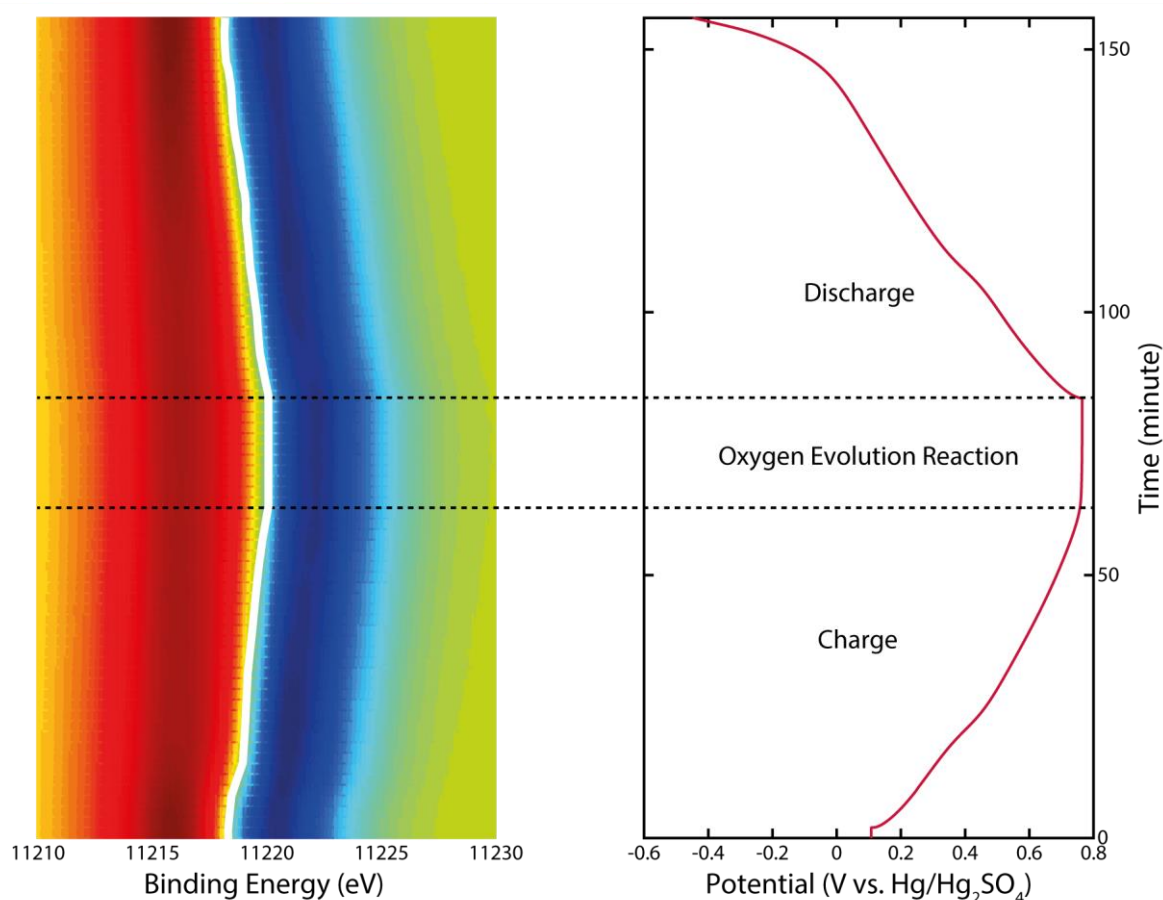


Figure V-4: Follow-up of the White Line energy (fingerprint of the Ir oxidation state) thanks to the derivative of the normalized absorption spectra as a function of the galvanostatic charge/discharge of the H_xIrO_4 phase in $HClO_4$ 0.5 mol.L^{-1} .

For meaningful comparison, we plotted the potential variation with respect to the Ir oxidation state and the H^+ content. The results (Figure V-3a) indicate a smooth and continuous decrease of the Ir oxidation state from 5 to 3.25 as the cell is discharged from 0.7 V ($x = 3$) to -0.5 V ($x = 4.75$). The equality between the total change of the iridium oxidation state (≈ 1.75), as deduced by XAS, and the amount of inserted H^+ (≈ 1.75) from electrochemical titration implies that the totality of the material present in each particle of the electrode is involved in

the charge storage mechanism as in $T - Nb_2O_5$ with lithium ions⁶⁶. In contrast, it differs from the typical pseudocapacitive $RuO_2 \cdot xH_2O$ where charge storage occurs mainly on the surface or near surface^{219–221}. This finding, together with the BET low surface area ($\approx 2 \text{ m}^2 \cdot \text{g}^{-1}$) highly questioned the core-shell mechanism previously proposed.²¹⁸

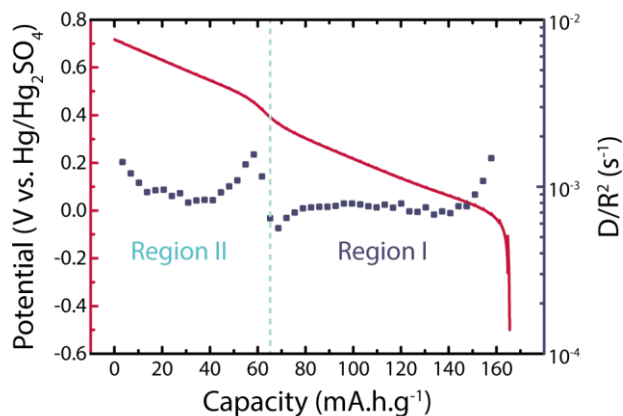


Figure V-5: GITT discharge curve of H_4IrO_4 with the estimation of the chemical diffusion coefficient of the involved species in the phase.

Besides, we electrochemically estimated the diffusion coefficient of involved species through this material by Galvanostatic Intermittent Titration Technique (Figure V-5) and the average particle radius was estimated by SEM. A value of $10^{-10} \text{ cm}^2 \cdot \text{s}^{-1}$ was found for region II that is much higher than $10^{-15} \text{ cm}^2 \cdot \text{s}^{-1}$ reported for Li^+ diffusion in LFP microparticles²²² but still slower than $10^{-5} \text{ cm}^2 \cdot \text{s}^{-1}$ for the proton diffusion in water. Interestingly, this proton diffusion in H_4IrO_4 is much higher than the value previously reported by Kim *et al.*²¹⁷ in amorphous TiO_2 ($10^{-15} \text{ cm}^2 \cdot \text{s}^{-1}$). On that basis, the high reversibility of the redox processes can therefore be explained by a transport process non-limited by diffusion. Interestingly, a higher diffusion coefficient was obtained through region II than in region I implying an easier diffusion of the involved species in the high potential region.

V.4 – Electrochemical-gravimetric investigation

V.4.a – Validation of the gravimetric regime

Advanced electrogravimetric analyses combining QCM with electrochemical methods of different type were performed to investigate the interfacial charge transfer properties in

H_xIrO_4 based electrodes. For these measurements, a thin layer containing 72 % of the active material was spray casted on the gold electrode of quartz resonators following the procedure described in the Chapter III and then electrochemically tested to ensure that its electrochemical signatures were entirely preserved. In order to ensure that the mechanical properties of the spray-coated electrodes were compatible with the EQCM measurements, the viscoelastic properties of the film and the particle-binder interaction were verified by EQCM with dissipation monitoring thanks to the protocol proposed in the Chapter II. The results are reported in the Figure V-6.

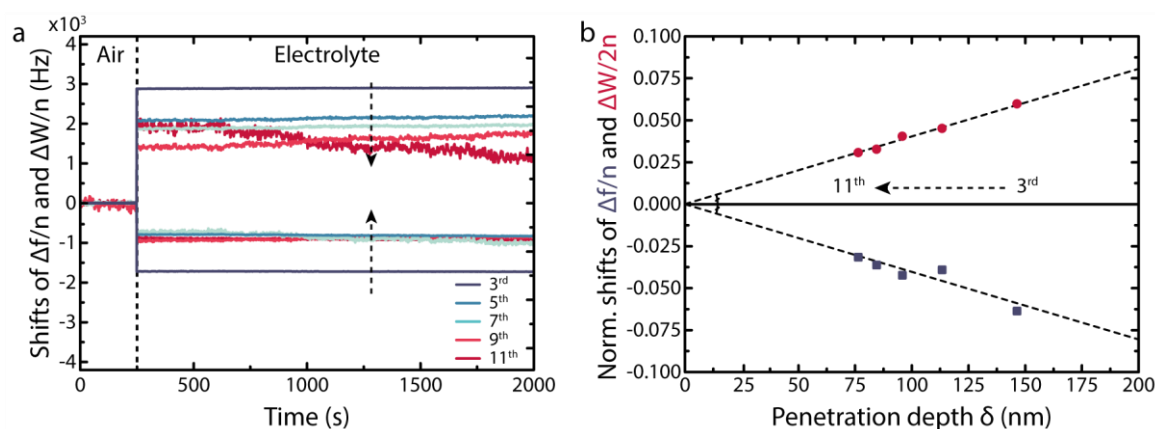


Figure V-6: (a) Shifts of frequency $\Delta f/n$ (negative) and resonance width $\Delta W/n$ (positive) at different overtones ($n = 3$ to $n = 11$) as a function of time when the H_xIrO_4 composite film is transferred from air to electrolyte. (b) Normalized (by overtone order as well as by $\rho_l f_0^2$) shifts of frequency $\Delta f/n$ (blue) and resonance width $\Delta W/2n$ (red) as a function of the penetration depth. Shifts are referenced to that of the film in air rather than to the bare crystal.

Apart from the $\Delta W/n$ at the 11^{th} overtone, $\Delta f/n$ and $\Delta W/n$ (Figure V-6a) are showing a non time-dependent behavior and decrease algebraically with the overtone order. These data indicate a rigid behavior of the prepared film under OCP so that changes of frequency and dissipation factors are solely attributed to hydrodynamic solid-liquid interactions.¹⁶⁶ Moreover a flat rigid surface in contact with liquid should be expressed by straight lines for all overtone orders and in contact with different liquids. To verify that our film behaves as a flat surface in contact with the electrolyte, $\Delta f/n$ and $\Delta W/2n$ were plotted as a function of the penetration depth δ of the transverse wave. The Figure V-6b depicts two straight lines of $\Delta f/n$ and $\Delta W/2n$ in function of δ demonstrating the rigid behavior of the film and that it can be assimilated to a flat surface under OCP. Nevertheless these findings do not prove the film rigidity retention during the material cycling. To this end the motional resistance was

measured during the cyclic voltammetry of the H_xIrO_4 phase, the results are plotted in the Figure V-7.

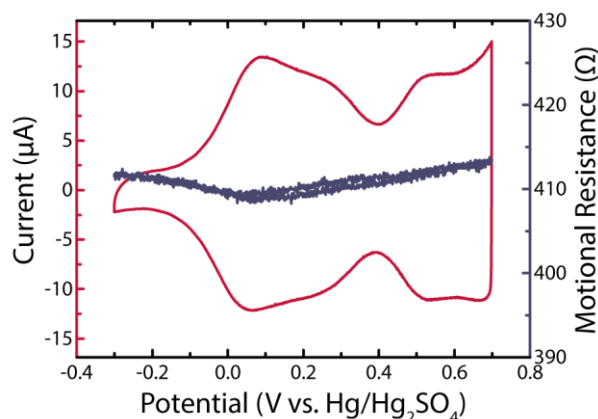


Figure V-7: Cyclic voltammetry and simultaneously measured motional resistance at $5 \text{ mV}\cdot\text{s}^{-1}$ in HClO_4 $0.5 \text{ mol}\cdot\text{L}^{-1}$.

The motional resistance, R , shows a variation of $5 \text{ } \Omega$ between its lower and higher values during the cycling at a scan rate of $5 \text{ mV}\cdot\text{s}^{-1}$ corresponding to a motional resistance change below 2 %. The motional resistance variations were always lower than $10 \text{ } \Omega$ independently of the applied scan rate; consequently, the viscosity changes at the vicinity of the H_xIrO_4 coated electrode during cycling were supposed to be negligible. As mentioned in Levi and Aurbach's works¹⁸⁸, this criterion can be employed to prove the rigidity of the prepared film during the proton release/uptake and therefore the gravimetric regime of the QCM response. The resonance width is not represented; however, the smallness of the motional resistance change upon cycling ensures that the $|\Delta W| \ll |\Delta f/n|$ condition is respected. Such testing protocol ensures that the Sauerbrey equation can be applied for extracting the values of mass change from the measured values of frequency change.

V.4.b – Kinetic comparison between the two regions

After the validation of the gravimetric regime, the CV analyses at different scan rates were performed along with the QCM measurements to characterize the mass variation of the electrode during cycling and the results are displayed in Figure V-8. Regarding the EQCM response of the thin layer at $5 \text{ mV}\cdot\text{s}^{-1}$, the electrochemistry shows the same features consisted of two distinct regions as for the bulk electrodes. A reduction of the voltage window at the low potential is noted due to the contribution of the double layer on the underlying gold

surface of the EQCM electrode. The QCM measurement simultaneously performed during CV at $5 \text{ mV}\cdot\text{s}^{-1}$ indicates two potential-dependent mass variation with two different slopes (Figure V-8, upper panel). A mass change occurs between -0.1 and $0.3 \text{ V vs. Hg/Hg}_2\text{SO}_4$ with a slope coefficient higher than that of the second mass change between 0.3 and $0.7 \text{ V vs. Hg/Hg}_2\text{SO}_4$. Note that these potential ranges correspond to Region I and Region II as defined previously for the bulk electrode (Figure V-3b). This result may indicate that different species may be involved in the charge compensation processes occurring in different potential domains.

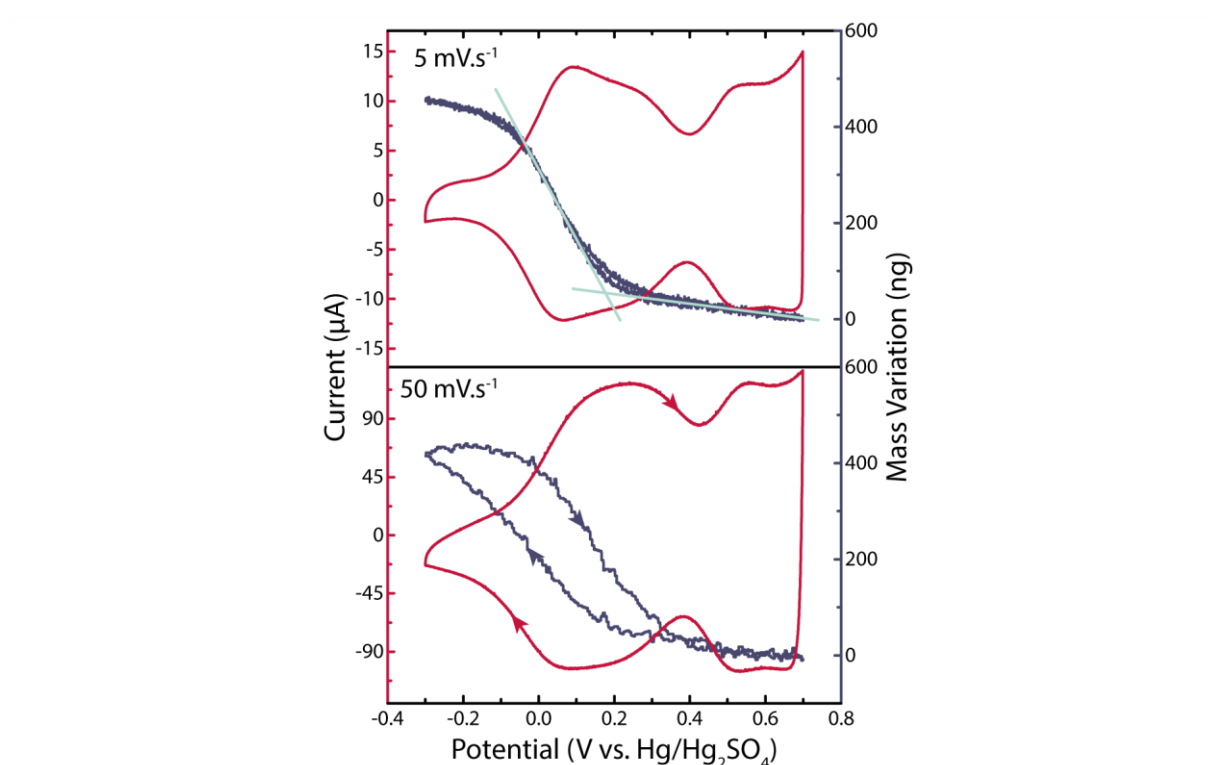


Figure V-8: EQCM measurement at 5 and $50 \text{ mV}\cdot\text{s}^{-1}$ of H_xIrO_4 in HClO_4 $0.5 \text{ mol}\cdot\text{L}^{-1}$.

We observed that increasing the CV scan rate from 5 to $50 \text{ mV}\cdot\text{s}^{-1}$ (Figure V-8, lower panel) results in a constancy of the electrochemical signature in region II as opposed to region I which shows the appearance of a hysteresis phenomenon. This hysteresis is reminiscent of a difference in the kinetics between the involved species in the two regions of the voltammogram with the slower species being in Region I. Equally, a similar trend can be observed for the mass variation which remains constant in Region II as opposed to Region I. Lastly, for sake of completion, the mass variation occurring before the Region I (Figure V-8) corresponds to the reorganization of the double layer on the substrate demonstrated by the square shape of the electrochemical curve (in contrast with the Figure V-3b) as it will be further evidenced latter.

V.4.c – Evidences of the water participation in the insertion mechanism

To obtain insights on the molar mass of the species taking part in the two regions of the voltammogram, the M/z value has been calculated thanks to the Equation II-7 for the CV performed at 5 mV.s^{-1} (Figure V-8, upper panel). The result of the calculation is represented in the Figure V-9.

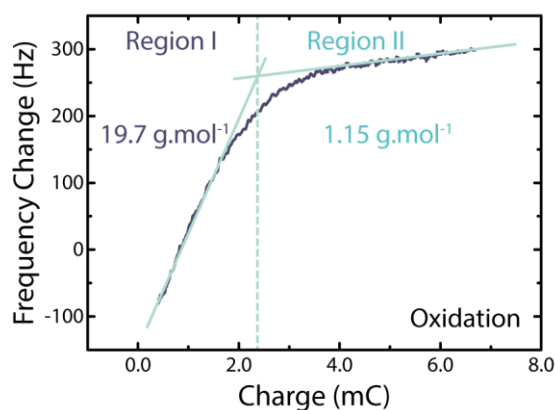


Figure V-9: M/z estimations from the slope of Δf and ΔQ during oxidation at a scan rate of 5 mV.s^{-1} of H_xIrO_4 in HClO_4 0.5 mol.L^{-1} .

A molar mass of 19.7 g.mol^{-1} was found for region I as opposed to 1.15 g.mol^{-1} for region II, which is very close to that of proton. In contrast, the molar mass calculated for Region I is close to that of hydronium (H_3O^+) or proton accompanied with a water molecule. Altogether, these results indicate a potential-dependent mechanism involving species of different molar masses. Thus, this multi-species process may have a different impact on the H_xIrO_4 structure depending on the potential range studied.

To tackle the structural consequences of electrochemical cycling on H_4IrO_4 , *ex situ* X-ray diffraction was performed on composite electrodes recovered from 3-electrodes Swagelok cells cycled to various depths of oxidation and reduction. The collected XRD patterns presented sharp peaks that were all indexed in a hexagonal $R\bar{3}m$ unit cell. Figure V-10a shows the variation of the interlayer distance (equal to $c/3$) as a function of the potential.

This interlayer distance does not vary linearly with the potential, it decreases more rapidly at low potential than at high potential, hence defining two domains. The two domains corresponding to regions I and II previously associated by EQCM to the uptake of $[\text{H}^+ (\text{H}_2\text{O})]$

and H^+ , respectively. Consistently, the larger variation of the c-axis occurs over the potential region corresponding to the uptake of the larger species.

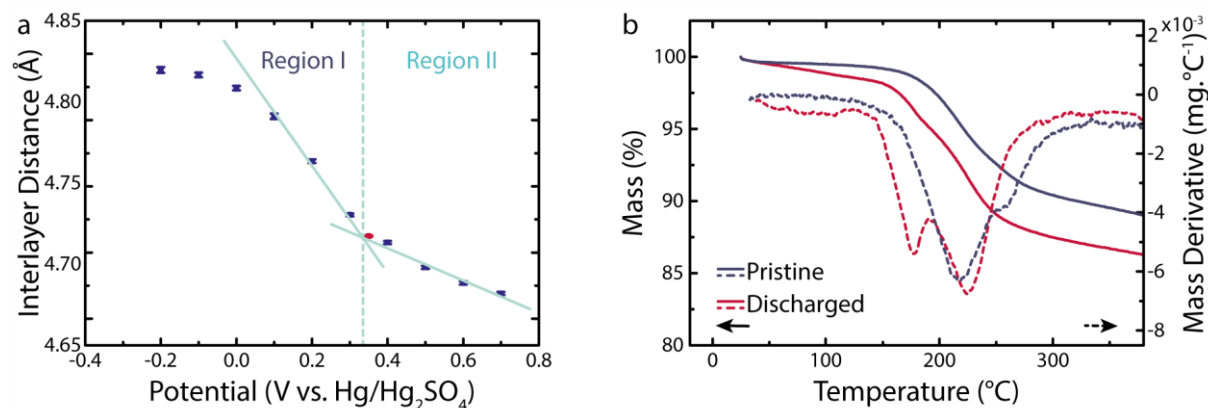


Figure V-10: (a) The interlayer distance as a function of the applied potential obtained by Rietveld refinement of *ex situ* X-Ray Diffraction on composite electrodes of H_4IrO_4 . The red dot corresponds to the pristine composite electrode. (b) Thermogravimetric analyses of a pristine composite electrode and a composite electrode discharged at -0.3 V vs. Hg/Hg_2SO_4 .

To reinforce this result, thermogravimetric analyses have been performed on discharged composite electrodes (-0.3 V vs. Hg/Hg_2SO_4) and on the pristine composite electrode for comparison (Figure V-10b). The derivative of the mass variation with respect to the temperature (Figure V-10b, dashed line) reveals the presence of a new population of water molecules at 175 $^\circ C$ while the population at 220 $^\circ C$ still remains for both pristine and discharged samples. As the water departure is associated to the structural hydroxyl groups, the observed lower temperature for water departure suggests the presence of another type of H_2O , most likely water molecules incorporated between the layers, which are easier to be removed from the structure. From the mass loss, we deduced the stoichiometry: $H_{4.6}IrO_4 \cdot 0.6 H_2O$ for the reduced sample. It is worth to mention that a cycled and retrieved sample at $x = 4$ is demonstrating the same thermogravimetric behavior as the pristine electrode. Altogether, EQCM, XRD and TGA measurements have well proved the incorporation of water molecules in the Region I, although larger changes in lattice parameters could have been expected. However, these techniques have not given direct indications on quantitative kinetic parameters associated to each species involved.

V.5 – Species determination and associated kinetics at the EEI

V.5.a – Identification of the nature of species and their dynamics at EEI

Finally, to determine the species involved in the charge compensation process and kinetics associated to their transfer, *ac*-electrogravimetry has been employed. Essential to this technique, alike typical EIS measurements, is the need to fit the data with a suitable model to extract parameters related to the interfacial transfer. The fitting methodology has been described in the Chapter II (see II.4.c). This method was then employed for the electrode-electrolyte interface (EEI) analysis of H_xIrO_4 composite electrode as shown schematically in the Figure II-9. The measurements were performed at various stationary potentials in the same potential range used for the EQCM measurements (Figure V-8). The *ac*-electrogravimetry results obtained at 0.15 V vs. $\text{Hg}/\text{Hg}_2\text{SO}_4$ (situated in Region I) are shown in Figure V-11.

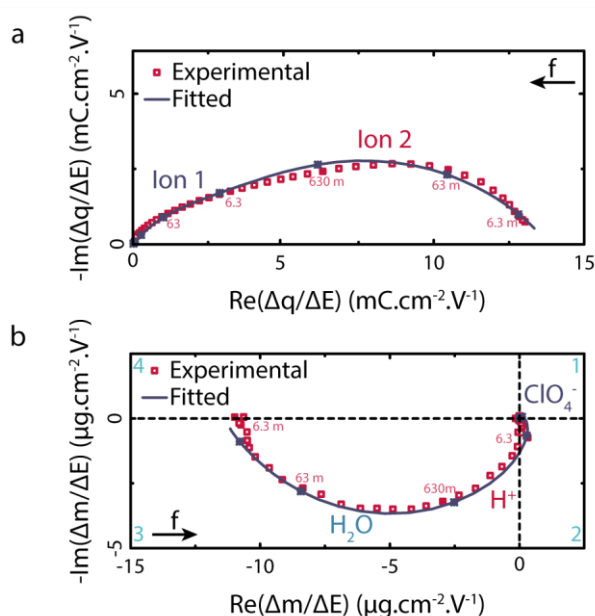


Figure V-11: *Ac*-electrogravimetry analyses of H_4IrO_4 . (a) Charge/potential $\Delta q/\Delta E(\omega)$ and (b) mass/potential $\Delta m/\Delta E(\omega)$ transfer functions at 0.15 V vs. $\text{Hg}/\text{Hg}_2\text{SO}_4$, both experimental and theoretical curves are given. The different loops are labelled with the involved species.

The charge/potential transfer function, $\Delta q/\Delta E(\omega)$, has been presented instead of classical impedance representation (*i.e.* potential/intensity, $\Delta E/\Delta I(\omega)$) for the same reasons as in the previous chapter. The collected spectrum of $\Delta q/\Delta E(\omega)$ at 0.15 V shows two loops implying that two charged species (ion 1 and ion 2) are involved in the charge compensation

process (Figure V-11a). Then, to identify and clarify the contribution of the charged and also uncharged species (free electrolyte molecules), the experimental mass/potential transfer function $\Delta m/\Delta E(\omega)$ is considered (Figure V-11b). One big loop appears in the 3rd quadrant at medium and low frequencies. It is noted that the loops in the 3rd quadrant are characteristic for cation contribution or free solvent molecules in the same flux direction as cations. Another small contribution appears at high frequency domain in the 1st quadrant. The loops in this latter are characteristic for anion contribution or free solvent molecules in the same flux direction of anions (as explained in the Figure II-10). The initial assessment of the experimental TFs in the Figure V-11 indicates: the charge/potential transfer function demonstrates the contribution of two charged species without a clear identification (either two cations, two anions, or one cation and one anion) and the mass/potential transfer function shows a slight contribution of one anion or one solvent molecule at high frequency and one cation or one solvent molecule at medium frequency domain.

Then, the experimental TFs were fitted with a model described in the Chapter II. Concerning experimental $\Delta q/\Delta E(\omega)$ TF, it was fitted with the theoretical equation given in Equation II-32, involving two charged species. A good agreement is evident between the experimental and theoretical curve in the Figure V-11a, both in terms of shape and frequency distribution. The fitting parameters, K_i (kinetics of transfer) and G_i (related to interfacial transfer resistance) are obtained for the two ions. At this stage, it is not possible to identify these ionic contributions. To do so, the mass/potential transfer function $\Delta m/\Delta E(\omega)$ is fitted using theoretical equation given in Equation II-35. The K_i and G_i parameters previously estimated in the fitting of the $\Delta q/\Delta E(\omega)$ TF are used. Then, the molar mass of the species (M_i parameters in Equation II-35) were estimated which can lead to a good fit of the experimental data. Several possibilities are considered. In the simpler case, one anion at high frequency and one cation at medium frequency are involved in the charge storage mechanism. The anion assignment is straightforward since perchlorate anions (ClO_4^-) are solely present in the electrolyte during the measurements. For cations, there are two possibilities *i.e.* hydronium ion (H_3O^+) and proton (H^+). Thus, two couples of charged species are possible: $\text{H}^+/\text{ClO}_4^-$ and $\text{H}_3\text{O}^+/\text{ClO}_4^-$. Both have been tested to fit the mass/potential transfer functions but neither of them were satisfactory due to the impossibility to fit the massive loop in the 3rd quadrant (Figure V-11b) with the low value of molar mass of the possible cations. In contrast, a more

robust model has been obtained by injecting free solvent molecules. This solvent contribution could not be distinguished at first glance due to not sufficiently different time constants between the water molecule and the cation species, which results in one merged loop as represented in the Figure V-12.

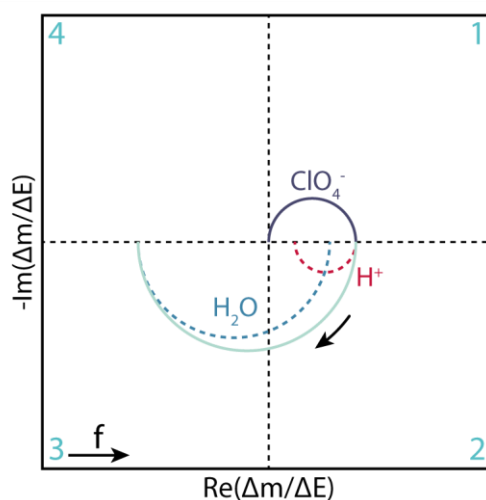


Figure V-12: Example of $\Delta m/\Delta E(\omega)$ TF for one anion (ClO_4^-) and one cation (H^+) plus the participation of one uncharged species (H_2O) in the same direction as the cation flux with close time constants.

Therefore, the model enlisting anions (ClO_4^-) at high frequency, cations (H^+) and solvent molecules (H_2O) at medium and low frequency was taken into account. The outcome of this fitting of the experimental TFs with this model is displayed in the Figure V-11 with the corresponding species identified in the mass/potential TF. Fits with hydronium ion instead of the proton have been considered but the partial mass/potential TF (a cross-check procedure of the fitting) where the cation contribution has been removed were not satisfactory (Figure V-13) which lead us to maintain the contribution of H^+ as the cationic species in our model.

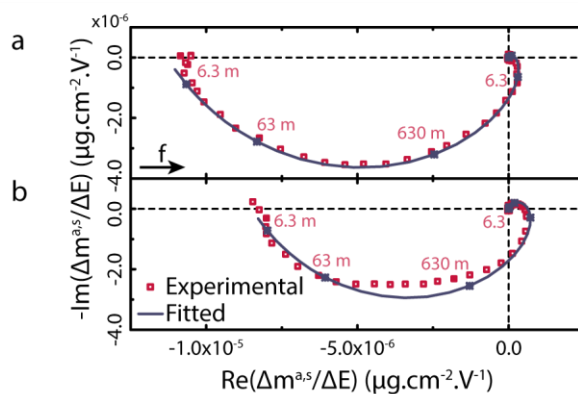


Figure V-13: Partial mass/potential transfer functions $\frac{\Delta m^{a,s}}{\Delta E}(\omega)$ at 0.15 V vs. Hg/Hg₂SO₄ where (a) the proton or (b) the hydronium ion contribution has been removed, both experimental and theoretical curves are given.

Thus, as a whole, *ac*-electrogravimetry has confirmed the contribution of water molecule and protons in the charge compensation associated to the Ir⁵⁺ → Ir^{3.25+} redox process while refuting the hydronium ions possibility. Surprisingly, there is also a minute participation of the perchlorate ions to the overall process and their contribution will be discussed quantitatively in the following.

V.5.b – Outcomes of the kinetic study

A similar fitting procedure described for the 0.15 V vs. Hg/Hg₂SO₄ (Figure V-11) was carried out for all the other measurements performed in the potential range from -0.3 to 0.7 V vs. Hg/Hg₂SO₄. The results of the fitting procedure provided the K_i (kinetics of transfer), G_i (related to interfacial transfer resistance by $Rt_i = \frac{1}{FG_i}$) and M_i parameter (molar mass, thus identification of the species). Although in different quantity and kinetics of transfer, the contribution of three different species (ClO₄⁻, H⁺ and H₂O) is found to be persistent at all the potentials studied. The obtained values are shown in the Figure V-14a.

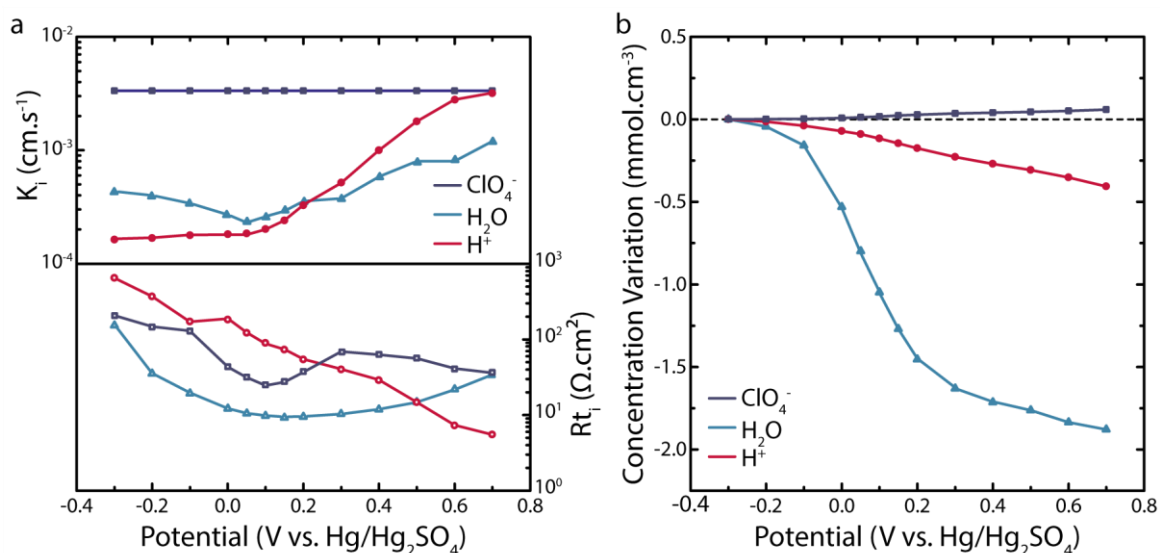


Figure V-14: (a) Evolution of kinetic parameters, K_i , interfacial transfer resistances, R_{t_i} and (b) relative concentration variation of each species, represented as a function of the potential.

Independently of the potential, the perchlorate anion has always a faster kinetic than that of the proton and the water molecule. The proton kinetics in contrast is potential dependent: they are slower than that of the water molecule in the potential range below 0.2 V vs. Hg/Hg₂SO₄. Beyond this potential, the proton kinetic increases rapidly to become as rapid as the anion species. Meanwhile, the water molecule keeps an almost steady kinetic throughout the overall potential window. While interfacial transfer resistance (R_{t_i}) of proton species decreases constantly from low to high potential in the Figure V-14a, note that of water shows a parabola shape with a minimum at 0.15 V vs. Hg/Hg₂SO₄ consistent with a water incorporation in the potential Region I, as suggested by the EQCM, TGA and *ex situ* XRD results. With a further calculation using the *ac*-electrogravimetry data, the concentration variation of the three different species in the active material film as a function of the potential can be determined (Equation II-38) represented in the Figure V-14b. The H⁺ concentration varies nearly linearly with increasing potential, hence proving its steady insertion in both Regions I and II. The water concentration in contrast undergoes a huge drop over the short potential window (-0.1 to 0.2 V vs. Hg/Hg₂SO₄) corresponding to Region I. Additionally it can be noted that the concentration variation related to anion (ClO₄⁻) is much smaller compared with cation and solvent concentration changes (Figure V-14b). Their fast kinetic led us to believe that their participation is rooted in their electroadsorption on the underlying gold surface of the EQCM and not as inherent part of the active material redox process. Even if the film at the surface of the electrode is homogeneous, some spots are indicating the contact between the electrolyte

and the gold surface as shown in the SEM picture of the Figure V-15a. Perchlorates are known for their lower affinity to be adsorbed on gold substrate that is why we selected them at the first place as counter ions instead of chlorides or sulfates.²²³

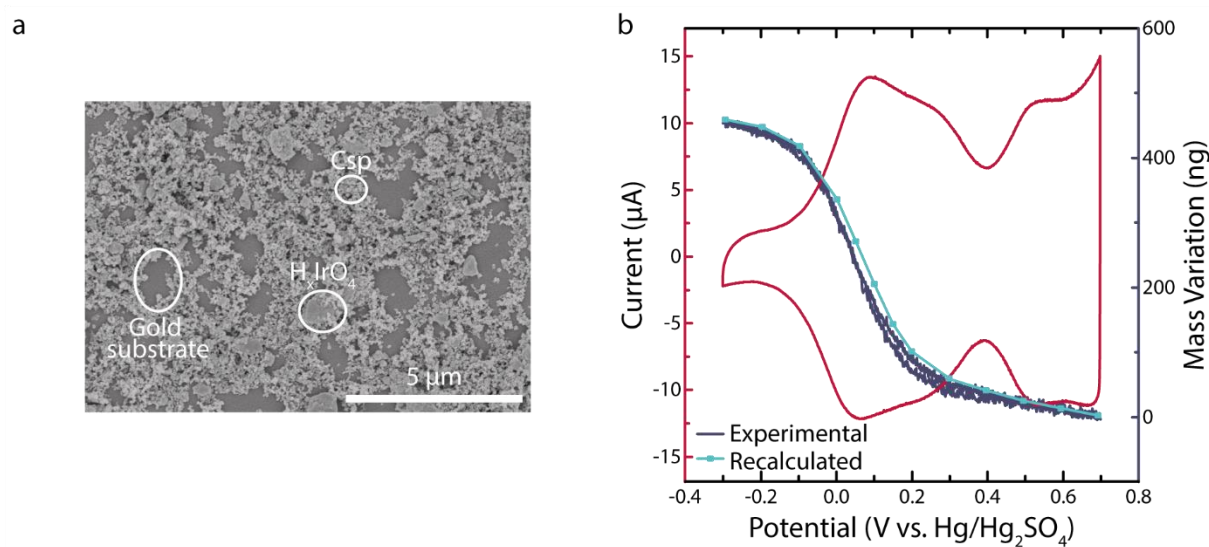


Figure V-15: (a) FEG-SEM image of a spray cast composite film of H_xIrO₄, Csp and PVDF on a gold EQCM electrode and (b) comparison of the mass variation by classical EQCM measurement (at 5 mV.s⁻¹) with recalculated mass variation by *ac*-electrogravimetry.

To ensure the robustness of our data analysis by *ac*-electrogravimetry, through which we claimed that the EQCM global mass variation (in Figure V-8 and Figure V-15b) can be deconvoluted into distinct contributions of ClO₄⁻, H⁺ and H₂O, a verification procedure is applied. The mass variation of each species has been recalculated using their concentration change in Figure V-14b. The total of these contributions (re-calculated from *ac*-electrogravimetry) was compared with the mass variation obtained by classical EQCM. The difference of active material mass loading between the film for classical EQCM and *ac*-electrogravimetry was taken into account in our calculations by a simple renormalization. These results nicely compare hence validating the model involving three different species contributing to charge compensation process in H_xIrO₄ composite electrode.

V.6 – Chapter conclusions

The electrochemical activity of H_xIrO₄ in aqueous media has been revisited. In comparison with the work of Perez *et al.*,²¹⁸ we emphasized the study on its mechanism *via*

the use of additional *in situ* analytical techniques, EQCM and *ac*-electrogravimetry, together with *operando* XAS. Interestingly, by increasing the acidity of the leaching solution, we could synthesize from Li_3IrO_4 a water-free protonated phase containing four protons (H_4IrO_4) as opposed to 3.4 for the $\text{H}_{3.4}\text{IrO}_4$ phase previously reported. Alike its predecessor, H_4IrO_4 was shown to reversibly exchange nearly $1.75 e^-$ per formula unit with the charge being counterbalanced by Ir whose oxidation state reversibly switches from +V ($\text{H}_3\text{Ir}^{5+}\text{O}_4$) to +III/+IV ($\text{H}_{4.75}\text{Ir}_{0.25}^{4+}\text{Ir}_{0.75}^{3+}\text{O}_4$), as deduced by XAS. However, cyclic voltammetry performed at different rates provided evidence for a potential-dependent mechanism with a threshold at 0.3 V vs. Hg/Hg₂SO₄. Additionally, *ex situ* XRD had revealed that the process was accompanied by a continuous but non-uniform variation of the lattice parameter providing evidence for a bulk rather than a core-shell mechanism, but also suggesting the presence of two different reacting species.

The potential dependence of the reacting species was confirmed by EQCM which also enables to identify, *via* mass determination, the two contributing species: H^+ and $\text{H}^+(\text{H}_2\text{O})$. Moreover, we could demonstrate that the proton was inserted on the whole potential window while water molecules are mostly inserted at low potentials as further confirmed by TGA analyses. Based on this evidence for water participation, the small c-lattice parameter variation ($\Delta c/3 = 0.12 \text{ \AA}$) when water molecules participate in the insertion process is at first surprising. However, Srimuk and co-workers²²⁴ have previously demonstrated the incorporation of one water molecule per sodium cation during the cycling of TiS_2 in aqueous electrolyte measured by classical EQCM was solely accompanied by small variation of the interlayer distance ($\Delta c = 0.06 \text{ \AA}$). Based on this work and the recent findings of Tepavcevic and co-workers²²⁵ who have studied the benefits of structural hydroxyl groups in enhancing the performance of electrochemically synthesized bi-layer V_2O_5 , we can propose a simple scenario to explain the small variation observed in the c-axis. We believe that alike in V_2O_5 , that protons in the interlayers forming structural hydroxyl groups maintain a sufficient interlayer spacing to permit the diffusion of cations and free solvent molecules as they preserve a solvating environment in the bilayer. To secure this explanation, it becomes essential to determine the water conformation and the proton position within this layer structure. Neutron experiments using acid-d₂ in deuterated water (D_2O) to prepare D_4IrO_4 have been performed; however, the

poor signal-to-noise ratio, probably caused by the low crystallization of the phase, made the data not treatable.

Lastly, *ac*-electrogravimetry was demonstrated to be of great help to provide insights into the origin of the kinetic difference spotted by cyclic voltammetry as it enabled the decoupling between electrode-electrolyte interface processes pertaining to the insertion of the two species. For instance, we clearly show that the proton transfer resistance at the interface is not affected by the concomitant water incorporation. In contrast, it is more dependent on the charge repulsion created by the accumulation of protons within the material during insertion. Turning to the water, its presence is slowing drastically the proton insertion kinetic due to steric hindrance. In short it must be recognized that in protonic aqueous system, water molecules can improve the electrode electrochemical capacity by shielding the proton charge as it has been already proven for Mg¹⁷⁹ or Zn-ion²²⁶ nonaqueous batteries where water acts as an additive. However, in our study this shielding effect has a prize since it negatively affects the kinetic of the insertion process. To the best of our knowledge, no detrimental influence of the incorporated water has been proven on the kinetic of insertion, neither no other compounds have shown a dependency of the inserted species as function of the applied potential. Moreover, we demonstrated that the desolvation process happening at the electrode-electrolyte interface is the rate limiting step for insertion (Region I). Therefore, water molecules could play a key role, since replacing an organic by an aqueous solvation shell, should reduce desolvation energy at the interface. As it has been shown for Zn-ion²²⁶ and more particularly in the two previous chapters, the partial water shell permits a faster insertion kinetic at the electrode-electrolyte interface by permitting a fast surface diffusion. However, contrary to the previous case studies, the water molecules are accompanying the proton into the lattice layers leading to the tuning of the interlayer and thus a stabilization of the cation between the layers. In the literature, the water co-intercalation into the lattice is proved in several layered materials without potential-dependent mechanism. Nonetheless, the present study demonstrates, with these two regions, a potential dependent mechanism that the water co-intercalation occurs at the expense of the insertion kinetic. Therefore, the tuning of the interlayer by solvent molecules permits the further intercalation of cations thanks to its charge shielding. However, the

kinetics of insertion suffer from the activation energy increase triggered by steric hindrance of the intercalated water molecules.

General conclusions

Through this Ph.D. thesis, the essential role played by the electrode–electrolyte interface (EEI) and its impact on the physicochemical properties of ion intercalation was explored. Electrogravimetric-based techniques derived from electrochemical quartz crystal microbalance (EQCM) have been developed and adjusted to characterize the electrode–electrolyte interface in battery systems. We selected model materials like LiFePO_4 , Prussian Blue analogs as well as new protonic iridate phase, H_xIrO_4 , to study the dynamic behavior of the EEI during the insertion of lithium and potassium ions, as well as protons in both organic and aqueous electrolytes. Special attention has been given to the solvation shell of alkali cations.

Obtaining reliable and artifact-free information from QCM-based techniques is not an easy task. To this end, appropriate strategies have been developed to get the best of the each methodology. First, we developed a multi-step process to prepare active material coatings in a reproducible way with a lateral and vertical homogeneity at the surface of the quartz resonator. The quality of the films obtained for gravimetric measurements was secured *via* multiharmonic QCM-D measurements that successfully revealed the hydrodynamic behavior of a flat surface film, rigidly attached to the resonator in both aqueous and non-aqueous electrolytes. In addition, a dedicated EQCM-cell was designed because of the absence of viable commercial alternative. It offers several advantages: mimic the battery configuration, ensure airtightness, display low impedance while offering reproducible data and showing high versatility as it can be used in both aqueous and non-aqueous electrolyte, and be compatible with QCM-based techniques. EQCM with motional resistance monitoring (EQCM-R) over EQCM-D has been privileged for its ease of application to battery material study. The motional resistance monitoring was used as a convenient viscoelastic indicator of the film properties upon cycling to avoid over/under estimation of the real mass change.

The higher rate capability of LFP particles in aqueous electrolyte compared with their organic counterparts was firstly investigated by classical electrochemical measurements. Then, EQCM-R measurements confirmed these performance discrepancies by directly assessing the partial or total $\text{Li}_{1-x}\text{FePO}_4$ delithiation conditions, depending on the potential scan rate, in the two different media. By comparing the experimental and theoretical mass

changes accompanying the insertion and extraction of Li^+ ions in both electrolytes, we provide evidence for a solvent-assisted insertion process with the number of solvent molecules pertaining to the solvation shell being markedly greater for water than for propylene carbonate-based electrolytes. This higher concentration variation of water molecules at the EEI of composite LFP electrode enables a faster insertion/extraction at the vicinity of the active material particle.

To obtain more insights on the battery insertion mechanism, the system was simplified by moving from Li-ion to K-ion chemistry, which proposed a smaller and weaker solvation shell for the inserting cation. K^+ insertion was demonstrated to follow the same rate capability discrepancy between aqueous and non-aqueous electrolytes, as we found for LFP. To identify the origin of this divergence, in-depth electrochemical analyses were performed to highlight the rate-limiting step in the insertion mechanism. Obtained results confirmed that the desolvation process happening at the electrode-electrolyte interface and most likely in the electrochemical double layer region is the cause of the kinetic discrepancy between aqueous and non-aqueous electrolyte. The electrogravimetric measurements demonstrated the presence of an additional frequency change to the theoretical mass uptake due to the sole potassium insertion, which was proved by *ac*-electrogravimetry to be due to the participation of the solvent molecules during the cation insertion at the electrode-electrolyte interface. A strong interaction between K^+ and these solvent molecules has been detected, as indicated by their close interfacial transfer kinetics. These measurements are the first direct visualization of the existence of a transition step, between solvated cation in the bulk electrolyte and a bare cation in the material, where the cation is partially solvated at the interface as demonstrated by the close transfer kinetics between the cation and solvent molecules.

The present studies on the Li-ion and K-ion chemistries demonstrated that in non-aqueous electrolytes, when descending the column of alkali metals, the number of solvent molecules participating in the partial solvation shell at the interface decreases to be inexistent for K-ion battery. However, the desolvation energy in the bulk of the electrolyte decreases when moving from lithium to potassium ions, explaining the better rate capability. The water-based electrolytes do not follow this trend, as the desolvation energy is always higher in aqueous electrolyte and yet exhibits better power performance. A partially hydrated cation

(or a strong interaction between cations and water molecules with close interfacial transfer kinetics) was always found in the electrochemical double layer region, which can be related to the formation of a layer of water molecules in the inner Helmholtz plane (IHP) enhancing the surface diffusion of the cation to an insertion site. Another parameter, which can have its importance on the insertion process, is the anion nature and its concentration, as they are specifically adsorbed in the IHP.

In continuity with the EEI analyses in alkali-metal ion batteries, the water molecules role in the interfacial transfer process and their influence on the overall kinetics was illustrated this time in a proton-based battery (pseudo-alkali metal), by studying the proton insertion in the H_xIrO_4 iridate phase. An arsenal of structural, compositional and electrochemical characterization techniques – XRD, TGA, *operando* XAS and EQCM – was employed to demonstrate the potential-dependent insertion mechanism and that two distinct reacting species were involved. The EQCM, supported by the TGA analysis revealed that the protons were inserted in the whole potential window; while water molecules are mostly inserted at low potentials. In protonic aqueous system, water molecules seems to improve the electrochemical capacity of the electrode by shielding the proton charge. However, in our study, this shielding effect has a prize since it adversely affects the kinetics of the insertion process. To the best of our knowledge, no detrimental influence of the incorporated water has been proven on the kinetics of insertion, neither no other compounds have shown a dependency of the inserted species as function of the applied potential. Therefore, water molecules could play a key role, since replacing an organic by an aqueous solvation shell, should reduce desolvation energy at the interface. As it has been shown in the two previous chapters, the partial water shell permits a faster insertion kinetics at the electrode-electrolyte interface by permitting a fast surface diffusion. Here, contrary to these previous case studies where water molecules cannot be inserted in the material, they accompany the proton into the lattice layers of the iridate phase, tuning the interlayer and thus stabilizing the cation between the layers. The water co-intercalation permits the further intercalation of cations thanks to its charge shielding, nonetheless at the expense of the insertion kinetic.

Overall, scrutiny of the battery electrode-electrolyte interface, provided by a broad spectrum of (electro)chemical characterization methods has delivered important insights on the insertion mechanism, which is known to be of paramount importance to enhance battery

General conclusions

performances and lifetime. The results provided in the framework of this Ph.D. thesis are expected to help in gaining a wider acceptance of EQCM based methods from the battery community. Studies focusing on a wider panel of active materials and a broader variety of electrode-electrolyte interface phenomena can already be anticipated. This work can be extended to the newly emerging multivalent ion chemistries to assess the impact of the charge number on the insertion mechanism. As mentioned previously, the anion nature and concentration are of great importance on the Inner Helmholtz Plane (IHP) structure and should influence the interfacial desolvation before insertion and therefore the system rate capability. In the following of H-based battery study, electrogravimetric methods should provide advanced mechanistic insights on the interlayer tuning and its impact on the faradaic and double layer processes. Finally yet importantly, as recounted in the literature, EQCM based techniques are methods of choice to characterize the SEI formation in its early stage to forecast its performance in practical applications.

Materials & Methods

M.1 – Material preparation and characterization

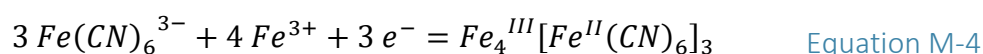
M.1.a – Used and synthesized battery materials

○ *Lithium iron phosphate (LFP)*

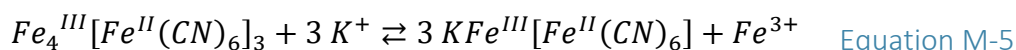
Lithium Iron Phosphate, LiFePO_4 , was purchased from Umicore, which presents a very controlled distribution of particle size around 200 nm. The particles possess a carbon-coating to improve the electronic conductivity of the electrode.

○ *Prussian Blue (PB)*

The Prussian Blue phase was prepared by electrodeposition at the surface of a gold disk electrode ($8.95 \text{ MHz} \pm 50 \text{ kHz}$, QA-A9M-AU(M)) or directly on one side of the gold patterned quartz resonator. The EQCM electrode was protected in a dedicated mask exposing only the gold surface area of 0.196 cm^2 . The phase was deposited from a solution containing 0.01 mol.L^{-1} HCl (37 %, Carlo Erba), 0.02 mol.L^{-1} $\text{K}_3[\text{Fe}(\text{CN})_6]$ (> 99 %, Sigma-Aldrich) and 0.02 mol.L^{-1} FeCl_3 (> 98%, Alfa Aesar). The solutions were prepared separately at higher concentration to be diluted to the desired concentration and mixed in the mentioned order prior usage. A 3 mm diameter graphite rod (Sigma-Aldrich) and Hg/Hg₂SO₄ (saturated K₂SO₄) protected with a frit containing a solution of K₂SO₄ 0.25 mol.L^{-1} (99 %, Alfa Aesar) are used as the counter and the reference electrode, respectively. The solution was stirred during with electrodeposition time. A $40 \mu\text{A.cm}^{-2}$ cathodic current ($-7.84 \mu\text{A}$ for a surface area of 0.196 cm^2) was applied during different period of time: 150, 300, 450 and 600 s, to obtain different thicknesses of PB film: 100, 200, 300 and 400 nm, respectively. The PB phase is formed following this redox equation:



A 1 μm thick film was prepared at the surface of a gold disk electrode to check the structural phase by X-ray diffraction. Then the films were cycled 15 times in aqueous medium containing $0.25 \text{ mol}\cdot\text{L}^{-1} \text{ K}_2\text{SO}_4$ pH 3.5 to insert potassium in the structure and leach one iron as described in the equation:



Then the films can be cycled in the same aqueous electrolyte or in nonaqueous electrolyte. For the latter, the films were dried under vacuum overnight at $80 \text{ }^\circ\text{C}$.

○ H_xIrO_4

Li_3IrO_4 was prepared by mixing metallic Ir and Li_2CO_3 in stoichiometric amounts followed by a heating treatment at 950°C for 24 h in air. Then, the resulting sample was acid-leached in $1 \text{ mol/L H}_2\text{SO}_4$ (95-97 %, Sigma-Aldrich) during 1 h with a fivefold excess of H^+ over exchangeable Li^+ in the material. The solid and the supernatant were separated by centrifugation and the sample was washed five times with distilled water prior to being dried overnight at $80 \text{ }^\circ\text{C}$ under vacuum.²¹⁸

M.1.b – Material characterization

○ X-ray diffraction (XRD)

X-ray diffraction (XRD) was performed to confirm the success of the synthesis and to analyze the structure of the material at different state-of-charge (*ex situ*, by stopping at different potentials during cycling) using a BRUKER D8 Advance diffractometer with Cu $\text{K}\alpha$ radiation ($\lambda_{\text{K}\alpha 1} = 1.54056 \text{ \AA}$, $\lambda_{\text{K}\alpha 2} = 1.54439 \text{ \AA}$). Rietveld refinement²²⁷ were performed to obtain structural parameters as implemented in the FullProf suite (P.E. Pearce and T. Marchandier are acknowledged for their contribution).²²⁸ The crystal structures shown in this work were drawn with the VESTA visualization program,²²⁹ using the crystallographic information obtained from Rietveld refinements.

○ *Thermogravimetric analysis (TGA)*

Thermogravimetric Analyses (TGA) were recorded with a Mettler Toledo TGA/DCS 3+ apparatus under argon by applying a heating rate of 5 K.min⁻¹ from 25 to 1000 °C using around 8-10 mg of material. The thermal stability of pristine materials, as well as the water uptake of active material present in cycled composite electrodes were investigated.

○ *Field emission gun scanning - electron microscopy (FEG-SEM)*

The morphology of the particles and the prepared films (by spray coating or electrodeposition) was observed by Scanning Electron Microscopy (SEM) with a SU-70 Hitachi FEG-SEM (accelerating voltage of 5 keV). Modified quartz resonators followed a particular preparation procedure. Its upper side, where the film is deposited, is electronically connected to the SEM stage through a copper tape. The sample was covered with a thin layer of gold (10 nm) using a plasma sputtering coater (MTI, GSL-1100X-SPC-12).

○ *Brunauer, Emmet and Teller analysis (BET)*

The specific surface area was determined using BET analysis on a Quantachrome ChemBET Pulsar from a single-point BET analysis performed after 12 h outgassing at 150°C. The measurements were performed by M. Ben Osman.

○ *X-ray absorption spectroscopy (XAS)*

Ex situ and *Operando* XAS measurements at the Ir L₃-edge were performed in a transmission mode at the ROCK beamline²³⁰ of synchrotron SOLEIL (France) with the help of A. Iadecola. A Si (111) channel-cut quick-XAS monochromator with an energy resolution of 2 eV at 11 keV was used. The intensity of the monochromatic X-ray beam was measured by three consecutive ionization detectors, as represented in the Figure M-16.

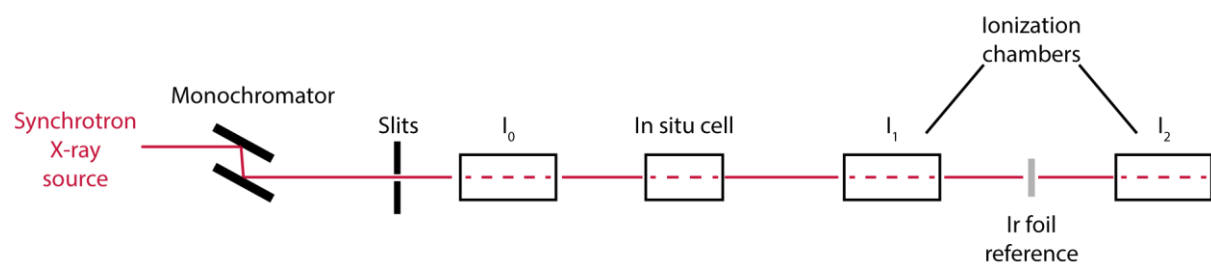


Figure M-16: Schematic representation of the XAS experiment performed at SOLEIL.

The *in situ* three-electrode cell (Figure M-17a) was placed between the first and the second ionization chambers. *Operando* XAS spectra were collected continuously and averaged out over periods of 120 s. The energy calibration was established with simultaneous absorption measurements on Ir metal foil placed between the second and the third ionization chambers. The energy calibration as well as the normalization was done using graphical interfaces available on the ROCK beamline.²³¹

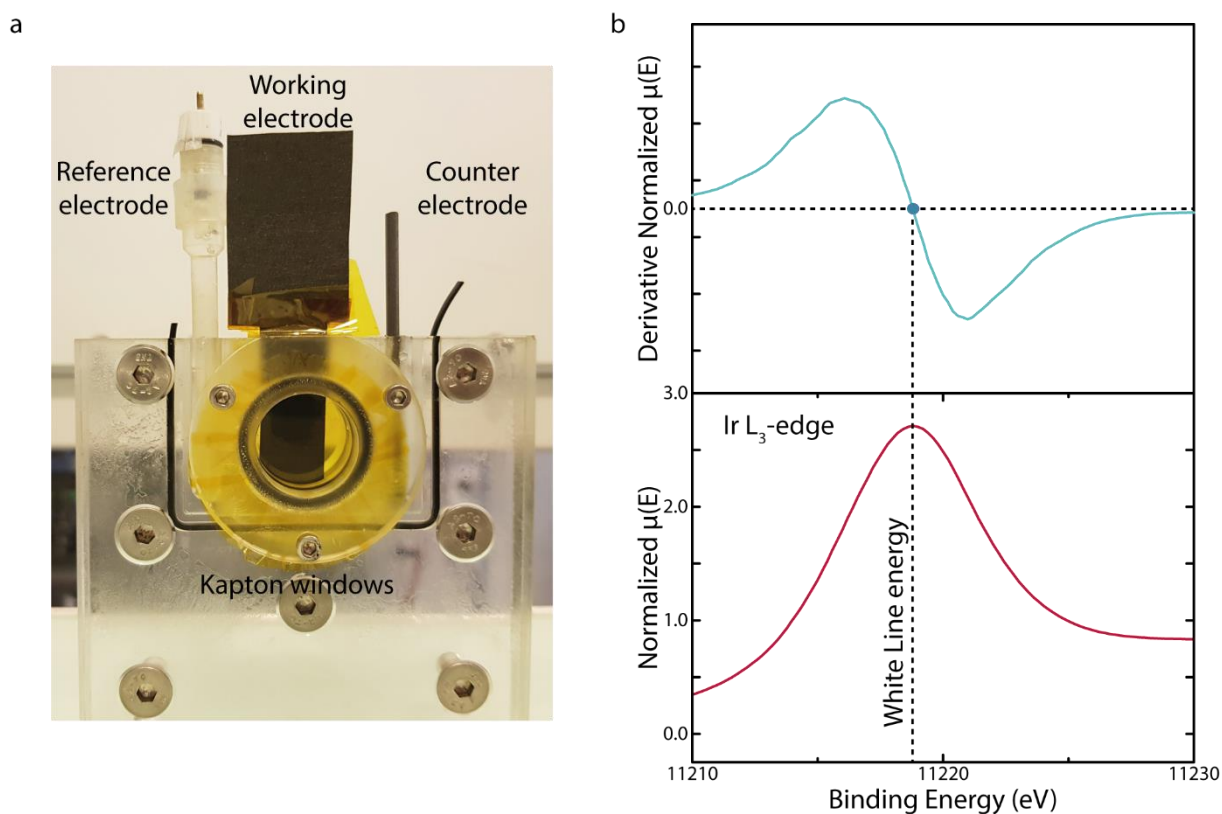


Figure M-17: *Operando* XAS data treatment and experimental setup. (a) Picture of the lab-made electrochemical cell for operating *operando* XAS experiments, using carbon paper loaded with $7 \text{ mg}\cdot\text{cm}^{-2}$ of H_xIrO_4 as working electrode, porous graphite rod as counter electrode and $\text{Hg}/\text{Hg}_2\text{SO}_4$ (saturated K_2SO_4) as reference electrode. (b) Determination of the White Line energy thanks to derivative of the normalized absorption spectrum with the binding energy for which the curve is equal to zero.

The White Line (WL) energy position taken at the zero crossing of the first derivative (Figure M-17b) was used as fingerprint of the oxidation state. K_3IrCl_6 , Li_2IrO_3 and Li_3IrO_4 were used as references for the oxidation state of Iridium +III, +IV and +V respectively.

M.2 – Classical electrochemical characterization

M.2.a – Electrode preparation

Self-standing PTFE electrodes were prepared for their easy handling. The selected active material was mixed with 10 wt.% Carbon super P (Csp, Timcal) and 5 wt.% PTFE (1 μ m, Sigma-Aldrich) in a mortar with the help of a few drops of volatile solvent, propan-2-ol (isopropanol, 99.5 %, Sigma-Aldrich). Then, the mixture is laminated with a roller several times, like a pastry puff, to obtain films with a thickness of 60-70 μ m and a density of material around 15 mg.cm⁻². 6.5 mm diameter electrodes (0.322 cm²) were punched from the Active material/Csp/PTFE film to be used as the working electrode. Counter electrodes were also prepared by this technique using overcapacitive carbon (YP50) as an active material for aqueous electrolytes.

M.2.b – Classical electrochemical setup

Routine electrochemical tests were performed using 2032 coin cells in a two-electrode configuration. The positive and negative electrodes were separated by two sheets of borosilicate glass fiber membranes (Whatman GF/D, VWR) soaked with the desired electrolyte. Self-standing electrodes of active material were used as the working electrode. Metallic Li or K were used as anodes by a small chunk of metal on a stainless steel current collector. Coin cells were sealed by an automatic crimping machine applying the same pressure to all cells (MTI, MSK-160E). All the cell parts were dried overnight at 80 °C before being assembled in an Ar-filled glovebox (MBraun, O₂ and H₂O < 0.1 ppm) before each experiments using non-aqueous electrolytes.

Electrochemical tests in acidic aqueous electrolyte were performed in three-electrode perfluoroalkoxy alkane (PFA) Swagelok cells. Glassy carbon current collectors were used instead of stainless steel to avoid corrosion. YP50 self-standing electrodes were used as negative electrodes. As for the reference electrode, a Hg/Hg₂SO₄ (saturated K₂SO₄) was used. The Figure M-18 depicts the electrochemical setup used in this Ph.D. manuscript.

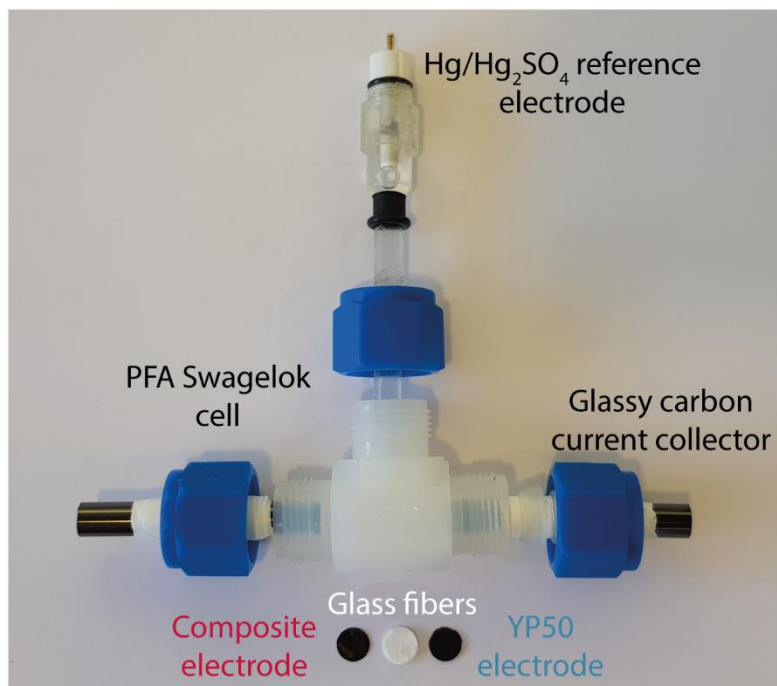


Figure M-18: Three-electrode Swagelok type electrochemical setup used for the tests in acidic aqueous electrolyte.

M.2.c – Electrochemical cycling

All electrochemical cycling tests were performed with a VMP3 potentiostat (Bio-Logic SAS). Electrochemical characterization was done in a galvanostatic mode, with a constant current applied between the working and the counter electrodes and the cell voltage (two-electrode setup) or electrode potentials (three-electrode setup) were measured. Or cyclic voltammetry was performed, the potential window is swept at a fixed rate and the intensity is measured. The current density (in galvanostatic mode) was chosen to correspond to a defined cycling rate for a given material. For example, at 1C, one cation is exchanged between the two electrodes in one hour. The rate capability was evaluated by varying the cycling rate. The same procedure was performed in cyclic voltammetry by changing the scan rate of the

potential. The cut-off potentials of cycling were selected to remain in the electrochemical stability window of the used electrolyte.

M.2.d – Diffusion coefficient determination

o Galvanostatic Intermittent Titration Technique (GITT)

The GITT procedure consists of a series of current pulses at 1C during 2 minutes, each followed by a relaxation time of 30 minutes, in which no current passes through the cell. During a discharge, the cell potential quickly falls to a value proportional to ohmic drop (iR), where R is the polarization resistance. Then, the potential slowly decreases, due to the galvanostatic discharge pulse, in order to maintain a constant concentration gradient. During the relaxation time, the composition in the electrode tends to become homogeneous by cations diffusion. Consequently, the potential suddenly increases by a value proportional to iR , and then it slowly increases, until the electrode is in equilibrium (*i.e.* when $dE/dt \approx 0$) and the open circuit potential of the cell is reached. Then, the following galvanostatic pulse is applied, followed by current interruption. This sequence of discharge pulse followed by a relaxation time is repeated until the battery is fully discharged. The chemical diffusion coefficient can be calculated at each step, with the following formula:²²²

$$D_{app} = \frac{4}{\pi} \left(\frac{iV_m}{zFS_e} \right)^2 \left[\frac{\frac{dE}{d\delta}}{\frac{dE}{d\sqrt{t}}} \right]^2 \quad \text{Equation M-6}$$

where i is the current (A), V_m is the molar volume of the active material ($\text{cm}^3 \cdot \text{mol}^{-1}$), z is the charge number, F is the Faraday's constant ($96485 \text{ C} \cdot \text{mol}^{-1}$), S_e is the electrode/electrolyte contact area (cm^2), $dE/d\delta$ is the slope of the coulometric titration curve and $dE/d\sqrt{t}$ is the slope of the linearized plot of the potential during the current pulse of duration. If sufficient small currents are applied for time intervals, $dE/d\sqrt{t}$ and the coulometric titration curve can be considered linear over the composition range involved in that step, the previous equation can be simplified into:

$$\frac{D_{app}}{R^2} = \frac{4}{9\pi\tau} \left(\frac{\Delta E_s}{\Delta E_t} \right)^2 \quad \text{Equation M-7}$$

where τ is the duration of the current pulse (s), R is the particle radius with the assumption of spherical particles, ΔE_s is the steady-state voltage change, due to the current pulse and ΔE_t is the voltage change during the constant current pulse. This following formula has been applied to each steps in order to obtain the D_{app}/R^2 ratio during the discharge.²³²

o Potentiostatic Intermittent Titration Technique (PITT)

The PITT procedure is based on a staircase potential signal applied to the system, as represented in the Figure M-19a. In the case of a planar electrode, Montella demonstrated that the current response of the system is dictated by the well known Cottrell relationship for short times and an exponential decay of diffusion current with respect to time for long times, if a restricted diffusion condition and diffusion control (very fast insertion reaction kinetics) are assumed.²³³

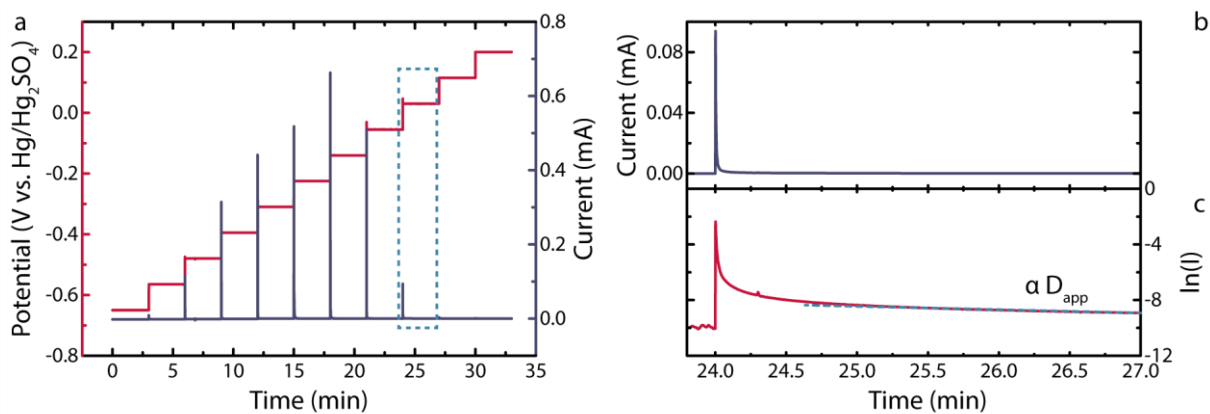


Figure M-19 : Apparent coefficient diffusion determination by PITT of K⁺ in Prussian Blue film (100 nm) in K₂SO₄ 0.25 mol.L⁻¹ aqueous electrolyte. (a) Applied potential staircases and current response of the system. Focus on (b) the current response and (c) the natural logarithm of the current response for the 0.030 V vs. Hg/Hg₂SO₄ staircase.

For short times, *i.e.* $t \ll \frac{L^2}{\pi^2 D_{app}}$,

$$I_d(t)_{st} = I_{Cottrell}(t) = - \frac{FA\sqrt{D_{app}}\Delta c}{\sqrt{\pi t}} \quad \text{Equation M-8}$$

For long times, *i.e.* $t \gg \frac{L^2}{\pi^2 D_{app}}$,

$$I_d(t)_{it} = 2FA \frac{D_{app}}{L} \Delta c \exp\left(-\frac{\pi^2 D_{app}}{4L^2} t\right) \quad \text{Equation M-9}$$

where F is the Faraday's constant (96485 C.mol^{-1}), A is the specific surface area (0.196 cm^2), Δc is the concentration variation in the film (mol.cm^{-3}), L is the film thickness (cm) and D_{app} is the apparent diffusion coefficient in the solid phase ($\text{cm}^2.\text{s}^{-1}$).

Then the apparent diffusion coefficient can be extracted from slope of the natural logarithm of the Equation M-9 (Figure M-19b and c), as it is independent of unknown variables.

$$\ln(I_d(t)_{it}) = \ln\left(2FA \frac{D_{app}}{L} \Delta c\right) - \frac{\pi^2 D_{app}}{4L^2} t \quad \text{Equation M-10}$$

This procedure permits to obtain the apparent diffusion coefficient of the inserted cation in the solid phase at different potentials.

○ Randles-Sevcik equation

The last procedure used to extract the apparent diffusion coefficient of the inserted cation in the solid phase was based on the Randles-Sevcik equation. To fulfill the conditions of validity of this equation, the diffusion length of the inserted cation within the host material needs to be much smaller than the smallest dimension of the material such that the cation gradient can be considered as a semi-infinite linear diffusion-like process normal to the material interface. Then, assuming a Nernstian redox reaction (*i.e.* a fast reversible electron transfer reaction), the absolute current peak value has a linear relationship (in oxidation and reduction) to the square root of the scan rate of the cyclic voltammetry, following this equation:²¹⁷

$$I_p = 0.4463 FS \sqrt{\frac{F}{RT} \frac{S_e}{S}} \sqrt{D_{app}} \chi C_{mat} \nu^{1/2} \quad \text{Equation M-11}$$

where F is the Faraday's constant (96485 C.mol^{-1}), R is the gas constant ($\text{J.K}^{-1}.\text{mol}^{-1}$), T is the temperature (K), S_e and S are the specific surface and geometric area, respectively (cm^2), x is the maximal mole fraction of inserted cation that can be inserted in the host material, C_{mat} is the concentration of the host material (mol.cm^{-3}), ν is the scan rate (V.s^{-1}), I_p is the value of the current peak (A) and D_{app} is the apparent diffusion coefficient of the inserted cation in the solid phase ($\text{cm}^2.\text{s}^{-1}$). An example of this procedure is represented in the following Figure M-20.

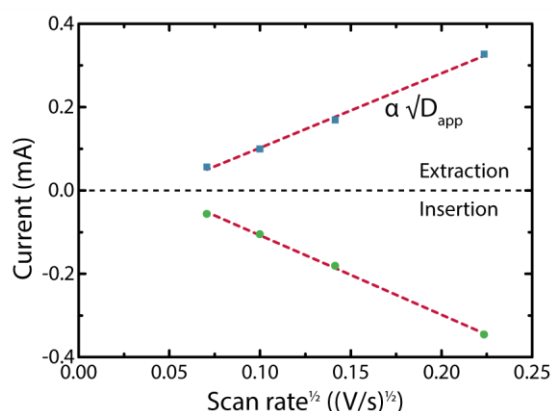


Figure M-20: Apparent diffusion coefficient determination of K^+ during insertion and extraction in a Prussian Blue film (100 nm) in K_2SO_4 0.25 mol.L^{-1} aqueous electrolyte by the Randles-Sevcik equation.

M.3 – Electrochemical-gravimetric analysis

M.3.a – EQCM electrode preparation

AT-cut 9 MHz quartz resonators patterned with gold electrodes on both sides were used as EQCM electrodes (SEIKO, $8.95 \text{ MHz} \pm 50 \text{ kHz}$, QA-A9M-AU(M)). The electroactive geometric surface area was equal to 0.196 cm^2 . The selected active material was mixed with 18 wt % Csp (Timcal) and 10 wt % PVDF-HFP (Kynar, Arkema) in 1-Methyl-2-pyrrolidinone (99.5 %, Alfa Aesar) by ultrasonication (Qsonica) to obtain a homogenous slurry with a concentration of 1 mg/mL . NMP is not prone to evaporation which is advantageous, considering the elevation of temperature during the ultrasonication step. The vial can also be cooled down with an ice bath. Then a $300 \mu\text{L}$ volume of slurry was spray casted with an airbrush (Timbertech, nozzle 0.5 mm) at a pressure of 4 bars on the gold electrode of the quartz

resonators. The resonator, placed in a mask exposing only the gold surface area, was kept at 140 °C on a hot plate to permit rapid solvent evaporation. This step was followed by a heating treatment on the hot plate at 200 °C during 1 h to enable the spreading of the PVDF-HFP ($T_{\text{melting}} = 180$ °C) on the surface of EQCM electrode. The electrode preparation was concluded by a treatment at 120 °C during 1 h under vacuum (Glass oven B-585 Drying, BUCHI) to displace the evaporation equilibrium of the non-volatile solvent. The resonant frequency (f) and the motional resistance (R) of the composite electrode was measured beforehand and after the casting protocol and frequency change between these two steps (Δf) are used to obtain the electrode loading, using Equation II-5. The morphology of the prepared film was checked by FEG-SEM. Prussian Blue films were directly prepared by electrodeposition on the EQCM resonator.

M.3.b – Airtight EQCM cell testing workbench

A labmade cell was designed specifically for EQCM measurements with its unique role of being used either with aqueous or organic electrolyte and was developed conjointly by CSE lab and Sphere ENERGY (presented in the Chapter III). The prepared quartz resonator was mounted between two perfluoroelastomer O-rings known for their non-swelling behavior in organic electrolyte. To check airtightness, the cell was sealed after injecting 500 μL of anhydrous dimethyl sulfoxide (H_2O 10 ppm, > 99.9 %, Sigma-Aldrich) inside an Ar filled glovebox ($\text{O}_2 < 0.1$ ppm, $\text{H}_2\text{O} < 0.1$ ppm). Then, the cell was kept outside the glovebox under ambient condition, for different time frames. With the aim of quantifying the water uptake, the solvent was withdrawn from the cell and injected with a syringe in a Karl Fischer titrator (899 Coulometer, Metrohm). The cell impedance was also measured by impedance spectroscopy using a SP-200 potentiostat (BioLogic) from 1 MHz to 100 mHz with 7 points per decade. The spectrum has been fitted with Z-fit software. To interrogate the cell thermal compartment, the resonant frequency change was measured in response to temperature stimuli from 25 to 45 °C using a temperature controlled oven (UN30, Memmert). The cell renderings were performed with the Autodesk Fusion 360 software.

M.3.c – Verification of hydrodynamic and viscoelastic properties in electrolyte

The previously described spray casting protocol has been applied to prepare films of active material with loading between 40-60 $\mu\text{g}\cdot\text{cm}^{-2}$ on Au-coated quartz resonator with fundamental frequency of 9 MHz (Advanced Wave Sensors S.L., Spain) and electroactive geometric surface equal to 0.196 cm^2 .

The resonant frequency, f , and the absolute dissipation factor, D , of the bare and loaded resonator in air were recorded at the different overtones with an Agilent 4294A impedance analyzer. The resonant frequency was obtained from the maximum of the electroacoustic admittance and the typical Butterworth-Van Dyke (BVD) equivalent circuit was used to fit this admittance to extract the values of the different component, defined in the Figure II-4a and Equation II-8. Then, the absolute dissipation factor was estimated thanks to the Equation II-13. The absolute dissipation factor, measured from the 3rd to the 11th overtone (total of 5), has been replaced by the resonant width thanks to Equation II-12. Then, the resonant frequency and the resonant width of the loaded resonator in electrolyte under Open-Circuit Potential (OCP) was recorded at the different overtones with an AWS A20 Platform (Advanced Wave Sensors S.L., Spain) to be compared with their analogous values of the loaded resonator in air.

Shifts of frequency and resonance widths are calculated to that of the coating in air rather than to the bare crystal and are normalized by overtone order as well as by $\rho_l f_0^2$ where ρ_l is the density of the liquid (approximated to the neat solvent) and f_0 is the fundamental frequency ($n = 1$). The data have been plotted as a function of the penetration depth δ , which characterizes the decay length of the shear wave across the boundary layer between the resonator and the electrolyte (Equation II-6). A Matlab script was developed to facilitate the data treatment between Network analyzer and dissipation monitoring measurements at different overtones.

M.3.d – Electrochemical-gravimetric measurements

The specifically designed EQCM cell was kept at 25 °C during the experiment thanks to a temperature-controlled oven. A commercial SEIKO QCM922A microbalance (Figure II-7b)

was connected to the cell through a BNC cable to monitor the resonance frequency change (Δf) along with the motional resistance (R) during the electrochemical processes. The microbalance was coupled with a SP-200 potentiostat (Bio-Logic SAS) in the “WE to ground” configuration, which permitted the recording of microbalance outputs and the realization of simultaneous electrochemical measurements, as depicted in the Figure II-7c. Finally, a computer centralized the control over the electrochemical and gravimetric measurements.

Prior to the measurement, the EQCM was calibrated to determine the experimental sensitivity coefficient (*i.e.* proportionality constant between the change of quartz frequency and change of mass) in the Sauerbrey equation (Equation II-5). The deposition electrolyte was a 0.05 mol.L⁻¹ CuSO₄ (> 99 %, Sigma-Aldrich) and 0.5 mol.L⁻¹ H₂SO₄ (98 %, Sigma-Aldrich) solution. The frequency change was measured during the electrodeposition process (galvanostatic or by using cyclic voltammetry) and the mass change is estimated thanks to the measured charge, Q , and the Faraday’s law, assuming reaction yield of 100 %.

The electrodes were cycled in the desired electrolyte: organic or aqueous. For both media, the EQCM electrode was used as the working electrode. For aqueous electrolyte, a 3 mm diameter graphite rod (Sigma-Aldrich) and Hg/Hg₂SO₄ (saturated K₂SO₄) were used as the counter and the reference electrodes, respectively. Whereas for organic electrolyte, lithium or potassium metal (99.9 %, Sigma-Aldrich) of 5 and 2 mm were punched to be used as both counter and reference electrodes. All the cell parts were dried overnight at 80 °C before being assembled in an Ar-filled glovebox (MBraun, O₂ and H₂O < 0.1 ppm), before each experiment using non-aqueous electrolytes.

M.3.e – Ac-electrogravimetry

Ac-electrogravimetry measurements were carried out by using a four-channel frequency response analyzer (Solartron 1254 FRA) and a laboratory-made potentiostat and QCM. The QCM was used under dynamic regime, working electrode (gold patterned quartz resonator) was polarized at a selected potential, and a small-amplitude potential perturbation (40 mV rms) was superimposed. The frequency range was between 63 kHz and 10 MHz for the potential modulation. The microbalance frequency change, Δf_w , corresponding to the mass

response, Δm , of the working electrode was measured simultaneously with the current response of the electrochemical system. It should be noted that the microbalance frequency change, Δf_w is generally around tens of hertz while the carrier frequency, f_m , is around 9 MHz (for a resonator operating at 9 MHz). In order to have a higher level of performance of the frequency/voltage (f/V) converter, the carrier frequency is reduced to a few hundred hertz (generally ≈ 400 Hz). Herein, a reference frequency synthesizer (Marconi Instrument 2023) is used to obtain a frequency difference of ≈ 400 Hz between the microbalance quartz frequency (f_w) and that of the reference synthesizer (f_{ref}) and becomes ($f_{ref} - f_w$).

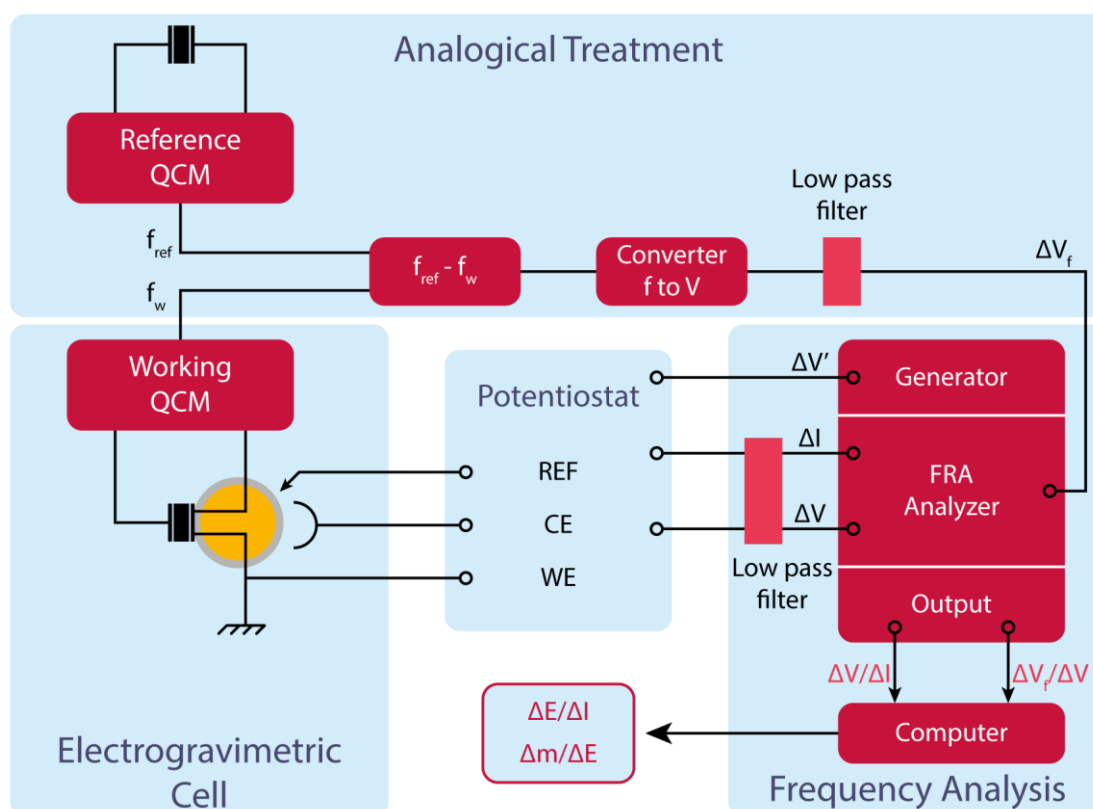


Figure M-21: Schematic representation of the different systems composing the *ac*-electrogravimetry setup at the *Laboratoire Interfaces et Systèmes Electrochimiques, Sorbonne University, Paris*.

One of the most important components of the experimental set-up is the f/V converter, where the analog processing is obtained by means of a phase lock loop circuit (Figure M-21). Through this component, the microbalance frequency signal is translated into the voltage signal and sent to the Frequency Response Analyzer, in the form of ΔV_f . Then, two main raw transfer functions (TFs), $\Delta V_f/\Delta V(\omega)$ (related to the electrogravimetric TF) and $\Delta V/\Delta I(\omega)$ (related to the classical impedance TF) are obtained simultaneously at a given

potential and frequency modulation, f (pulsation $\omega = 2\pi f$). In these raw TFs, ΔV is the raw potential response, which takes into account the electrolyte resistance ($\Delta E = \Delta V - (R_{el} \times \Delta I)$).

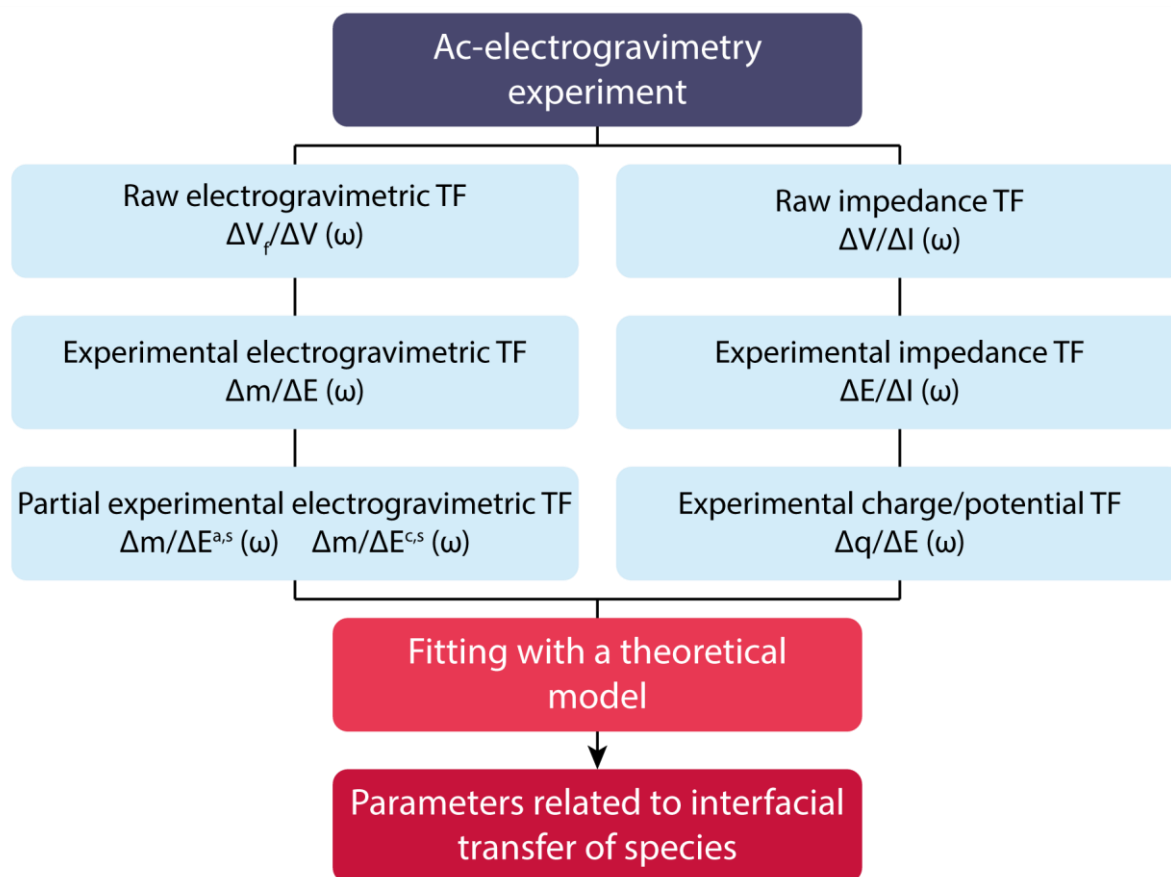


Figure M-22: Ac-electrogravimetry data treatment roadmap.

The Figure M-22 shows the road map of how to obtain main experimental TFs from an *ac*-electrogravimetry experiment (shown for a cation (c), an anion (a) and solvent (s)). Mathcad Software version 15 (PTC) was used to calculate the experimental electrogravimetric TF $(\Delta m/\Delta E)(\omega)$ and the classical electrochemical impedance $(\Delta E/\Delta I)(\omega)$, from the raw TFs $\Delta V_f/\Delta V(\omega)$ and $\Delta V/\Delta I(\omega)$, respectively. The experimental TFs given above are fitted with the theoretical expressions defined in a model based on the interfacial flux of species under polarization, using the Mathcad script. Relevant parameters regarding the nature of the species transferred (atomic weight, M_i , for i = cation, anion or solvent), together with their interfacial transfer dynamics (K_i), transfer resistance ($Rt_i = \frac{1}{FG_i}$) and their concentration variation (ΔC_i) in the electrode are estimated. The interface is characterized at different working potentials thanks to this procedure.²³⁴

M.4 – Classical Molecular Dynamics simulations

Classical MD simulations of 1 mol.L⁻¹ LiClO₄ in H₂O and in propylene carbonate (PC) between two planar Au(100) electrodes at a fixed potential difference of 0V have been performed with the MetalWalls code.²³⁵ Each electrode is made of 5 layers, 162 Au atoms each, while the electrolyte is composed of 100 LiClO₄ ion pairs and 5500 H₂O molecules for the aqueous system and of 100 LiClO₄ ion pairs and 1170 PC molecules for the non-aqueous system.

The SPC/E²³⁶ model was chosen for water, while force field parameters for PC were taken from OPLS²³⁷ with scaled charges adopted in Chaudhari *et al.*²³⁸ The Lennard-Jones parameters for Li⁺ were taken from OPLS,²³⁷ while force field parameters for ClO₄⁻ from Liu *et al.*²³⁹ Finally, Lennard-Jones parameters introduced by Heinz *et al.* were adopted for Au(100).²⁴⁰ Mixed Lennard–Jones parameters for all of the different atom types were obtained using the Lorentz–Berthelot combination rules.

2D periodic boundary conditions have been employed, with no periodicity on the direction normal to the Au surface and box dimensions along x and y directions of L_x = L_y = 36.63 Å. Electrostatic interactions were computed using a 2D Ewald summation method, with a cut-off of 12 Å for the short-range part. The simulation boxes were equilibrated at constant atmospheric pressure by applying a constant pressure force to the electrodes. The electrodes separation was then fixed to the equilibrium value of 128.0 Å and 129.5 Å for LiClO₄ in H₂O and LiClO₄ in PC, respectively. An equilibration run of 2 ns in the NVT ensemble (T = 298 K) has been then performed. After equilibration, production runs of 17 ns and 36 ns for LiClO₄ in H₂O and in PC, respectively, have been collected in the NVT ensemble (T = 298 K) using a timestep of 1 fs.

Glossary

AM	Active material
BET	Brunauer, Emmet and Teller analysis
BVD	Butterworth-Van Dyke
CCUS	Carbon Capture Utilization and Storage
CEI	Cathode Electrolyte Interphase
Csp	Carbon Super P
CV	Cyclic voltammetry
DEC	Diethyl carbonate
DEMS	Differential Electrochemical Mass Spectroscopy
DMC	Dimethyl carbonate
EC	Ethylene carbonate
EDL	Electrochemical double layer
EEL	Electrode-electrolyte interface
EIS	Electrochemical Impedance Spectroscopy
EMC	Ethyl methyl carbonate
EQCM	Electrochemical Quartz Crystal Microbalance
ESI-MS	ElectroSpray Ionization Mass Spectroscopy
FEG-SEM	Field Emission Gun - Scanning Electron Microscopy
GCD	Galvanostatic charge/discharge
GCPL	Galvanostatic cycling with potential limitation
GITT	Galvanostatic Intermittent Titration Technique
H	Proton
H ₂ O	Water
H ₃ O ⁺	Hydronium
HClO ₄	Perchloric acid
HF	High frequency
HOMO	Highest occupied molecular orbital
IHP	Inner Helmholtz Plane

Glossary

K	Potassium
K ₂ SO ₄	Potassium sulfate
KPF ₆	Potassium hexafluorophosphate
LCO	LiCoO ₂
LF	Low frequency
LFP	LiFePO ₄
Li	Lithium
LiBOB	Lithium bis(oxalate)borate
LiClO ₄	Lithium perchlorate
LiPF ₆	Lithium hexafluorophosphate
LiTFSI	Lithium bis(trifluoromethanesulfonyl)imide
LMO	LiMn ₂ O ₄
LTO	Li ₄ Ti ₅ O ₁₂
LUMO	Lowest unoccupied molecular orbital
MF	Middle frequency
Na	Sodium
NA	Network analyzer
NiMH	Nickel-metal hydride
NMC	LiNi _x Co _y Mn _z O ₂
NMP	1-Methyl-2-pyrrolidinone
NMR	Nuclear Magnetic Resonance spectroscopy
OCP	Open-Circuit Potential
OEMS	Online Electrochemical Mass Spectrometry
OHP	Outer Helmholtz Plane
PB	Prussian Blue
PC	Propylene carbonate
PFA	Perfluoroalkoxy
PITT	Potentiostatic Intermittent Titration Technique
PP	Polypropylene
PTFE	Polytetrafluoroethylene
PVD	Physical vapor deposition

PVDF	Polyvinylidene fluoride
PVDF-HFP	Poly(vinylidene fluoride)-co-hexafluoropropylene
QCM	Quartz Crystal Microbalance
QCM-D	Quartz Crystal Microbalance with dissipation monitoring
QCM-R	Quartz Crystal Microbalance with motional resistance monitoring
SEI	Solid Electrolyte Interphase
SLI	Start Light and Ignition
Solar PV	Solar Photovoltaic
TF	Transfer function
TGA	Thermogravimetric analysis
VFT	Vacuum filtration-and-transfer
XAS	X-ray absorption spectroscopy
XRD	X-ray diffraction

Glossary

A	Piezoelectrically active area	0.196 cm ²
C _f	Sensitivity factor or calibration factor	1.20 ng/Hz
c _q	Transverse velocity in AT-cut quartz	3.34 10 ⁵ cm.s ⁻¹
D	Dissipation factor	
D _{app}	Apparent diffusion coefficient	cm ² .s ⁻¹
e	Elementary charge	1.60 10 ⁻¹⁹ C
e ₂₆	Piezoelectric stress coefficient	9.65 10 ⁻² A.s.m ⁻²
F	Faraday constant	96485 C.mol ⁻¹
f ₀	Resonant frequency of the fundamental	MHz
G	Inverse of the transfer resistance	mol.v ⁻¹ .s ⁻¹ .cm ⁻²
I	Electrolyte ionic strength	mol.L ⁻¹
K	Kinetics of transfer	cm.s ⁻¹
k _B	Boltzmann constant	1.38 10 ⁻²³ J.K ⁻¹
M	Molar mass	g.mol ⁻¹
n	Overtone number	
N _A	Avogadro constant	6.02 10 ²³ mol ⁻¹
Q _{ox}	Measured charge in oxidation	C
R	Particle radius	m
R	Gas constant	8.314 J.K ⁻¹ .mol ⁻¹
R _t	Interfacial transfer resistance	Ω.cm ²
S	Specific surface area	cm ²
T _b	Boiling point	°C
T _m	Melting point	°C
V _m	Molar volume	cm ³ .mol ⁻¹
W	Bandwidth	Hz
Γ	Half-bandwidth	Hz
Δf	Frequency change	Hz
Δm	Mass change	ng
δ _n	Penetration depth	nm
ε ₀	Vacuum permittivity	8.84 10 ⁻¹² F.m ⁻¹
ε _R	Relative dielectric constant	

η_l	Dynamic viscosity	mPa.s
λ_D	Debye length	nm
μ_q	Shear modulus of the quartz crystal	$2.947 \cdot 10^{11} \text{ g.cm}^{-1}.\text{s}^{-2}$
ν	Scan rate	V.s^{-1}
ρ_l	Volumetric mass density	g.cm^{-3}
ρ_q	Density of quartz	2.648 g.cm^{-3}

References

- (1) United Nations. *Adoption Of The Paris Agreement* **2015**.
- (2) Royal Society. *Climate change: A Summary of the Science* **2010**.
- (3) National Oceanic and Atmospheric Administration. *State of the Climate: Global Climate* **2019**.
- (4) International Energy Agency. *World Energy Outlook* **2019**.
- (5) Ritchie, H.; Roser, M. *Energy, Our World in Data* **2020**.
- (6) BP. *Statistical Review of World Energy* **2019**.
- (7) Avicenne Energy. *The Rechargeable Battery Market and Main Trends 2018-2030* **2019**.
- (8) International Energy Agency. *Global EV Outlook* **2019**.
- (9) Volta, A. XVII. On the Electricity Excited by the Mere Contact of Conducting Substances of Different Kinds. In a Letter from Mr. Alexander Volta, F. R. S. Professor of Natural Philosophy in the University of Pavia, to the Rt. Hon. Sir Joseph Banks, Bart. K.B. P. R. S. *Philosophical Transactions of the Royal Society of London* **1800**, 90, 403–431. <https://doi.org/10.1098/rstl.1800.0018>.
- (10) Leclanché, G. *Quelques observations sur l'emploi des piles électriques*; 1867.
- (11) Whittingham, M. S. History, Evolution, and Future Status of Energy Storage. *Proceedings of the IEEE* **2012**, 100 (Special Centennial Issue), 1518–1534. <https://doi.org/10.1109/JPROC.2012.2190170>.
- (12) Placke, T.; Kloepsch, R.; Dühnen, S.; Winter, M. Lithium Ion, Lithium Metal, and Alternative Rechargeable Battery Technologies: The Odyssey for High Energy Density. *J Solid State Electrochem* **2017**, 21 (7), 1939–1964. <https://doi.org/10.1007/s10008-017-3610-7>.
- (13) Tarascon, J.-M.; Armand, M. Issues and Challenges Facing Rechargeable Lithium Batteries. *Nature* **2001**, 414 (6861), 359–367. <https://doi.org/10.1038/35104644>.
- (14) Schmuch, R.; Wagner, R.; Hörpel, G.; Placke, T.; Winter, M. Performance and Cost of Materials for Lithium-Based Rechargeable Automotive Batteries. *Nat Energy* **2018**, 3 (4), 267–278. <https://doi.org/10.1038/s41560-018-0107-2>.
- (15) Kubota, K.; Dahbi, M.; Hosaka, T.; Kumakura, S.; Komaba, S. Towards K-Ion and Na-Ion Batteries as “Beyond Li-Ion.” *The Chemical Record* **2018**, 18 (4), 459–479. <https://doi.org/10.1002/tcr.201700057>.
- (16) Rouxel, J.; Danot, M.; Bichon, M. Les Composites Intercalaires NaxTiS₂. Etude Générale Des Phases NaxTiS₂ et KxTiS₂. *Bull Soc Chim* **1971**, 11, 3930–3936.
- (17) Whittingham, M. S. Intercalation Chemistry and Energy Storage. *Journal of Solid State Chemistry* **1979**, 29 (3), 303–310. [https://doi.org/10.1016/0022-4596\(79\)90187-7](https://doi.org/10.1016/0022-4596(79)90187-7).
- (18) Whittingham, M. S. Electrical Energy Storage and Intercalation Chemistry. *Science* **1976**, 192 (4244), 1126–1127. <https://doi.org/10.1126/science.192.4244.1126>.
- (19) Whittingham, M. S. Chalcogenide Battery. US4009052A, February 22, 1977.
- (20) Blomgren, G. E. The Development and Future of Lithium Ion Batteries. *J. Electrochem. Soc.* **2016**, 164 (1), A5019. <https://doi.org/10.1149/2.0251701jes>.
- (21) Lazzari, M.; Scrosati, B. A Cyclable Lithium Organic Electrolyte Cell Based on Two Intercalation Electrodes. *J. Electrochem. Soc.* **1980**, 127 (3), 773. <https://doi.org/10.1149/1.2129753>.

References

- (22) Mizushima, K.; Jones, P. C.; Wiseman, P. J.; Goodenough, J. B. Li_xCoO_2 ($0 < x < 1$): A New Cathode Material for Batteries Oh High Energy Density. *Materials Research Bulletin* **1980**, *15* (6), 783–789. [https://doi.org/10.1016/0025-5408\(80\)90012-4](https://doi.org/10.1016/0025-5408(80)90012-4).
- (23) Yazami, R.; Touzain, Ph. A Reversible Graphite-Lithium Negative Electrode for Electrochemical Generators. *Journal of Power Sources* **1983**, *9* (3), 365–371. [https://doi.org/10.1016/0378-7753\(83\)87040-2](https://doi.org/10.1016/0378-7753(83)87040-2).
- (24) Basu, S. Ambient Temperature Rechargeable Battery. US4423125A, December 27, 1983.
- (25) Yoshino, A.; Sanechika, K.; Nakajima, T. Secondary Battery. US4668595A, May 26, 1987.
- (26) Yoshino, A. The Birth of the Lithium-Ion Battery. *Angewandte Chemie International Edition* **2012**, *51* (24), 5798–5800. <https://doi.org/10.1002/anie.201105006>.
- (27) Fujimoto, M.; Yoshinaga, N.; Ueno, K.; Furukawa, N.; Nohma, T.; Takahashi, M. Lithium Secondary Battery. US5686138A, November 11, 1997.
- (28) Fong, R.; Sacken, U. von; Dahn, J. R. Studies of Lithium Intercalation into Carbons Using Nonaqueous Electrochemical Cells. *J. Electrochem. Soc.* **1990**, *137* (7), 2009. <https://doi.org/10.1149/1.2086855>.
- (29) Guyomard, D.; Tarascon, J. M. Rechargeable $\text{Li}_{1+x}\text{Mn}_2\text{O}_4$ / Carbon Cells with a New Electrolyte Composition: Potentiostatic Studies and Application to Practical Cells. *J. Electrochem. Soc.* **1993**, *140* (11), 3071. <https://doi.org/10.1149/1.2220987>.
- (30) Zhang, H.; Li, C.; Eshetu, G. G.; Laruelle, S.; Grugeon, S.; Zaghbi, K.; Julien, C.; Mauger, A.; Guyomard, D.; Rojo, T.; Gisbert-Trejo, N.; Passerini, S.; Huang, X.; Zhou, Z.; Johansson, P.; Forsyth, M. From Solid-Solution Electrodes and the Rocking-Chair Concept to Today's Batteries. *Angewandte Chemie International Edition* **2020**, *59* (2), 534–538. <https://doi.org/10.1002/anie.201913923>.
- (31) Xie, J.; Lu, Y.-C. A Retrospective on Lithium-Ion Batteries. *Nat Commun* **2020**, *11* (1), 2499. <https://doi.org/10.1038/s41467-020-16259-9>.
- (32) The Royal Swedish Academy of Sciences. The Nobel Prize in Chemistry 2019. [nobelprize.org](https://www.nobelprize.org).
- (33) Grosjean, C.; Miranda, P. H.; Perrin, M.; Poggi, P. Assessment of World Lithium Resources and Consequences of Their Geographic Distribution on the Expected Development of the Electric Vehicle Industry. *Renewable and Sustainable Energy Reviews* **2012**, *16* (3), 1735–1744. <https://doi.org/10.1016/j.rser.2011.11.023>.
- (34) Carmichael, R. S. *Practical Handbook of Physical Properties of Rocks and Minerals*; CRC Press, 1988.
- (35) Speirs, J.; Contestabile, M.; Houari, Y.; Gross, R. The Future of Lithium Availability for Electric Vehicle Batteries. *Renewable and Sustainable Energy Reviews* **2014**, *35*, 183–193. <https://doi.org/10.1016/j.rser.2014.04.018>.
- (36) Larcher, D.; Tarascon, J.-M. Towards Greener and More Sustainable Batteries for Electrical Energy Storage. *Nat. Chem.* **2015**, *7* (1), 19–29. <https://doi.org/10.1038/nchem.2085>.
- (37) Armand, M.; Tarascon, J.-M. Building Better Batteries. *Nature* **2008**, *451* (7179), 652–657. <https://doi.org/10.1038/451652a>.
- (38) Yabuuchi, N.; Kubota, K.; Dahbi, M.; Komaba, S. Research Development on Sodium-Ion Batteries. *Chem. Rev.* **2014**, *114* (23), 11636–11682. <https://doi.org/10.1021/cr500192f>.
- (39) Braconnier, J.-J.; Delmas, C.; Fouassier, C.; Hagenmuller, P. Comportement electrochimique des phases Na_xCoO_2 . *Materials Research Bulletin* **1980**, *15* (12), 1797–1804. [https://doi.org/10.1016/0025-5408\(80\)90199-3](https://doi.org/10.1016/0025-5408(80)90199-3).

- (40) Eftekhari, A. Potassium Secondary Cell Based on Prussian Blue Cathode. *Journal of Power Sources* **2004**, *126* (1–2), 221–228. <https://doi.org/10.1016/j.jpowsour.2003.08.007>.
- (41) Hwang, J.-Y.; Myung, S.-T.; Sun, Y.-K. Recent Progress in Rechargeable Potassium Batteries. *Advanced Functional Materials* **2018**, *28* (43). <https://doi.org/10.1002/adfm.201802938>.
- (42) Jian, Z.; Luo, W.; Ji, X. Carbon Electrodes for K-Ion Batteries. *J. Am. Chem. Soc.* **2015**, *137* (36), 11566–11569. <https://doi.org/10.1021/jacs.5b06809>.
- (43) Komaba, S.; Hasegawa, T.; Dahbi, M.; Kubota, K. Potassium Intercalation into Graphite to Realize High-Voltage/High-Power Potassium-Ion Batteries and Potassium-Ion Capacitors. *Electrochemistry Communications* **2015**, *60*, 172–175. <https://doi.org/10.1016/j.elecom.2015.09.002>.
- (44) Luo, W.; Wan, J.; Ozdemir, B.; Bao, W.; Chen, Y.; Dai, J.; Lin, H.; Xu, Y.; Gu, F.; Barone, V.; Hu, L. Potassium Ion Batteries with Graphitic Materials. *Nano Lett.* **2015**, *15* (11), 7671–7677. <https://doi.org/10.1021/acs.nanolett.5b03667>.
- (45) Stevens, D. A.; Dahn, J. R. High Capacity Anode Materials for Rechargeable Sodium-Ion Batteries. *J. Electrochem. Soc.* **2000**, *147* (4), 1271. <https://doi.org/10.1149/1.1393348>.
- (46) Komaba, S.; Murata, W.; Ishikawa, T.; Yabuuchi, N.; Ozeki, T.; Nakayama, T.; Ogata, A.; Gotoh, K.; Fujiwara, K. Electrochemical Na Insertion and Solid Electrolyte Interphase for Hard-Carbon Electrodes and Application to Na-Ion Batteries. *Advanced Functional Materials* **2011**, *21* (20), 3859–3867. <https://doi.org/10.1002/adfm.201100854>.
- (47) Dahbi, M.; Yabuuchi, N.; Kubota, K.; Tokiwa, K.; Komaba, S. Negative Electrodes for Na-Ion Batteries. *Phys. Chem. Chem. Phys.* **2014**, *16* (29), 15007–15028. <https://doi.org/10.1039/C4CP00826J>.
- (48) Deng, J.; Luo, W.-B.; Chou, S.-L.; Liu, H.-K.; Dou, S.-X. Sodium-Ion Batteries: From Academic Research to Practical Commercialization. *Advanced Energy Materials* **2018**, *8* (4), 1701428. <https://doi.org/10.1002/aenm.201701428>.
- (49) Mariyappan, S.; Wang, Q.; Tarascon, J. M. Will Sodium Layered Oxides Ever Be Competitive for Sodium Ion Battery Applications? *J. Electrochem. Soc.* **2018**, *165* (16), A3714–A3722. <https://doi.org/10.1149/2.0201816jes>.
- (50) Vaalma, C.; Buchholz, D.; Passerini, S. Non-Aqueous Potassium-Ion Batteries: A Review. *Current Opinion in Electrochemistry* **2018**, *9*, 41–48. <https://doi.org/10.1016/j.coelec.2018.03.031>.
- (51) Tarascon, J.-M. Na-Ion versus Li-Ion Batteries: Complementarity Rather than Competitiveness. *Joule* **2020**. <https://doi.org/10.1016/j.joule.2020.06.003>.
- (52) Simon, P.; Gogotsi, Y.; Dunn, B. Where Do Batteries End and Supercapacitors Begin? *Science* **2014**, *343* (6176), 1210–1211. <https://doi.org/10.1126/science.1249625>.
- (53) Shao, Y.; El-Kady, M. F.; Sun, J.; Li, Y.; Zhang, Q.; Zhu, M.; Wang, H.; Dunn, B.; Kaner, R. B. Design and Mechanisms of Asymmetric Supercapacitors. *Chem. Rev.* **2018**, *118* (18), 9233–9280. <https://doi.org/10.1021/acs.chemrev.8b00252>.
- (54) Costentin, C.; Porter, T. R.; Savéant, J.-M. How Do Pseudocapacitors Store Energy? Theoretical Analysis and Experimental Illustration. *ACS Appl. Mater. Interfaces* **2017**, *9* (10), 8649–8658. <https://doi.org/10.1021/acsami.6b14100>.
- (55) Costentin, C.; Porter, T. R.; Savéant, J.-M. Nature of Electronic Conduction in “Pseudocapacitive” Films: Transition from the Insulator State to Band-Conduction. *ACS Appl. Mater. Interfaces* **2019**, *11* (32), 28769–28773. <https://doi.org/10.1021/acsami.9b05240>.

References

- (56) Grahame, D. C. Properties of the Electrical Double Layer at a Mercury Surface. I. Methods of Measurement and Interpretation of Results. *J. Am. Chem. Soc.* **1941**, *63* (5), 1207–1215. <https://doi.org/10.1021/ja01850a014>.
- (57) Conway, B. E.; Gileadi, E. Kinetic Theory of Pseudo-Capacitance and Electrode Reactions at Appreciable Surface Coverage. *Trans. Faraday Soc.* **1962**, *58* (0), 2493–2509. <https://doi.org/10.1039/TF9625802493>.
- (58) Srinivasan, S.; Gileadi, E. The Potential-Sweep Method: A Theoretical Analysis. *Electrochimica Acta* **1966**, *11* (3), 321–335. [https://doi.org/10.1016/0013-4686\(66\)87043-3](https://doi.org/10.1016/0013-4686(66)87043-3).
- (59) Trasatti, S.; Buzzanca, G. Ruthenium Dioxide: A New Interesting Electrode Material. Solid State Structure and Electrochemical Behaviour. *Journal of Electroanalytical Chemistry and Interfacial Electrochemistry* **1971**, *29* (2), A1–A5. [https://doi.org/10.1016/S0022-0728\(71\)80111-0](https://doi.org/10.1016/S0022-0728(71)80111-0).
- (60) Ardizzone, S.; Fregonara, G.; Trasatti, S. “Inner” and “Outer” Active Surface of RuO₂ Electrodes. *Electrochimica Acta* **1990**, *35* (1), 263–267. [https://doi.org/10.1016/0013-4686\(90\)85068-X](https://doi.org/10.1016/0013-4686(90)85068-X).
- (61) Lee, H. Y.; Goodenough, J. B. Supercapacitor Behavior with KCl Electrolyte. *Journal of Solid State Chemistry* **1999**, *144* (1), 220–223. <https://doi.org/10.1006/jssc.1998.8128>.
- (62) Snook, G. A.; Kao, P.; Best, A. S. Conducting-Polymer-Based Supercapacitor Devices and Electrodes. *Journal of Power Sources* **2011**, *196* (1), 1–12. <https://doi.org/10.1016/j.jpowsour.2010.06.084>.
- (63) Augustyn, V.; Come, J.; Lowe, M. A.; Kim, J. W.; Taberna, P.-L.; Tolbert, S. H.; Abruña, H. D.; Simon, P.; Dunn, B. High-Rate Electrochemical Energy Storage through Li⁺ Intercalation Pseudocapacitance. *Nature Mater* **2013**, *12* (6), 518–522. <https://doi.org/10.1038/nmat3601>.
- (64) Naguib, M.; Kurtoglu, M.; Presser, V.; Lu, J.; Niu, J.; Heon, M.; Hultman, L.; Gogotsi, Y.; Barsoum, M. W. Two-Dimensional Nanocrystals Produced by Exfoliation of Ti₃AlC₂. *Advanced Materials* **2011**, *23* (37), 4248–4253. <https://doi.org/10.1002/adma.201102306>.
- (65) Fleischmann, S.; Mitchell, J. B.; Wang, R.; Zhan, C.; Jiang, D.; Presser, V.; Augustyn, V. Pseudocapacitance: From Fundamental Understanding to High Power Energy Storage Materials. *Chem. Rev.* **2020**. <https://doi.org/10.1021/acs.chemrev.0c00170>.
- (66) Augustyn, V.; Simon, P.; Dunn, B. Pseudocapacitive Oxide Materials for High-Rate Electrochemical Energy Storage. *Energy Environ. Sci.* **2014**, *7* (5), 1597–1614. <https://doi.org/10.1039/c3ee44164d>.
- (67) Okubo, M.; Hosono, E.; Kim, J.; Enomoto, M.; Kojima, N.; Kudo, T.; Zhou, H.; Honma, I. Nanosize Effect on High-Rate Li-Ion Intercalation in LiCoO₂ Electrode. *J. Am. Chem. Soc.* **2007**, *129* (23), 7444–7452. <https://doi.org/10.1021/ja0681927>.
- (68) Li, Y.; Dai, H. Recent Advances in Zinc–Air Batteries. *Chem. Soc. Rev.* **2014**, *43* (15), 5257–5275. <https://doi.org/10.1039/C4CS00015C>.
- (69) Palmer, N. J. Secondary Metal/Air Cell. US3650837A, March 21, 1972.
- (70) Abraham, K. M.; Jiang, Z. A Polymer Electrolyte-Based Rechargeable Lithium/Oxygen Battery. *J. Electrochem. Soc.* **1996**, *143* (1), 1. <https://doi.org/10.1149/1.1836378>.
- (71) Choi, J. W.; Aurbach, D. Promise and Reality of Post-Lithium-Ion Batteries with High Energy Densities. *Nature Reviews Materials* **2016**, *1* (4), 1–16. <https://doi.org/10.1038/natrevmats.2016.13>.

- (72) McLarnon, F. R.; Cairns, E. J. The Secondary Alkaline Zinc Electrode. *J. Electrochem. Soc.* **1991**, *138* (2), 645. <https://doi.org/10.1149/1.2085653>.
- (73) Shen, Y.; Kordesch, K. The Mechanism of Capacity Fade of Rechargeable Alkaline Manganese Dioxide Zinc Cells. *Journal of Power Sources* **2000**, *87* (1), 162–166. [https://doi.org/10.1016/S0378-7753\(99\)00476-0](https://doi.org/10.1016/S0378-7753(99)00476-0).
- (74) Alfaruqi, M. H.; Gim, J.; Kim, S.; Song, J.; Jo, J.; Kim, S.; Mathew, V.; Kim, J. Enhanced Reversible Divalent Zinc Storage in a Structurally Stable α -MnO₂ Nanorod Electrode. *Journal of Power Sources* **2015**, *288*, 320–327. <https://doi.org/10.1016/j.jpowsour.2015.04.140>.
- (75) Xu, C.; Li, B.; Du, H.; Kang, F. Energetic Zinc Ion Chemistry: The Rechargeable Zinc Ion Battery. *Angewandte Chemie International Edition* **2012**, *51* (4), 933–935. <https://doi.org/10.1002/anie.201106307>.
- (76) Pan, H.; Shao, Y.; Yan, P.; Cheng, Y.; Han, K. S.; Nie, Z.; Wang, C.; Yang, J.; Li, X.; Bhattacharya, P.; Mueller, K. T.; Liu, J. Reversible Aqueous Zinc/Manganese Oxide Energy Storage from Conversion Reactions. *Nature Energy* **2016**, *1* (5), 16039-. <https://doi.org/10.1038/nenergy.2016.39>.
- (77) Sun, W.; Wang, F.; Hou, S.; Yang, C.; Fan, X.; Ma, Z.; Gao, T.; Han, F.; Hu, R.; Zhu, M.; Wang, C. Zn/MnO₂ Battery Chemistry With H⁺ and Zn²⁺ Coinsertion. *Journal of the American Chemical Society* **2017**, *139* (29), 9775–9778. <https://doi.org/10.1021/jacs.7b04471>.
- (78) Guo, X.; Zhou, J.; Bai, C.; Li, X.; Fang, G.; Liang, S. Zn/MnO₂ Battery Chemistry with Dissolution-Deposition Mechanism. *Materials Today Energy* **2020**, *16*, 100396. <https://doi.org/10.1016/j.mtener.2020.100396>.
- (79) Soundharrajan, V.; Sambandam, B.; Kim, S.; Islam, S.; Jo, J.; Kim, S.; Mathew, V.; Sun, Y.; Kim, J. The Dominant Role of Mn²⁺ Additive on the Electrochemical Reaction in ZnMn₂O₄ Cathode for Aqueous Zinc-Ion Batteries. *Energy Storage Materials* **2020**, *28*, 407–417. <https://doi.org/10.1016/j.ensm.2019.12.021>.
- (80) Yang, J.; Cao, J.; Peng, Y.; Yang, W.; Barg, S.; Liu, Z.; Kinloch, I. A.; Bissett, M. A.; Dryfe, R. A. W. Unravelling the Mechanism of Rechargeable Aqueous Zn–MnO₂ Batteries: Implementation of Charging Process by Electrodeposition of MnO₂. *ChemSusChem* **2020**. <https://doi.org/10.1002/cssc.202001216>.
- (81) Lee, B.; Seo, H. R.; Lee, H. R.; Yoon, C. S.; Kim, J. H.; Chung, K. Y.; Cho, B. W.; Oh, S. H. Critical Role of PH Evolution of Electrolyte in the Reaction Mechanism for Rechargeable Zinc Batteries. *ChemSusChem* **2016**, *9* (20), 2948–2956. <https://doi.org/10.1002/cssc.201600702>.
- (82) Bischoff, C. F.; Fitz, O. S.; Burns, J.; Bauer, M.; Gentischer, H.; Birke, K. P.; Henning, H.-M.; Biro, D. Revealing the Local PH Value Changes of Acidic Aqueous Zinc Ion Batteries with a Manganese Dioxide Electrode during Cycling. *J. Electrochem. Soc.* **2020**, *167* (2), 020545. <https://doi.org/10.1149/1945-7111/ab6c57>.
- (83) Janek, J.; Zeier, W. G. A Solid Future for Battery Development. *Nat Energy* **2016**, *1* (9), 16141. <https://doi.org/10.1038/nenergy.2016.141>.
- (84) Wenzel, S.; Randau, S.; Leichtweiß, T.; Weber, D. A.; Sann, J.; Zeier, W. G.; Janek, J. Direct Observation of the Interfacial Instability of the Fast Ionic Conductor Li₁₀GeP₂S₁₂ at the Lithium Metal Anode. *Chem. Mater.* **2016**, *28* (7), 2400–2407. <https://doi.org/10.1021/acs.chemmater.6b00610>.
- (85) Han, F.; Westover, A. S.; Yue, J.; Fan, X.; Wang, F.; Chi, M.; Leonard, D. N.; Dudney, N. J.; Wang, H.; Wang, C. High Electronic Conductivity as the Origin of Lithium Dendrite

References

- Formation within Solid Electrolytes. *Nature Energy* **2019**, *4* (3), 187–196. <https://doi.org/10.1038/s41560-018-0312-z>.
- (86) Lewis, J. A.; Tippens, J.; Cortes, F. J. Q.; McDowell, M. T. Chemo-Mechanical Challenges in Solid-State Batteries. *Trends in Chemistry* **2019**, *1* (9), 845–857. <https://doi.org/10.1016/j.trechm.2019.06.013>.
- (87) Rougier, A.; Gravereau, P.; Delmas, C. Optimization of the Composition of the $\text{Li}_{1-z}\text{Ni}_1 + z\text{O}_2$ Electrode Materials: Structural, Magnetic, and Electrochemical Studies. *J. Electrochem. Soc.* **1996**, *143* (4), 1168. <https://doi.org/10.1149/1.1836614>.
- (88) Gu, M.; Belharouak, I.; Zheng, J.; Wu, H.; Xiao, J.; Genc, A.; Amine, K.; Thevuthasan, S.; Baer, D. R.; Zhang, J.-G.; Browning, N. D.; Liu, J.; Wang, C. Formation of the Spinel Phase in the Layered Composite Cathode Used in Li-Ion Batteries. *ACS Nano* **2013**, *7* (1), 760–767. <https://doi.org/10.1021/nn305065u>.
- (89) Tu, J.; Zhao, X. B.; Cao, G. S.; Zhuang, D. G.; Zhu, T. J.; Tu, J. P. Enhanced Cycling Stability of LiMn_2O_4 by Surface Modification with Melting Impregnation Method. *Electrochimica Acta* **2006**, *51* (28), 6456–6462. <https://doi.org/10.1016/j.electacta.2006.04.031>.
- (90) Kalyani, P.; Kalaiselvi, N. Various Aspects of LiNiO_2 Chemistry: A Review. *Science and Technology of Advanced Materials* **2005**, *6* (6), 689–703. <https://doi.org/10.1016/j.stam.2005.06.001>.
- (91) Chen, C. H.; Liu, J.; Stoll, M. E.; Henriksen, G.; Vissers, D. R.; Amine, K. Aluminum-Doped Lithium Nickel Cobalt Oxide Electrodes for High-Power Lithium-Ion Batteries. *Journal of Power Sources* **2004**, *128* (2), 278–285. <https://doi.org/10.1016/j.jpowsour.2003.10.009>.
- (92) Rossen, E.; Jones, C. D. W.; Dahn, J. R. Structure and Electrochemistry of $\text{Li}_x\text{Mn}_y\text{Ni}_{1-y}\text{O}_2$. *Solid State Ionics* **1992**, *57* (3), 311–318. [https://doi.org/10.1016/0167-2738\(92\)90164-K](https://doi.org/10.1016/0167-2738(92)90164-K).
- (93) Yabuuchi, N.; Ohzuku, T. Novel Lithium Insertion Material of $\text{LiCo}_{1/3}\text{Ni}_{1/3}\text{Mn}_{1/3}\text{O}_2$ for Advanced Lithium-Ion Batteries. *Journal of Power Sources* **2003**, *119–121*, 171–174. [https://doi.org/10.1016/S0378-7753\(03\)00173-3](https://doi.org/10.1016/S0378-7753(03)00173-3).
- (94) Nitta, N.; Wu, F.; Lee, J. T.; Yushin, G. Li-Ion Battery Materials: Present and Future. *Materials Today* **2015**, *18* (5), 252–264. <https://doi.org/10.1016/j.mattod.2014.10.040>.
- (95) Nanjundaswamy, K. S.; Padhi, A. K.; Goodenough, J. B.; Okada, S.; Ohtsuka, H.; Arai, H.; Yamaki, J. Synthesis, Redox Potential Evaluation and Electrochemical Characteristics of NASICON-Related-3D Framework Compounds. *Solid State Ionics* **1996**, *92* (1), 1–10. [https://doi.org/10.1016/S0167-2738\(96\)00472-9](https://doi.org/10.1016/S0167-2738(96)00472-9).
- (96) Armand, M.; Gauthier, M.; Magnan, J.-F.; Ravet, N. Method for Synthesis of Carbon-Coated Redox Materials with Controlled Size. US20040033360A1, February 19, 2004.
- (97) James, A. C. W. P.; Goodenough, J. B. Structure and Bonding in Li_2MoO_3 and $\text{Li}_{2-x}\text{MoO}_3$ ($0 \leq x \leq 1.7$). *Journal of Solid State Chemistry* **1988**, *76* (1), 87–96. [https://doi.org/10.1016/0022-4596\(88\)90194-6](https://doi.org/10.1016/0022-4596(88)90194-6).
- (98) Kobayashi, H.; Kanno, R.; Kawamoto, Y.; Tabuchi, M.; Nakamura, O. Physical Properties of the De-Lithiated $\text{Li}_2 - x\text{RuO}_3$ with the Layered Structure. *Solid State Ionics* **1996**, *86–88*, 859–863. [https://doi.org/10.1016/0167-2738\(96\)00194-4](https://doi.org/10.1016/0167-2738(96)00194-4).
- (99) Kalyani, P.; Chitra, S.; Mohan, T.; Gopukumar, S. Lithium Metal Rechargeable Cells Using Li_2MnO_3 as the Positive Electrode. *Journal of Power Sources* **1999**, *80* (1), 103–106. [https://doi.org/10.1016/S0378-7753\(99\)00066-X](https://doi.org/10.1016/S0378-7753(99)00066-X).
- (100) Lu, Z.; Dahn, J. R. Understanding the Anomalous Capacity of $\text{Li} / \text{Li} [\text{Ni}_x \text{Li} (1 / 3 - 2x / 3) \text{Mn} (2 / 3 - x / 3)] \text{O}_2$ Cells Using In Situ X-Ray Diffraction and Electrochemical Studies. *J. Electrochem. Soc.* **2002**, *149* (7), A815. <https://doi.org/10.1149/1.1480014>.

- (101) Rozier, P.; Tarascon, J. M. Review—Li-Rich Layered Oxide Cathodes for Next-Generation Li-Ion Batteries: Chances and Challenges. *J. Electrochem. Soc.* **2015**, *162* (14), A2490. <https://doi.org/10.1149/2.0111514jes>.
- (102) Lu, Z.; MacNeil, D. D.; Dahn, J. R. Layered Cathode Materials $\text{Li} [\text{Ni}_x \text{Li} (1 / 3 - 2x / 3) \text{Mn} (2 / 3 - x / 3)] \text{O}_2$ for Lithium-Ion Batteries. *Electrochem. Solid-State Lett.* **2001**, *4* (11), A191. <https://doi.org/10.1149/1.1407994>.
- (103) Armstrong, A. R.; Holzapfel, M.; Novák, P.; Johnson, C. S.; Kang, S.-H.; Thackeray, M. M.; Bruce, P. G. Demonstrating Oxygen Loss and Associated Structural Reorganization in the Lithium Battery Cathode $\text{Li} [\text{Ni}_0.2 \text{Li}_0.2 \text{Mn}_0.6] \text{O}_2$. *Journal of the American Chemical Society* **2006**, *128* (26), 8694–8698.
- (104) Streich, D.; Erk, C.; Guéguen, A.; Müller, P.; Chesneau, F.-F.; Berg, E. J. Operando Monitoring of Early Ni-Mediated Surface Reconstruction in Layered Lithiated Ni–Co–Mn Oxides. *J. Phys. Chem. C* **2017**, *121* (25), 13481–13486. <https://doi.org/10.1021/acs.jpcc.7b02303>.
- (105) Assat, G.; Tarascon, J.-M. Fundamental Understanding and Practical Challenges of Anionic Redox Activity in Li-Ion Batteries. *Nat Energy* **2018**, *3* (5), 373–386. <https://doi.org/10.1038/s41560-018-0097-0>.
- (106) Park, C.-M.; Kim, J.-H.; Kim, H.; Sohn, H.-J. Li-Alloy Based Anode Materials for Li Secondary Batteries. *Chem. Soc. Rev.* **2010**, *39* (8), 3115–3141. <https://doi.org/10.1039/B919877F>.
- (107) Zhang, W.-J. A Review of the Electrochemical Performance of Alloy Anodes for Lithium-Ion Batteries. *Journal of Power Sources* **2011**, *196* (1), 13–24. <https://doi.org/10.1016/j.jpowsour.2010.07.020>.
- (108) Xu, K. Nonaqueous Liquid Electrolytes for Lithium-Based Rechargeable Batteries. *Chem. Rev.* **2004**, *104* (10), 4303–4418. <https://doi.org/10.1021/cr030203g>.
- (109) Harris, W. S. *Electrochemical Studies in Cyclic Esters*; UCRL-8381; Univ. of California, Berkeley, CA (United States), 1958. <https://doi.org/10.2172/4305596>.
- (110) Pistoia, G.; De Rossi, M.; Scrosati, B. Study of the Behavior of Ethylene Carbonate as a Nonaqueous Battery Solvent. *J. Electrochem. Soc.; (United States)* **1970**, *117*. <https://doi.org/10.1149/1.2407550>.
- (111) Peled, E.; Golodnitsky, D.; Ardel, G. Advanced Model for Solid Electrolyte Interphase Electrodes in Liquid and Polymer Electrolytes. *J. Electrochem. Soc.* **1997**, *144* (8), L208. <https://doi.org/10.1149/1.1837858>.
- (112) Peled, E.; Menkin, S. Review—SEI: Past, Present and Future. *J. Electrochem. Soc.* **2017**, *164* (7), A1703–A1719. <https://doi.org/10.1149/2.1441707jes>.
- (113) Edström, K.; Gustafsson, T.; Thomas, J. O. The Cathode–Electrolyte Interface in the Li-Ion Battery. *Electrochimica Acta* **2004**, *50* (2), 397–403. <https://doi.org/10.1016/j.electacta.2004.03.049>.
- (114) Liu, Y.-M.; Nicolau, B.; Esbenschade, J. L.; Gewirth, A. A. Characterization of the Cathode Electrolyte Interface in Lithium Ion Batteries by Desorption Electrospray Ionization Mass Spectrometry. *Anal. Chem.* **2016**, *88* (14), 7171–7177. <https://doi.org/10.1021/acs.analchem.6b01292>.
- (115) Bassett, K. L.; Çapraz, Ö. Ö.; Özdogru, B.; Gewirth, A. A.; Sottos, N. R. Cathode/Electrolyte Interface-Dependent Changes in Stress and Strain in Lithium Iron Phosphate Composite Cathodes. *J. Electrochem. Soc.* **2019**, *166* (12), A2707. <https://doi.org/10.1149/2.1391912jes>.

References

- (116) Goodenough, J. B.; Kim, Y. Challenges for Rechargeable Li Batteries. *Chem. Mater.* **2010**, *22* (3), 587–603. <https://doi.org/10.1021/cm901452z>.
- (117) Peljo, P.; Girault, H. H. Electrochemical Potential Window of Battery Electrolytes: The HOMO–LUMO Misconception. *Energy Environ. Sci.* **2018**, *11* (9), 2306–2309. <https://doi.org/10.1039/C8EE01286E>.
- (118) Chen, W.; Ambrosio, F.; Miceli, G.; Pasquarello, A. *Ab Initio* Electronic Structure of Liquid Water. *Phys. Rev. Lett.* **2016**, *117* (18), 186401. <https://doi.org/10.1103/PhysRevLett.117.186401>.
- (119) Haynes, W. M. *CRC Handbook of Chemistry and Physics*; CRC Press, 2014.
- (120) Zaban, A.; Aurbach, D. Impedance Spectroscopy of Lithium and Nickel Electrodes in Propylene Carbonate Solutions of Different Lithium Salts A Comparative Study. *Journal of Power Sources* **1995**, *54* (2), 289–295. [https://doi.org/10.1016/0378-7753\(94\)02086-l](https://doi.org/10.1016/0378-7753(94)02086-l).
- (121) Wood, D. L.; Li, J.; Daniel, C. Prospects for Reducing the Processing Cost of Lithium Ion Batteries. *Journal of Power Sources* **2015**, *275*, 234–242. <https://doi.org/10.1016/j.jpowsour.2014.11.019>.
- (122) Vetter, J.; Novák, P.; Wagner, M. R.; Veit, C.; Möller, K.-C.; Besenhard, J. O.; Winter, M.; Wohlfahrt-Mehrens, M.; Vogler, C.; Hammouche, A. Ageing Mechanisms in Lithium-Ion Batteries. *Journal of Power Sources* **2005**, *147* (1–2), 269–281. <https://doi.org/10.1016/j.jpowsour.2005.01.006>.
- (123) Yamada, Y.; Wang, J.; Ko, S.; Watanabe, E.; Yamada, A. Advances and Issues in Developing Salt-Concentrated Battery Electrolytes. *Nat Energy* **2019**, *4* (4), 269–280. <https://doi.org/10.1038/s41560-019-0336-z>.
- (124) Shannon, R. D. Revised Effective Ionic Radii and Systematic Studies of Interatomic Distances in Halides and Chalcogenides. *Acta Crystallographica Section A* **1976**, *32* (5), 751–767. <https://doi.org/10.1107/S0567739476001551>.
- (125) Matsuda, Y.; Nakashima, H.; Morita, M.; Takasu, Y. Behavior of Some Ions in Mixed Organic Electrolytes of High Energy Density Batteries. *J. Electrochem. Soc.* **1981**, *128* (12), 2552. <https://doi.org/10.1149/1.2127289>.
- (126) Moon, M. J.; Jhon, M. S. The Studies on the Hydration Energy and Water Structures in Dilute Aqueous Solution. *BCSJ* **1986**, *59* (4), 1215–1222. <https://doi.org/10.1246/bcsj.59.1215>.
- (127) Xu, K.; von Wald Cresce, A. Li⁺ -Solvation/Desolvation Dictates Interphasial Processes on Graphitic Anode in Li Ion Cells. *J. Mater. Res.* **2012**, *27* (18), 2327–2341. <https://doi.org/10.1557/jmr.2012.104>.
- (128) Augustyn, V. Tuning the Interlayer of Transition Metal Oxides for Electrochemical Energy Storage. *Journal of Materials Research* **2017**, *32* (1), 2–15. <https://doi.org/10.1557/jmr.2016.337>.
- (129) Jow, T. R.; Delp, S. A.; Allen, J. L.; Jones, J.-P.; Smart, M. C. Factors Limiting Li⁺ Charge Transfer Kinetics in Li-Ion Batteries. *J. Electrochem. Soc.* **2018**, *165* (2), A361–A367. <https://doi.org/10.1149/2.1221802jes>.
- (130) Xu, K. “Charge-Transfer” Process at Graphite/Electrolyte Interface and the Solvation Sheath Structure of Li⁺ in Nonaqueous Electrolytes. *Journal of The Electrochemical Society* **2007**, *154* (3), A162–A167. <https://doi.org/10.1149/1.2409866>.
- (131) Xu, K.; Lam, Y.; Zhang, S. S.; Jow, T. R.; Curtis, T. B. Solvation Sheath of Li⁺ in Nonaqueous Electrolytes and Its Implication of Graphite/Electrolyte Interface Chemistry. *J. Phys. Chem. C* **2007**, *111* (20), 7411–7421. <https://doi.org/10.1021/jp068691u>.

- (132) Yamada, Y.; Iriyama, Y.; Abe, T.; Ogumi, Z. Kinetics of Lithium Ion Transfer at the Interface between Graphite and Liquid Electrolytes: Effects of Solvent and Surface Film. *Langmuir* **2009**, *25* (21), 12766–12770. <https://doi.org/10.1021/la901829v>.
- (133) Bruce, P. G.; Saidi, M. Y. The Mechanism of Electrointercalation. *Journal of Electroanalytical Chemistry* **1992**, *322* (1), 93–105. [https://doi.org/10.1016/0022-0728\(92\)80069-G](https://doi.org/10.1016/0022-0728(92)80069-G).
- (134) Nakayama, M.; Ikuta, H.; Uchimoto, Y.; Wakihara, M. Study on the AC Impedance Spectroscopy for the Li Insertion Reaction of $\text{Li}_x\text{La}_{1/3}\text{NbO}_3$ at the Electrode–Electrolyte Interface. *The Journal of Physical Chemistry B* **2003**, *107* (38), 10603–10607. <https://doi.org/10.1021/jp036059k>.
- (135) Okumura, T.; Fukutsuka, T.; Matsumoto, K.; Orikasa, Y.; Arai, H.; Ogumi, Z.; Uchimoto, Y. Lithium-Ion Transfer Reaction at the Interface between Partially Fluorinated Insertion Electrodes and Electrolyte Solutions. *J. Phys. Chem. C* **2011**, *115* (26), 12990–12994. <https://doi.org/10.1021/jp202967d>.
- (136) Mizuno, Y.; Okubo, M.; Asakura, D.; Saito, T.; Hosono, E.; Saito, Y.; Oh-ishi, K.; Kudo, T.; Zhou, H. Impedance Spectroscopic Study on Interfacial Ion Transfers in Cyanide-Bridged Coordination Polymer Electrode with Organic Electrolyte. *Electrochimica Acta* **2012**, *63*, 139–145. <https://doi.org/10.1016/j.electacta.2011.12.068>.
- (137) Curie, J.; Curie, P. Développement par compression de l'électricité polaire dans les cristaux hémihédres à faces inclinées. *Bulletin de Minéralogie* **1880**, *3* (4), 90–93. <https://doi.org/10.3406/bulmi.1880.1564>.
- (138) Lippmann, G. Principe de la conservation de l'électricité, ou second principe de la théorie des phénomènes électriques. *J. Phys. Theor. Appl.* **1881**, *10* (1), 381–394. <https://doi.org/10.1051/jphystap:0188100100038100>.
- (139) Curie, J.; Curie, P. Contractions et Dilatations Produites Par Des Tensions Électriques Dans Les Cristaux Hémihédres à Faces Inclinées. *Compt. Rend* **1881**, *93*, 1137–1140.
- (140) Buttry, D. A.; Ward, M. D. Measurement of Interfacial Processes at Electrode Surfaces with the Electrochemical Quartz Crystal Microbalance. *Chemical Reviews* **1992**, *92* (6), 1355–1379.
- (141) PAUPORTÉ, T.; LINCOT, D. *Microbalance à Cristal de Quartz*; Ed. Techniques Ingénieur, 2006.
- (142) Sauerbrey, G. Verwendung von Schwingquarzen Zur Wägung Dünner Schichten Und Zur Mikrowägung. *Zeitschrift für Physik A Hadrons and Nuclei* **1959**, *155* (2), 206–222.
- (143) Nomura, T.; Okuhara, M. Frequency Shifts of Piezoelectric Quartz Crystals Immersed in Organic Liquids. *Analytica Chimica Acta* **1982**, *142*, 281–284. [https://doi.org/10.1016/S0003-2670\(01\)95290-0](https://doi.org/10.1016/S0003-2670(01)95290-0).
- (144) Bandey, H. L.; Martin, S. J.; Cernosek, R. W.; Hillman, A. R. Modeling the Responses of Thickness-Shear Mode Resonators under Various Loading Conditions. *Anal. Chem.* **1999**, *71* (11), 2205–2214. <https://doi.org/10.1021/ac981272b>.
- (145) Hillman, A. R. The EQCM: Electrogravimetry with a Light Touch. *Journal of Solid State Electrochemistry* **2011**, *15* (7–8), 1647–1660. <https://doi.org/10.1007/s10008-011-1371-2>.
- (146) Kanazawa, K. K.; Gordon, J. G. The Oscillation Frequency of a Quartz Resonator in Contact with Liquid. *Analytica Chimica Acta* **1985**, *175*, 99–105.
- (147) *Piezoelectric Transducers and Applications*; Arnau Vives, A., Ed.; Springer Berlin Heidelberg: Berlin, Heidelberg, 2004. <https://doi.org/10.1007/978-3-662-05361-4>.

References

- (148) Johannsmann, D. *The Quartz Crystal Microbalance in Soft Matter Research: Fundamentals and Modeling*; Soft and Biological Matter; Springer International Publishing, 2015. <https://doi.org/10.1007/978-3-319-07836-6>.
- (149) Rodahl, M.; Höök, F.; Krozer, A.; Brzezinski, P.; Kasemo, B. Quartz Crystal Microbalance Setup for Frequency and Q-factor Measurements in Gaseous and Liquid Environments. *Review of Scientific Instruments* **1995**, *66* (7), 3924–3930. <https://doi.org/10.1063/1.1145396>.
- (150) Rodahl, M.; Höök, F.; Fredriksson, C.; Keller, C. A.; Krozer, A.; Brzezinski, P.; Voinova, M.; Kasemo, B. Simultaneous Frequency and Dissipation Factor QCM Measurements of Biomolecular Adsorption and Cell Adhesion. *Faraday Discussions* **1997**, *107* (0), 229–246. <https://doi.org/10.1039/A703137H>.
- (151) Montagut, Y. J.; García, J. V.; Jiménez, Y.; March, C.; Montoya, A.; Arnau, A. Frequency-Shift vs Phase-Shift Characterization of in-Liquid Quartz Crystal Microbalance Applications. *Review of Scientific Instruments* **2011**, *82* (6), 064702. <https://doi.org/10.1063/1.3598340>.
- (152) Aurbach, D.; Zaban, A. The Application of EQCM to the Study of the Electrochemical Behavior of Propylene Carbonate Solutions. *Journal of Electroanalytical Chemistry* **1995**, *393* (1–2), 43–53.
- (153) Kwon, K.; Kong, F.; McLarnon, F.; Evans, J. W. Characterization of the SEI on a Carbon Film Electrode by Combined EQCM and Spectroscopic Ellipsometry. *J. Electrochem. Soc.* **2003**, *150* (2), A229–A233. <https://doi.org/10.1149/1.1538223>.
- (154) Kwon, K.; Evans, J. W. Comparison between Cyclic Voltammetry and Chronoamperometry When Coupled with EQCM for the Study of the SEI on a Carbon Film Electrode. *Electrochimica Acta* **2004**, *49* (6), 867–872. <https://doi.org/10.1016/j.electacta.2003.09.038>.
- (155) Li, J.-T.; Chen, S.-R.; Fan, X.-Y.; Huang, L.; Sun, S.-G. Studies of the Interfacial Properties of an Electroplated Sn Thin Film Electrode/Electrolyte Using in Situ MFTIRS and EQCM. *Langmuir* **2007**, *23* (26), 13174–13180. <https://doi.org/10.1021/la701168x>.
- (156) Liu, T.; Lin, L.; Bi, X.; Tian, L.; Yang, K.; Liu, J.; Li, M.; Chen, Z.; Lu, J.; Amine, K.; Xu, K.; Pan, F. In Situ Quantification of Interphasial Chemistry in Li-Ion Battery. *Nature Nanotechnology* **2019**, *14* (1), 50–56. <https://doi.org/10.1038/s41565-018-0284-y>.
- (157) Dubouis, N.; Lemaire, P.; Mirvaux, B.; Salager, E.; Deschamps, M.; Grimaud, A. The Role of the Hydrogen Evolution Reaction in the Solid–Electrolyte Interphase Formation Mechanism for “Water-in-Salt” Electrolytes. *Energy Environ. Sci.* **2018**, *11* (12), 3491–3499. <https://doi.org/10.1039/C8EE02456A>.
- (158) Yang, Z.; Gewirth, A. A.; Trahey, L. Investigation of Fluoroethylene Carbonate Effects on Tin-Based Lithium-Ion Battery Electrodes. *ACS Appl. Mater. Interfaces* **2015**, *7* (12), 6557–6566. <https://doi.org/10.1021/am508593s>.
- (159) Yang, Z.; Dixon, M. C.; Erck, R. A.; Trahey, L. Quantification of the Mass and Viscoelasticity of Interfacial Films on Tin Anodes Using EQCM-D. *ACS Appl. Mater. Interfaces* **2015**, *7* (48), 26585–26594. <https://doi.org/10.1021/acsami.5b07966>.
- (160) Dargel, V.; Shpigel, N.; Sigalov, S.; Nayak, P.; Levi, M. D.; Daikhin, L.; Aurbach, D. In Situ Real-Time Gravimetric and Viscoelastic Probing of Surface Films Formation on Lithium Batteries Electrodes. *Nature Communications* **2017**, *8* (1). <https://doi.org/10.1038/s41467-017-01722-x>.

- (161) Kitz, P. G.; Lacey, M. J.; Novák, P.; Berg, E. J. Operando EQCM-D with Simultaneous in Situ EIS: New Insights into Interphase Formation in Li Ion Batteries. *Analytical Chemistry* **2019**, *91* (3), 2296–2303. <https://doi.org/10.1021/acs.analchem.8b04924>.
- (162) Kitz, P. G.; Novák, P.; Berg, E. J. Influence of Water Contamination on the SEI Formation in Li-Ion Cells: An Operando EQCM-D Study. *ACS Appl. Mater. Interfaces* **2020**, *12* (13), 15934–15942. <https://doi.org/10.1021/acsami.0c01642>.
- (163) Kitz, P. G.; Lacey, M. J.; Novák, P.; Berg, E. J. Operando Investigation of the Solid Electrolyte Interphase Mechanical and Transport Properties Formed from Vinylene Carbonate and Fluoroethylene Carbonate. *Journal of Power Sources* **2020**, *477*, 228567. <https://doi.org/10.1016/j.jpowsour.2020.228567>.
- (164) Mozhzhukhina, N.; Flores, E.; Lundström, R.; Nyström, V.; Kitz, P. G.; Edström, K.; Berg, E. J. Direct Operando Observation of Double Layer Charging and Early Solid Electrolyte Interphase Formation in Li-Ion Battery Electrolytes. *J. Phys. Chem. Lett.* **2020**, *11* (10), 4119–4123. <https://doi.org/10.1021/acs.jpcllett.0c01089>.
- (165) Shpigel, N.; Levi, M. D.; Sigalov, S.; Girshevitz, O.; Aurbach, D.; Daikhin, L.; Jäckel, N.; Presser, V. Non-Invasive In Situ Dynamic Monitoring of Elastic Properties of Composite Battery Electrodes by EQCM-D. *Angew. Chem. Int. Ed.* **2015**, *54* (42), 12353–12356. <https://doi.org/10.1002/anie.201501787>.
- (166) Dargel, V.; Levi, M. D.; Daikhin, L.; Aurbach, D. In Situ Tracking of Hydrodynamic and Viscoelastic Changes in Electrophoretically Deposited LiFePO₄ Electrodes during Their Charging/Discharging. *Russian Journal of Electrochemistry* **2017**, *53* (9), 980–993. <https://doi.org/10.1134/S1023193517090038>.
- (167) Dargel, V.; Jäckel, N.; Shpigel, N.; Sigalov, S.; Levi, M. D.; Daikhin, L.; Presser, V.; Aurbach, D. In Situ Multilength-Scale Tracking of Dimensional and Viscoelastic Changes in Composite Battery Electrodes. *ACS Applied Materials & Interfaces* **2017**, *9* (33), 27664–27675. <https://doi.org/10.1021/acsami.7b06243>.
- (168) Shpigel, N.; Sigalov, S.; Levi, M. D.; Mathis, T.; Daikhin, L.; Janes, A.; Lust, E.; Gogotsi, Y.; Aurbach, D. In Situ Acoustic Diagnostics of Particle-Binder Interactions in Battery Electrodes. *Joule* **2018**, *2* (5), 988–1003. <https://doi.org/10.1016/j.joule.2018.02.014>.
- (169) Shpigel, N.; Levi, M. D.; Cheng, X.; Cao, T.; Wu, R.; Mathis, T. S.; Zhang, Y.; Aurbach, D.; Gogotsi, Y. Diffusion-Induced Transient Stresses in Li-Battery Electrodes Imaged by Electrochemical Quartz Crystal Microbalance with Dissipation Monitoring and Environmental Scanning Electron Microscopy. *ACS Energy Lett.* **2019**, 1907–1917. <https://doi.org/10.1021/acsenerylett.9b00884>.
- (170) Levi, M. D.; Shpigel, N.; Sigalov, S.; Dargel, V.; Daikhin, L.; Aurbach, D. In Situ Porous Structure Characterization of Electrodes for Energy Storage and Conversion by EQCM-D: A Review. *Electrochimica Acta* **2017**, *232*, 271–284. <https://doi.org/10.1016/j.electacta.2017.02.149>.
- (171) Levi, M. D.; Daikhin, L.; Aurbach, D.; Presser, V. Quartz Crystal Microbalance with Dissipation Monitoring (EQCM-D) for in-Situ Studies of Electrodes for Supercapacitors and Batteries: A Mini-Review. *Electrochemistry Communications* **2016**, *67*, 16–21. <https://doi.org/10.1016/j.elecom.2016.03.006>.
- (172) Shpigel, N.; Levi, M. D.; Aurbach, D. EQCM-D Technique for Complex Mechanical Characterization of Energy Storage Electrodes: Background and Practical Guide. *Energy Storage Materials* **2019**, *21*, 399–413. <https://doi.org/10.1016/j.ensm.2019.05.026>.

References

- (173) Yang, Y.; Shu, D.; Yu, H.; Xia, X.; Lin, Z. G. Investigations of Lithium Manganese Oxide Materials for Lithium-Ion Batteries. *Journal of Power Sources* **1997**, *65* (1–2), 227–230. [https://doi.org/10.1016/S0378-7753\(97\)02476-2](https://doi.org/10.1016/S0378-7753(97)02476-2).
- (174) Shouji, E.; A. Buttry, D. EQCM Measurements of Solvent Transport during Li+ Intercalation in V2O5 Xerogel Films. *Electrochimica Acta* **2000**, *45* (22), 3757–3764. [https://doi.org/10.1016/S0013-4686\(00\)00471-0](https://doi.org/10.1016/S0013-4686(00)00471-0).
- (175) Bueno, P. R.; Faria, R. C.; Avellaneda, C. O.; Leite, E. R.; Bulhões, L. O. S. Li+ Insertion into Pure and Doped Amorphous WO3 Films. Correlations between Coloration Kinetics, Charge and Mass Accumulation. *Solid State Ionics* **2003**, *158* (3), 415–426. [https://doi.org/10.1016/S0167-2738\(02\)00907-4](https://doi.org/10.1016/S0167-2738(02)00907-4).
- (176) Razzaghi, F.; Debiemme-Chouvy, C.; Pillier, F.; Perrot, H.; Sel, O. Ion Intercalation Dynamics of Electrosynthesized Mesoporous WO3 Thin Films Studied by Multi-Scale Coupled Electrogravimetric Methods. *Phys. Chem. Chem. Phys.* **2015**, *17* (22), 14773–14787. <https://doi.org/10.1039/C5CP00336A>.
- (177) Bueno, P. R.; Faria, R. C.; Bulhões, L. O. S. EQCM Study during Lithium Insertion/Deinsertion Processes in Nb2O5 Films Prepared by Polymeric Precursor Method. *Solid State Ionics* **2005**, *176* (11–12), 1175–1180. <https://doi.org/10.1016/j.ssi.2005.02.007>.
- (178) Arias, C. R.; Debiemme-Chouvy, C.; Gabrielli, C.; Laberty-Robert, C.; Pailleret, A.; Perrot, H.; Sel, O. New Insights into Pseudocapacitive Charge-Storage Mechanisms in Li-Birnessite Type MnO₂ Monitored by Fast Quartz Crystal Microbalance Methods. *The Journal of Physical Chemistry C* **2014**, *118* (46), 26551–26559. <https://doi.org/10.1021/jp508543h>.
- (179) Song, J.; Noked, M.; Gillette, E.; Duay, J.; Rubloff, G.; Lee, S. B. Activation of a MnO₂ Cathode by Water-Stimulated Mg²⁺ Insertion for a Magnesium Ion Battery. *Physical Chemistry Chemical Physics* **2015**, *17* (7), 5256–5264. <https://doi.org/10.1039/C4CP05591H>.
- (180) Zhu, D.; Zhang, L.; Huang, Y.; Li, J.; Fan, H.; Wang, H. Ethylmethyl Carbonate's Role in Hexafluorophosphate Storage in Graphite Electrodes. *ACS Appl. Energy Mater.* **2019**, *2* (11), 8031–8038. <https://doi.org/10.1021/acsaem.9b01508>.
- (181) Levi, M. D.; Sigalov, S.; Salitra, G.; Elazari, R.; Aurbach, D. Assessing the Solvation Numbers of Electrolytic Ions Confined in Carbon Nanopores under Dynamic Charging Conditions. *J. Phys. Chem. Lett.* **2011**, *2* (2), 120–124. <https://doi.org/10.1021/jz1016922>.
- (182) Tsai, W.-Y.; Taberna, P.-L.; Simon, P. Electrochemical Quartz Crystal Microbalance (EQCM) Study of Ion Dynamics in Nanoporous Carbons. *Journal of the American Chemical Society* **2014**, *136* (24), 8722–8728. <https://doi.org/10.1021/ja503449w>.
- (183) Shpigel, N.; Levi, M. D.; Sigalov, S.; Daikhin, L.; Aurbach, D. In Situ Real-Time Mechanical and Morphological Characterization of Electrodes for Electrochemical Energy Storage and Conversion by Electrochemical Quartz Crystal Microbalance with Dissipation Monitoring. *Acc. Chem. Res.* **2018**, *51* (1), 69–79. <https://doi.org/10.1021/acs.accounts.7b00477>.
- (184) Gabrielli, C.; García-Jareño, J. J.; Keddah, M.; Perrot, H.; Vicente, F. Ac-Electrogravimetry Study of Electroactive Thin Films. I. Application to Prussian Blue. *J. Phys. Chem. B* **2002**, *106* (12), 3182–3191. <https://doi.org/10.1021/jp013924x>.
- (185) Jackson, A.; Hillman, A. R.; Bruckenstein, S.; Jureviciute, I. Modelling Mobile Species Population Changes in Electroactive Films under Thermodynamically and Kinetically

- Controlled Conditions. *Journal of Electroanalytical Chemistry* **2002**, 524–525, 90–102. [https://doi.org/10.1016/S0022-0728\(02\)00765-9](https://doi.org/10.1016/S0022-0728(02)00765-9).
- (186) Kim, L. T. T.; Gabrielli, C.; Perrot, H.; Garcia-Jareno, J.; Vicente, F. Redox Switching of Prussian Blue Thin Films Investigated by Ac-Electrogravimetry. *Electrochim. Acta* **2012**, 84, 35–48. <https://doi.org/10.1016/j.electacta.2012.06.049>.
- (187) Jakab, S.; Picart, S.; Tribollet, B.; Rousseau, P.; Perrot, H.; Gabrielli, C. Study of the Dissolution of Thin Films of Cerium Oxide by Using a GaPO₄ Crystal Microbalance. *Anal. Chem.* **2009**, 81 (13), 5139–5145. <https://doi.org/10.1021/ac900826u>.
- (188) Levi, M. D.; Salitra, G.; Levy, N.; Aurbach, D.; Maier, J. Application of a Quartz-Crystal Microbalance to Measure Ionic Fluxes in Microporous Carbons for Energy Storage. *Nature Materials* **2009**, 8 (11), 872–875. <https://doi.org/10.1038/nmat2559>.
- (189) Yunker, P. J.; Still, T.; Lohr, M. A.; Yodh, A. G. Suppression of the Coffee-Ring Effect by Shape-Dependent Capillary Interactions. *Nature* **2011**, 476 (7360), 308–311. <https://doi.org/10.1038/nature10344>.
- (190) Barbosa, J. C.; Dias, J. P.; Lanceros-Méndez, S.; Costa, C. M. Recent Advances in Poly(Vinylidene Fluoride) and Its Copolymers for Lithium-Ion Battery Separators. *Membranes (Basel)* **2018**, 8 (3), 45. <https://doi.org/10.3390/membranes8030045>.
- (191) Cambon, O.; Haines, J.; Fraysse, G.; Keen, D. A.; Tucker, M. G. Piezoelectric Properties at High Temperature in Alpha-Quartz Materials. *J. Phys. IV France* **2005**, 126, 27–30. <https://doi.org/10.1051/jp4:2005126006>.
- (192) Zhang, Q.; Levi, M. D.; Chai, Y.; Zhang, X.; Xiao, D.; Dou, Q.; Ma, P.; Ji, H.; Yan, X. Vacuum Filtration-and-Transfer Technique Helps Electrochemical Quartz Crystal Microbalance to Reveal Accurate Charge Storage in Supercapacitors. *Small Methods* **2019**, 3 (11), 1900246. <https://doi.org/10.1002/smt.201900246>.
- (193) O'sullivan, C. K.; Guilbault, G. G. Commercial Quartz Crystal Microbalances—Theory and Applications. *Biosensors and bioelectronics* **1999**, 14 (8), 663–670.
- (194) Agrisuelas, J.; Gabrielli, C.; García-Jareño, J. J.; Perrot, H.; Sel, O.; Vicente, F. Viscoelastic Potential-Induced Changes in Acoustically Thin Films Explored by Quartz Crystal Microbalance with Motional Resistance Monitoring. *Electrochimica Acta* **2015**, 176, 1454–1463. <https://doi.org/10.1016/j.electacta.2015.07.131>.
- (195) Aurbach, D.; Markovsky, B.; Salitra, G.; Markevich, E.; Talyossef, Y.; Koltypin, M.; Nazar, L.; Ellis, B.; Kovacheva, D. Review on Electrode–Electrolyte Solution Interactions, Related to Cathode Materials for Li-Ion Batteries. *Journal of Power Sources* **2007**, 165 (2), 491–499. <https://doi.org/10.1016/j.jpowsour.2006.10.025>.
- (196) Tsionsky, V.; Daikhin, L.; Gileadi, E. Weighing Ions in Solution with the Quartz Crystal Microbalance. *J. Electrochem. Soc.* **1995**, 142 (12), L233–L234. <https://doi.org/10.1149/1.2048509>.
- (197) Mason, P. E.; Ansell, S.; Neilson, G. W.; Rempe, S. B. Neutron Scattering Studies of the Hydration Structure of Li⁺. *J. Phys. Chem. B* **2015**, 119 (5), 2003–2009. <https://doi.org/10.1021/jp511508n>.
- (198) Zeng, X.; Liu, Q.; Chen, M.; Leng, L.; Shu, T.; Du, L.; Song, H.; Liao, S. Electrochemical Behavior of Spherical LiFePO₄/C Nanomaterial in Aqueous Electrolyte, and Novel Aqueous Rechargeable Lithium Battery with LiFePO₄/C Anode. *Electrochimica Acta* **2015**, 177, 277–282. <https://doi.org/10.1016/j.electacta.2014.12.088>.
- (199) Song, X.; Liu, T.; Amine, J.; Duan, Y.; Zheng, J.; Lin, Y.; Pan, F. In-Situ Mass-Electrochemical Study of Surface Redox Potential and Interfacial Chemical Reactions of

References

- Li(Na)FePO₄ Nanocrystals for Li(Na)-Ion Batteries. *Nano Energy* **2017**, *37*, 90–97. <https://doi.org/10.1016/j.nanoen.2017.05.019>.
- (200) Zheng, J.; Hou, Y.; Duan, Y.; Song, X.; Wei, Y.; Liu, T.; Hu, J.; Guo, H.; Zhuo, Z.; Liu, L.; Chang, Z.; Wang, X.; Zherebetsky, D.; Fang, Y.; Lin, Y.; Xu, K.; Wang, L.-W.; Wu, Y.; Pan, F. Janus Solid–Liquid Interface Enabling Ultrahigh Charging and Discharging Rate for Advanced Lithium-Ion Batteries. *Nano Lett.* **2015**, *15* (9), 6102–6109. <https://doi.org/10.1021/acs.nanolett.5b02379>.
- (201) Mathew, V.; Kim, S.; Kang, J.; Gim, J.; Song, J.; Baboo, J. P.; Park, W.; Ahn, D.; Han, J.; Gu, L.; Wang, Y.; Hu, Y.-S.; Sun, Y.-K.; Kim, J. Amorphous Iron Phosphate: Potential Host for Various Charge Carrier Ions. *NPG Asia Materials* **2014**, *6* (10), e138–e138. <https://doi.org/10.1038/am.2014.98>.
- (202) Buser, H. J.; Schwarzenbach, D.; Petter, W.; Ludi, A. The Crystal Structure of Prussian Blue: Fe₄[Fe(CN)₆]₃.XH₂O. *Inorg. Chem.* **1977**, *16* (11), 2704–2710. <https://doi.org/10.1021/ic50177a008>.
- (203) Herren, F.; Fischer, P.; Ludi, A.; Haelg, W. Neutron Diffraction Study of Prussian Blue, Fe₄[Fe(CN)₆]₃.XH₂O. Location of Water Molecules and Long-Range Magnetic Order. *Inorg. Chem.* **1980**, *19* (4), 956–959. <https://doi.org/10.1021/ic50206a032>.
- (204) Itaya, K.; Akahoshi, H.; Toshima, S. Electrochemistry of Prussian Blue Modified Electrodes: An Electrochemical Preparation Method. *J. Electrochem. Soc.* **1982**, *129* (7), 1498. <https://doi.org/10.1149/1.2124191>.
- (205) García-Jareño, J. J.; Sanmatías, A.; Vicente, F.; Gabrielli, C.; Keddou, M.; Perrot, H. Study of Prussian Blue (PB) Films by Ac-Electrogravimetry: Influence of PB Morphology on Ions Movement. *Electrochimica Acta* **2000**, *45* (22), 3765–3776. [https://doi.org/10.1016/S0013-4686\(00\)00470-9](https://doi.org/10.1016/S0013-4686(00)00470-9).
- (206) Wang, F.; Varenne, F.; Ortiz, D.; Pinzio, V.; Mostafavi, M.; Caer, S. L. Degradation Mechanisms of the Ethylene Carbonate/Diethyl Carbonate Mixture Studied by Radiolysis. *ChemPhysChem* **2017**, *18*, 2799–2806. <https://doi.org/10.1002/cphc.201700320>.
- (207) Naejus, R.; Damas, C.; Lemordant, D.; Coudert, R.; Willmann, P. Excess Thermodynamic Properties of the Ethylene Carbonate–Trifluoroethyl Methyl Carbonate and Propylene Carbonate–Trifluoroethyl Methyl Carbonate Systems at T= (298.15 or 315.15) K. *The Journal of Chemical Thermodynamics* **2002**, *34* (6), 795–806. <https://doi.org/10.1006/jcht.2001.0877>.
- (208) Tsionsky, V. Response of the Electrochemical Quartz Crystal Microbalance for Gold Electrodes in the Double-Layer Region. *Journal of The Electrochemical Society* **1996**, *143* (7), 2240. <https://doi.org/10.1149/1.1836987>.
- (209) Lück, J.; Latz, A. Theory of Reactions at Electrified Interfaces. *Physical Chemistry Chemical Physics* **2016**, *18* (27), 17799–17804. <https://doi.org/10.1039/C6CP02681H>.
- (210) Lück, J.; Latz, A. Modeling of the Electrochemical Double Layer and Its Impact on Intercalation Reactions. *Physical Chemistry Chemical Physics* **2018**, *20* (44), 27804–27821. <https://doi.org/10.1039/C8CP05113E>.
- (211) Li, Y.; Chen, H.; Lim, K.; Deng, H. D.; Lim, J.; Fraggadakis, D.; Attia, P. M.; Lee, S. C.; Jin, N.; Moškon, J.; Guan, Z.; Gent, W. E.; Hong, J.; Yu, Y.-S.; Gaberšček, M.; Islam, M. S.; Bazant, M. Z.; Chueh, W. C. Fluid-Enhanced Surface Diffusion Controls Intraparticle Phase Transformations. *Nature Materials* **2018**, *17* (10), 915–922. <https://doi.org/10.1038/s41563-018-0168-4>.

- (212) Wang, R.; Boyd, S.; Bonnesen, P. V.; Augustyn, V. Effect of Water in a Non-Aqueous Electrolyte on Electrochemical Mg²⁺ Insertion into WO₃. *Journal of Power Sources* **2020**, 477, 229015. <https://doi.org/10.1016/j.jpowsour.2020.229015>.
- (213) Hu, J.; Ren, W.; Chen, X.; Li, Y.; Huang, W.; Yang, K.; Yang, L.; Lin, Y.; Zheng, J.; Pan, F. The Role of Anions on the Helmholtz Plane for the Solid-Liquid Interface in Aqueous Rechargeable Lithium Batteries. *Nano Energy* **2020**, 74, 104864. <https://doi.org/10.1016/j.nanoen.2020.104864>.
- (214) Zeng, X.; Hao, J.; Wang, Z.; Mao, J.; Guo, Z. Recent Progress and Perspectives on Aqueous Zn-Based Rechargeable Batteries with Mild Aqueous Electrolytes. *Energy Storage Materials* **2019**, 20, 410–437. <https://doi.org/10.1016/j.ensm.2019.04.022>.
- (215) Liu, S.; Hu, J. J.; Yan, N. F.; Pan, G. L.; Li, G. R.; Gao, X. P. Aluminum Storage Behavior of Anatase TiO₂ Nanotube Arrays in Aqueous Solution for Aluminum Ion Batteries. *Energy Environ. Sci.* **2012**, 5 (12), 9743. <https://doi.org/10.1039/c2ee22987k>.
- (216) Liu, S.; Ye, S. H.; Li, C. Z.; Pan, G. L.; Gao, X. P. Rechargeable Aqueous Lithium-Ion Battery of TiO₂/LiMn₂O₄ with a High Voltage. *J. Electrochem. Soc.* **2011**, 158 (12), A1490–A1497. <https://doi.org/10.1149/2.094112jes>.
- (217) Kim, Y.-S.; Krieger, S.; Harris, K. D.; Costentin, C.; Limoges, B.; Balland, V. Evidencing Fast, Massive, and Reversible H⁺ Insertion in Nanostructured TiO₂ Electrodes at Neutral PH. Where Do Protons Come From? *J. Phys. Chem. C* **2017**, 121 (19), 10325–10335. <https://doi.org/10.1021/acs.jpcc.7b02395>.
- (218) Perez, A. J.; Beer, R.; Lin, Z.; Salager, E.; Taberna, P.-L.; Abakumov, A. M.; Simon, P.; Tarascon, J.-M. Proton Ion Exchange Reaction in Li₃IrO₄: A Way to New H_{3+x}IrO₄ Phases Electrochemically Active in Both Aqueous and Nonaqueous Electrolytes. *Advanced Energy Materials* **2018**, 8 (13), 1702855. <https://doi.org/10.1002/aenm.201702855>.
- (219) Long, J. W.; Swider, K. E.; Merzbacher, C. I.; Rolison, D. R. Voltammetric Characterization of Ruthenium Oxide-Based Aerogels and Other RuO₂ Solids: The Nature of Capacitance in Nanostructured Materials. *Langmuir* **1999**, 15 (3), 780–785. <https://doi.org/10.1021/la980785a>.
- (220) Dmowski, W.; Egami, T.; Swider-Lyons, K. E.; Love, C. T.; Rolison, D. R. Local Atomic Structure and Conduction Mechanism of Nanocrystalline Hydrous RuO₂ from X-Ray Scattering. *J. Phys. Chem. B* **2002**, 106 (49), 12677–12683. <https://doi.org/10.1021/jp026228l>.
- (221) Liu, Y.; Zhou, F.; Ozolins, V. Ab Initio Study of the Charge-Storage Mechanisms in RuO₂-Based Electrochemical Ultracapacitors. *J. Phys. Chem. C* **2012**, 116 (1), 1450–1457. <https://doi.org/10.1021/jp207616s>.
- (222) Prosini, P. Determination of the Chemical Diffusion Coefficient of Lithium in LiFePO₄. *Solid State Ionics* **2002**, 148 (1–2), 45–51. [https://doi.org/10.1016/S0167-2738\(02\)00134-0](https://doi.org/10.1016/S0167-2738(02)00134-0).
- (223) Kasuya, M.; Sogawa, T.; Masuda, T.; Kamijo, T.; Uosaki, K.; Kurihara, K. Anion Adsorption on Gold Electrodes Studied by Electrochemical Surface Forces Measurement. *J. Phys. Chem. C* **2016**, 120 (29), 15986–15992. <https://doi.org/10.1021/acs.jpcc.5b12683>.
- (224) Srimuk, P.; Lee, J.; Budak, Ö.; Choi, J.; Chen, M.; Feng, G.; Prehal, C.; Presser, V. In Situ Tracking of Partial Sodium Desolvation of Materials with Capacitive, Pseudocapacitive, and Battery-like Charge/Discharge Behavior in Aqueous Electrolytes. *Langmuir* **2018**, 34 (44), 13132–13143. <https://doi.org/10.1021/acs.langmuir.8b02485>.

References

- (225) Tepavcevic, S.; Connell, J. G.; Lopes, P. P.; Bachhav, M.; Key, B.; Valero-Vidal, C.; Crumlin, E. J.; Stamenkovic, V. R.; Markovic, N. M. Role of Structural Hydroxyl Groups in Enhancing Performance of Electrochemically-Synthesized Bilayer V₂O₅. *Nano Energy* **2018**, *53*, 449–457. <https://doi.org/10.1016/j.nanoen.2018.09.005>.
- (226) Kundu, D.; Hosseini Vajargah, S.; Wan, L.; Adams, B.; Prendergast, D.; Nazar, L. F. Aqueous vs. Nonaqueous Zn-Ion Batteries: Consequences of the Desolvation Penalty at the Interface. *Energy & Environmental Science* **2018**, *11* (4), 881–892. <https://doi.org/10.1039/C8EE00378E>.
- (227) Rietveld, H. M. A Profile Refinement Method for Nuclear and Magnetic Structures. *J Appl Cryst* **1969**, *2* (2), 65–71. <https://doi.org/10.1107/S0021889869006558>.
- (228) Rodriguez-Carvajal, J. Recent Advances in Magnetic Structure Determination by Neutron Powder Diffraction. *Physica B: Condensed Matter* **1993**, *192* (1–2), 55–69. [https://doi.org/10.1016/0921-4526\(93\)90108-I](https://doi.org/10.1016/0921-4526(93)90108-I).
- (229) Momma, K.; Izumi, F. VESTA 3 for Three-Dimensional Visualization of Crystal, Volumetric and Morphology Data. *J Appl Cryst* **2011**, *44* (6), 1272–1276. <https://doi.org/10.1107/S0021889811038970>.
- (230) Briois, V.; La Fontaine, C.; Belin, S.; Barthe, L.; Moreno, T.; Pinty, V.; Carcy, A.; Girardot, R.; Fonda, E. ROCK: The New Quick-EXAFS Beamline at SOLEIL. *J. Phys.: Conf. Ser.* **2016**, *712*, 012149. <https://doi.org/10.1088/1742-6596/712/1/012149>.
- (231) Lesage, C.; Devers, E.; Legens, C.; Fernandes, G.; Roudenko, O.; Briois, V. High Pressure Cell for Edge Jumping X-Ray Absorption Spectroscopy: Applications to Industrial Liquid Sulfidation of Hydrotreatment Catalysts. *Catalysis Today* **2019**, *336*, 63–73. <https://doi.org/10.1016/j.cattod.2019.01.081>.
- (232) Autolab. Galvanostatic Intermittent Titration Technique. *Application Note BAT03* **2014**.
- (233) Montella, C. Discussion of the Potential Step Method for the Determination of the Diffusion Coefficients of Guest Species in Host Materials Part I. Influence of Charge Transfer Kinetics and Ohmic Potential Drop. *Journal of Electroanalytical Chemistry* **2002**, *23*.
- (234) Gabrielli, C.; Keddam, M.; Nadi, N.; Perrot, H. Ions and Solvent Transport across Conducting Polymers Investigated by Ac Electrogravimetry. Application to Polyaniline. *Journal of Electroanalytical Chemistry* **2000**, *485* (2), 101–113. [https://doi.org/10.1016/S0022-0728\(00\)00093-0](https://doi.org/10.1016/S0022-0728(00)00093-0).
- (235) Marin-Laflèche, A.; Haefele, M.; Scalfi, L.; Coretti, A.; Dufils, T.; Jeanmairet, G.; Reed, S. K.; Serva, A.; Berthin, R.; Bacon, C.; Bonella, S.; Rotenberg, B.; Madden, P. A.; Salanne, M. MetalWalls: A Classical Molecular Dynamics Software Dedicated to the Simulation of Electrochemical Systems. *Journal of Open Source Software* **2020**, *5* (53), 2373. <https://doi.org/10.21105/joss.02373>.
- (236) Berendsen, H. J. C.; Grigera, J. R.; Straatsma, T. P. The Missing Term in Effective Pair Potentials. *J. Phys. Chem.* **1987**, *91* (24), 6269–6271. <https://doi.org/10.1021/j100308a038>.
- (237) Jorgensen, W. L.; Maxwell, D. S.; Tirado-Rives, J. Development and Testing of the OPLS All-Atom Force Field on Conformational Energetics and Properties of Organic Liquids. *J. Am. Chem. Soc.* **1996**, *118* (45), 11225–11236. <https://doi.org/10.1021/ja9621760>.
- (238) Chaudhari, M. I.; Nair, J. R.; Pratt, L. R.; Soto, F. A.; Balbuena, P. B.; Rempe, S. B. Scaling Atomic Partial Charges of Carbonate Solvents for Lithium Ion Solvation and Diffusion. *J. Chem. Theory Comput.* **2016**, *12* (12), 5709–5718. <https://doi.org/10.1021/acs.jctc.6b00824>.

- (239) Liu, X.; Zhang, S.; Zhou, G.; Wu, G.; Yuan, X.; Yao, X. New Force Field for Molecular Simulation of Guanidinium-Based Ionic Liquids. *J. Phys. Chem. B* **2006**, *110* (24), 12062–12071. <https://doi.org/10.1021/jp060834p>.
- (240) Heinz, H.; Vaia, R. A.; Farmer, B. L.; Naik, R. R. Accurate Simulation of Surfaces and Interfaces of Face-Centered Cubic Metals Using 12–6 and 9–6 Lennard-Jones Potentials. *J. Phys. Chem. C* **2008**, *112* (44), 17281–17290. <https://doi.org/10.1021/jp801931d>.

Résumé

Exploration des mécanismes interfaciaux présents dans les batteries métal-ion par EQCM avancée

La recherche ainsi que les progrès technologiques dans le domaine des batteries Li-ion ont été stimulés très tôt par l'émergence des appareils électroniques portatifs et, plus récemment, par la demande constamment croissante des marchés de la mobilité électrique et des réseaux électriques. Mais des améliorations en termes de puissance, durée de vie, autonomie, coût et durabilité sont encore réalisables. La clé de ces améliorations est la maîtrise des interfaces électrode-électrolyte (IEE) en matière de transfert de charge et de transport qui sont liés au mouvement des ions alcalins solvatés. Cette étude vise à mieux comprendre la science fondamentale de l'IEE par l'exploitation des techniques électrogravimétriques basées sur la microbalance à cristal de quartz avec couplage électrochimique (EQCM).

Tout d'abord, nous donnons une description exhaustive des mesures électrogravimétriques ainsi que de l'instrumentation développée avant d'appliquer nos stratégies expérimentales pour entrer dans la vie privée de ces interfaces. Ensuite, l'étude des chimies Li-ion et K-ion est réalisée en électrolyte aqueux ainsi que non-aqueux. Plus particulièrement, nous démontrons le rôle crucial de l'étape de désolvatation sur les performances en puissance de l'électrode. Etape que nous avons rationalisé en nombre de molécules de solvant participant à la sphère de solvation à l'IEE dans les deux électrolytes, défaisant ainsi les idées répandues basées sur les différences de conductivité ionique ou autre. Enfin, par souci d'exhaustivité, le rôle des molécules d'eau dans le processus de transfert interfacial et leur influence sur la cinétique globale dans une batterie à proton est exploré.

Mots-clés : Batterie, EQCM, Métal-ion, Interface électrode-électrolyte, Solvation, Mécanisme d'insertion

Abstract

Exploring interface mechanisms in metal-ion batteries *via* advanced EQCM

Research and technological improvements in rechargeable Li-ion batteries were driven early by the emergence of portable electronic devices and more recently by ever-increasing electric vehicle and power grid markets. Yet, advances in terms of power rate, lifetime, autonomy, cost and sustainability are still feasible. Key to these improvements is the mastering of the electrode-electrolyte interfaces (EEI) in respect of charge transfer and transport that are linked to the motion of the solvated alkali metal ions. This work aims to provide more insight into the underlying science of the EEI by exploiting electrogravimetric-based techniques derived from electrochemical quartz crystal microbalance (EQCM).

To begin with, we give a comprehensive description of the fundamentals of the electrogravimetric measurements together with the developed technical setups prior to unroll our experimental strategies to get into the private life of these interfaces. Then, this thesis enlists the study of Li-ion and K-ion chemistries in both aqueous and non-aqueous electrolytes. More specifically, we demonstrate the crucial role of the desolvation step on the electrode rate capability, that we rationalized in terms of number of solvent molecules pertaining to the solvation shell at the EEI in both electrolytes, hence defeating previous beliefs based on ionic conductivity differences or else. Lastly, for the sake of completeness, the role of the water molecules in the interfacial transfer process and their influence on the overall kinetics in a proton-based battery is explored.

Keywords: Battery, EQCM, Metal-ion, Electrode-electrolyte interface, Solvation, Insertion mechanism